Bioresource Technology 157 (2014) 14–21

Contents lists available at ScienceDirect

Bioresource Technology

journal homepage: www.elsevier.com/locate/biortech

The influence of supramolecular structure of cellulose allomorphs on the interactions with cellulose-binding domain, CBD3b from *Paenibacillus barcinonensis*

Diana Ciolacu [a], Alina Iulia Chiriac [b], F.I. Javier Pastor [b], Vanja Kokol [c,*]

[a] "Petru Poni" Institute of Macromolecular Chemistry, 41A Grigore Ghica Voda Alley, 700487 Iasi, Romania
[b] Department of Microbiology, Faculty of Biology, University of Barcelona, Av. Diagonal 643, 08028 Barcelona, Spain
[c] University of Maribor, Institute of Engineering Materials and Design, Smetanova ulica 17, 2000 Maribor, Slovenia

HIGHLIGHTS

- The recombinant CBD of endoglucanase Cel9B from *Paenibacillus barcinonensis* is used.
- The highest CBD adsorption capacity is recorded for the most crystalline cellulose I.
- The CBD adsorption kinetic is rendered by surface area and porosity of cellulose.
- The CBD desorption is related to hydrophobic interactions with cellulose allomorphs.
- Temperature and pH medium have important influence on CBD desorption.

GRAPHICAL ABSTRACT

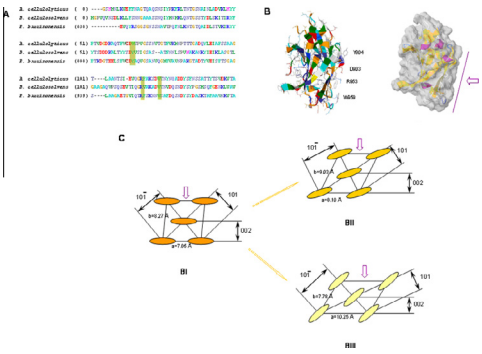

ARTICLE INFO

Article history:
Received 19 September 2013
Received in revised form 6 January 2014
Accepted 8 January 2014
Available online 27 January 2014

Keywords:
Cellulose allomorphs
Endoglucanase
Cellulose binding domain
Adsorption
Desorption

ABSTRACT

The interaction of recombinant cellulose-binding domains (CBDs) of endoglucanase Cel9B from *Paenibacillus barcinonensis* with different cotton cellulose allomorphs (I, II and III) has been investigated, in order to bring new insights regarding the CBD adsorption and desorption processes. The highest CBD adsorption capacity was recorded for cellulose I, confirming the affinity of proteins to the most crystalline substrate. The weakening and splitting of the hydrogen bonds within cellulose structure after CBD adsorption, as well as a decrease of the crystallinity degree were identified by ATR-FTIR spectroscopy and XRD. The CBD's adsorption kinetic was shown to be rendered by properties as, specific surface area and porosity, being confirmed by dynamic vapor sorption measurements. An important influence of temperature (25, 37 and 50 °C) and/or pH medium (4, 5.5, 7 and 10) on the CBD desorption capacity was confirmed, being related to the hydrophobic interactions formed between the CBD and the cellulose allomorphs.

1. Introduction

Cellulose, the most abundant polymer in nature, plays a major role in daily life by representing an important economic investment. The physical properties of cellulose, as well as their chemical behavior and reactivity, are strongly influenced by the arrangement of the cellulose molecules with respect to each other and to the fiber axis. Several crystal structures of cellulose are recognized which differ in unit cell dimensions and chain polarity. The natural form of cellulose, so-called cellulose I, was found to be a composite of cellulose Iα and Iβ crystalline forms. This can easily

* Corresponding author. Tel.: +386 2 220 7896; fax: +386 2 220 7990.
E-mail address: vanja.kokol@um.si (V. Kokol).

http://dx.doi.org/10.1016/j.biortech.2014.01.027
0960-8524/

be converted into the crystalline form of cellulose II by regeneration or mercerization processes. Another crystalline form known as cellulose III can be prepared in anhydrous liquid ammonia or in organic amines. Amorphous cellulose has often been used to understand the behavior of the non-crystalline domains within cellulose, under various conditions. Generally, it is prepared by ball-milling of cellulose, deacetylation of cellulose acetate under non-aqueous alkaline conditions and regeneration of cellulose solution within aqueous media or into non-aqueous media (Ciolacu et al., 2011). The structural differences in cellulose in terms of crystalline and amorphous contents and the sizes and shapes of the crystallites, allow a variable target for the binding modules and the enzymes action on the cell wall.

Most cellulases display a modular structure that, besides a catalytic domain, comprises accessory domains as carbohydrate-binding modules (CBMs), linker or repeat regions, and Fn3 modules (Chiriac et al., 2010). A carbohydrate-binding module (CBM) is defined as a contiguous, independently-folding sequence of amino acids found within the primary structure of a carbohydrate-active enzyme which interacts with a carbohydrate but does not chemically modify its structure (Abbott and Boraston, 2012). CBMs, previously known as cellulose binding domains (CBDs), can significantly contribute to the activity of the enzymes against cellulosic substrates by increasing enzyme–substrate proximity, enhancing accessibility, and modifying the surfaces of the cellulose crystals. It was also found that this module has a determinant role in the adsorption of proteins onto different lignocellulosic substances, as lignin preparations (Pareek et al., 2013). Three basic properties have contributed to CBDs being perfect candidates for many applications: CBDs are usually independent folding units and therefore can function autonomously in chimeric proteins since the attachment matrices are abundant and inexpensive and have excellent chemical and physical properties, and the binding specificities can be controlled, and therefore the right solution can be adapted to an existing problem (Shoseyov et al., 2006).

Due to industrial reasons and to the considerable potential in biotechnology, applied microbiology and immunology, there is much interest in the nature of the binding of CBDs on cellulose. Nowadays there are still controversies about the interaction mode of CBD with cellulose. CBDs from the same organism can differ in their binding specificity and occasionally, two CBDs located on the same enzyme can also exhibit this distinction (Ciolacu et al., 2010). It was established that the binding sites of families I, II and III CBDs are adapted to bind to a surface, while family IV CBD binds to a single molecule (Shoseyov and Warren, 1997). Moreover, the binding process takes place on both crystalline and amorphous regions from cellulose for families I, II and III CBDs, while family IV CBDs do not bind to crystalline cellulose.

To the best of our knowledge there are no reports regarding CBD adsorption on different allomorphic forms of cellulose, even considering the studies regarding the binding preference of CBD for cellulose substrates. Therefore, there is a need to examine the adsorption of CBD on celluloses I, II and III. As the enzyme, a recombinant CBD from *Paenibacillus barcinonensis* was used which is a newly-identified species that shows a multiple-enzyme β-glycanase system correlated with its high polysaccharide degrading potential (Pastor et al., 2001; Sánchez et al., 2004, 2005). This recombinant CBD belongs to modular cellulase Cel9B from *P. barcinonensis*, and has been previously characterized and classified in family III (CBM3b) (Chiriac et al., 2010). The interactions of CBD with cellulose allomorphs were investigated regarding their binding capacity and the structural changes induced, which were characterized by ATR-FTIR spectroscopy and the X-ray diffraction method (XRD). Dynamic vapor sorption (DVS) was applied to provide more information about the adsorption process at the surface of cellulose. In addition, the desorption process under different conditions of temperature (25, 37 and 50 °C) and pH (4, 5.5, 7 and 10), has been investigated.

2. Methods

2.1. Materials

Three cellulose allomorphs were prepared: as *cellulose I* (BI), cotton cellulose (Arshad Enterprises, Pakistan) was used, having been extracted for 8 h in a Soxhlet extractor using an ethanol–benzene mixture; *cellulose II* (BII) was prepared by treating BI in 17.5% NaOH for 24 h at 15 °C; and *cellulose III* (BIII) was prepared by soaking BI in 100% ethylenediamine for 24 h at 15 °C. *Amorphous cellulose* (Ba) was prepared based on the SO_2-diethylamine-dimethylsulfoxide (SO_2-DEA-DMSO) solvent system for the dissolution of cellulose by using ethanol as the regeneration medium (Ciolacu et al., 2011). The CBD from *P. barcinonensis* (*Paenibacillus* sp. strain BP-23) was purified from the recombinant strain *Escherichia coli* BLR (DE3) pET28aCBD2, which expressed the isolated CBD3b (Chiriac et al., 2010). The apparent molecular weight of the recombinant CBD3b, as determined by SDS–PAGE, was 17 kDa. All the other chemicals used were of the highest purity available commercially.

2.2. CBD adsorption and desorption studies

The adsorption studies were performed mixing 3 mg of the different cellulose allomorphs (BI, BII, and BIII) and amorphous cellulose (Ba) with 1.8 mg of CBD in 1 ml of Tris buffer (50 mM, pH7) and incubated for 2 h at 25 °C, using gentle rotation (600 rpm). In parallel, the blank samples were prepared similarly but without CBD. Afterwards the fibers were centrifuged at 5000 rpm for 5 min and the CBD concentration in supernatant (P_F, μM) was measured using a TECAN Infinite M200 spectrophotometer. The protein concentration was determined by the Lowry method (Bio-Rad *DC* Protein assay) and the bound CBD (P_B, μM) calculated by Eq. (1):

$$P_B = [(P_T - P_F)/m] \times V \ (\mu mol/g) \quad (1)$$

where P_T – the initial concentration of CBD (μM); P_F – the free CBD concentration (μM); P_B – the bound CBD concentration (μM); m – the mass of cellulose fibers (g); V – the volume of the buffer (L).

The protein adsorption on cellulose was fitted to a Langmuir isotherm which assumes that the adsorption can be described by single adsorption equilibrium constant and a maximal adsorption capacity. The data were analyzed by non-linear regression analysis of $1/P_B$ versus $1/P_F$ and the distribution coefficient, R was defined as:

$$R = K_d \cdot P_{Max} \quad (2)$$

where P_{Max} – the maximum protein adsorption (μmol CBD/g); K_d – the dissociation constant (L/μmol).

The fibers were washed with the same volume of buffer, centrifuged at 5000 rpm for 5 min and lyophilized using a Mini Lyotrap freeze-dryer.

For desorption experiments 3 mg of different cellulose allomorphs treated with CBD (BI-CBD, BII-CBD, BIII-CBD) and CBD-treated amorphous cellulose (Ba-CBD) per mL of different buffer solutions (pHs of 4, 5.5, 7 and 10) were washed for 1 h at different temperatures (25, 35 and 50 °C), with gentle rotation (600 rpm). The blank samples were prepared in parallel Afterwards the fibers were centrifuged at 5000 rpm for 5 min and the CBD concentration in supernatant was measured in a TECAN Infinite M200 spectrophotometer. The desorbed protein was measured by the Lowry method.

2.3. Dynamic vapor sorption (DVS)

Dynamic water vapor sorption capacity of the cellulose allomorphs was measured by using IGAsorp, a fully automated gravimetric analyzer, supplied by Hiden Analytical, Warrington (UK). The water vapors sorption capacity was measured at 25 °C within the 0–90% relative humidity range (RH) in a dynamic regime. The fibers were dried at 25 °C in flowing nitrogen until the weight of the sample was in equilibrium at RH < 1% by considering the dry mass. After this, the measurements began with the sorption curve until the maximum level for RH had been reached, and then with desorption curve by decreasing the vapor pressure.

2.4. X-ray diffraction analysis (XRD)

The cellulosic samples were analyzed by a Bruker D8 X-ray diffractometer using CuKα radiation ($\lambda = 1.5418$ Å) generated at 30 mA and 40 kV for a range of diffraction angle (2θ) between 10–50°. PeakFIT v4.11 (SYSTAT Software Inc.) software has been used for the data processing. The structural parameters were calculated using TOPAS 4.2 (Bruker-AXS, Germany) software.

The crystallinity index (CrI) of the cellulose samples was established by Eq. (3) and the lattice spacings (d-spacings) were calculated by using Eq. (4):

$$CrI(\%) = [S_C/(S_C + S_A)] \times 100 \quad (3)$$

$$\lambda = 2d_{hkl} \times \sin\theta \quad (4)$$

where S_C – the surface of the crystalline area; S_A – the surface of the amorphous area; d_{hkl} – the lattice spacing within one of the crystallographic planes; λ – the X-ray wavelength (0.154 nm); 2θ – the corresponding Bragg angle (°).

The crystallite size was calculated based on the width of the diffraction patterns (Krässig, 1993):

$$D_{(hkl)} = k \times \lambda/\beta \times \cos\theta \quad (5)$$

where $D_{(hkl)}$ – the size of crystallite (nm); k – the Scherrer constant (0.94); β – the full-width at half of the reflection.

2.5. ATR-FTIR analysis

ATR-FTIR spectra were recorded using a Perkin-Elmer Spectrum One GX FT-IR spectrometer with Golden Gate ATR attachment and diamond crystal. The absorbance measurements were carried out within the range of 400–4000 cm^{-1} and a resolution of 4 cm^{-1}. The length of hydrogen bonds (R) was determined on the basis of the frequency shift ($\Delta\nu$) of the OH absorption band (Ciolacu et al., 2010):

$$\Delta\nu = 4.43 \times 10^3(2.84 - R) \quad (6)$$

The energy of the H-bonds was calculated from the equation (Ciolacu et al., 2010):

$$E_H = (1/k) \times [(\nu_0 - \nu)/\nu_0] \quad (7)$$

where ν_o – the standard frequency corresponding to free –OH groups (3600 cm^{-1}); ν – the frequency of the bonded –OH groups; $k = 1.68 \times 10^{-2}$ $kcal^{-1}$. The asymmetric index (a/b) was determined from the ratio between the segment widths at half the height of the OH absorption band. The crystallinity ratio ($Cr.R$) of the cellulose was evaluated by the absorbance ratios, as $Cr.R._1 = A_{1430}/A_{899}$ and $Cr.R._2 = A_{1372}/A_{2900}$ (Salmén et al., 2005).

2.6. Structure determination and refinement

The 3D model of the CBD of Cel9B from *P. barcinonensis* was generated using the online modeling software Swiss-Model, Expasy (http://swissmodel.expasy.org/) by running the entire Cel9B sequence (GenBank entry: CAB38941.1) in the alignment mode. The output PDB file generated was visualized using the open-source Java viewer for chemical structures in 3D. Sequence alignment was performed online using Blastp from the NCBI web page (http://blast.ncbi.nlm.nih.gov/).

3. Results and discussion

3.1. Influence of the supramolecular structure of cellulose allomorphs on CBD adsorption

The ability of the recombinant CBD3b from *P. barcinonensis* to bind onto different cellulose allomorphs (BI, BII and BIII) and amorphous cellulose (Ba) was studied. The highest concentration of bounded CBD was recorded for BI, followed by BIII and BII, while Ba showed the lowest amount of bounded CBD (Fig. 1a). These differences in CBD adsorption could be explained by differences in the specific surface areas and crystalline structure of the samples, and confirms the affinity of protein for the most crystalline substrates. The higher adsorption rate of CBD to BIII than BII can be explained by the slight reversibility of cellulose III to cellulose I accompanied by a partial recrystallization, in the presence of aqueous media during CBD adsorption process.

The quantitative response of the adsorption process was determined by measuring the concentration of bound CBD (P_B) as a function of the free CBD concentration (P_F) (Fig. 1b). The linear response obtained from the isotherms proved that the lateral protein–protein interactions did not significantly influence the binding of the CBD. The slopes of the binding isotherms were further used to estimate the apparent affinity of CBD to cellulose allomorphs and to amorphous cellulose. The index to estimate the affinity is the dissociation constant, K_d, while the maximum protein adsorption P_{Max} and the distribution coefficient R were selected as the indexes of the binding capacity. Thus, a smaller value of the dissociation constant means a greater affinity of CBD toward substratum (Ciolacu et al., 2010). The cellulose adsorption parameters of CBD to cellulosic substrates are presented in Table 1.

The data showed that the affinity of CBD was higher for all cellulose allomorphs than for amorphous cellulose. Moreover, by comparing the samples BI and Ba it was observed that the affinity for the most crystalline substrate was almost two times higher than for the amorphous one. Regarding the maximum molar amounts of adsorbed protein, P_{Max}, the highest value was shown by BI (5.86 μmol/g), followed by BIII (5.485 μmol/g) and BII (5.362 μmol/g). This could be explained by the crystallinity of the samples, which appeared to be a key parameter regarding the CBD binding capacity. Based on the data reported in literature the highly crystalline forms of cellulose, like absorbent cotton were able to bind substantially more CBD (~6.4 μmol CBD/g substrate), while the more processed fibrous cellulose, containing less of the native crystalline form, bound only ~0.2 μmol/g CBD (Goldstein et al., 1993). Thus, it can be concluded that CBD has a distinct preference for more crystalline cellulose and the affinity decreases with any increasing of the less ordered structure within the cellulose.

3.1.1. Dynamic water vapors sorption measurement (DVS)

The proportions of the crystalline and amorphous fraction within a given cellulose substrate have been considered for a long time as the major factor influencing the accessibility and reactivity of

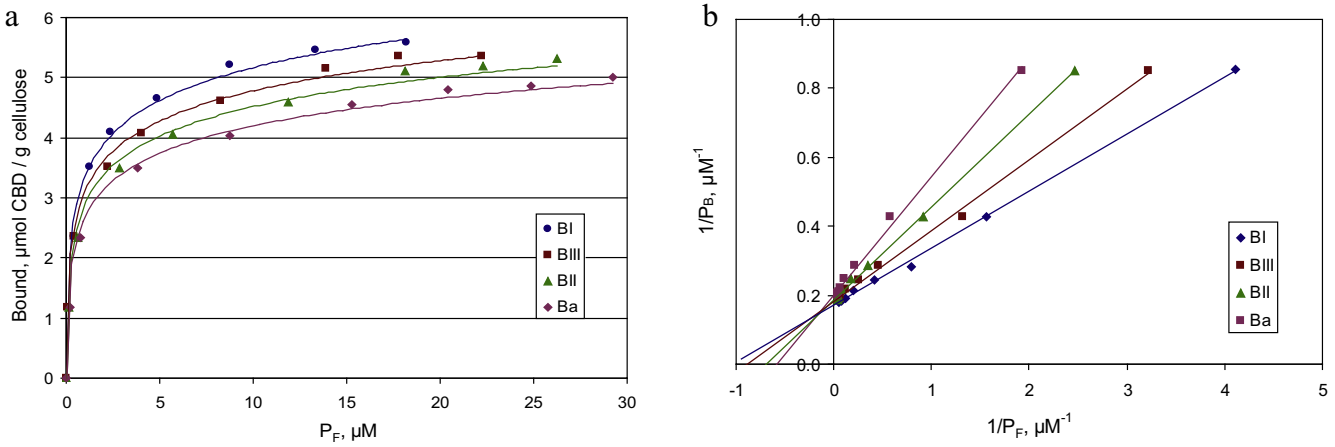

Fig. 1. The adsorption isotherms (a) and the non-linear regression (b) of CBD binding to the cellulose allomorphs (BI, BII, BIII)) and amorphous cellulose (Ba).

Table 1
Langmuir CBD adsorption parameters on cellulose.

Sample	K_d, L/μmol	P_{Max}, μmol/g	R, L/g
BI	0.970	5.862	5.683
BII	1.448	5.362	7.765
BIII	1.125	5.485	6.172
Ba	1.701	4.960	8.437

the fibers (Krässig, 1993). Nowadays, it is generally known that the accessibility of cellulase to cellulose depends on the structural properties, namely surface area, porosity, crystallinity index, and the degree of polymerization (Ogeda et al., 2012). Due to the fact that the accessibility of water to cellulose can be directly associated with the water sorption ability and depends on the cellulose's internal geometric structures (Ogeda et al., 2012), DVS analysis was used as a precise method to establish those interactions. At a given relative humidity, the total water vapor uptake depends largely on the cellulose's physical structure. Therefore, it is widely used for the characterization of cellulose microstructure, including the specific surface area and the porous structure of hydrophilic cellulosic materials, which are relevant factors regarding the accessibility and reactivity of cellulose fibers (Ioelovich and Leykin, 2011).

Water vapors sorption behavior was evaluated on the basis of the Brunaeur-Emmet-Teller (BET) and Guggenheim-Anderson-de Boer (GAB) models. The BET model is commonly used for modeling the sorption isotherm for water activities ranging from 0.05 to 0.35, while the GAB model is used for modeling the sorption isotherm on a wider range. In order to estimate the average pore size the model of Barett, Joyner and Halenda (BJF model) was applied by considering the pores to be cylindrical:

$$r_{pm} = 2 \times V_{lip}/A \quad (8)$$

where V_{liq} – the liquid volume (mL); r_{pm} – the average pore size (nm); A – the BET surface area (m^2/g).

The average pore size (rpm) of cellulose allomorphs, established from the desorption branch, decrease in the order BI (1.53 nm) > BII (1.43 nm) > BIII (1.32 nm), as a result of the different chemical treatments. In the same time the internal surface area (ABET) was found to be ~237.23 m^2/g for BII, a higher value when it is compared with ~184.7 m^2/g for BIII and ~152.33 m^2/g for BI, respectively. It has been observed that the A_{BET} values obtained by BET model are in a good agreement with those of A_{GAB}, determined by GAB model. The increase of internal surface area suggested that new accessible surfaces were open after the mercerization process, fact which implied a disruption of interfibrillar hydrogen bonds. An opposite trend was recorded for BIII with a slightly increased of A_{BET} value, even if was expected to be higher then BII. A justification of this behavior is related to the ability of BIII to return to the original cellulose structure, preserving the increased existing pores.

Generally, the maximum amount of the CBD that can be absorbed on the cellulosic substrate depends directly on the accessibility of substrate sites. Therefore to improve the accessibility of cellulose fibers, the pores must be opened and the highly-ordered regions must be altered. Thus, the highest amount of absorbed CBD (5.862 μmol/g) was recorded for BI, which presents the highest average pore size, followed by BIII and BII, respectively.

3.1.2. XRD measurements

In the literature there are only a few references available regarding the effect of CBD binding on cellulose, which used XRD as an evaluation method (Ciolacu et al., 2010; Hall et al., 2011). This study is thus the first one regarding the CBD adsorption on different allomorphic forms of cellulose. The diffraction peaks were derived by peak fitting with Lorentzian functions, while the amorphous peak with Gaussian functions, which was added to a third-order polynomial baseline that represents diffuse scattering.

The diffractogram of BI-CBD is typical for cellulose I, with its characteristic reflexes corresponding to the planes (101), ($10\bar{1}$) and (002), at 14.8°, 16.6° and 22.7° angles, respectively. It was recorded an intensity decrease of (002) plane in comparison with BI, which confirmed the decrease of the sample's crystallinity. This observation is sustained by the known fact that the diminution of crystallinity is reflected in a decrease of the (002) plane (Ford et al., 2010). A noticeable decrease of the crystallinity was recorded for the BII-CBD, where the intensity of (002) plane decreased together with those of (101) and ($10\bar{1}$) peaks, while preserving the crystalline structure of cellulose II. Instead, the diffractogram of BIII-CBD recorded a partial reversion to cellulose I, explained by the reversibility in the presence of the water-based medium of the allomorphic form of cellulose III. Thus, for BIII the peak for (101) plane is located at 11.8°, while the ($10\bar{1}$) and (002) planes were superimposed at a Bragg angle of 21°. In the diffractogram of BIII-CBD the reflection of the (101) plane was maintained at approximately the same value 11.9° but the new (101) and ($10\bar{1}$) peaks characteristic for cellulose I appeared at 14° and 15°. In regard to the (002) peak, a new reflection appeared at a higher Bragg angle 22°, corresponding to cellulose I. This reversibility of cellulose III to cellulose I implied only a partial recrystallization, the crystals remaining mainly with distortion and fragmentation

Cellulose (2014) 21:203–219
DOI 10.1007/s10570-013-0118-x

ORIGINAL PAPER

Changes of supramolecular cellulose structure and accessibility induced by the processive endoglucanase Cel9B from *Paenibacillus barcinonensis*

Alina I. Chiriac · Francisco I. Javier Pastor · Valentin I. Popa · Magdalena Aflori · Diana Ciolacu

Received: 27 May 2013 / Accepted: 19 November 2013 / Published online: 27 November 2013

Abstract A newly identified cellulase with a high polysaccharide degrading potential and a processive mode of action, has been evaluated on cellulose fibers. Cellulase Cel9B from *Paenibacillus barcinonensis* is a modular endoglucanase with the domain structure GH9-CBM3c-Fn3-CBM3b, consisting of a family nine catalytic module GH9, an auxiliary module CBM3c, a fibronectin-like module Fn3, and a functional cellulose binding module CBM3b. The whole cellulase Cel9B (E1) and two truncated forms of the enzyme that consist of the catalytic module linked to the auxiliary module, GH9-CBM3c (E2), and of the cellulose binding module of the enzyme, CBM3b (CBD), were applied to softwood dissolving pulp. The changes in the supramolecular structure and morphology of the fibres after the enzymatic treatment were evaluated by viscosimetry, X-ray diffraction (XRD), thermogravimetric analysis, differential scanning calorimetry and scanning electron microscopy (SEM). XRD studies provided the crystallite size, interplanar distances and crystallinity index of the samples before and after the enzymatic treatment. The treatment with cellulases E1 and E2 decreased the degree of polymerization and increased the crystallinity index of the pulp. Both E1 and E2 had a pronounced capacity for removing fuzz and improved the smoothness and surface appearance of the fibers, as shown by SEM. On the other hand, CBD proved to be less effective under the tested conditions. Moreover, the solubility of dissolving pulp in alkaline solutions has been evaluated as an indirect measure of cellulose accessibility. A notable enhancement in alkaline solubility of the samples treated with the cellulases was observed.

Keywords Endoglucanase · Dissolving pulp · Alkali solubility · XRD · TG/DG · DSC

A. I. Chiriac · F. I. J. Pastor
Department of Microbiology, Faculty of Biology, University of Barcelona, Av. Diagonal 643, 08028 Barcelona, Spain

V. I. Popa
Faculty of Chemical Engineering and Environmental Protection, "Gheorghe Asachi" Technical University, Bvd. Mangeron No 71, 700050 Iasi, Romania

M. Aflori · D. Ciolacu (✉)
Department of Physical Chemistry of Polymers, "Petru Poni" Institute of Macromolecular Chemistry, 41A Grigore Ghica Voda Alley, 700487 Iasi, Romania
e-mail: dciolacu@icmpp.ro

Introduction

Cellulose, the most abundant and common biopolymer on our planet, is used in a wide range of applications, from building materials and clothing to biomaterials and pharmaceutical products. Cellulose consists of linear chains of β-1,4-linked glucose residues that in the native state form an extensive hydrogen-bonded

network that gives rise to tightly packed crystalline structures (elementary fibrils) that are involved in a hierarchical supramolecular organization that also includes microfibrils and the cellulose fibres (Zhang and Lynd 2004). Despite the large number of hydroxyl groups, the packed structure of cellulose gives it low reactivity and makes it recalcitrant to biodegradation. Only the cellulose molecules on the surfaces of the fibrils or fibril aggregates and those between the crystallites in the cell wall are accessible to most solvents and reagents (Engstrom et al. 2006).

The accessibility of cellulose is of great importance for the production of cellulose derivatives and regenerated cellulose, where a homogeneous substitution of the hydroxyl groups of cellulose chains is desirable in order to obtain quality products (Klemm et al. 2002). Nevertheless, the compact structure of the cellulose complicates the accessibility of functional groups heterogeneous substitution frequently results. The activation of cellulose, which is defined as the opening of the supramolecular structure of cellulose to solvent and chemicals, is a necessary step for its dissolution. This can be done for example by chemical, mechanical, thermal or enzymatic treatments, either separated or in combination, and consists of opening the inner pore structure, disrupting fibrillar aggregation, and reducing crystallinity to increase availability of hydroxyl groups. Among other methods, the one that best suits the current environmental requirements is the treatment with cellulose-degrading enzymes. Evaluation of different types of these enzymes has shown that endoglucanases have potential application to increase the reactivity of cellulose (Rahkamo et al. 1996, 1998; Cao and Tan 2005, 2006; Henriksson et al. 2005).

Cellulases are widely used in industrial applications such as in food, pulp and paper, textile, surfactants and bioethanol production (Bhat 2000). Cellulases are usually multidomain enzymes, comprising, apart from the catalytic domain (GH), one or more ancillary domains such as carbohydrate binding modules (CBMs). These binding modules improve enzyme performance by increasing enzyme–substrate proximity, enhancing accessibility, and modifying the surface of cellulose (Tomme et al. 1998). They can differ widely in their binding kinetics and specificity (Carrard et al. 2000; Boraston et al. 2004).

Paenibacillus barcinonensis is a newly identified species that shows a multiple-enzyme β-glycanase system correlated with its high polysaccharide degrading potential (Pastor et al. 2001; Sánchez et al. 2003, 2005). Cellulase Cel9B from *Paenibacillus barcinonensis* is a modular family nine endoglucanase with a processive mode of action. It possesses the modular structure GH9-CBM3c-Fn3-CBM3b, where GH9 is a family nine catalytic module, CBM3c is an auxiliary module, Fn3 is a fibronectin-like module, and CBM3b is a functional cellulose binding module (Pastor et al. 2001). In previous work the enzyme was applied to eucalyptus pulps and resulted in a biorefining effect that notably improved mechanical properties of paper (García et al. 2002). Several truncated enzymes derived from Cel9B were recently constructed and evaluated in order to determine the module(s) of the enzyme responsible for the beneficial effect found (Chiriac et al. 2010). One of the cellulases constructed from the structure GH9-CBM3c showed an increased effect when compared to the whole enzyme, while the isolated binding module CBM3b showed only a minor effect on mechanical properties, although SEM analysis clearly showed that both enzymes modified fiber surfaces (Cadena et al. 2010).

To analyze whether the beneficial action on paper grade pulp could be extrapolated to other pulps and in order to extend the study and seek new applications, we have studied the effect of the whole enzyme Cel9B (E1), the truncated cellulase GH9-CBM3c (E2) and the recombinant cellulose binding module CBM3b (CBD) on dissolving pulp from spruce wood. Modifications of supramolecular structures and the morphology of the fibers have been evaluated by viscosimetric measurements, as well as by X-ray diffraction (XRD), thermogravimetry (TG/DTG), differential scanning calorimetry (DSC), and scanning electron microscopy (SEM). The alkali solubility of cellulose has been also evaluated as an indirect measure of the cellulose accessibility.

Materials and methods

Materials

Spruce dissolving pulp (Extranier F) was purchased from Rayonier, USA and was coded as Dpulp. The enzymes applied were cellulase Cel9B from *Paenibacillus barcinonensis*, which is a modular endoglucanase with the structure GH9-CBM3c-Fn3-CBM3b

Table 1 Enzyme doses applied

Samples	Enzymatic activity (U/g)	
	CMCase	Avicelase
E1-C1	100	1
E1-C2	200	2
E2-C1	100	0.5
E2-C2	200	1

(E1), a truncated derivative of the cellulase with the structure GH9-CBM3c (E2), and a recombinant cellulose binding module CBM3b (CBD) derived from the enzyme. They were purified from recombinant *Escherichia coli* clones carrying the respective encoding genes. E1 and E2 show cellulase activity as they contain the catalytic module GH9, while CBD does not show hydrolytic activity on cellulose (Chiriac et al. 2010). The whole enzyme E1 and the truncated form E2 have typical hydrolytic properties of endoglucanases. Their saccharification activities against amorphous celluloses, such as carboxymethyl cellulose (CMC), are much higher (100–200×) than activities against crystalline cellulosic substrates, such as Avicel. However, the ratio between activity on CMC (CMCase) and activity on Avicel (Avicelase) is different in the two cellulases. E1 and E2 show the same activity on CMC, but E1 is twice more active on Avicel than E2 (Chiriac et al. 2010). The activities of E1 and E2 are shown as international units (IU) (Table 1). One unit of enzymatic activity was defined as the amount of enzyme that releases 1 µmol of reducing sugar equivalent per minute under the assay conditions described. All other chemicals and reagents used were of analytical grade.

Enzymatic treatment of pulp

Before the enzymatic treatment, the pulp was disintegrated in a standard disintegrator Frank-PTI (T 205 sp-02 Tappi Test Method 2002) and left for hydration over night in the reaction buffer. Samples of 0.5 g of oven dry pulp (odp) at 1 % consistency were incubated with the enzymes in 50 mM acetate buffer, pH 5.5 at 50 °C in a 250 ml Erlenmeyer flask, under 200 rpm stirring in a water bath shaker. E1 and E2 were applied at 1 Avicelase U/g odp, for 24 h (E1-C1t1, E2-C2t1) or 72 h (E2-C2t2). E1 was also applied at 2 Avicelase units for 24 h (E1-C2t1), while E2 was also applied at 0.5 Avicelase U/g odp for 24 h (E2-C1t1). In addition, one cellulosic sample was pretreated with ultrasound at 35 kHz for 1 h and subsequently treated with E1 at 2 Avicelase U/g odp for 24 h (E1-C2USt1). The enzyme doses of E1 and E2 are shown in Table 1. As CBD does not have hydrolytic activity, its dose was normalized in µmol/g odp. CBD was applied at 0.5 or 1 µmol/g odp for 24 h (CBD-C1 and CBD-C2). The amount of reducing sugar released from pulps was determined using the method of Nelson and Somogyi (Chiriac et al. 2010).

Determination of alkali solubility

The effect of the different enzymes on the supramolecular structure of dissolving pulp was studied by an indirect method, alkaline solubility. The method was applied to the control (Dpulp) and the enzymatic treated samples (E1-C2t1, E2-C2t1 and CBD-C2).

The solubility of cellulose in 8.5 % alkali was determined as described by Isogai and Atalla (1998). Samples of 0.5 g cellulose (odp) were mixed with 1.25 g of NaOH crystals and 13.45 ml of distilled water. The samples were vigorously stirred and then kept at −25 °C for 24 h. Samples were then brought to room temperature and the NaOH concentration was adjusted to 5 % by adding distilled water. The soluble cellulose fraction was separated from the insoluble one by filtration on a glass filter (G3). The insoluble fraction was successively washed with solutions of 5 % NaOH, 1 % NaOH, distilled water, 1 % acetic acid and distilled water and was dried in an oven for 3 days at 30 °C. Samples were heated at 105 °C and weighed to determine the absolute dry weight. The dissolution degree of cellulose was expressed with the following formula:

$$S(\%) = [(m_0 - m_f)/m_0] \cdot 100$$

where S is solubility degree, m_0, is the initial amount of cellulose and m_f is the amount of cellulose retained on glass filter.

Degree of polymerization

The degree of polymerization (DP) of the studied samples was calculated from the intrinsic viscosity of the corresponding solutions of the samples in 1 M

cupriethylendiamine, method according to Tappi Test Method T230 om-89 (Tappi Test Method 1997).

X-ray diffraction analysis

The cellulosic fibers were pressed into discs using a cylindrical steel mold with a diameter of 1.3 cm and a pressure of about 500 MPa, in a laboratory press. The diffractograms of the cellulosic samples were recorded by a Bruker D8 X-ray diffractometer using CuKα radiation (λ = 1.5418 Å) generated at 30 mA and 40 kV for a range of diffraction angle (2θ) between 10 and 50°. The Mecury 3.1 program from the Cambridge Crystallographic Data Centre (CSD System) was used to simulate diffraction patterns for comparisons with the experimental patterns. The experimental diffraction patterns exhibited peaks that were deconvoluted from background scattering by using Lorentzian functions, while the diffraction pattern of the amorphous component was approximated by a Gaussian function curve-fitting analysis. The structural parameters were calculated using TOPAS 4.2 software (Bruker-AXS, Germany).

The crystallinity index (Icr) was calculated based on the following formula (Sun et al. 2009; Park et al. 2010):

$$I_{cr}(\%) = \frac{S_C}{S_C + S_A} \cdot 100 \quad (1)$$

where S_C is the area under the crystalline peaks and S_A is the remaining (amorphous) area.

The lattice spacings (d-spacings) were calculated using Bragg equation:

$$\lambda = 2d_{hkl} \cdot \sin\theta \quad (2)$$

where d_{hkl} is the lattice spacing of the hkl crystallographic planes, λ is the X-ray wavelength, and 2θ is the corresponding Bragg angle.The crystallite size was calculated based on the width of the diffraction peaks, from the Scherrer equation (Krässig 1993):

$$D_{(hkl)} = \frac{k \cdot \lambda}{\beta \cdot \cos\theta} \quad (3)$$

where $D_{(hkl)}$ is the size of crystallite (nm), k is the Scherrer constant (0.94), λ is the X-ray wavelength (0.15418 nm) and β is the full-width at half-maximum of the reflection hkl, measured (radians)in 2θ, and θ is half of the 2θ value for the corresponding Bragg peak.

Thermogravimetric analysis

Cellulose samples of 5–10 mg were placed in an aluminum oxide crucible and analyzed in a Mettler Toledo TGA/SDTA 851 device with a heating rate of 10 °C/min, at temperatures ranging from 25 to 700 °C, under a nitrogen atmosphere. Prior to analysis, the samples were placed in a desiccator at a constant relative humidity of 65 %, for 7 days and a temperature of 20 °C. The kinetic interpretation was performed with the STARe software offered by Mettler Toledo. To ensure data reproducibility, several thermograms were recorded for each sample.

Differential scanning calorimetry

Differential scanning calorimetry studies were performed using a Mettler Toledo DSC1. The cellulose samples, measured in closed lid aluminum pans, were heated at a rate of 10 °C/min under a nitrogen atmosphere, from 10 to 300 °C. The cellulosic samples were conditioned in a desiccator for 72 h, at a constant relative humidity of 65 % and temperature of 20 °C, until constant weights.

Scanning electron microscopy

The surface appearance of the fibers was analyzed with a HITACHI S 2300 scanning electron microscope. Prior to analysis the samples were covered with a gold layer using a SPS Polos Spin Coater.

Results and discussion

Enzymatic hydrolysis

In the present study the effectiveness of cellulase E1, a family 9 modular endoglucanase from *Paenibacillus barcinonensis*, and of two truncated forms of the enzyme, cellulase E2 and CBD have been evaluated. E1 is the whole enzyme, which contains a functional carbohydrate binding module. E2 consists of the enzyme devoid of this module, and CBD is the isolated carbohydrate binding module. Cellulases E1 and E2 are endoglucanases: they have high activity on amorphous cellulose (CMC) and low activity on crystalline cellulose (Avicel). However, they have differences in substrate specificity, E1 being twice as

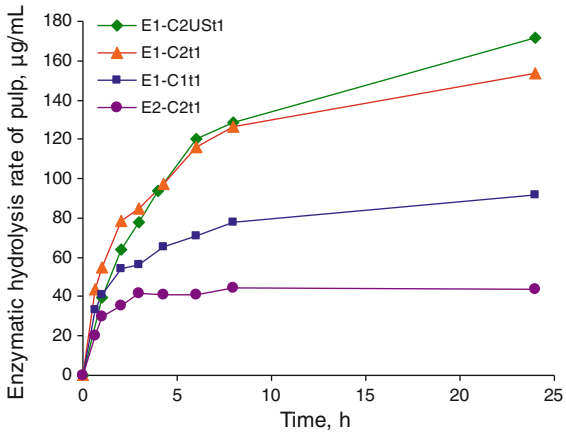

Fig. 1 Enzymatic hydrolysis rate of pulp

active as E2 on Avicel. On the other hand, CBD does not have hydrolytic activity on cellulosic substrates.

Dissolving pulp (Dpulp) was treated with the different enzymes (E1, E2 and CBD) and as a first evaluation of their effect on pulps, the rate of cellulose hydrolysis was determined (Fig. 1).

A rapid release of reducing sugars was observed in the first hours of the treatments, but slowed down as the incubation progressed in time. Cellulase E1 released sugars more rapidly than did cellulase E2. When the two cellulases were applied at the same dose (measured as CMCase units—200 U/g odp), cellulase E1 (E1-C2t1) released a remarkably higher amount of sugars from pulps (154.8 µg/mL) than did cellulase E2 (E2-C2t1) (47.5 µg/mL). This probably reflects the differences in the Avicelase units among the enzyme preparations tested, as Avicelase activity of E1-C2t1 (2 U/g odp) is higher than that of E2-C2t1 (1 U/g odp). However, when the dose of E1 was reduced to equivalence the Avicelase units to 1 U/g odp, although the release of sugars was decreased, it was still higher than E2. In this way the amount of sugars released by E1-C1t1 was 86 µg/mL. This is probably a consequence of a better accessibility for E1 to the crystalline portions of cellulosic fibers than for E2, which lacks the carbohydrate binding module contained in the whole enzyme (Chiriac et al. 2010). To improve the enzymatic hydrolysis process, pulp was pretreated with ultrasound for 1 h. An increase of the amount of reducing sugar from 154.8 µg/mL (E1-C2t1) to 171.9 µg/mL (E1-C2USt1) was recorded. Treatment with the isolated cellulose binding module, CBD, did not release sugars from pulps, as was expected.

Influence of enzymatic hydrolysis on the supramolecular structure

X-ray diffraction

X-ray diffraction was applied to investigate the changes in the crystalline structure of the enzymatically treated cellulose pulps. The diffractograms of the reference (Dpulp) and the enzymatic treated samples are shown in Fig. 2. The diffraction patterns of all samples are characteristic of cellulose I.

To display the intensities, positions and Miller indices of the individual diffraction peaks that contribute to the diffractograms, the Mercury program was used to calculate a pattern with very narrow peaks. By using the crystal structure information file (.cif) from the crystal structure of Nishiyama et al. (2002) and Mercury's default peak width at half height (pwhm) value of 0.1°, a simulated pattern with peaks mostly without overlapping was obtained (French and Santiago Cintrón 2013; French 2014).

For Dpulp, this "deconvolution" reveals three main contributors of intensity to the three peaks that have Miller indices of (200), found at a Bragg angle of 22.55°, as well as the 2θ reflections at 14.71° and 16.63°, respectively, assigned to the (1–10) and (110) lattice planes (Fig. 2a). A sharpening and an increase of the intensity profiles corresponding to the reflection of the (200) crystallographic plane was observed for all enzyme-treated samples.

The greatest increase of the intensity of (200) reflection was for the samples treated with cellulase E2 (Fig. 2b). This observation indicates the presence of better-defined crystalline domains and is confirmed by the increased values of the crystallinity index (Icr). The increase in crystallinity of the residue obtained after the enzymatic hydrolysis (Table 2) suggests that the hydrolysis of amorphous cellulose could be favored over that of the crystalline cellulose. The crystal structure extent within the cellulose structure has an important effect on the performance of the enzymatic hydrolysis, a fact that can be better explained by determining the crystallite size (D) and the lattice spacing (d-spacing) values. The calculation of the crystallite size normal to the *hkl* planes was done based on the estimation of the peak width at half-maximum amplitude, while the d-spacings of the (1–10), (110) and (200) peaks were calculated with the Bragg equation (Table 2).

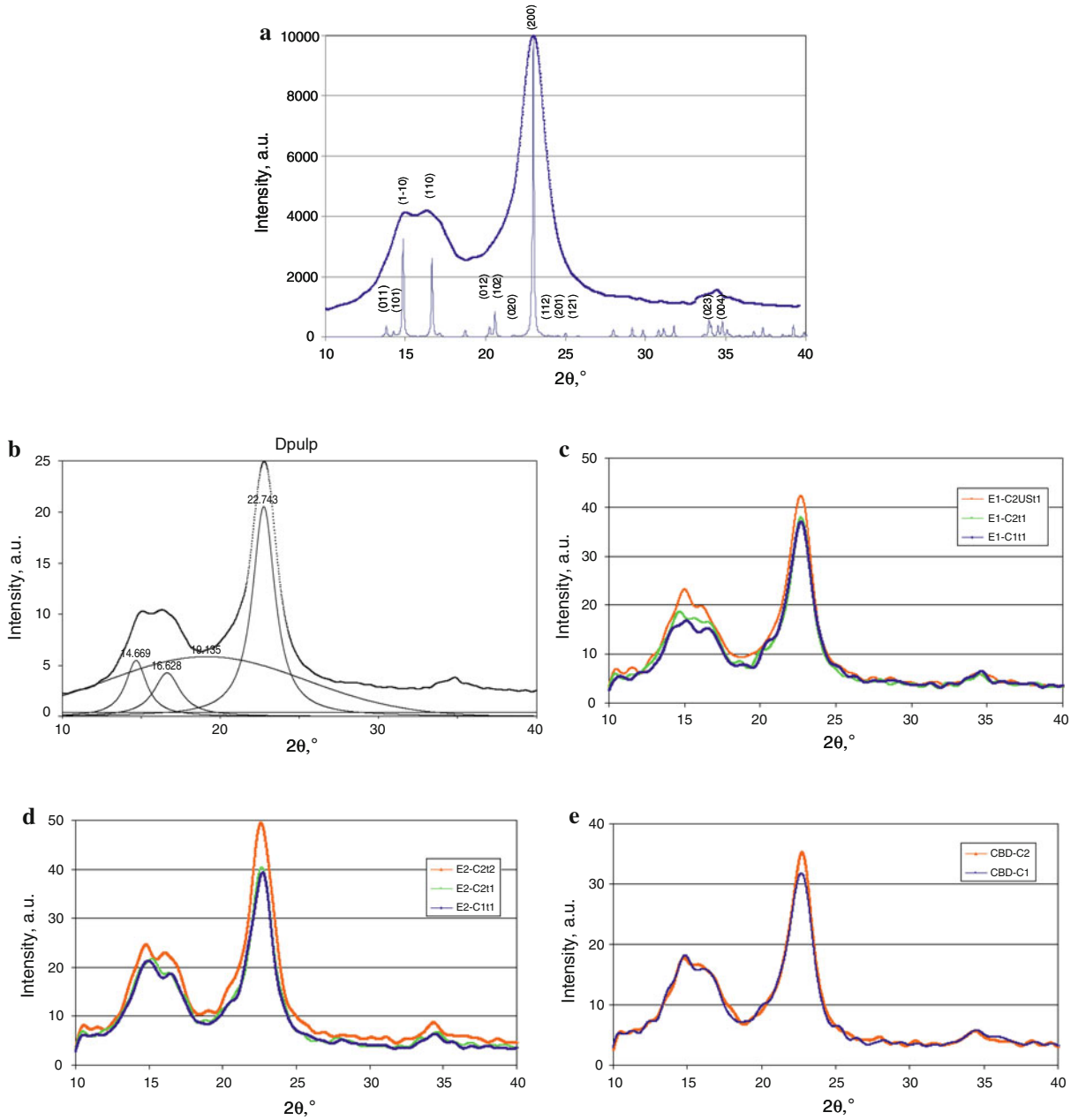

Fig. 2 X-ray diffraction patterns of **a** cellulose I (*thick line*—experimental cellulose I pattern; *thin line*—pattern obtained by using Mercury's default pwhm of 0.1°); **b** cellulose I (Dpulp) with deconvoluted peaks; **c** pulp treated with E1; **d** pulp treated with E2; **e** pulp treated with CBD

The d-spacing values determined based on XRD method for control pulp (D pulp) are 6.24, 5.26 and 3.92 Å, corresponding to (1–10), (110) and (200) crystallographic planes, respectively. An increase of the lattice spacing for (110) and (200) planes can be observed for enzymatically treated samples, in comparison with the plane (1–10).

Moreover, taking into account the crystallite size data from Table 2, an increase corresponding to the (200) plane was observed, which could be due to predominant hydrolysis of smaller crystallites or to lateral aggregation of the remaining crystallites (Penttilä et al. 2013).

The increase of the crystallite size might be surprising since no cellulose was added during the enzymatic

treatment, but it could be explained by co-crystallization (Duchemin et al. 2012). The co-crystallization process was observed after wetting and drying of cellulosic pulp (Newman 2004; Rondeau-Mouro et al. 2011) and it consists of the removal of the non-cellulosic polysaccharide chains between exterior cellulose chains and formation of a bigger crystallite. Mazeau (2011) and Mazeau and Charlier (2012) claim that the co-crystallization process occurs mainly on (110) and (200) planes, in particular on (110) crystallographic plane, when both considering. The same trend was observed also in our study, when control pulp was treated with different enzymes, especially in case of the samples treated with the cellulase E2.

In the case of samples CBD-C1 and CBD-C2 the increase of the crystallite size corresponding to (200) plane, could be explained by the adsorptions of CBD on the surface of cellulose crystals, which is known to be the preferred binding site for the cellulose-binding domains (Liu et al. 2011; Penttilä et al. 2013).

The polymerization degree of pulps was also determined. Cellulase-treated samples showed a consistent decrease in DP when compared to control pulps (Table 2). Also, the cellulose substrate was more degraded when was treated with cellulase E1, showing lower DP than pulps treated with E2. Furthermore, the pretreatment of cellulose with ultrasound (E1-C2USt1) resulted in greater depolymerisation of the samples in comparison with E1-C2t1, accompanied by a slight increase in crystallinity index. Pulp samples treated with CBD, without hydrolytic activity, showed only slight changes in DP.

Even though endoglucanases preferentially degrade amorphous cellulose and an increase of the total percentage of crystalline cellulose would be expected as indicated by some studies (Cao and Tan 2005, 2006; Ciolacu et al. 2008), other authors show that the crystallinity index (Icr) remains unchanged after enzymatic hydrolysis (Lenze et al. 1990; Puls and Wood 1991; Zhang and Lynd 2004). In the present study the treatment with the endoglucanases tested, cellulases E1 and E2, led to an increase of the Icr. The lower values recorded for the crystallinity index of samples treated with E1, in comparison with E2, may be due to the fact that these endoglucanases have a minor activity on crystalline cellulose, that is higher in E1 than in E2. Alternatively the difference among the cellulases can be related to the hydrolysis mechanism of cellulase E1, which is a processive endoglucanase and not a typical endoglucanase (Chiriac et al. 2010).

Thermal analysis

Thermal analysis may be defined as a set of techniques (DTA, DSC and TG) used to describe the physical or chemical changes of substances, as a function of temperature (Ciolacu and Popa 2006). Changes in latent heat in a chemical substance are detectable by DSC, while the progressive mass loss is detectable by thermogravimetry (TG) or differential thermogravimetry (DTG).

Table 2 Crystallite size (D), lattice spacings (d-Spacing), crystallinity index (Icr) and polymerization degree (DP) of control pulp and pulps treated with enzymes

Samples	D[a] (nm)			d-Spacing[b] (Å)			Icr (%)	DP
	(1–10)	(110)	(200)	(1–10)	(110)	(200)		
Dpulp	6.1	6.5	5.9	6.24	5.26	3.92	56.43	1.573
E1-C1t1	4.3	5.2	5.6	5.93	5.23	3.99	61.58	1.387
E1-C2t1	4.0	6.5	6.2	5.95	5.28	3.91	62.68	1.364
E1-C2USt1	5.4	5.4	6.4	6.02	5.51	3.91	64.03	1.334
E2-C1t1	3.9	7.2	6.1	6.09	5.32	3.88	64.48	1.475
E2-C2t1	4.4	7.1	6.5	5.92	5.20	3.88	65.74	1.374
E2-C2t2	5.1	7.8	8.1	5.89	5.30	3.93	70.55	1.432
CBD-C1	5.1	6.2	7.2	5.63	5.28	3.89	57.55	1.524
CBD-C2	6.1	6.6	7.3	5.89	5.29	3.85	59.86	1.518

[a] Crystallite size in the direction perpendicular to each plane

[b] d-Spacing of the main equatorial peaks of cellulose

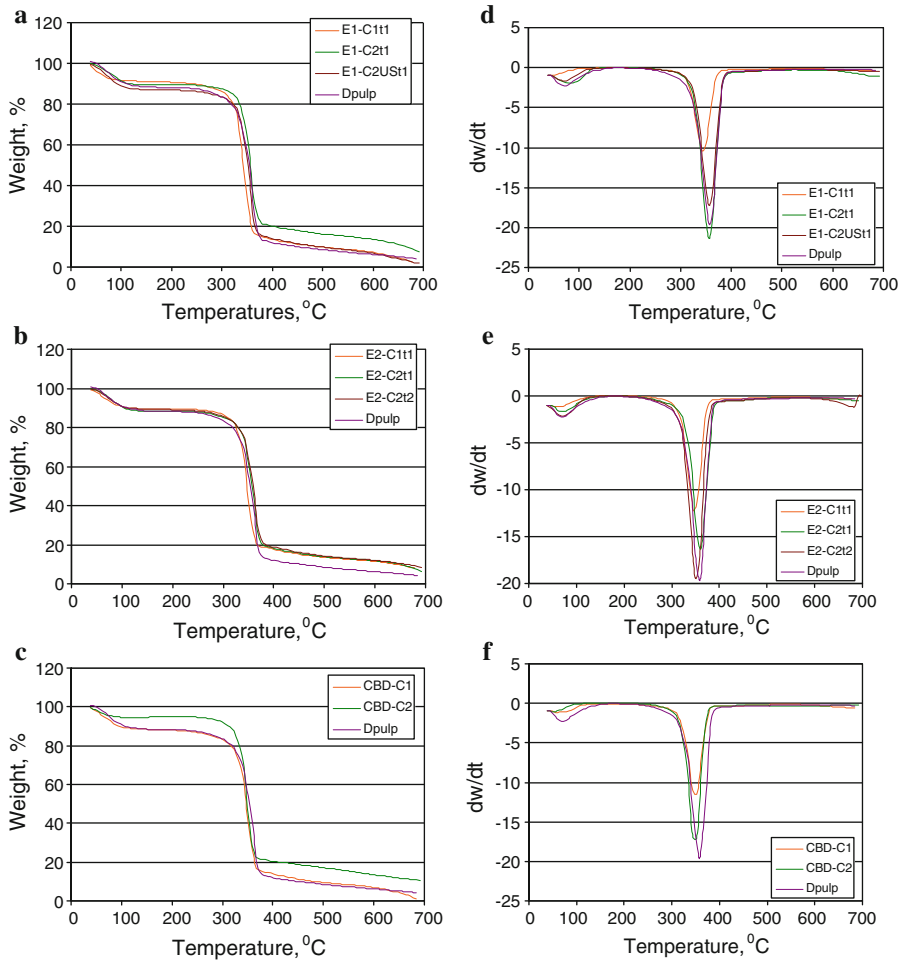

Fig. 3 TG and DTG curves for **a**, **d** pulp treated with cellulase E1, **b**, **e** pulp treated with cellulase E2 and **c**, **f** pulp treated with CBD

Thermogravimetric analysis

The behavior during the thermooxidative destruction of the cellulose samples treated with the different enzymes was studied by thermogravimetric analysis (Fig. 3). The thermal decomposition of cellulose involves at least two processes in addition to simple desorption of physically bound water (Ciolacu and Popa 2006). The first is the increase of cellulose–cellulose hydrogen bonding of cellulose chains, with the evaporation of absorbed water (until 115 °C, dehydration), the second is the unzipping of the cellulose chain and levoglucosan formation from the monomer units (until 380 °C, the main decomposition stage) and the third reaction is the decomposition of the dehydrated products to yield char and volatile products.

Several parameters can be identified within the thermograms, such as T_{onset} which is the initial temperature of each thermogravimetric step. T_{peak} is the temperature corresponding to the maximum rate of mass loss, and T_{end} is the temperature of the end of step. Also, the mass loss for each stage can be determined, i.e., W_I which is the amount of desorbed water (10–115 °C), and W_{II}, the mass loss for the stage corresponding to the thermal degradation (115–380 °C).

Figure 3a–c shows that untreated cellulose begins to decompose at a lower temperature (T_{onset} = 314 °C) when compared to enzymatically treated samples (Table 3). This behavior is explained by the fact that the non-crystalline region decomposes more actively than the crystalline region. Also, the intermolecular hydrogen bonds between chains are stronger in the crystalline region than those from amorphous area and require more energy to break before the decomposition process can proceed (Morgado and Frollini 2011). This means that more

Table 3 Thermogravimetric characteristics and the kinetic parameters for the second stage of thermal degradation of control pulp and pulps treated with enzymes

Sample	II stage				R_{600} (%)	Ea (kJ/mol)	ln A	n
	T_{onse} (°C)	T_{peak} (°C)	T_{endset} (°C)	W_{II} (%)				
Dpulp	314	355	373	84.12	6.35	215.24	36.47	0.56
E1-C1t1	335	359	374	96.24	7.72	347.47	61.97	1.22
E1-C2t1	329	359	376	82.46	13.60	347.15	61.97	1.31
E1-C2USt1	336	359	373	85.07	7.04	330.98	58.63	1.04
E2-C1t1	338	360	377	81.58	11.55	340.71	60.49	1.18
E2-C2t1	334	361	379	82.46	11.77	298.50	52.19	0.99
E2-C2t2	334	362	378	81.13	11.99	280.23	48.55	0.87
CBD-C1	337	356	376	87.03	7.18	313.63	55.20	1.09
CBD-C2	334	360	368	84.40	13.77	298.90	52.55	0.63

crystalline samples, such as the enzymatically treated pulps, have higher thermal stability than the control pulp (Dpulp). These results are in good agreement with the data obtained from X-ray diffraction method, regarding the crystallinity index.

From DTG curves (Fig. 3d–f) can be seen that the temperatures corresponding to the maximum rate of decomposition (T_{peak}) were shifted towards higher temperatures for the enzyme-treated samples, as from 355 °C corresponding to Dpulp to 359 °C for the samples treated with E1, 362 °C for the samples treated with E2 and 360 °C for those treated with CBD (Table 3). This fact can be correlated with the data of the crystallinity index (Icr) and the crystallite size (D). Thus, an increase in the crystallinity index and in the crystallite size corresponding to (200) reflection, determined an increase of the decomposition temperature of cellulose residues (Calahorra et al. 1989; Ciolacu and Popa 2006; Kim et al. 2010; Poletto et al. 2012).

The char fraction remaining after thermal decomposition of celluloses is an expression of the crystallinity index of the samples. Thus, the increase of the crystallinity index of enzyme treated samples leads to an increase of the obtained char (R_{600}). Similar results were also observed by Yue et al. (2012). Moreover, an increase of the char with the decrease of the polymerization degree was recorded (Gurgel et al. 2012).

To evaluate the influence of the supramolecular organization of cellulose over the course of thermal degradation reaction, the kinetic parameters were determined. The application of the Freemann-Caroll method led to a kinetic processing of the thermogravimetric data, based on the equation (Grigoriu et al. 2009):

$$\frac{\Delta \ln \frac{d\alpha}{dT}}{\Delta \ln(1-\alpha)} = n - \frac{Ea}{R} \cdot \frac{\Delta(1/T)}{\Delta \ln(1-\alpha)} \quad (4)$$

where $d\alpha/dT$ is the conversion degree; α is the conversion defined as $\alpha = (w_0 - w)/(w_0 - w_\infty)$, w_0 and w_∞ being the initial and final weights, and w the weight at any time; T is the absolute temperature recorded on the thermogram and R is the gas constant.

The weight loss kinetic parameters, as the activation energy (Ea), pre-exponential factor (A) and the reaction order (n), for the control pulp and the enzymatic treated samples were determined (Table 3).

The activation energy corresponding to the II stage of cellulose decomposition increased sharply for the samples treated with enzymes, showing a maximum value at enzyme concentration of C1 and at a time t1 (from 215.24 kJ/mol of Dpulp, to 347.47 kJ/mol of E1-C1t1, 340.71 kJ/mol of E2-C1t1 and 313.63 kJ/mol of CBD-C1, respectively). For each enzyme a progressive decrease of Ea was observed with increasing enzyme concentration or time of treatment. This behavior was confirmed also by the data reported by Gurgel et al. (2012). The differences that appear between the Ea values (determined according to the Freeman-Carroll method) correspond to different enzyme actions and could be correlated with the degree of polymerization. Thus, the decrease of Ea for the samples of each enzyme corresponds to a decrease in the DP of cellulose (Calahorra et al. 1989; Gurgel et al. 2012).

The reaction order (n) for dissolving pulp was 0.56 and increased during the enzymatic treatments to 1.18 (for the samples treated with E2) and until 1.31 (for the

samples treated with E1). Thus, it can be considered that the thermal decomposition of enzyme treated celluloses follows the first order kinetics. Also, similarly to what was found for Ea, when we compare the samples treated with the same enzyme, it was found that the reaction order decreased as the degree of polymerization decreased, as also observed by Calahorra et al. (1989).

The results obtained from the thermogravimetric analysis indicate changes in the supramolecular structure of samples, as a consequence of the enzymatic degradation process, and thus, this method could be used as a complementary characterization technique for these types of materials.

Differential scanning calorimetry

The modifications induced by the enzymes on the supramolecular structure of pulps and implicitly on the accessibility of the samples, were evaluated through DSC. The samples were first conditioned at a constant relative humidity of 65 %, at a temperature of 20 °C, for 72 h and after that the thermograms were recorded until 300 °C. The action of the enzymes on cellulosic samples was investigated by measuring the changes in the amount of water that was bound to fibers, expressed as the enthalpy of evaporation.

Because the area of the endothermic peak is directly correlated to the variation in the enthalpy of the cellulosic samples, the DSC method can be applied to measure the enthalpy of evaporation with the following equation (Grigoriu et al. 2009):

$$\Delta H = \frac{S \cdot k}{E \cdot m_x} \quad (5)$$

where ΔH is the enthalpy of evaporation (J/g), E is the sensitivity of the calorimeter (4.02 μV/mW), S is the peak area (mm^2), k is the correction factor (μV) and m_x is the mass of the dried sample (mg).

During the enzymatic hydrolysis of the dissolving pulp, with the different enzymes (E1, E2 and CBD) at different times (24 and 72 h) and concentrations (C1 and C2), an increase of the endothermic peak was recorded, explained by the sorption of a higher amount of water (Fig. 4). This indicated an increase of the accessibility of the cellulosic samples.

It is well known that the capacity of the cellulose fiber for water absorption depends largely on the availability of the free hydroxyl groups and it is generally considered that water absorption occurs almost entirely in the amorphous regions of cellulose, neglecting the free hydroxyl groups that may be present on the surfaces of crystallites. Thus, the modifications that appear in the dimensions of the amorphous area within cellulose fibers can be identified through the DSC method, by the changes in the amount of water bound to cellulose.

Taking into account the data regarding the enthalpy of evaporation of cellulosic samples (Table 4), differences in actions of enzyme E2 in comparison with E1 can be observed as a function of the specific activity of each enzyme.

The endo-cleavages from the amorphous regions increased at the higher enzyme concentration and the fragments were released from the cellulose molecules with an increase in the amount of reducing sugars and a decrease in the absorbed water and of the enthalpy of evaporation, respectively (Table 4). Also, a good

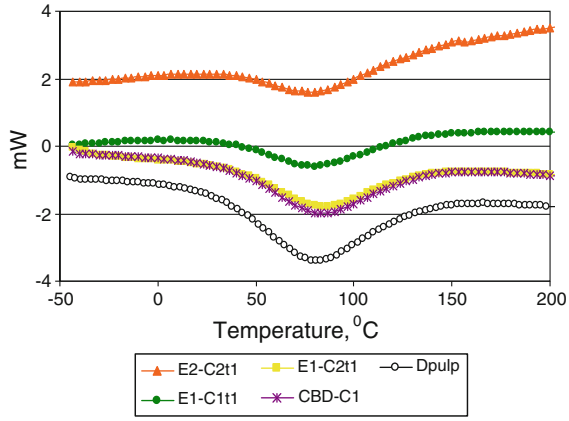

Fig. 4 DSC curves for control pulp and pulps treated with enzymes

Table 4 Values of the evaporation enthalpy for control pulp and pulps treated with enzymes

Sample	Tonset (°C)	Tpeak (°C)	Tendset (°C)	ΔH (J/g)
Dpulp	30	80	134	163.42
E1-C1t1	35	81	131	134.90
E1-C2t1	60	82	116	147.64
E2-C1t1	38	86	132	161.32
E2-C2t1	43	81	132	126.04
CBD-C1	36	83	133	159.72
CBD-C2	40	85	130	148.67

correlation was observed between the enthalpy of evaporation and the degree of polymerization data. Thus, the effect of enzymatic hydrolysis is reflected in a decrease of the DP accompanied by a decrease of ΔH values. Hoshino et al. (1999) studied the effect of enzymatic treatment on the hygroscopic properties of cotton cellulose, using a highly purified endo-type cellulase from *Streptomyces* sp. KSM-26, and also observed that the rapid decrease in the size of the amorphous regions decreases the number of sites for adsorption of moisture to a low level. These observations are in agreement with the increase in XRD crystallinity of the Dpulp after enzymatic hydrolysis and suggest that the hydrolysis of amorphous cellulose could be favored over that of the crystalline cellulose.

Comparing the group of samples treated with the same enzyme, we can observe that for cellulase E1, which possesses the cellulose binding module, a higher concentration leads to an increase of the evaporation enthalpy, from 134.9 J/g (E1-C1t1) to 147.64 J/g (E1-C2t1), a fact explained by a pronounced action of cellulase on crystalline region, and thus an increase of the amorphous area. These data are correlated with the values obtained for the amount of the reducing sugar which increases from 92 μg/mL (E1-C1t1) to 154 μg/mL (E1-C2t1). At the same time, the action of cellulase E2, which is more active on amorphous regions, leads to a decrease of the evaporation enthalpy from 161.32 J/g (E2-C1t1) to 126.04 J/g (E2-C2t1) due to a decrease of the less ordered regions and increased crystalline fraction, which is more resistant to the cellulose action.

The treatment with the isolated CBD affects the supramolecular structure of cellulose in a small percentage, as was expected. The decrease of the ΔH values for the CBD treated samples could be explained by the binding of enzyme at the surface of cellulose.

Analysis of fiber morphology

Scanning electron microscopy analysis of fibers morphology showed that cellulases E1 and E2 change the surface appearance of the fibers (Fig. 5).

The control pulp (Dpulp) and the sample treated with buffer (Blank pulp, Bk) presented a fibrillated or hairy aspect. Similar behavior was shown by fibers treated with the cellulose binding module, CBD. On the other hand, fibers treated with cellulases E1 or E2 had much smoother and cleaner surfaces. In this way, E2-treated fibers had a smoother appearance and only a few outbound fibrils compared to the control fibers. E1 cellulase showed a more pronounced peeling effect than E2. This effect increased with the enzyme dose, yielding fibers with a completely clean surface when treated with the higher E1 dose. Both cellulases seem to weaken the fibrils and mechanical stirring lead to detachment of the salient fibrils from the fiber surface. The wall delamination increased with the enzyme dose and the time of the treatment, and was enough in the case of E1 to get totally clean fibers. This cleaning effect is probably due to the ability of the cellulases tested to weaken the wall and suggests an improvement in the accessibility and chemical reactivity of this type of pulp by cellulases E1 and E2. In fact, the pilling effect lead to an increased surface area and so far increased accessibility for the reagents as observed by Ibarra et al. (2010). Other researchers have also described a cleaning effect for cellulases (Mansfield et al. 1997; Buschle-Diller et al. 1994; Liu et al. 2009).

These observations are in agreement with the ability of these cellulases to enhance the mechanical refining of the pulp as described in a previous work, which can be equally explained by a softening of the external wall of cellulose fibers (Cadena et al. 2010). Nevertheless, for cellulases E1 and E2, the modifying ability of fibers is of interest since cellulases are used for this purpose in laundry and textile industry, namely to restore cloth softness and cotton finishing, respectively, as already discussed above. They have a pronounced capability to remove pilling without attacking the structural integrity of the fibers, since a weakening of the fibers is undesired.

Alkali solubility

One of the most important activation methods, which could be used also at industrial level, is the swelling of cellulose in NaOH solutions. Cellulose is partially soluble in aqueous solutions of NaOH, the degree of dissolution depending on the nature and characteristics of cellulose (Ciolacu and Popa 2005). Alkali solubility is a related parameter to accessibility of cellulose to reactants, an important factor for the production of cellulose derivatives.

In order to analyze the influence of enzyme action on the accessibility of dissolving pulp, the alkali solubility of cellulose (in 8.5 % NaOH solution at low

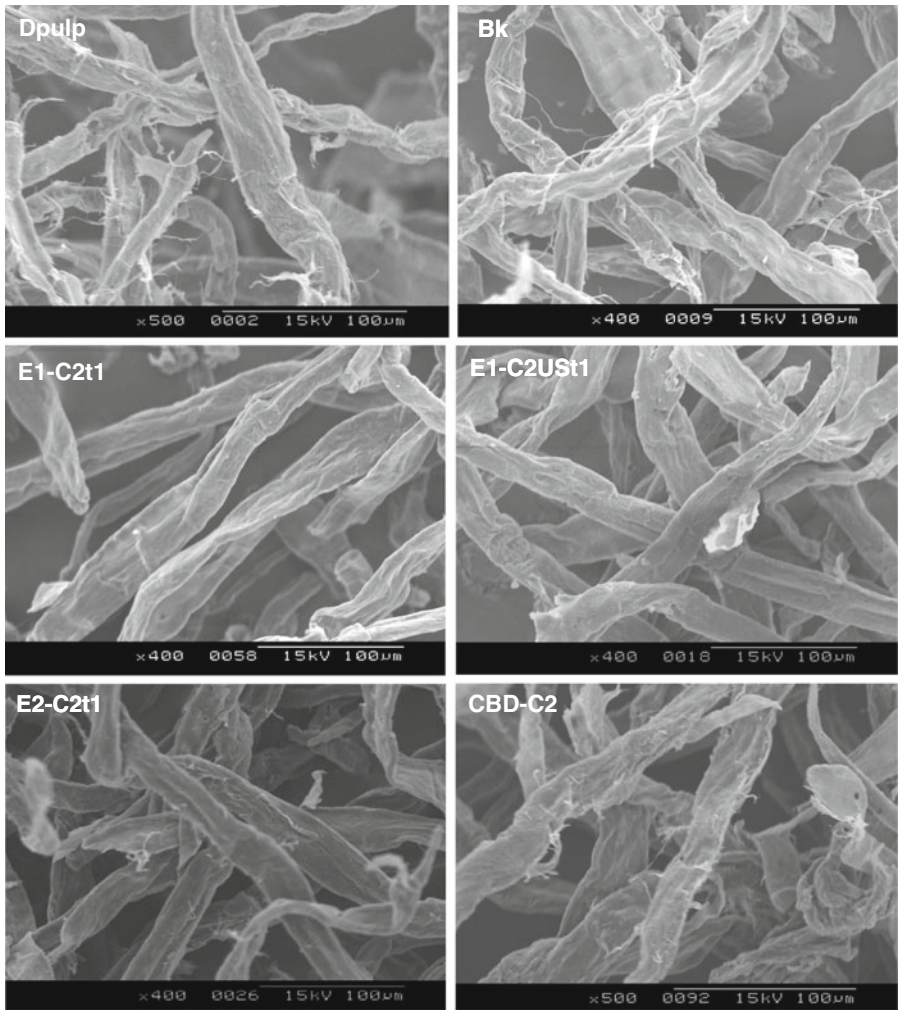

Fig. 5 SEM micrographs of the untreated pulps (Dpulp, Bk) and pulps treated with enzymes

temperature) of pulps treated with E1-C2t1, E2-C2t1 and CBD-C2t1 was determined.

Pulps treated with enzymes showed a notable increase of solubility in alkali. In this way while untreated dissolving pulp showed a degree of dissolution of 19 %, samples treated with E1 or E2 showed a solubility of 25 and 22 %, respectively. Treatment with CBD did not produce a significant effect on cellulose solubility (Fig. 6). Taking into account the results it can be concluded that an enzymatic pretreatment of cellulose leads to an increased solubility by increasing the accessibility of samples.

Similar results have been obtained by Cao and Tan (2006) who described an increase of solubility and accessibility of samples treated with crude cellulases from *Humicola insolens*, and also with an endoglucanase from *Aspergillus sp*. The authors found that the action of these cellulases increases both alkaline solubility and crystallinity of samples by the

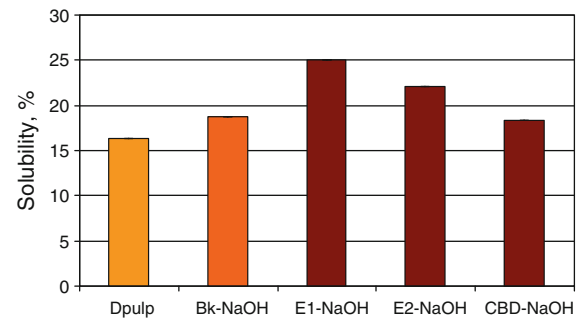

Fig. 6 Solubility in NaOH solution of control pulp, blank pulp and enzyme treated pulps

ability of these enzymes to decrease the polymerization degree and to break down some of the hydrogen bonds of cellulose. Rahkamo et al. (1996) described a 26 % increased alkali solubility using *Tricoderma reesei* endoglucanase II (EGII). Henriksson et al. (2005) reported considerable increased reactivity of the dissolving pulp even for very low dose treatment with a commercial cellulase.

The small difference between the effects of the two cellulases is undoubtedly due to the presence of the cellulose binding domain CBM3b in the E1 molecule (whole enzyme). The molecular binding mechanism of CBDs might destabilize the intermolecular hydrogen bonding within crystalline cellulose fibrils (Tormo et al. 1996) that could explain the ability of non-hydrolytic disruption of fibers proposed for CBDs (Din et al. 1991; Kataeva et al. 2002). Relying on this, the relaxation of the crystal structure should induce an improvement in the accessibility of cellulose. However, we didn't observe an improvement in the alkali solubility of cellulose after treatment with CBD (CBM3b) in the tested conditions. An extended study of the application parameters would be necessary to determine the effect of the CBD on the accessibility and reactivity of cellulose. This would be interesting since its presence in E1 influenced the effectiveness of this cellulase as a biorefining aid (Cadena et al. 2010) even though treatment with CBD did not substantially affect mechanical properties of eucalyptus pulps,. As reported in this work the catalytic domain of E1 and E2 (GH9) was responsible for the endoglucanase effect on pulp. Meanwhile the CBD had an intramolecular synergistic effect. The importance of the catalytic domain for the endoglucanase action on pulps has been demonstrated also by Ibarra et al. (2010). They showed that the retaining mechanism of endoglucanases is an ineffective way to improve the cellulose reactivity, while endoglucanases with inverting mechanism, E1 and E2 falling into this category, can be efficiently applied. Therefore, they propose inverting cellulases, preferably with a CBD, as agents in the viscose process to improve the cellulose accessibility and reactivity and thus lower demand for carbon disulfide and its environmental impact.

Cellulose fibers that remained insoluble after the alkali treatment were analyzed by XRD and SEM.

From X-ray diffractograms, the first aspect that can be observed is the presence of crystalline structure of cellulose II, obtained after the treatment with NaOH solution (Fig. 7). The three main peaks have Miller indices of (1–10), (110) and (020), which correspond to Bragg angles of 12.18°, 20.17° and 21.62°, respectively (French 2014). The peak positions of cellulose II (Fig. 7a) will not agree exactly with those corresponding to the alkali-treated samples (Fig. 7b, c), possibly because of crystallite size variations resulting in different long-range compressive forces on the crystals and unit cells (French and Santiago Cintrón 2013; Nishiyama et al. 2012) as well as incomplete conversion to cellulose II.

Calculation of the crystallite sizes normal to the hkl planes were based on the estimation of the peak width at half-the-maximum amplitude (Table 5). The crystallite dimensions of three main equatorial reflections were determined, (1–10), (110) and (020), which measured the crystallite width (Ciolacu et al. 2011).

Table 5 shows that the (1–10) and (020) d-spacings of the alkali treated samples increase in all cases, in comparison with the samples not treated with alkali (Table 2), while the crystallite size normal to the (110) plane recorded a decrease. The same behavior was observed by Wang et al. (2008) who studied the dissolution behavior of enzyme pre-treated cotton fibers in NaOH/urea solution. The alkali treatment reduced the crystallinity index of all samples and the Icr of Dpulp, was reduced from 56.43 to 45.64 % (Dpulp-NaOH). Regarding the Icr of enzyme treated samples, the highest value was recorded by the pulp treated with E1 (48.88 %), while pulp treated with E2 showed an Icr of 46.28 %. These results are in good correlation with the solubility data, because a greater solubility reflects a higher release of the low-molecular weight fractions from the amorphous regions of celluloses which are more accessible as a result of the first step of enzymatic degradation.

The results obtained from X-ray diffraction suggest that as a first step, cellulose was attacked by cellulase in the direction of the (020) plane, cutting cellulose molecules. Then, the NaOH solution interacts with the cellulose crystal to break the inter- and intramolecular hydrogen bonds, reducing the length of cellulose crystal. Thus, enzymatic attack enhances the dissolution of cellulose, without changing the crystal type but slightly increases the crystallinity index. Subsequent treatment with NaOH solution at low temperature modified the crystal form from cellulose I to cellulose II, accompanied by a decreased crystallinity index and an increase of the accessibility of the cellulosic, results

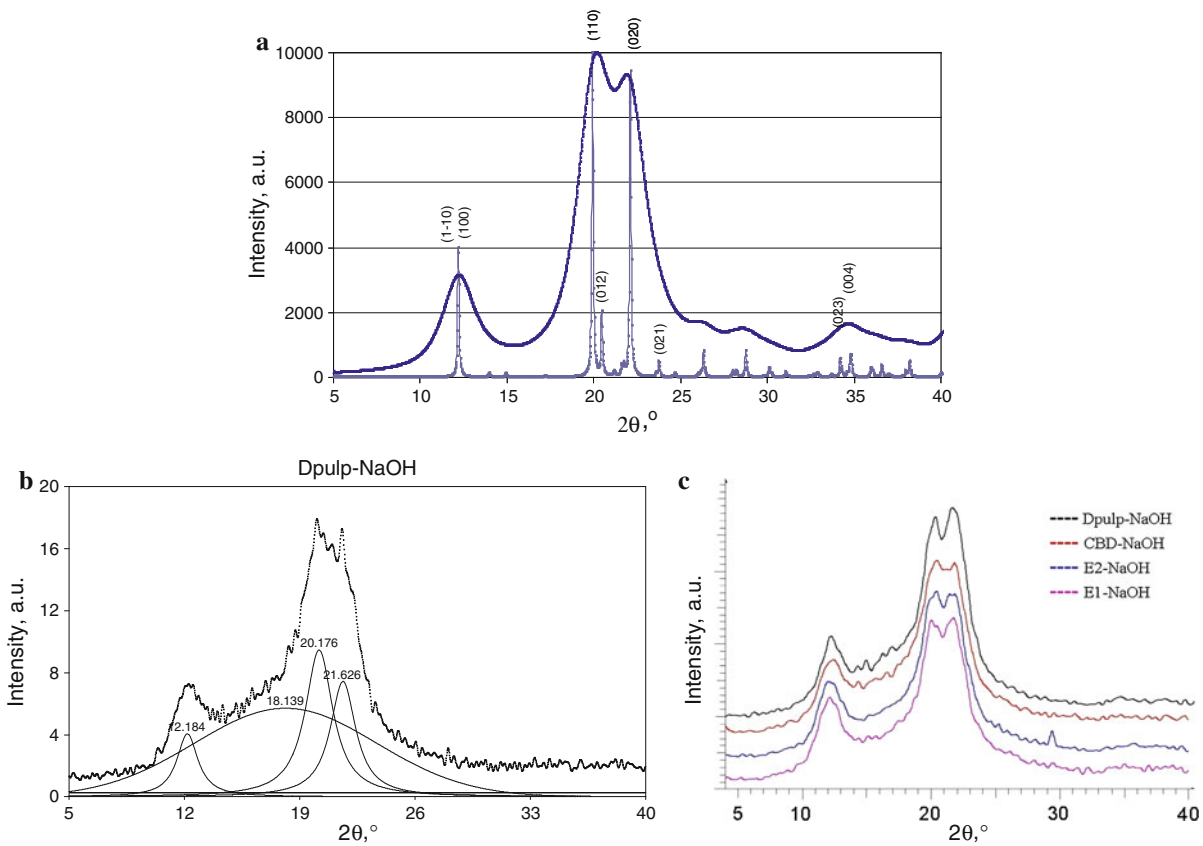

Fig. 7 X-ray diffraction patterns of **a** cellulose II (*thick line*—pattern obtained by using Mercury's pwhm of 1.8°; *thin line*—pattern obtained by using Mercury's default pwhm of 0.1°); **b** cellulose II (Dpulp-NaOH) with deconvoluted peaks; **c** alkali treated dissolving pulp and alkali treated pulps obtained after enzymatic treatment

Table 5 Crystallite size (D), lattice spacings (d-Spacing) and crystallinity index (Icr) of alkali treated pulps

Samples	D[a] (nm)			d-Spacing[b] (Å)			Icr (%)
	(1–10)	(110)	(020)	(1–10)	(110)	(020)	
Dpulp-NaOH	5.8	7.9	4.7	7.34	4.45	4.10	45.64
E1-NaOH	5.2	7.8	5.7	7.49	4.51	4.13	48.88
E2-NaOH	5.0	6.1	4.7	7.49	4.46	4.10	46.28
CBD-NaOH	4.8	7.3	4.1	7.25	4.38	4.06	43.46

[a] Crystallite size in the direction perpendicular to each plane

[b] d-Spacing of the main equatorial peaks of cellulose

that are important factors in controlling the fibers' reactivity.

The SEM micrographs reveal the effect on the NaOH solution on the surface morphology of the enzyme treated pulps (Fig. 8).

Treatment with NaOH caused a pronounced effect on the morphology of cellulosic fibers. The surfaces of the alkali-treated samples look smoother than those of fibers before the alkaline treatment (Fig. 5), as a result of the elimination of the salient fibrils and of the fragments stuck to the fibers. Moreover, the alkali treatment seems to permit a separation of the fiber bundles into individual fibers that show a more swollen and straightened state in comparison with

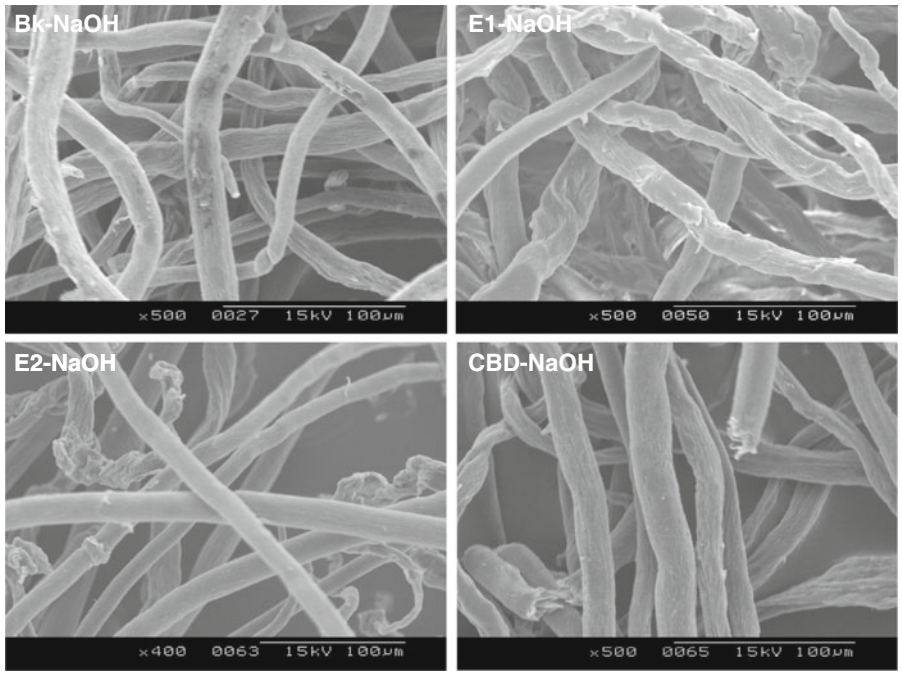

Fig. 8 SEM micrographs of the alkali treated samples

the highly twisted untreated fibers. The NaOH solution influenced the fine structure of cellulosic samples by changing the fibers from the crystalline form of cellulose I–cellulose II, as was demonstrated by XRD. In addition, alkali solution has been reported to fill the central cavity (the lumen) almost entirely, so the fibers become more cylindrical and lose their convolutions, inducing a smoother and shinier texture (Navard et al. 2012). In case of the E1-NaOH sample it is obvious that the surfaces of the fibers became a bit rougher as a result of the pronounced action of cellulase E1, which permitted a rapid release of sugars and thus left the surface more accessible to reagent.

Conclusions

Current investigation demonstrated the influence of different treatments with a family GH9 modular endoglucanase from *Paenibacillus barcinonensis* (E1) and two derivatives of this enzyme (E2 and CBD), on the supramolecular structure of dissolving pulp. E1 and E2 have endoglucanase activity while CBD is an isolated cellulose binding domain without hydrolytic activity. Application of E1 and E2 produced a rapid release of sugars in the first hours of the treatments, followed by a slowed rate as the incubation progressed in time. A decrease of the degree of polymerization was observed, with the lowest DP values found for pulps obtained after hydrolysis with cellulase E1. XRD measurements of the cellulosic fibers reveal an increase of the crystallinity index during the enzymatic hydrolysis, most evident for cellulase E2. Moreover, there was an increase in the crystallite size perpendicular to the (200) plane. Ultrasonication caused a more accentuated depolymerization of the cellulosic samples and increased the crystallinity of the sample. The thermal decomposition revealed a decrease in the activation energy correlated with the decreased degree of polymerization and it was also observed that the enzyme-treated samples have higher thermal stability than the untreated cellulose. SEM shown a pronounced capacity of the enzymes to remove fuzz and improved the smoothness and surface appearance of the fibers, a fact more pronounced for cellulase E1. In addition, the results from this work showed that enzymatic hydrolysis enhanced the dissolution degree of cellulose in NaOH solution at low temperature, which indicates the potential application of the cellulases E1 and E2 for increasing the reactivity of cellulose.

Acknowledgments This work was partially supported by the Spanish Ministry of Education and Science, grant No CTQ2010-20238-C03-02. Iulia Chiriac held a FI grant from Generalitat de Catalunya. Dr. Diana Ciolacu acknowledges the financial support of European Social Fund—"Cristofor I. Simionescu" Postdoctoral Fellowship Programme (ID POSDRU/89/1.5/S/55216), Sectoral Operational Programme Human Resources Development 2007–2013.

References

Bhat MK (2000) Cellulases and related enzymes in biotechnology. Biotechnol Adv 18:355–383

Boraston AB, Bolam DN, Gilbert HJ, Davies GJ (2004) Carbohydrate-binding modules: fine-tuning polysaccharide recognition. Biochem J 382:769–781

Buschle-Diller G, Zeronian S, Pan N, Yoon M (1994) Enzymatic hydrolysis of cotton, linen, ramie, and viscose rayon fabrics. Text Res J 64:270–279

Cadena EM, Chriac AI, Pastor FIJ, Diaz P, Vidal T, Torres AL (2010) Use of cellulases and recombinant cellulose binding domains for refining TCF kraft pulp. Biotechnol Progress 26:960–967

Calahorra ME, Cortázar M, Eguiazábal JI, Guzmán GM (1989) Thermogravimetric analysis of cellulose—effect of the molecular-weight on thermal-decomposition. J Appl Polym Sci 37:3305–3314

Cao Y, Tan H (2005) Study on crystal structures of enzyme-hydrolyzed cellulosic materials by X-ray diffraction. Enzyme Microb Tech 36:314–317

Cao Y, Tan H (2006) Improvement of alkali solubility of cellulose with enzymatic treatment. Appl Microbiol Biot 70:176–182

Carrard G, Koivula A, Söderlund H, Béguin P (2000) Cellulose-binding domains promote hydrolysis of different sites on crystalline cellulose. Proc Natl Acad Sci USA 97:10342–10347

Chiriac AI, Cadena EM, Vidal T, Torres AL, Diaz P, Pastor FIJ (2010) Engineering a family 9 processive endoglucanase from Paenibacillus barcinonensis displaying a novel architecture. Appl Microbiol Biotechnol 86:1125–1134

Ciolacu D, Popa VI (2005) Structural changes of cellulose determined by dissolution in aqueous alkali solution. Cell Chem Technol 39:179–188

Ciolacu D, Popa VI (2006) Study on the thermal degradation of cellulose allomorphs. Cell Chem Technol 40:445–449

Ciolacu D, Ciolacu F, Popa VI (2008) Supramolecular structure—a key parameter for cellulose biodegradation. Macromol Symp 272:136–142

Ciolacu D, Gorgieva S, Tampu D, Kokol V (2011) Enzymatic hydrolysis of different allomorphic forms of microcrystalline cellulose. Cellulose 18:1527–1541

Din N, Gilkes NR, Tekant B, Miller RC, Warren RA, Kilburn DG (1991) Non-hydrolytic disruption of cellulose fibres by the binding domain of a bacterial cellulase. Nat Biotechnol 9:1096–1099

Duchemin B, Thuault A, Vicente A, Rigaud B, Fernandez C, Eve S (2012) Ultrastructure of cellulose crystallites in flax textile fibres. Cellulose 19:1837–1854

Engstrom A, Ek M, Henriksson G (2006) Improved accessibility and reactivity of dissolving pulp for the viscose process: pretreatment with monocomponent endoglucanase. Biomacromolecules 7:2027–2031

French AD (2014) Idealized powder diffraction patterns for cellulose polymorphs. Cellulose. doi:10.1007/s10570-013-0030-4

French AD, Santiago Cintrón M (2013) Cellulose polymorphy, crystallite size, and the Segal crystallinity index. Cellulose 20:583–588

García O, Torres AL, Colom JF, Pastor FIJ, Díaz P, Vidal T (2002) Effect of cellulase-assisted refining on the properties of dried and never-dried Eucalyptus pulp. Cellulose 9:115–125

Grigoriu AM, Luca C, Lisa G, Grigoriu A (2009) On the thermal stability of flax fabrics grafted with monochlorotriazinyl-β-cyclodextrin and treated with cinnamic derivatives. Cell Chem Technol 43:153–161

Gurgel LVA, Marabezi K, Ramos LA, Curvelo AAS (2012) Characterization of depolymerized residues from extremely low acid hydrolysis (ELA) of sugarcane bagasse cellulose: effects of degree of polymerization, crystallinity and crystallite size on thermal decomposition. Ind Crop Prod 36:560–571

Henriksson G, Christiernin M, Agnemo R (2005) Monocomponent endoglucanase treatment increases the reactivity of softwood sulphite dissolving pulp. J Ind Microbiol Biot 32:211–214

Hoshino E, Wada Y, Nishizawa K (1999) Improvements in the hygroscopic properties of cotton cellulose by treatment with an endo-type cellulase from *Streptomyces* sp. KSM-26. J Biosci Bioeng 88:519–525

Ibarra D, Köpcke V, Ek M (2010) Behavior of different monocomponent endoglucanases on the accessibility and reactivity of dissolving-grade pulps for viscose process. Enzyme Microb Tech 47:355–362

Isogai A, Atalla RH (1998) Dissolution of cellulose in aqueous NaOH solutions. Cellulose 5:309–319

Kataeva IA, Seidel RD, Shah A, West LT, Li X, Ljungdahl LG (2002) The fibronectin type 3-like repeat from the Clostridium thermocellum cellobiohydrolase CbhA promotes hydrolysis of cellulose by modifying its surface. Appl Environ Microbiol 68:4292–4300

Kim UJ, Eom SH, Wada M (2010) Thermal decomposition of native cellulose: influence on crystallite size. Polym Degradr Stabil 95:778–781

Klemm D, Schmauder HP, Heinze T (2002) Cellulose. In: Vandamme EJ, De Baets S, Steinbüchel A (eds) Biopolymers, vol 6. Wiley-VCH, Weinheim, pp 275–319

Krässig HA (1993) Methods of fiber structure characterization. In: Huglin MB (ed) Cellulose: structure, accessibility and reactivity, polymer monographs, chap 3, vol 11. Gordon and Breach Science Publishers, Philadelphia, pp 43–149

Lenze J, Esterbauer H, Sattler W, Schurz J, Wrentschur E (1990) Changes of structure and morphology of regenerated cellulose caused by acid and enzymatic hydrolysis. J Appl Poly Sci 41:1315–1326

Liu H, Fu S, Zhu JY, Li H, Zhan H (2009) Visualization of enzymatic hydrolysis of cellulose using AFM phase imaging. Enzyme Microb Tech 45:274–279

Liu YS, Baker JO, Zeng Y, Himmel ME, Haas T, Ding SY (2011) Cellobiohydrolase hydrolyzes crystalline cellulose on hydrophobic faces. J Biol Chem 286:11195–11201

Mansfield SD, Jong ED, Stephens RS, Saddler JN (1997) Physical characterization of enzymatically modified kraft pulp fibers. J Biotechnol 57:205–216

Mazeau K (2011) On the external morphology of native cellulose microfibrils. Carbohydr Polym 84:524–532

Mazeau K, Charlier L (2012) The molecular basis of the adsorption of xylans on cellulose surface. Cellulose 19:337–349

Morgado DL, Frollini E (2011) Thermal decomposition of mercerized linter cellulose and its acetates obtained from a homogeneous reaction. Polímeros 21:111–117

Navard P, Wendler F, Meister F, Bercea M, Budtova T (2012) Preparation and properties of cellulose solutions. In: Navard P (ed) The European Polysaccharide network of excellence (EPNOE), chap 5. Springer, Wien, pp 91–152

Newman RH (2004) Carbon-^{13}NMR evidence for cocrystallization of cellulose as a mechanism for hornification of bleached kraft pulp. Cellulose 11:45–52

Nishiyama Y, Langan P, Chanzy H (2002) Crystal structure and hydrogen-bonding system in cellulose Iβ from synchrotron X-ray and neutron fiber diffraction. J Am Chem Soc 124(31):9074–9082

Nishiyama Y, Johnson GP, French AD (2012) Diffraction from nonperiodic models of cellulose crystals. Cellulose 19:319–336

Park S, Baker JO, Himmel ME, Parilla PA, Johnson DK (2010) Cellulose crystallinity index: measurement techniques and their impact on interpreting cellulase performance. Biotechnol Biofuels 3:1–10

Pastor FIJ, Pujol X, Blanco A, Vidal T, Torres AL, Díaz P (2001) Molecular cloning and characterization of a multidomain endoglucanase from Paenibacillus sp BP-23: evaluation of its performance in pulp refining. Appl Microbiol Biot 55:61–68

Penttilä PA, Várnai A, Pere J, Tammelin T, Salmén L, Siika-Aho M, Viikari L, Serimaa R (2013) Xylan as limiting factor in enzymatic hydrolysis of nanocellulose. Biores Technol 129:135–141

Poletto M, Zattera AJ, Forte MMC, Santana RMC (2012) Thermal decomposition of wood: influence of wood components and cellulose crystallite size. Biores Technol 109:148–153

Puls J, Wood TM (1991) The degradation pattern of cellulose by extracellular cellulases of aerobic and anaerobic microorganisms. Biores Technol 36:15–19

Rahkamo L, Siika-Aho M, Vehviläinen M, Dolk M, Viikari L, Nousiainen P, Buchert J (1996) Modification of hardwood dissolving pulp with purified *Trichoderma reesei* cellulases. Cellulose 3:153–163

Rahkamo L, Viikari L, Buchert J, Paakkari T, Suortti T (1998) Enzymatic and alkaline treatments of hardwood dissolving pulp. Cellulose 5:79–88

Rondeau-Mouro C, Bizot H, Bertrand D (2011) Chemometric analyses of the ^{1}H–^{13}C cross-polarization build-up of celluloses NMR spectra: a novel approach for characterizing the cellulose crystallites. Carbohydr Polym 84:539–549

Sánchez MM, Pastor FIJ, Diaz P (2003) Exo-mode of action of cellobiohydrolase Cel48C from *Paenibacillus* sp. BP-23, a unique type of cellulase among Bacillales. Eur J Biochem 270:2913–2919

Sánchez MM, Fritze D, Blanco A, Spröer C, Tindall BJ, Schumann P, Kroppenstedt RM, Diaz P, Pastor FIJ (2005) Paenibacillus barcinonensis sp. nov., a xylanase-producing bacterium isolated from a rice field in the Ebro River delta. Int J Syst Evol Microbiol 55:935–939

Sun Y, Zhuang J, Lin L, Ouyang P (2009) Clean conversion of cellulose into fermentable glucose. Biotechnol Adv 27:625–632

Tappi Test Method (1997) Viscosity of pulp. T230 om-94

Tappi Test Method (2002) Forming handsheets for physical tests of pulp. T205 sp-02

Tomme P, Boraston A, McLean B, Kormos J, Creagh AL, Sturch K, Gilkes NR, Haynes CA, Warren RA, Kilburn DG (1998) Characterization and affinity applications of cellulose-binding domains. J Chromatogr B Biomed Sci Appl 7(15):283–296

Tormo J, Lamed R, Chirino AJ, Morag E, Bayer EA, Shoham Y, Steitz TA (1996) Crystal structure of a bacterial family-III cellulose-binding domain: a general mechanism for attachment to cellulose. EMBO J 15:5739–5751

Wang Y, Zhao Y, Deng Y (2008) Effect of enzymatic treatment on cotton fiber dissolution in NaOH/urea solution at cold temperature. Carbohyd Polym 72:178–184

Yue Y, Zhou C, French AD, Xia G, Han G, Wang Q, Wu Q (2012) Comparative properties of cellulose nano-crystals from native and mercerized cotton fibers. Cellulose 19:1173–1187

Zhang YP, Lynd LR (2004) Toward an aggregated understanding of enzymatic hydrolysis of cellulose: noncomplexed cellulase systems. Biotechnol Bioeng 88:797–824

Cellulose (2011) 18:1527–1541
DOI 10.1007/s10570-011-9601-4

Enzymatic hydrolysis of different allomorphic forms of microcrystalline cellulose

Diana Ciolacu · Selestina Gorgieva · Daniel Tampu · Vanja Kokol

Received: 19 April 2011 / Accepted: 26 September 2011 / Published online: 8 October 2011

Abstract This paper investigates the enzymatic hydrolysis of three main allomorphic forms of microcrystalline cellulose using different cellulases, from *Trichoderma reesei* and from *Aspergillus niger,* respectively. It was demonstrated that both the morphological and crystalline structures are important parameters that have a great influence on the course of the hydrolysis process. The efficiency of the enzymatic hydrolysis of cellulosic substrates was estimated by the amounts of reducing sugar and by the yield of the reaction. Changes in the average particle sizes of the cellulose allomorphs were determined during enzymatic hydrolysis. The accumulation of soluble sugar within the supernatant was used as a measure of the biodegradation process's efficiency, and was established by HPLC-SEC analysis. Any modifications in the supramolecular structure of the cellulosic residues resulting from the enzymatic hydrolysis were determined by X-ray diffraction. The action of each cellulase was demonstrated by a reduction in the crystalline index and the crystallite dimensions of the corresponding allomorphic forms. The crystalline structure of allomorphic forms I and II did not suffer significant modifications, while cellulose III recorded a partial return to the crystalline structure of cellulose I. The microstructures of cellulose allomorph residues were presented using optical microscopy and scanning electron microscopy.

Keywords Cellulose allomorphs · Cellulases · Particle size · XRD · HPLC-SEC · SEM

D. Ciolacu · S. Gorgieva · V. Kokol (✉)
Institute for Engineering Materials and Design, University of Maribor, Smetanova ul. 17, SI-2000 Maribor, Slovenia
e-mail: vanja.kokol@uni-mb.si

D. Ciolacu · D. Tampu
"Petru Poni" Institute of Macromolecular Chemistry, 41A Grigore Ghica Voda Alley, 700487 Iasi, Romania

Introduction

Cellulose, the most abundant polysaccharide on earth is an almost inexhaustible renewable raw material with an expanded role as a source of fuels and commodity chemicals for the future. Throughout industry, the biological conversion of cellulose materials to glucose has proved to be a useful method for obtaining valuable products, such as bioethanol and various chemicals, without competing with food/feed production (Varma 2004).

Cellulose has also been considered recently as an attractive starting material for making nano- and micro-materials with unique physical and chemical properties. Several methods have been proposed on how to prepare and isolate these materials from various resources, involving acid hydrolysis, mechanical treatments (Azizi Samir et al. 2005; Habibi et al. 2010; Das et al. 2010) and more recently enzymatic

pretreatments (Paakko et al. 2007; Siqueira et al. 2010; Siró and Plackett 2010).

The enzymatic hydrolysis of cellulose is a complex process which has been studied intensively over the last few decades. However, these studies have generally been oriented towards the physiological characteristics of cellulolytic microorganisms, and also on the biochemical properties of the enzymes synthesized by them (Mansfield and Meder 2003; Russell et al. 2009). The widely-accepted mechanism for enzymatic cellulose hydrolysis suggests that three different types of cellulases work synergistically in a cellulase complex during this process, producing a valuable key intermediate that can be further transformed into various other materials and chemicals (Davies and Henrissat 1995; Lynd et al. 2002; Gusakov et al. 2007): (1) endoglucanases (EG: EC 3.2.1.4) which randomly hydrolyze accessible intramolecular β-1,4-glucosidic bonds in cellulose-chains at internal positions, generating oligosaccharides of various lengths and, consequently, new-chains ends (Liu et al. 2009); (2) exoglucanases (cellobiohydrolases, CBH: EC 3.2.1.91) acting on the chain-termini to release soluble cellobiose or glucose, as major products, and (3) β-glucosidases (BGL: EC 3.2.1.21) which hydrolyze cellobiose to glucose, in order to eliminate cellobiose inhibition (Kumar et al. 2008).

It was also found that the slow reaction and the decreasing rates as the conversion proceeds can be directly related to the cellulose properties (insoluble nature, crystallinity, surface area, porosity, degree of polymerization, etc.), the features of the enzymatic process (deactivation, inhibition, adsorption, processivity, synergy), the mass-transfer (substrate adsorption, bulk and pore diffusion, etc.) and the intrinsic kinetics (Zhang and Lynd 2004; Yeh et al. 2010; MacLellan 2010; Bansal et al. 2010; Karmakar and Ray 2011). However, one cellulose feature that has not yet been investigated refers to the effect of the variety of physical structures adopted by the cellulose macromolecules being in different crystalline forms, on biodegradation. There have only a few studies on the relationship between the fine-structure of cellulose allomorphs and their enzymatic hydrolysis available so far (Weimer and Odt 1995; Pu et al. 2006; Ciolacu 2007; Ciolacu et al. 2007, 2008).

Four major types of cellulose allomorphs have been reported based on X-ray diffraction patterns: celluloses I, II, III, and IV (Ciolacu and Popa 2010a, b). The natural form of cellulose, so-called cellulose I, is the most important crystalline form of cellulose and the most abundant. It can be found within the major structural components of all plant cell-walls and represents the largest biomass on earth. Furthermore, native cellulose has been found to be a composite of cellulose Iα and Iβ crystalline forms (Atalla and VanderHart 1984; Nishiyama et al. 2002, 2003). The cellulose I form can be easily converted into the second crystalline form of cellulose II by regeneration or mercerization processes. The transition from cellulose I to cellulose II is irreversible, and this implies that cellulose II is a stable form as compared with the metastable cellulose I. The other crystalline forms known as cellulose III and cellulose IV can be derived from both cellulose I and II, using different treatments. Thus, cellulose III can be prepared by soaking cellulose samples in anhydrous liquid ammonia at −80 °C or in organic amine (Wada et al. 2004a, 2006), followed by removal of the reagent, while cellulose IV can be obtained from thermal treatments in glycerol at about 260 °C (Wada et al. 2004b).

The allomorphs of cellulose are different from the supramolecular structure point of view, such as the dimensions of monoclinic unit cell, densities of intra- and inter-chain bonds, polarity, and the packing degrees of macromolecular chains. Generally, the crystalline domains of native cellulose are formed almost exclusively from cellulose I, thus the cellulose allomorphs may be considered as analogue substrates, and represent useful materials for testing the hydrolysis mechanism of cellulose at the molecular level (Ciolacu and Popa 2010a). Thus, the aim of this research was to examine the influence of different supramolecular architectures of the allomorphic forms of microcrystalline cellulose (cellulose I, II and III) on their enzymatic hydrolysis, by using endoglucanase enzymes from different fungi, and by analyzing those structural changes occurring during the hydrolysis process.

Experimental part

Materials

Three forms of crystalline cellulose were used throughout the study. Avicel PH-101, purchased from Sigma–Aldrich: Fluka, was used as *cellulose* I—AI. Mercerized cellulose with a crystalline form of

cellulose II (AII) was prepared from microcrystalline cellulose by soaking it in 17.5% NaOH for 24 h at 15° C, followed by washing thoroughly with distilled water and air-dried. Samples with the crystalline form of *cellulose III* were prepared from microcrystalline cellulose by soaking them in organic amine (100% ethylenediamine) for 24 h at room-temperature, followed by washing with anhydrous methanol, and finally air-dried. Two endo-type cellulases (EC 3.2.1.4) from different sources, *Trichoderma reesei* (C8546, ≥1 U/mg solid) and *Aspergillus niger* (C1184, ≥0.3 U/mg solid) were purchased from Sigma–Aldrich. All other chemicals and reagents used were of analytical grade.

Methods and measurements

Enzymatic hydrolysis of cellulose

The allomorphs were subjected to enzymatic hydrolyses by comparing the action of two different cellulases, one from *Trichoderma reesei* (*T. reesei*) and one from *Aspergillus niger* (*A. niger*). After preswelling of 0.5 g cellulosic substrate in 15 mL 1 M citrate buffer (pH 4.8), 5 mL of enzyme solution with a concentration of 30 U/mL was added. The flask was placed in an incubator at 37 °C and 80 rpm. Samples were withdrawn at different time-periods, namely at 24 h (marked with 1), 48 h (marked with 2), and 72 h (marked with 3), then centrifuged and the supernatant refrigerated. As functions of the type of cellulase used for the enzymatic hydrolysis reaction, the obtained cellulosic residues was marked with "a" for *T. reesei* and with "b" for *A. niger*. The samples were analyzed for any sugar-content reduction by the dinitrosalicylic acid (DNS) method, after appropriate dilution (Miller 1959).

Particles size and size distribution

The particle size analysis was performed by laser diffractometry (Malvern Particle Mastersizer 2000, Malvern Instruments Ltd., Malvern, UK). This instrument was calibrated with deionized water. All the samples were subjected to sonication for 10 s and stirred at 1,750 rpm to ensure good dispersion in the aqueous medium. All the measurements were done in triplicate and, the average data reported.

High performance size-exclusion chromatography (HPLC-SEC)

Size-exclusion chromatography was used to evaluate the molecular weights ($\bar{M}$ w) of the degraded products from the enzymatic hydrolysis of cellulose. The analyses were performed using the High Performance Liquid Chromatography System (Agilent Technologies 1200 Series) connected with a Refractive Index detector (RID). PL aquagel-OH column (Agilent Technologies) with dimensions of 300 × 7.5 mm and pore-size 8 μm was used for the determination of $\bar{M}$w compounds. The column's compartment temperature was increased to 40 °C in order to enhance the chromatogram resolution. As the mobile phase, highly-pure Milly Q water from Millipore Systems was used at a flow rate of 1 mL/min. The samples were filtered through a 0.22 μm PVDF membrane filter (Rotilabo–Spritzenfilter) before injection. 20 μL of supernatants were injected into the system and the analysis was carried out for 30 min. Polysaccharide standard with a known molecular weight was used to estimate the calibration curve for determining the sample's molecular weight. HPLC-SEC data were evaluated using CHEM STATION (Agilent Technologies) computer software.

X-ray diffraction analysis

Wide-angle X-ray diffraction was performed on a Bruker-AXS: D8 ADVANCE apparatus, equipped with a transmission-type goniometer, using Ni-filtered Cu-Kα radiation at 40 kV. The goniometer was scanned stepwise every 10° from 10° to 40° within the 2θ range. The resulting diffraction patterns exhibited peaks which were deconvoluted from a background scattering by using Lorenzian functions, while the diffraction pattern of an artificially amorphicized sample was approximated by a Gaussian functions curve fitting analysis (Ciolacu 2007). The structural parameters were calculated using TOPAS 4.2 (Bruker-AXS, Germany) and DIFFRAC.EVA V1.1 (Bruker-AXS, Germany) software.

Estimation of the crystallinity indexes (CrI) of the cellulose samples was established by using the following equation (Sun et al. 2009):

$$\text{Cr.I.} = [\text{Ac}/(\text{Aa} + \text{Ac})] \times 100\,(\%) \quad (1)$$

where Ac is the surface of the crystalline area, and Aa is the surface of the amorphous area.

The lattice spacings (d-spacings) were calculated using Bragg equation:

$$\lambda = 2d_{hkl} \cdot \sin\theta \quad (2)$$

where d_{hkl} is the lattice-spacing within one of the crystallographic planes, λ is the X-ray wavelength, and 2θ is the corresponding Bragg-angle.

The crystallite size was calculated based on the widths of the diffraction patterns, using the Scherrer equation (Krässig 1993):

$$D_{(hkl)} = \frac{k \cdot \lambda}{\beta \cdot \cos\theta} \quad (3)$$

where $D_{(hkl)}$ is the size of the crystallite (nm), k is the Scherrer constant (0.94), λ is the X-ray wavelength (0.154 nm), and β is the full-width at half-the-maximum of the reflection hkl, measured in 2θ, the corresponding Bragg-angle.

Optical microscopy

The cellulosic samples were examined using Leica DM 2500 M optical microscope, in polarized light, at room temperature, and a magnification of 500×.

SEM analysis

The morphologies of the cellulosic samples were studied by SEM on a FEI QUANTA 200 3D low-vacuum scanning electron microscope. The fibers were coated with gold particles before examination.

Results and discussion

Enzymatic hydrolysis

The reaction rates from enzymatic hydrolysis were identified for all three polymorphic forms of microcrystalline cellulose (AI, AII and AIII), under a separate action of *A. niger* and *T. reesei* cellulases, with a concentration of 30 U/mL. The efficiency of enzymatic hydrolysis regarding the cellulosic substrates was estimated by the amount of sugar released into reaction filtrate, and also by the yield during the reaction.

Table 1 presents the concentration values of the reducing sugar, obtained after 72 h of enzymatic hydrolysis. The highest hydrolysis rate for cellulose II indicates that the chemical modification of cellulose, i.e. treatment with NaOH solution, caused a decrease in crystallinity degree, and thus an implicit increase in the accessibility of the cellulosic substrate, facts which are important factors when controlling a heterogeneous hydrolysis reaction. The values obtained for cellulose III in comparison with cellulose I, confirm the partial reversion of cellulose III to cellulose I, while also retaining a certain disorganized state at the level of the supramolecular structure, thus making it more accessible to enzymatic attack. This could explain the progress of the hydrolysis rate which was higher in case of cellulose III, rather than cellulose I.

The data regarding the yield during the enzymatic hydrolysis reaction of the cellulose allomorphs suggests that the action of the cellulase from *A. niger* was more pronounced compared to the cellulase from *T. reesei*, and that the efficiency of the reaction increased throughout the whole incubation time, from 24 to 72 h. The most affected substrate was cellulose II, whose yield values were between 54 and 62% in the case of *T. reesei* cellulase, and between 68 and 84% for *A. niger* cellulase. Cellulose I was the least affected, where for the treatment with *T. reesei* cellulase obtained a yield from the reaction of between 6 and 10%.

The influence of the cellulase type on the progress of an enzymatic hydrolysis reaction (Fig. 1), being reflected by the concentration values of the reducing sugars, indicated that the action of *A. niger* cellulase was more evident than the *T. reesei* cellulase. In the case of the cellulose allomorphs hydrolyzed in the presence of *T. reesei* cellulase, the rate of enzymatic degradation was higher during the first 24 h, after which it remained constant. An explanation for this behavior is that during enzymatic degradation, the cellulolytic enzymes attacked more of the amorphous fraction of the substrate. Accordingly, during the progress of the hydrolysis, the rate of reaction decreased as a result of the presence of the crystalline fraction, being more resistant to the cellulase action. Irreversible adsorption or non-specific binding of cellulases can be present besides the thermal inactivation of enzymes (Mussatto et al. 2008). On the other hand, a slower degradation rate of the cellulose allomorphs was recorded with *A. niger* cellulase over the first 24 h of incubation compared to *T. reesei*

Table 1 Enzymatic hydrolysis of cellulose allomorphs

Cellulose allomorph	Type of cellulase	Total sugars[a] (g/L)	η^b (%)		
			24 h	48 h	72 h
AIa	*Trichoderma reesei*	1.412	6	8	10
AIIa		1.671	54	60	62
AIIIa		1.495	17	18	18
AIb	*Aspergillus niger*	1.600	21	37	43
AIIb		1.850	68	70	84
AIIIb		1.740	19	31	37

[a] Determined on the basis of the dinitrosalicylic acid (DNS) method

[b] Calculated on the basis of substrate dry weight before and after hydrolysis

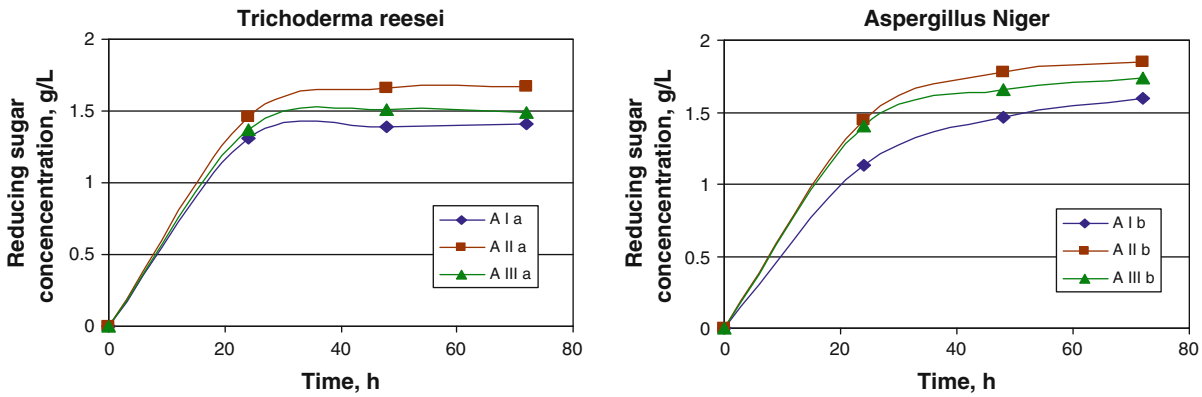

Fig. 1 The progress of enzymatic hydrolysis regarding different cellulose allomorphs using different cellulases

cellulase, but after 24 h of incubation *A. niger* cellulase exhibited higher cellulolytic activity on all three cellulose allomorphs tested by a continued increase in the reaction rate. An explanation could be the fact that *T. reesei*-strain is deficient in *β*-glucosidase, which is essential for converting cellobiose into glucose, while *A. niger* has proved to be a very good producer of this, although, based on the enzyme producer data, endo-glucanases should be the main enzymes in the products. However, looking generally, *β*-glucosidase causes deglycosylation of the substrates and produces gentiobiose, which is a strong inducer of cellulases. Thus, the main product of the hydrolysis with *T. reesei* would be cellobiose, which is a strong inhibitor of endo- and exo-glucanases, and the accumulation of cellobiose would significantly slow-down the overall hydrolysis process (Ahamed and Vermette 2008). The similar behaviour, regarding the fact that *A. niger* cellulase is more efficient than *T. reesei*, was emphasized by Al-Zuhair (2008) using carboxymethylcellulose and wood-chips as cellulosic substrates.

A strong chemical modification of cellulosic substratum was shown by taking into account the structural differences of the allomorphic forms of cellulose, which led to a decrease of crystalline region, permitting an increase in the hydrolysis rate. The fact that the allomorphic form of cellulose II presented a higher hydrolysis rate than cellulose I is explained by the differences which appeared in the intra- and intermolecular bonds of supramolecular structure for each type of allomorph. As was previously shown, the values obtained for the biodegradation rate of cellulose III reflect a partial reversal to the crystalline form of cellulose I.

Particle-size distribution

The effect of enzymatic hydrolysis was also studied by particle-size distribution (PSD) and it was observed

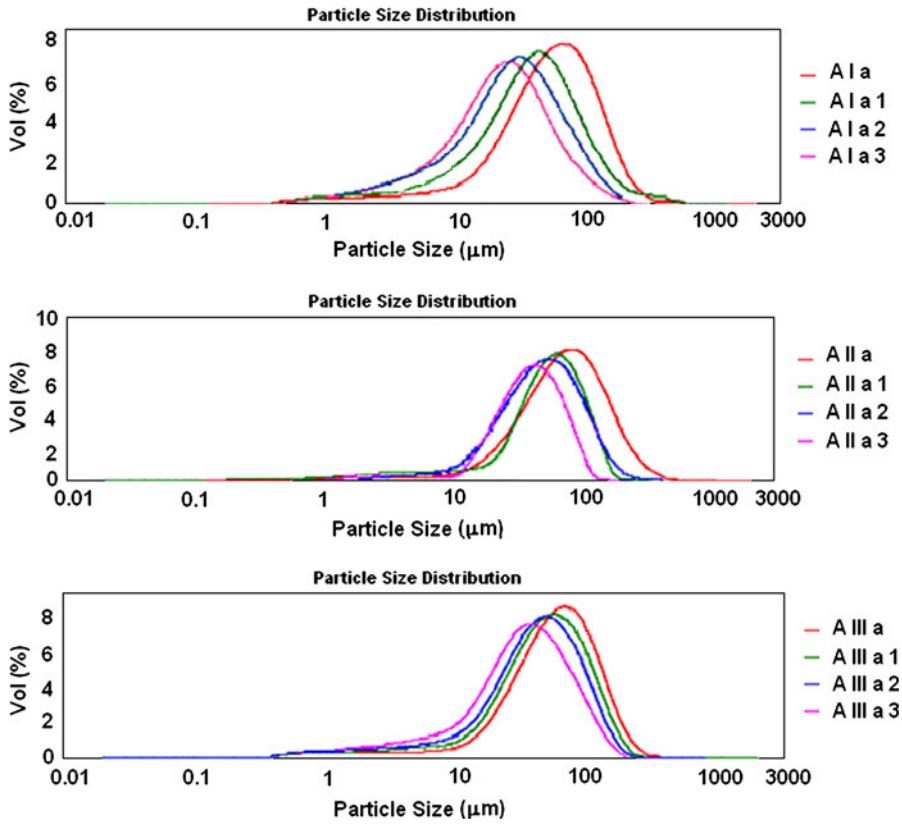

Fig. 2 Particle size distribution for untreated cellulose allomorphs, and those treated with *T. reesei* cellulase

that modifications depend on both the supramolecular structures of cellulose allomorphs and the activities of the cellulases (Figs. 2, 3).

During enzymatic hydrolysis reaction, the cellulosic allomorphs were cut into small particles, and the quantities of these increased with any increase in incubation time. By comparing the enzymatic degradation of cellulose I using both cellulases, a decrease in particle dimensions could be observed, which was higher for *A. niger* cellulase (between 54.96 µm for AI and 17.8 µm for AI b3), than for *T. reseei* cellulase, being 20.50 µm for AI a3.

Figure 4 presents the changes in the average particle sizes of the cellulose allomorphs along the enzymatic degradation, in the presence of both cellulases. It can be identified that the supramolecular structures of the cellulose allomorphs have different influences on the courses of their enzymatic degradations. The most remarkable size-reduction was recorded for cellulose II, which suffered a decrease in the average diameter of its particles, of 68% in the presence of *A. niger* cellulase and of 62% for *T. reesei* cellulase. Generally, the average diameters of cellulose allomorphs decrease monotonically with any increase in the enzymatic hydrolysis time, and these samples usually exhibit a bimodal particle size distribution.

High-performance size exclusion chromatography

As presented, the enzymatic degradation of cellulose allomorphs is accompanied by the release of soluble sugars, which may consist of a significant amount of glucose, as well as other degradation products, such as cellobiose, cellotriose, etc. (Zhang and Lynd 2004). The accumulation of soluble sugar in the supernatant was used as a measure of the enzymatic hydrolysis process efficiency. Thus it was observed an increase in the hydrolytic efficiency with the reaction time.

Figure 5 shows typical SEC chromatograms of the degradation products obtained after the enzymatic hydrolysis of cellulose II, at different reaction times, using *A. niger* cellulase. This example was selected because in the presence of this cellulase, cellulose II recorded the highest concentration of reducing sugars, compared to the other cellulose allomorphs. The chromatograms show a peak corresponding to higher

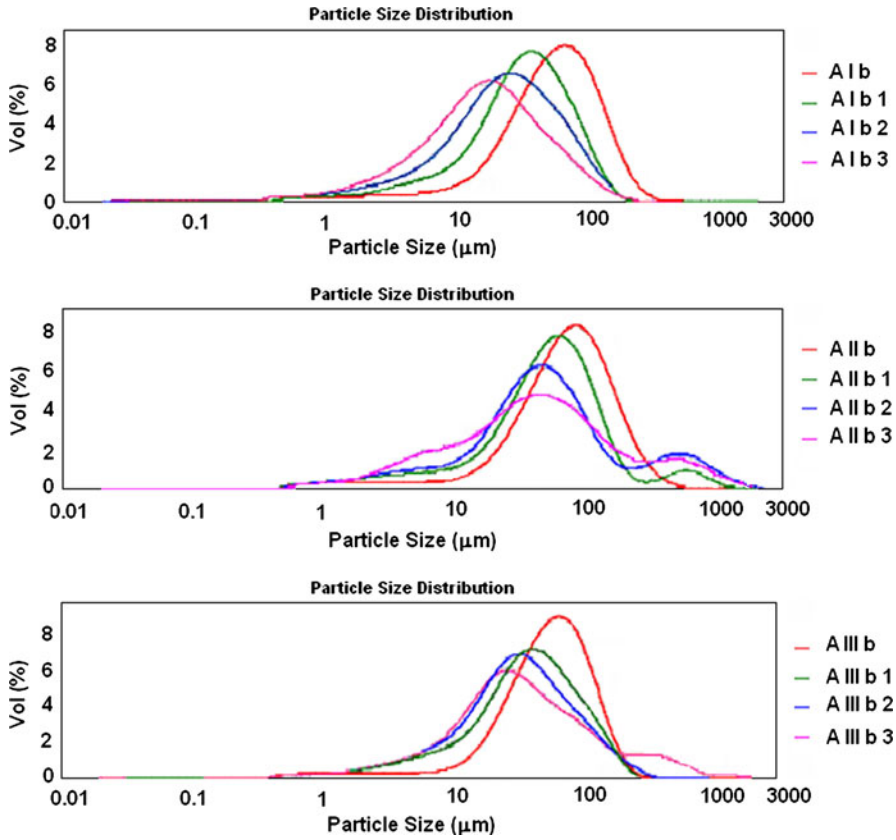

Fig. 3 Particle size distribution for untreated cellulose allomorphs, and those treated with *A. niger* cellulase

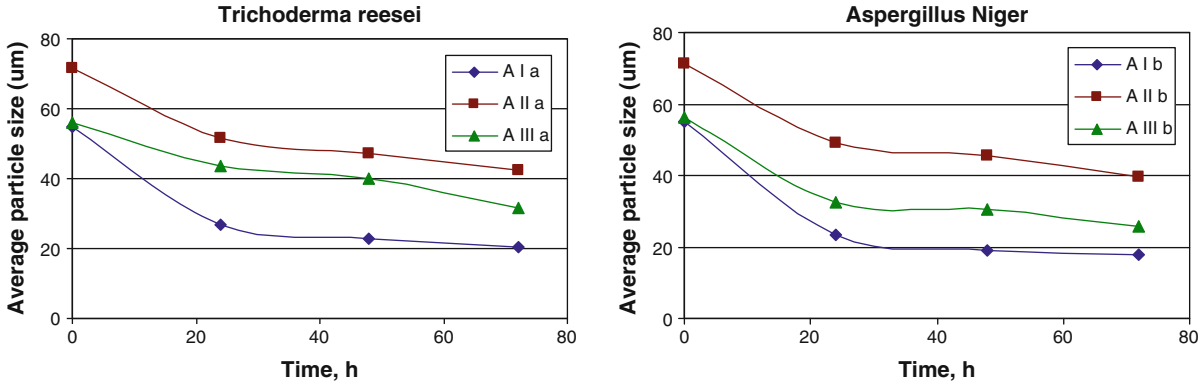

Fig. 4 The influence of enzymatic hydrolysis time on particle size distribution for studied cellulose allomorphs

$\bar{M}$w fractions (retention time between 14 and 16 min) and a main peak in the time interval between 18 and 20 min, corresponding to oligomeric fragments (in this case, glucose). The other peaks, which appear between 16 and 17 min, corresponding to cellotriose (peak 3) and cellobiose (peak 4) are shown in Tables 2 and 3. Comparing the data regarding the areas recorded for the main peak (at a retention time of around 18 min) with the other ones, it can be also observed that the higher the reaction time, the higher the extension of enzymatic hydrolysis.

The supramolecular structure of cellulose allomorphs has an important effect on the hydrolysis reaction. Thus, the highest quantity of glucose (peak 5) was recorded for cellulose II. The next allomorphic substrate able to degrade is cellulose III, followed by

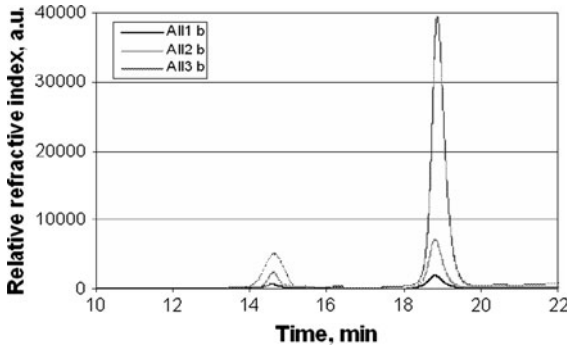

Fig. 5 HPLC-SEC analysis of those degradation products released upon the hydrolysis of cellulose II in the presence of *A. niger*

cellulose I. The explanation for this behaviour is the reversibility of cellulose III to I, with the maintaining of a more relaxed structure, thus permitting a better digestion of this cellulosic substrate. The obtained data are in good correlation with those regarding the reducing sugar concentrations.

Taking into account the whole values from Tables 2 and 3, it can be observed that important differences appeared in the peak areas with respect to the $\bar{M}$w and the retention-time. The characteristic retention-times were successfully identified for each type of cellulase which appeared between 14 and 15 min and for glucose which appeared between 18 and 20 min (spectra not shown). An average molecular mass ($\bar{M}$w) of 76 kDa was found for *A. niger* cellulase (Table 3), while for *T. reesei* a molecular weight of 50 kDa (Table 2) being within the range reported for this cellulase, $\bar{M}$w of 46–52 kDa (Lyagin et al. 2011). The molecular weight of glucose obtained from enzymatic hydrolysis of cellulose allomorphs was 180 Da, and all the intermediary peaks corresponding to different cello-oligosaccharides (cellobiose,

Table 2 The retention times and the areas of the main peaks determined from HPLC-SEC analysis of the solutions obtained after treatment of cellulose allomorphs with *T. reesei* cellulase

Samples treated with *T. reesei* cellulase	Area (%)				
	Peak 1	Peak 2	Peak 3	Peak 4	Peak 5
Retention time (min)	14.82	15.38	16.46	17.74	18.84
AI1a	55.32	–	0.34	6.64	37.67
AI2a	36.89	–	3.07	7.56	52.46
AI3a	33.21	–	5.62	–	61.16
AII1a	–	–	44.32	–	55.66
AII2a	–	–	35.56	–	57.57
AII3a	–	–	33.56	–	61.36
AIII1a	–	–	49.37	1.36	49.27
AIII2a	–	–	36.65	–	56.78
AIII3a	–	–	31.93	–	59.92

Table 3 The retention times and the areas of the main peaks determined from HPLC-SEC analysis of the solutions obtained after treatment of cellulose allomorphs with *A. niger* cellulase

Samples treated with *A. niger* cellulase	Area (%)				
	Peak 1	Peak 2	Peak 3	Peak 4	Peak 5
Retention time (min)	14.7	15.16	16.35	17.16	18.84
AI1b	29.02	–	1.79	2.07	67.11
AI2b	27.32	–	–	4.58	68.08
AI3b	26.78	–	–	–	70.48
AII1b	32.22	–	–	–	67.77
AII2b	27.52	–	1.69	–	70.77
AII3b	24.24	–	–	–	72.90
AIII1b	31.47	–	–	–	68.52
AIII2b	–	–	30.47	–	69.51
AIII3b	–	–	18.35	–	70.77

cellotriose, etc.) obtained after enzymatic degradation of cellulosic substrates. Thus the obtained data for each cellulose allomorph indicated a decrease in the cellulase content and an increase of the glucose content in the reaction mixture, during the enzymatic hydrolysis process. Moreover, a lot of peaks were observed in the chromatograms recorded for *T. reesei* cellulase corresponding to oligomeric fragments, instead of *A. niger* cellulase where higher peaks were detected corresponding to cellulase (peak 1) and glucose (peak 5). This observation sustains the conclusion regarding the different actions of each cellulase on the cellulosic substrates, as explained previously, i.e. that *A. niger* cellulase exhibited higher cellulolytic activity on cellulose allomorphs than *T. reesei*.

X-ray diffraction

Deconvolution of the peaks using a soft PeakFit 4.11 was performed in order to identify the structural modifications suffered by the allomorphic forms of microcrystalline cellulose during the process of enzymatic hydrolysis.

X-ray diffractograms of the residues obtained after enzymatic degradation of cellulose I (Fig. 6) show an important decrease of the characteristic crystal lattice with the maximum intensity at (020) found in diffractograms at a Bragg-angle of 22°, as well as intensities of (101) and (10$\bar{1}$) lattice diffractions at 14° and 16°, respectively. This fact indicates a decrease of the crystallinity index of the samples while maintaining the crystalline form characteristic of cellulose I. in regard to the enzymatic hydrolysis in the presence of *T. reesei*, the reduction in intensities of the peaks were more remarkable than those treated with *A. niger*, for cellulose I.

In the case of cellulose II (Fig. 7), the diffractograms confirmed the preservation of the crystalline structure of cellulose II after the cellulase action. However, more important modifications appeared at the intensity of the characteristic crystallographic peaks and implicitly in the crystalline index for cellulose II treated with *T. reesei* cellulase. If the modifications observed in the diffractograms of the allomorphic forms of cellulose I and II was not exactly dramatically, a partial reversibility was observed of cellulose III to the cellulose I (Fig. 8).

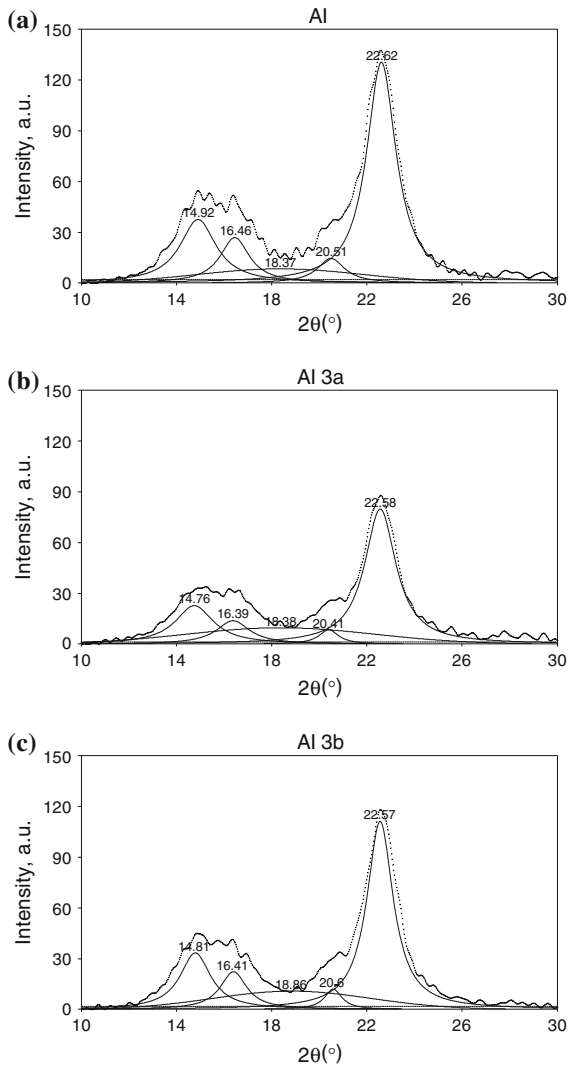

Fig. 6 X-ray diffraction profiles of cellulose I, untreated (**a**) and treated with cellulases from *T. reesei* (**b**) and *A. niger* (**c**) for 72 h

Generally, the diffractogram of cellulose III contain a peak (101) of around 11°, while the peaks at (10$\bar{1}$) and (002) are superimposed at a Bragg-angle of 21°. The transformation of microcrystalline cellulose to cellulose III is incomplete in the present case. However, in the diffractograms of the residues obtained after the enzymatic hydrolysis of cellulose III, the reflection of plane (101) appeared at approximately the same value for the untreated as well as for the enzymatically-treated cellulose. Instead, near the characteristic peak at (002) another reflection of the plane (002) appeared at higher values for the 2θ angle,

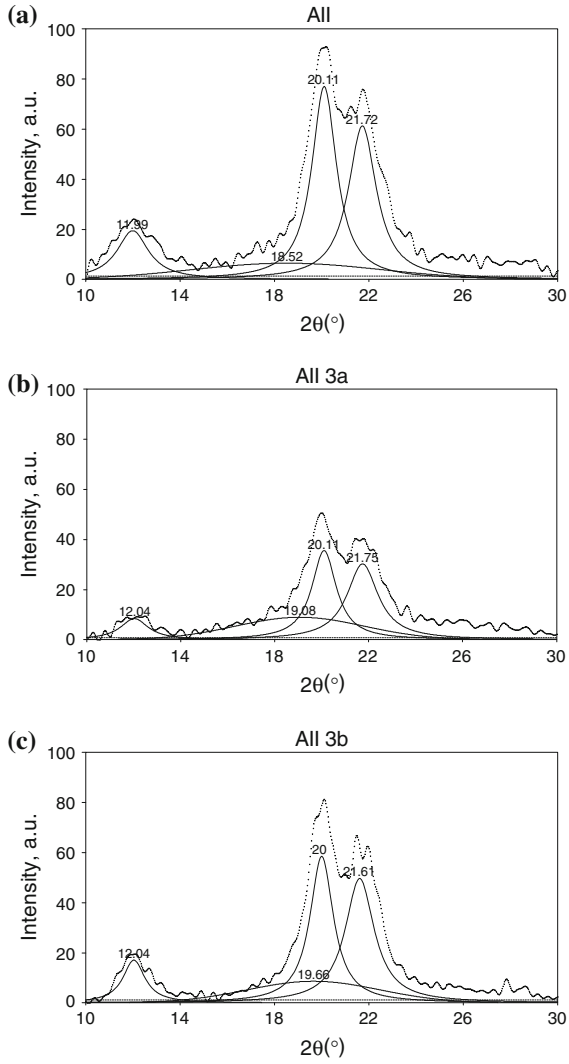

Fig. 7 X-ray diffraction profiles of cellulose II, untreated (**a**) and treated with cellulases from *T. reesei* (**b**) and *A. niger* (**c**) for 72 h

and characteristic for cellulose I (at 22°). The presence of peaks at (101) and (10$\bar{1}$) as characteristic for cellulose I, were also clearly in evidence, which appeared at Bragg-angles of 14° and 15°. These observations confirmed the partial reversion of cellulose III to cellulose I and led us to assume that there is a juxtaposition for the reflection of the (002) plane of cellulose III with that of cellulose I. An explanation for this reversibility is the presence of a water-based medium over a long period of time. This characteristic of the allomorphic form of cellulose III is generally known, which implied only a partial recrystallization, the crystals remained mainly within the distortion and fragmentation (Ciolacu and Popa 2010a, b).

Tables 4 and 5 present those changes that took place during the enzymatic treatment of the cellulose allomorphs, regarding the crystallite dimension (D), lattice spacing (d-spacings), and the crystalline index (CrI). A stronger action of *T. reesei* cellulase against *A. niger* cellulase on the cellulosic substrates can be observed in terms of decreased crystallinity. An explanation of the differences which appear between these two enzymes is the fact that *T. reesei* cellulase hydrolyzed more the amorphous part, while *A. niger* cellulase simultaneously degraded the crystalline and amorphous areas. The obtained data regarding the concentration of reducing sugar, discussed previously, supports this conclusion.

Generally, the X-ray diffraction pattern of cellulose I represents three equal reflections as (101), (10$\bar{1}$) and (002), have many reflections on the layer-lines and two reflections (020) and (040) on the meridian (Hu and Hsieh, 1996). The first three peaks appeared at approximately 14°, 16°, and 22°, respectively, the peak at about 20° corresponding to the (021) reflection, whereas the (040) reflection is at about 34° (Fig. 6). Four distinct and independent reflections were observed in the case of cellulose II, at (101), (10$\bar{1}$), (002), and (040), which were located at Bragg-angles of 11°, 20°, 21°, and 34°, respectively. By transformation from cellulose I to cellulose III, the diffraction pattern modified and, in this case, the reflection at (101) was now at 11°, while the reflections at (10$\bar{1}$) and (002) overlapped at 21°.

Calculation of those crystallite dimensions normal to the hkl planes was come out based on the estimation of the peak width at half-the-maximum amplitude. The crystallite dimensions of four main equatorial reflections were determined and within these, (101), (10$\bar{1}$) and (002) were measured for crystallite width, while the reflection at (040) indicated the crystallite length. The (040) reflection was used to measure the lateral length of the cellulosic samples because this occurs in a direction orthogonal to the longitudinal direction of the microfibril (Garvey et al. 2005).

An increase from cellulose I to cellulose II and III, respectively, was recorded in the case of the crystallite size of untreated cellulose allomorphs along the (10$\bar{1}$) direction, while for the sizes along the other directions, at (101) and (002), a decrease in the dimensions of the

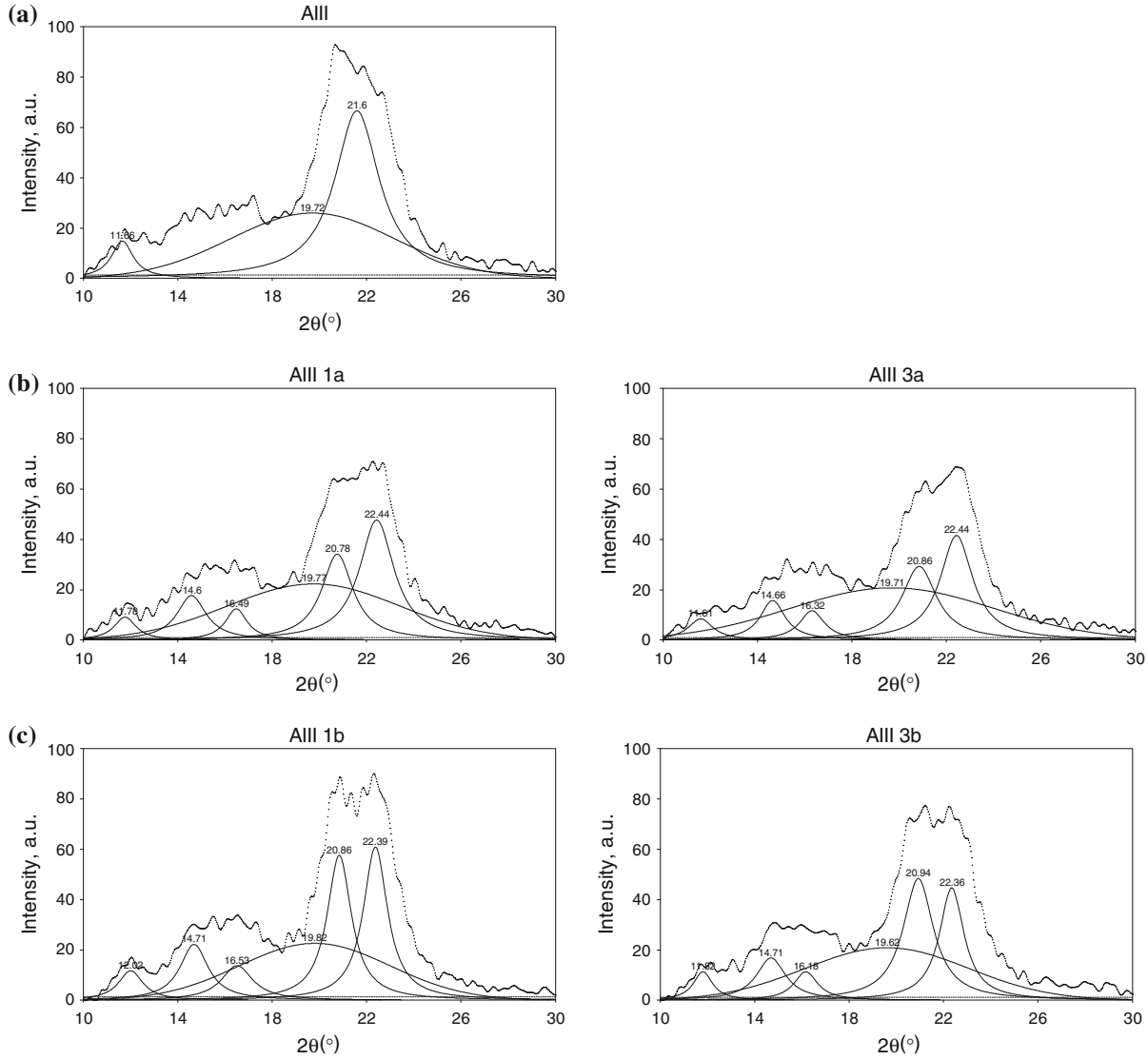

Fig. 8 X-ray diffraction profiles of cellulose III, untreated (**a**) and treated with cellulases from *T. reesei* (**b**) and *A. niger* (**c**) for 24 h (1) and 72 h (3)

same order was shown. A relationship between the crystallinity index and the crystallite dimensions was observed for the enzymatically-treated cellulose allomorphs, namely, the lower the CrI of the sample, the smaller the obtained dimensions of the crystallite. Only for the apparent crystallite size of the (040) peak was recorded a slight increase in the dimension, with an increase in the hydrolysis reaction time. Sun et al. (2009) also reported an increase in the crystallite dimension at the reflection (040) accompanied by a decrease in the dimensions for the other main reflections during the process of microcrystalline cellulose conversion into fermentable glucose, within the formic acid reaction system.

The d-spacing of the (101), (10$\bar{1}$), (002) and (040) peaks for each diffractogram were calculated using Bragg's equation. Taking in account all cellulose allomorphs, cellulose I presented smaller d-spacing compared to cellulose II and cellulose III. Based on the literature, the smaller d-spacing in cellulose I indicates a stronger hydrophobic interaction (Wada et al. 2010). In addition, the hydrophobic attraction would act as a

Table 4 X-ray diffraction parameters of untreated cellulose allomorphs and treated with *T. reesei* cellulase

Samples	Time (h)	D[a] (nm)				d-Spacing[b] (Å)				CrI[c] (%)
		(101)	(10$\bar{1}$)	(002)	(040)	(101)	(10$\bar{1}$)	(002)	(040)	
AI	0	5.3	5.2	8.8	8.3	5.94	5.33	3.90	2.61	87
AI1a	24	5.4	5.7	8.2	9.7	5.90	5.29	3.93	2.61	84
AI2a	48	4.9	5.0	7.2	9.6	5.97	5.31	3.91	2.62	79
AI3a	72	4.3	4.8	8.2	9.8	6.05	5.32	3.90	2.61	76
AII	0	5.1	7.5	8.5	8.6	7.50	4.41	4.10	2.60	85
AII1a	24	5.3	7.5	8.3	12.1	6.92	4.46	4.06	2.60	80
AII2a	48	4.8	7.0	8.7	14.2	7.22	4.43	4.13	2.58	72
AII3a	72	4.0	6.5	7.5	13.6	7.57	4.01	4.01	2.52	63
AIII	0	4.0	8.2	8.2	9.5	7.58	4.26	4.26	2.64	59
AIII1a	24	4.5	7.8	7.8	10.2	7.34	3.93	3.93	2.65	64
AIII2a	48	3.9	8.5	8.5	12.3	7.25	3.91	3.91	2.62	63
AIII3a	72	3.6	7.4	7.4	13.2	7.33	3.92	3.92	2.68	60

[a] Crystallite size perpendicular to the direction of each plane

[b] d-Spacing of typical three equatorial peaks of cellulose

[c] Crystalline index

Table 5 X-ray diffraction parameters of untreated cellulose allomorphs and treated with *A. niger* cellulase

Samples	Time	D[a] (nm)				d-Spacing[b] (Å)				CrI[c] (%)
		(101)	(10$\bar{1}$)	(002)	(040)	(101)	(10$\bar{1}$)	(002)	(040)	
AI	0	5.3	5.2	8.8	8.3	5.94	5.33	3.90	2.61	87
AI1b	24	5.3	4.7	7.6	12.4	6.01	5.33	3.91	2.63	85
AI2b	48	6.3	5.1	7.0	14.7	6.03	5.42	3.93	2.60	82
AI3b	72	4.8	4.5	8.4	14.6	6.01	5.38	3.91	2.62	80
AII	0	5.1	7.5	8.5	8.6	7.50	4.41	4.10	2.60	85
AII1b	24	5.2	7.6	9.7	15.0	7.36	4.48	4.07	2.62	83
AII2b	48	5.0	8.4	7.5	16.1	7.31	4.46	4.04	2.63	81
AII3b	72	5.1	6.8	6.7	16.8	7.31	4.47	4.07	2.60	78
AIII	0	4.0	8.2	8.2	9.5	7.58	4.26	4.26	2.64	59
AIII1b	24	4.3	8.2	8.2	14.5	7.29	4.28	4.28	2.64	58
AIII2b	48	5.3	8.0	8.0	14.9	7.50	4.27	4.27	2.56	55
AIII3b	72	3.7	5.5	5.5	14.7	7.46	3.95	3.95	2.55	53

[a] Crystallite size perpendicular to the direction of each plane

[b] d-Spacing of typical three equatorial peaks of cellulose

[c] Crystalline index

main factor for resisting enzymatic hydrolysis by cellulase, while hydrogen-bonds in the first layer of cellulose crystallites could become unstable in water. Thus, this modification from cellulose I to cellulose II and III, respectively, which has weaker hydrophobic interaction, could enhance the hydrolysis rate by cellulolytic enzyme, observation which is in agreement with the data achieved during this study. The obtained values showed a very slight decreasing tendency for the main reflections, (101), (10$\bar{1}$) and (002), while the data remained the same for (040). Similar observations have been reported in literature (Hayashia et al. 1997).

Optical microscopy

Microscopic photographs with magnifications of 500× were performed for the untreated microcrystalline cellulose and for those treated with *T. reesei* (AIa 3) and *A. niger* (AIb 3) cellulases, over 72 h (Fig. 9). The micrographs of the cellulosic samples showed a decrease in the fibers dimensions with any increase in the enzymatic hydrolysis time. The effect of particle reduction is more evident in the presence of *A. niger* cellulase, being already shown to have a much more powerful action on cellulose substrate than *T. reesei* cellulase, which exhibited the most serious shape deformation caused by fiber damages.

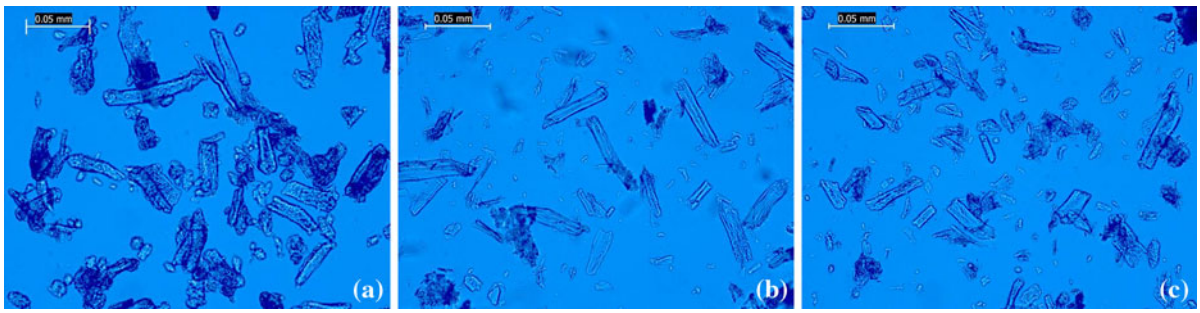

Fig. 9 Microscopic aspects of initial microcrystalline cellulose, untreated (**a**) and treated with cellulase from *T. reesei* (**b**) and *A. niger* (**c**) for 72 h

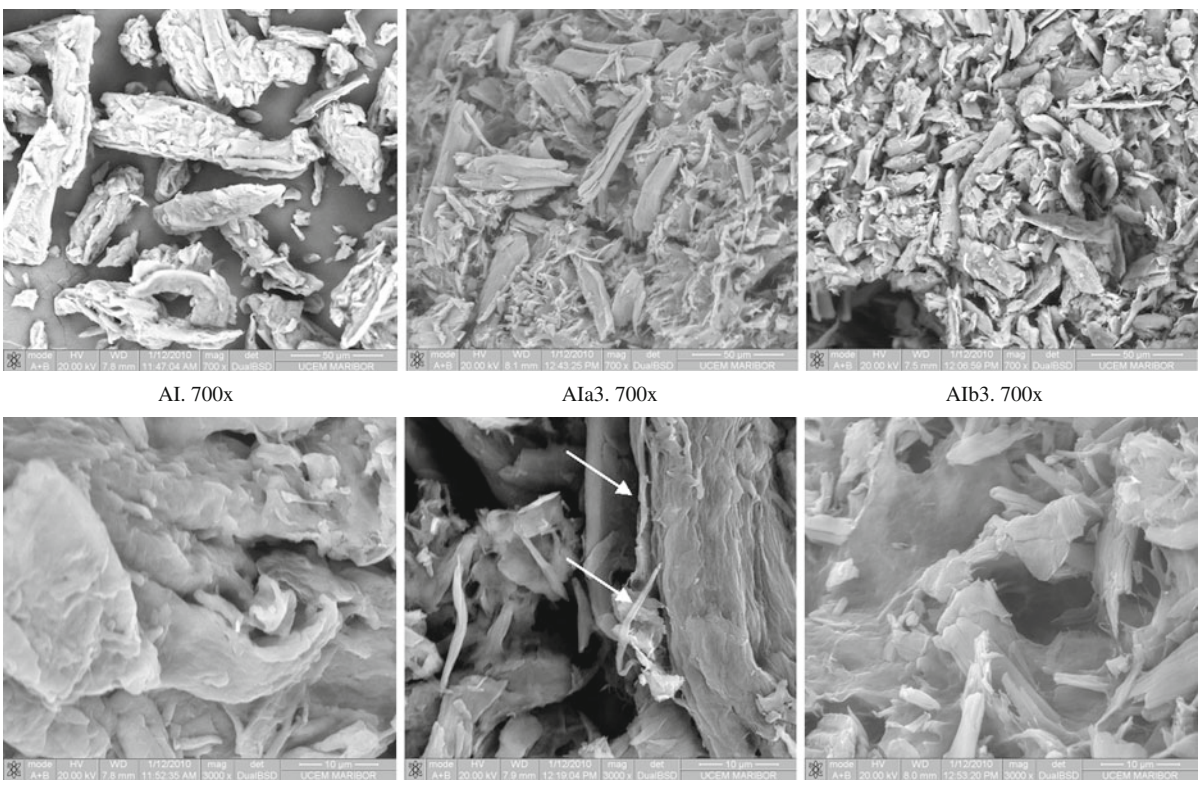

Fig. 10 SEM images of initial microcrystalline cellulose, untreated (AI) and treated with cellulases from *T. reesei* (AIa3) and *A. niger* (AIb3) for 72 h

Scanning electron microscopy (SEM)

Supramolecular structural changes in the untreated and differently-treated microcrystalline cellulose were observed using a scanning electronic microscope (SEM). The SEM images presented in Fig. 10 clearly show the morphological differences between the native cellulose and that treated with *T. reesei* or *A. niger* cellulases over 72 h.

The initial particle of microcrystalline cellulose appears fibrous and bulky. After 72 h of enzymatic hydrolysis the dimensions of the particle became lower and thinner. This aspect was more evident in the case of cellulose treated with *A. niger* cellulase, where the particle had the smallest dimension. The cellulosic fragments and breaks along the cellulosic fibers could be observed at a magnification of 700× (AIb3), which meant that the cellulase broke enough glucosidal bonds to weaken the microfibril surfaces and caused splitting. In the case of cellulose treated with *T. reesei* (AIa3), individual microfibrils could be identified at a magnification of 3000x, as a result of the cellulase action.

Conclusion

The effects of cellulose polymorphism on its biodegradability were evaluated using cellulases from different fungus, *T. reesei* and *A. niger*. It was observed that the hydrolysis rate of cellulose to reducing sugars was more evident for the crystalline structure of allomorphic forms II. Beside, in the presence of aqueous media, cellulose III suffered a partial return to the crystalline structure of cellulose I, the fact which could explain the slower progress of enzymatic degradation rate in comparison with cellulose II.

HPLC-SEC results confirmed the accumulated amount of glucose and other degradation products, being consequently used as a measure of the enzymatic reaction efficiency. During the enzymatic hydrolysis, the scissions of the cellulosic macromolecular chains were evidenced by different modifications in the particle sizes of obtained celluloses, suggesting that the process depends on the supramolecular structures of the cellulose allomorphs and the activities of the cellulases.

Cellulose II was the most affected substrate, which suffered a decrease in the particle average diameter of 68 and 62%, in the presence of *A. niger* and *T. reesei* cellulase, respectively, being related to the difference in hydrolytic actions of cellulases; *T. reesei* hydrolyzes mainly the amorphous part, while *A. niger* simultaneously degrades the crystalline and amorphous areas.

Moreover, a decrease in the crystallinity index and the crystallite dimensions, evaluated by the X-ray diffraction of the enzymatically-treated allomorphs, proves the hydrolytic chain degradation. The microscopic investigation of cellulose allomorphs emphasizes all the statements by showing a decrease in the fiber dimensions with an increase of the enzymatic hydrolysis time. The results of this study generate the hypothesis that the enzymatic hydrolysis process could expand the possibilities for the synthesis of new cellulosic materials with controlled structure–function relationships.

Acknowledgments This research was supported by the Marie Curie Transfer of Knowledge Fellowship of the EC FP6 under the contract nr. MTKD-CT-2005-029540-POLYSURF.

References

Ahamed A, Vermette P (2008) Enhanced enzyme production from mixed cultures of Trichoderma reesei RUT-C30 and Aspergillus niger LMA grown as fed batch in a stirred tank bioreactor. Biochem Eng J 42:41–46

Al-Zuhair S (2008) The effect of crystallinity of cellulose on the rate of reducing sugars production by heterogeneous enzymatic hydrolysis. Bioresour Techn 99:4078–4085

Atalla RH, VanderHart DL (1984) Native cellulose: a composite of two distinct crystalline forms. Science 223:283–285

Azizi Samir MAS, Alloin F, Dufresne A (2005) Review of recent research into cellulosic whiskers, their properties and their application in nanocomposite field. Biomacromol 6(2):612–626

Bansal P, Hall M, Realff MJ, Lee JH, Bommarius AS (2010) Multivariate statistical analysis of X-ray data from cellulose: a new method to determine degree of crystallinity and predict hydrolysis rates. Bioresour Tech 101:4461–4471

Ciolacu D (2007) On the supramolecular structure of cellulose allomorphs after enzymatic degradation. J Optoelectron Adv Mater 9(4):1033–1037

Ciolacu D, Popa VI (2010a) Cellulose allomorphs: structure, accessibility and reactivity, series: polymer science and technology. Nova Science Publishers, Inc., United States

Ciolacu D, Popa VI (2010b) Cellulose allomorphs–overview and perspectives. In: Lejeune A, Deprez T (eds) Cellulose: structure and properties, derivatives and industrial uses. Nova Science Publishers, Inc., United States, pp 1–38

Ciolacu D, Ciolacu F, Dumitriu R, Vasile C, Popa VI (2007) Kinetics aspects in the enzymatic hydrolysis of cellulose allomorphs. Cellulose Chem Tech 41(1):35–40

Ciolacu D, Ciolacu F, Popa VI (2008) Supramolecular structure–a key parameter for cellulose biodegradation. Macromol Symp 272(1):136–142

Das K, Ray D, Bandyopadhyay NR, Sengupta S (2010) Study of the properties of microcrystalline cellulose particles from different renewable resources by XRD, FTIR, nanoindentation, TGA and SEM. J Polym Environ 18:355–363

Davies G, Henrissat B (1995) Structures and mechanisms of glycosyl hydrolases. Structure 3(9):853–859

Garvey CJ, Parker IH, Simon GP (2005) On the interpretation of X-ray diffraction powder patterns in terms of the nanostructure of cellulose I fibres. Macromol Chem Phys 206: 1568–1575

Gusakov AV, Salanovich TN, Antonov AI, Usti-nov BB, Okunev ON, Burlingame R, Emalfarb M, Baez M, Sinitsyn AP (2007) Design of highly efficient cellulase mixtures for enzymatic hydrolysis of cellulose. Biotechnol Bioeng 97:1028–1038

Habibi Y, Lucia LA, Rojas OJ (2010) Cellulose nanocrystals: chemistry, self-sssembly, and applications. Chem Rev 110(6): 3479–3500

Hayashia N, Sugiyama J, Okano T, Ishihara M (1997) The enzymatic susceptibility of cellulose microfibrils of the algal-bacterial type and the cotton-ramie type. Carbohydr Res 305(2):261–269

Hu XP, Hsieh YL (1996) Crystalline structure of developing cotton fibers. J Polym Sci B Polym Phys 34:1451–1459

Karmakar M, Ray RR (2011) Current trends in research and application of microbial cellulases. Res J Microbiol 6: 41–53

Krässig HA (1993) Methods of fiber structure characterization. In: Huglin MB (ed) Cellulose: structure, accessibility and reactivity, polymer monographs, vol 11, chapter 3. Gordon and Breach Science Publishers, Philadelphia, pp 43–149

Kumar R, Singh S, Singh OV (2008) Bioconversion of lignocellulosic biomass: biochemical and molecular perspectives. J Ind Microbiol Biotechnol 35:377–391

Liu H, Fu SY, Zhu JY, Li H, Zhan HY (2009) Vizualization of enzymatic hydrolysis of cellulose using AFM phase imaging. Enzyme Microb Technol 45:274–281

Lyagin E, Drews A, Bhattacharya S, Kraume M (2011) Continuous membrane-based screening system for biocatalysis. Membranes 1:70–79

Lynd LR, Weimer PJ, van Zyl WH, Pretorius IS (2002) Microbial cellulose utilization: fundamentals and biotechnology. Microbiol Mol Biol Rev 66:506

MacLellan J (2010) Strategies to enhance enzymatic hydrolysis of cellulose in lignocellulosic biomass. MMG 445 Basic Biotech e-J 6:31–35

Mansfield SD, Meder R (2003) Cellulose hydrolysis—the role of monocomponent cellulases in crystalline cellulose degradation. Cellulose 10:159–169

Miller GL (1959) Use of dinitrosalicylic acid reagent for determination of reducing sugar. Anal Chem 31(3):426–428

Mussatto SI, Fernandes M, Milagres AMF, Roberto IC (2008) Effect of hemicellulose and lignin on enzymatic hydrolysis of cellulose from brewer's spent grain. Enz Microb Tech 43:124–129

Nishiyama Y, Langan P, Chanzy H (2002) Crystal structure and hydrogen-bonding system in cellulose Iβ from synchrotron X-ray and neutron fiber diffraction. J Am Chem Soc 124: 9074–9082

Nishiyama Y, Sugiyama J, Chanzy H, Langan P (2003) Crystal structure and hydrogen bonding system in cellulose Iα from synchrotron X-ray and neutron fiber diffraction. J Am Chem Soc 125:14300–14306

Paakko M, Ankerfors M, Kosonen H, Nykanen A, Ahola S, Osterberg M, Ruokolainen J, Laine J, Larsson PT, Ikkala O, Lindstrom T (2007) Enzymatic hydrolysis combined with mechanical shearing and high-pressure homogenization for nanoscale cellulose fibrils and strong gels. Biomacromol 8:1934–1941

Pu Y, Ziemer C, Ragauskas AJ (2006) CP/MAS 13C NMR analysis of cellulase treated bleached softwood kraft pulp. Carbohydr Res 341(5):591–597

Russell JB, Muck RE, Weimer PJ (2009) Quantitative analysis of cellulose degradation and growth of cellulolytic bacteria in the rumen. FEMS Microbiol Ecol 67(2):183–197

Siqueira G, Tapin-Lingua S, Bras J, da Silva Perez D, Dufresne A (2010) Morphological investigation of nanoparticles obtained from combined mechanical shearing, and enzymatic and acid hydrolysis of sisal fibers. Cellulose 17: 1147–1158

Siró I, Plackett D (2010) Microfibrillated cellulose and nanocomposite materials: a review. Cellulose 17(3):459–494

Sun Y, Zhuang J, Lin L, Ouyang P (2009) Clean conversion of cellulose into fermentable glucose. Biotech Adv 27: 625–632

Varma AJ (2004) Biodegradable polymers from renewable forest resources. In: Smith R (ed) Biodegradable polymers for industrial applications. Woodhead Publishing Limited, Cambridge, p 223

Wada M, Chanzy H, Nishiyama Y, Langan P (2004a) Cellulose IIII crystal structure and hydrogen bonding by synchrotron X-ray and neutron fiber diffraction. Macromol 37(23): 8548–8555

Wada M, Heux L, Sugiyama J (2004b) Polymorphism of cellulose I family: reinvestigation of cellulose IVI. Biomacromol 5:1385–1391

Wada M, Nishiyama Y, Langan P (2006) X-ray structure of ammonia-cellulose I: new insights into the conversion of cellulose I to cellulose IIII. Macromol 39(8):2947–2952

Wada M, Ike M, Tokuyasu K (2010) Enzymatic hydrolysis of cellulose I is greatly accelerated via its conversion to the cellulose II hydrate form. Polym Degrad Stab 95:543–548

Weimer PJ, Odt CL (1995) Cellulose degradation by ruminai microbes: physiological and hydrolytic diversity among ruminai cellulolytic bacteria. In: Saddler JN, Penner MH (eds) Enzymatic degradation of insoluble carbohydrates, chapter 18, ACS symposium series, vol 618, pp 291–304

Yeh AI, Huang YC, Chen SH (2010) Effect of particle size on the rate of enzymatic hydrolysis of cellulose. Carbohydr Polym 79:192–199

Zhang YHP, Lynd LR (2004) Toward an aggregated understanding of enzymatic hydrolysis of cellulose: noncomplexed cellulase systems. Biotechnol Bioeng 88(7):797–824

gels

MDPI

Article

One-Step Preparation of Carboxymethyl Cellulose—Phytic Acid Hydrogels with Potential for Biomedical Applications

Alina Ghilan [1], Loredana Elena Nita [1], Daniela Pamfil [2], Natalia Simionescu [3], Nita Tudorachi [1], Daniela Rusu [4], Alina Gabriela Rusu [1], Maria Bercea [1], Irina Rosca [3], Diana Elena Ciolacu [1,*] and Aurica P. Chiriac [1]

[1] Department of Natural Polymers, Bioactive and Biocompatible Materials, "Petru Poni" Institute of Macromolecular Chemistry, 700487 Iasi, Romania
[2] Department of Polymer Physical Chemistry, "Petru Poni" Institute of Macromolecular Chemistry, 700487 Iasi, Romania
[3] Centre of Advanced Research in Bionanoconjugates and Biopolymers, "Petru Poni" Institute of Macromolecular Chemistry, 700487 Iasi, Romania
[4] Department of Physics of Polymers and Polymeric Materials, "Petru Poni" Institute of Macromolecular Chemistry, 700487 Iasi, Romania
* Correspondence: dciolacu@icmpp.ro

Abstract: Hydrogels based on natural, biodegradable materials have gained considerable interest in the medical field due to their improved drug delivery profiles and tissue-mimicking architecture. In this regard, this study was devoted to the preparation and characterization of new physically crosslinked hydrogels based on carboxymethyl cellulose and an unconventional crosslinking agent, phytic acid. Phytic acid, in addition to its antioxidant and antibacterial effects, can improve the biological properties and stability of gels, without adding toxicity. Fourier transform infrared (FTIR) spectroscopy, rheological studies and thermal analysis confirmed the hydrogel formation. The influence of the ratio between the cellulose derivative and the crosslinker upon the morphological structure and water uptake was evidenced by scanning electron microscopy (SEM) and swelling measurements in simulated body fluids. Furthermore, procaine was entrapped within the hydrogels and used as a model drug for in vitro studies, which highlighted the dependence of the drug release on the phytic acid content of the matrix. The materials demonstrated antibacterial effects against *Escherichia coli* and *Staphylococcus aureus* bacteria. The biocompatibility was assessed on fibroblast cells, and according to our results, hydrogels can improve cell viability highlighting the potential of these systems as therapeutic scaffolds for skin tissue engineering.

Keywords: carboxymethyl cellulose; phytic acid; hydrogels; biomedical applications

Citation: Ghilan, A.; Nita, L.E.; Pamfil, D.; Simionescu, N.; Tudorachi, N.; Rusu, D.; Rusu, A.G.; Bercea, M.; Rosca, I.; Ciolacu, D.E.; et al. One-Step Preparation of Carboxymethyl Cellulose—Phytic Acid Hydrogels with Potential for Biomedical Applications. *Gels* **2022**, *8*, 647. https://doi.org/10.3390/gels8100647

Academic Editor: Yi Cao

Received: 14 September 2022
Accepted: 9 October 2022
Published: 12 October 2022

1. Introduction

Carboxymethyl cellulose (CMC), one of the most important polysaccharides, is an anionic, water-soluble derivative of cellulose [1]. It has attracted considerable scientific attention and is widely used in a variety of biomedical applications due to its inherent properties such as biocompatibility, biodegradability, tissue resemblance, enhanced water solubility, cost-effectiveness, high stability, non-toxicity and wide range of possible chemical reactions [2]. Among the most attractive biomedical applications, we list: drug delivery [3,4], tissue engineering [5], wound dressing [6], diagnosis of various diseases [7], bone tissue engineering [8], sensing matrices [9], dental materials [10], ophthalmic applications [11] and bioinks for 3D printing [12,13]. These applications revealed by the literature emphasize the appealing possibility of extending CMC's applicability to new and unconventional uses. Moreover, pristine CMC has been shown to be compatible with mucous membranes, bone and skin and can maintain a moist environment in the areas around a wound, which will help increase the extracellular matrix (ECM) and reepithelialization [2]. Additionally, it can activate macrophages and increase cytokine levels in wounds [14]. In this regard, this

study presents a new approach for using CMC as a starting material in the preparation of a novel hydrogel that could be applied as a dressing material.

Hydrogels are three-dimensional polymer networks that can hold large amounts of water, have flexible physical properties and have the ability to be processed into various shapes and sizes. They are also similar to natural tissues and can protect unstable drugs from degradation [15]. However, although numerous types of hydrogels have been developed, the extending of their applications area has some limitations resulting from the complex, irreproducible processing techniques, as well as the synthesis of hydrogels using toxic materials [16]. It is important to add that in the case of CMC, epichlorohydrin is often used, and studies have shown that it can produce a large amount of poisonous and carcinogenic byproducts in strong alkaline conditions [17].

Therefore, this study focused on obtaining a nontoxic, eco-friendly, highly biodegradable hydrogel from an edible crosslinker—phytic acid (PA)—by using a simple processing method that does not require complicated procedures or synthetic reagents other than CMC, PA and water.

PA, also known as inositol hexakisphosphate or inositol polyphosphate, is a major component of plant seeds and can be considered a promising candidate for naturally crosslinking scaffolds. This compound has many hydroxyl-bearing phosphoric groups and exhibits excellent antioxidant and chelating capabilities. Crosslinking between PA and natural polymers could happen upon bonding anions of PA to cations of such a polymer, but also through the formation of hydrogen bonds due to the presence of hydroxyl groups within the structure of the compound [18]. Thus, PA presents versatility in obtaining of functional materials for medical applications. In the literature, this molecule has been crosslinked with polymers such as alginate [19], chitosan [20], carboxymethyl chitosan [21], poly(vinyl alcohol) [22], poly((trimethylamino)ethyl methacrylate chloride) [23], polyacrylamide/chitosan [24] and polyaniline [25] to create various hydrogels for biomedicine. To avoid the conventional application of crosslinkers with higher cytotoxicity, the authors agreed on the significance of using naturally derived crosslinking agents. Moreover, PA has a wide range of biological activities, such as antibacterial, antidiabetic, anti-inflammatory, anticancer, antioxidant, antiangiogenic, antiulcer, antiviral, hypoallergenic, lipid-lowering, immunomodulatory and neuroprotective effects [26].

Due to its countless proven properties, an intensive investigation of the synthesis and characterization of CMC/PA hydrogels is being carried out in the present paper. Additionally, in order to exploit their properties that recommend them as potential drug delivery systems, procaine was chosen as a hydrophilic model drug. Procaine (P) is a local anesthetic known to reduce bleeding and accelerate the wound-healing process, and it has the ability to treat a large variety of infections [27].

2. Results and Discussions

The addition of PA to CMC promoted the formation of hydrogels stabilized by intermolecular bonds between the functional groups of both compounds, which are schematically exemplified in Figure 1. Moreover, as can be seen from the vial inversion test, stable gels are formed at all proposed ratios between the polysaccharide and PA.

2.1. FTIR Spectroscopy Analysis

Figure 2 shows the FTIR analysis of the CMC and CMC/PA hydrogels, while the PA spectrum is found in the inset. The FTIR spectrum of pure CMC shows a broad absorption band at 3464 cm^{-1}, due to the stretching frequency of the –OH groups, while the stretching vibration of the C−H groups can be seen at 2916 cm^{-1}. A strong absorption band related to carboxylates' COO^- asymmetric (1605 cm^{-1}) and symmetric stretches (1425 cm^{-1}) and a band at 1329 cm^{-1} attributed to CH_2 scissoring were recorded. An absorption band with multiple peaks in the 1113–1004 cm^{-1} range is attributed to the ether bonds in the cellulose backbone [28]. The most representative bands in the PA spectrum can be found at 1632 cm^{-1} and 1401 cm^{-1}, attributed to the stretching frequencies of the P=O groups,

and at 1265 cm^{-1}, attributed to the frequencies of the P–O–C groups. The distant band at 3650–3200 cm^{-1} is attributed to –OH vibrations [29].

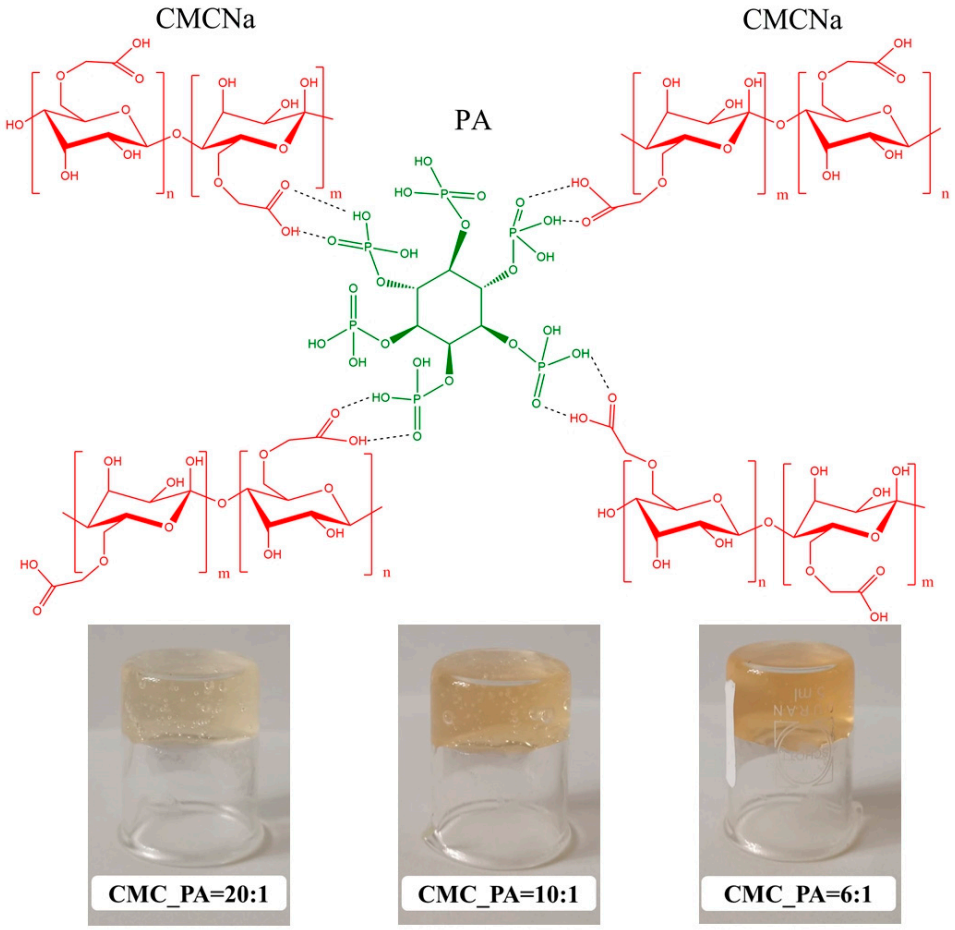

Figure 1. Schematic illustration for the formation of CMC/PA hydrogels and the inverted vial test.

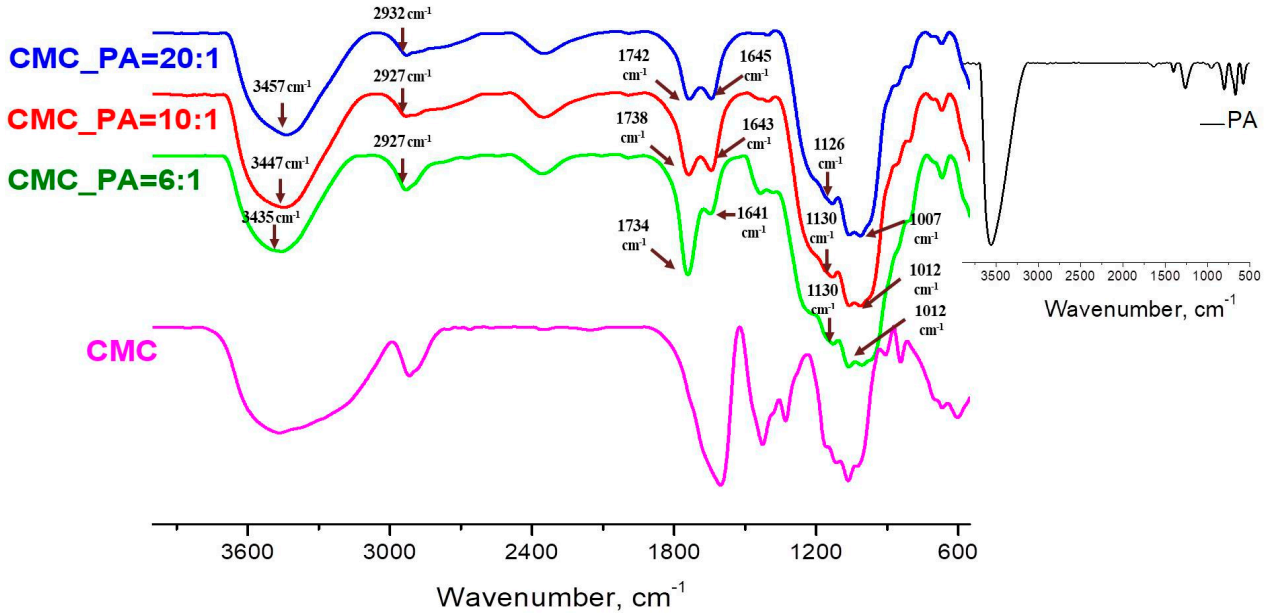

Figure 2. FTIR spectra of the hydrogels of CMC/PA and pure CMC; the spectrum of PA can be found in the insert.

The IR spectra of the CMC/PA structures clearly show the presence of the characteristic bands of their parent components, and thus both compounds participate in the formation of the gel (Table 1). As a general trend for the characterized hydrogels, it can be observed that the broad band in the region 3650–3200 cm^{-1} attributed to the OH vibration shifts to lower wavelengths with the increase of the PA content in the mixture. Moreover, the stretching frequencies of the P=O groups, as well as the anti-symmetric and symmetric frequencies of the P–O–C groups, move also to lower frequencies. These shifts demonstrate the occurrence of intermolecular bonds between the CMC and the crosslinking agent. The OH band of the associated species absorbs at lower wavenumbers because of the fact that the formation of the hydrogen bonds weaken the OH band, thus indicating an increase in the interactions between CMC and PA. Therefore, a high feed ratio of PA determines a greater crosslinking of CMC by PA [30]. Another area of interest that shows changes, an increase in the intensity of the peaks and a shift towards higher wavelengths, is represented by the characteristic region of the $COO-$ groups in CMC. Thus, in the spectra of hydrogels, the carboxylate band disappears (1603 cm^{-1}) and is replaced by a band at 1742 cm^{-1} attributed to the carboxylic acid group COOH. This behavior can be explained by the substitution of Na^+ by H^+ in the CMC polymer chains during the acidification promoted by PA, which acts as well as an ion donor. We can conclude that the addition of PA to CMC engendered the formation of hydrogels stabilized by intermolecular bonds between the functional groups of both compounds.

Table 1. FTIR characteristic bands and their assignment for the studied hydrogels.

Wavenumber, cm^{-1}			Type of Vibration	
CMC_PA = 20:1	**CMC_PA = 10:1**	**CMC_PA = 6:1**		
3457 2932	3447 2927	3435 2927	–OH C–H	CMC- and PA-related stretching modes
1742	1738	1734	COOH	CMC-related stretching modes
1645 1126	1643 1130	1641 1130	P=O P–O–C	PA-related stretching modes
1061–1007	1058–1012	1058–1012	C–O and C-O-C	CMC-related stretching modes

2.2. Swelling Tests

Figure 3 illustrates the equilibrium degree of swelling (SDE) of the CMC/PA hydrogel samples with various amounts of PA crosslinker. The compounds exhibited high SDE, as they absorbed the phosphate buffer solution at a pH = 7.4. By comparing the degree of swelling of the samples, a lower absorption is observed as the amount of crosslinker increases. However, although the highest amount of buffer is absorbed at the lowest PA content (CMC_PA = 20:1, SDE = 374%), the sample with the lowest SDE was CMC_PA = 10:1 (SDE = 172%) and not CMC_PA = 6:1 (SDE = 235%), as was expected. Thus, it follows that the optimal ratio at which a stable network is obtained is 10:1. An increase in the amount of the crosslinker results in a network with larger and more irregular meshes, a statement that will be demonstrated by SEM microscopy.

Taken together, these results demonstrated that the hydrophilicity of CMC/PA hydrogels can vary in correlation with the CMC/PA ratio. Considering that swelling behavior is crucial for promoting a moist microenvironment that aids the wound-healing process, they may be therefore suitable for wound dressings and skin tissue substitutes.

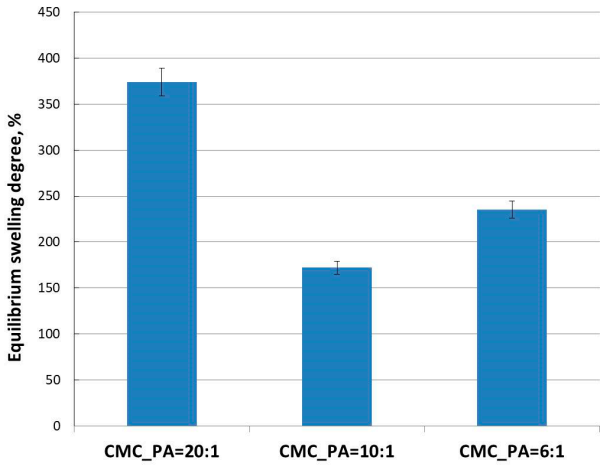

Figure 3. Equilibrium degree of swelling of the hydrogels at different CMC/PA molar ratios.

2.3. Rheological Studies

Figure 4 presents the rheological behavior of the gels in different shear conditions. In the linear range of viscoelasticity, the elastic (G′) and viscous (G″) moduli are independent of the strain (γ) (Figure 4a). Gel-like structure is depicted for all CMC/PA samples: G′ > G″ (Figure 4a,b), and tanδ < 1 (Figure 4c); in similar conditions, CMC behaves as a structured fluid ($G' \sim \omega^{0.66}$ and $G'' \sim \omega^{0.57}$). G′ and G″ present the highest values for the sample CMC_PA = 20:1. Additionally, the values of the shear viscosity are higher as CMC content increases (Figure 4d). The sample morphology (the crosslinking density and the pore distribution) influences the rheological behavior. All CMC/PA samples present tanδ < 1, whereas for CMC, tanδ > 1 at low and moderate values of oscillation frequency. However, CMC_PA = 10:1 shows the highest degree of viscoelasticity, i.e., the maximum difference between the elastic and viscous moduli (minimum values of tanδ, Figure 4c).

The flow curves shown in Figure 4d show a Newtonian region at low shear rates and a non-Newtonian behavior for moderate and high shear rates when the shear viscosity scales as $\dot{\gamma}^{-(0.66 \div 0.7)}$.

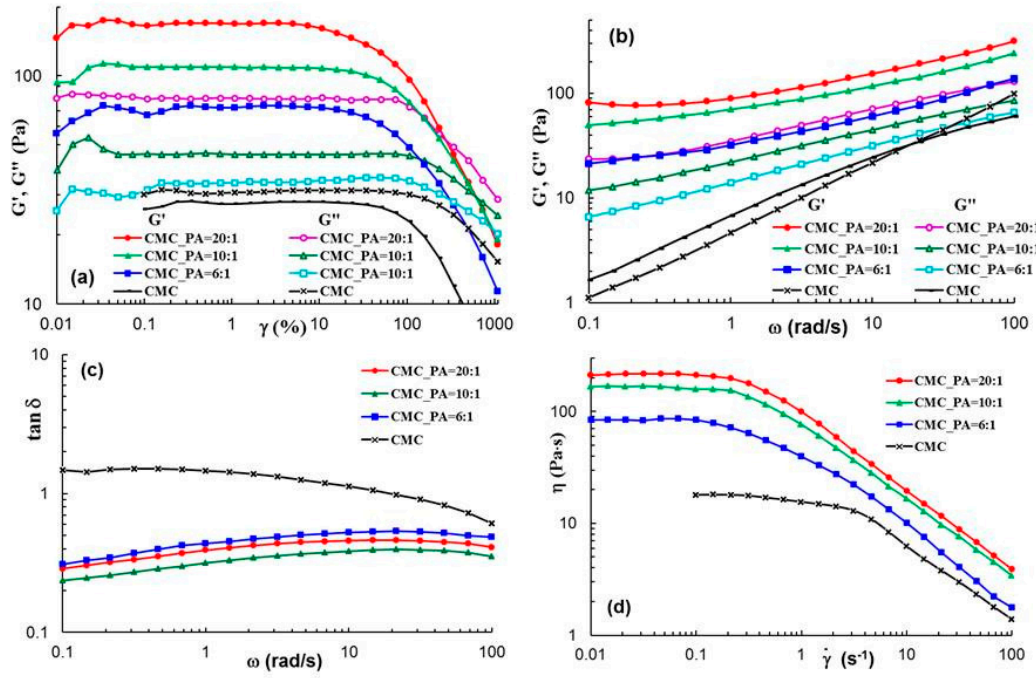

Figure 4. Rheological behavior of the samples in different shear conditions: amplitude sweep (**a**), frequency sweep (**b**,**c**) and shear flow (**d**) at 25 °C.

2.4. Scanning Electron Microscopy Analysis

In order to decode the relationship between the material structure and the capacity for loading and subsequent release of drugs from hydrogels with different crosslinker content, SEM images of freeze-dried gels were obtained (Figure 5). A highly porous network with fine and interconnected pores was observed for all three samples, allowing the absorption of a large amount of solvent. This interconnected pore structure facilitates the diffusion of the solvent molecules in and out through it. This aspect is also in line with the requirements for soft tissue engineering, where it is desirable for the pores to be highly interconnected to aid cell proliferation, differentiation and subsequent tissue formation [31].

Furthermore, an increase in the crosslinking density induces changes in the morphology of the network. Therefore, in the case of the sample with the highest amount of crosslinker (CMC_PA = 6:1), a distinct morphology could be observed compared to the other two samples, with the network showing larger and more irregular pores.

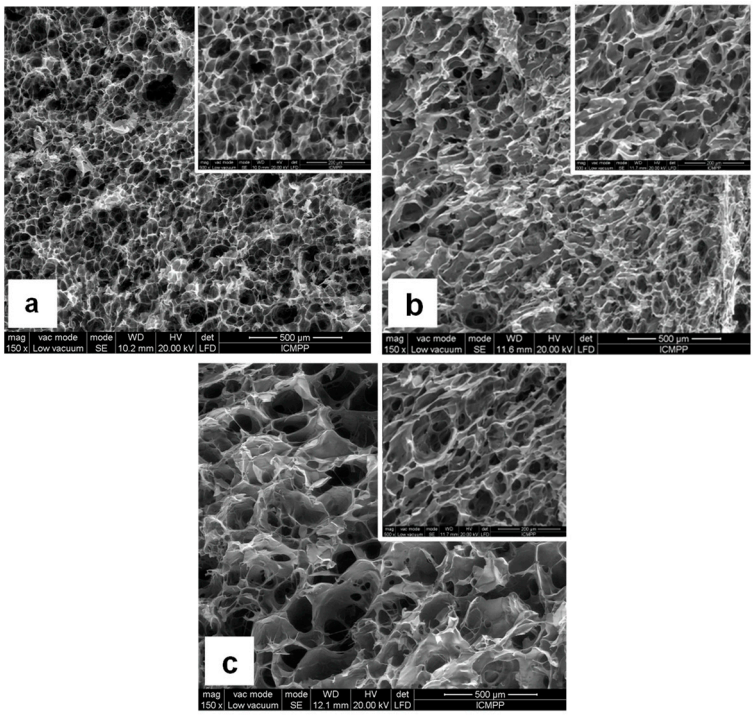

Figure 5. SEM micrographs of freeze-dried hydrogels: (**a**) CMC_PA = 20:1; (**b**) CMC_PA = 10:1; (**c**) CMC_PA = 6:1.

2.5. Thermal Behavior

Figure 6 exhibits primary thermograms (TG) and derivative thermograms (DTG) for CMC and CMC-based hydrogels, while the main thermal parameters are included in Table 2. The thermal degradation of CMC and CMC hydrogels takes place in four stages. At the beginning of the decomposition process (first stage), mass losses are around 12.55% for CMC and from 2.4–4.55% in the case of the hydrogels, these losses being a consequence of moisture removal and evaporation of bound water [32]. This process takes place up to a temperature of about 230 °C for CMC and 168 °C for the gels. In the second stage of the decomposition, the reduced mass loss in hydrogels is due to the physical crosslinking bridges occurring between CMC and PA, while for CMC it is related to the depolymerization of glycosyl units to volatile species by the cleavage of the chains [33]. This process is favored by the reactions of intramolecular and intermolecular rearrangements, resulting in a biochar formation with highly arranged structure and thermal stability. The weight loss was 29.96% for CMC, while for gels it varied between 4.48 and 15.93%, depending on the PA ratio in the hydrogel systems. The mass losses occurring in the third stage of degradation are attributed to pyrolytic decomposition by breaking the C–O–C

bonds present in the glycosidic ring of CMC, degradation of the inositol structure in PA and depolymerization processes and degradation of the side groups [34]. In the last stage of degradation (the fourth stage), the main weight losses are attributed to the fragmentation of molecules associated with pyrolytic decomposition leading to the formation of aromatic units and the decomposition of carbonaceous residues. From the above presented data, we can conclude that the CMC/PA hydrogels are more thermally stable than the native CMC (as seen from the T_{20} and T_{25} values in Table 2). By representing the amount of residue left after thermal decomposition according to the PA content (Figure 6c), a better thermal stability is observed in the case of the CMC_PA = 10:1 sample, thus resulting in the fact that the gels present an increased number of physical interactions that induce higher stability in the polymer network, behavior in good agreement with the swelling data (Figure 3).

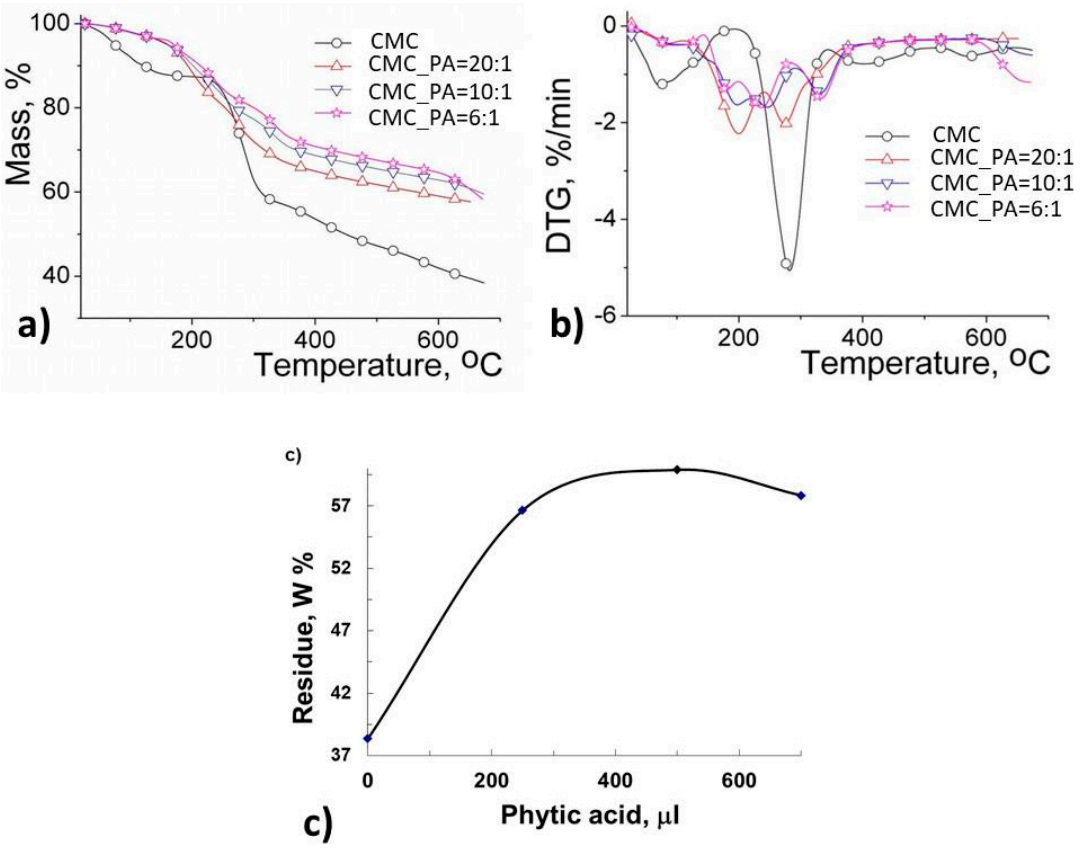

Figure 6. (**a**) TG and (**b**) DTG curves of CMC and CMC/PA hydrogels and (**c**) the residual percentage depending on the amount of PA in the synthesis.

Table 2. Thermal parameters of CMC and CMC/PA hydrogels.

Sample	Heating Rate °C/min	Degradation Stage	T_{onset} °C	T_{peak} °C	W %	T_{20} °C	T_{25} °C
CMC	10	I	35	78	12.55	263	274
		II	229	285	29.96		
		III	356	408	10.23		
		IV	536	569	8.90		
		residue			38.36		

Table 2. *Cont.*

Sample	Heating Rate °C/min	Degradation Stage	T_{onset} °C	T_{peak} °C	W %	T_{20} °C	T_{25} °C
CMC_PA = 20:1	10	I II III IV residue	31 147 254 305	77 200 275 -	2.39 15.93 11.00 13.04 57.64	264	281
CMC_PA = 10:1	10	I II III IV residue	40 168 232 304	74 198 249 332	4.55 8.03 9.17 18.77 59.48	269	321
CMC_PA = 6:1	10	I II III IV residue	45 156 215 303	75 180 238 334	3.52 4.48 10.79 23.07 58.14	301	341

T_{onset}—the temperature at which the thermal degradation starts; T_{peak}—the temperature at which the degradation rate is maximum; T_{20}, T_{25}—the temperatures corresponding to 20% and 25% mass losses; W—mass losses.

2.6. In Vitro Studies of Procaine Release

The in vitro release profiles of procaine from the CMC/PA hydrogel samples under simulated physiological conditions (T = 37 °C, pH = 7.4) are shown in Figure 7. A typical biphasic release pattern is observed, namely a burst release followed by a slower sustained release. This can be explained by the highly hygroscopic nature of CMC as a result of its hydrophilic carboxylate groups in the polymer backbone, which causes a rapid hydration of the network, followed by a fast release of the drug. As a general finding, the drug release results showed a similar trend to that of the swelling results.

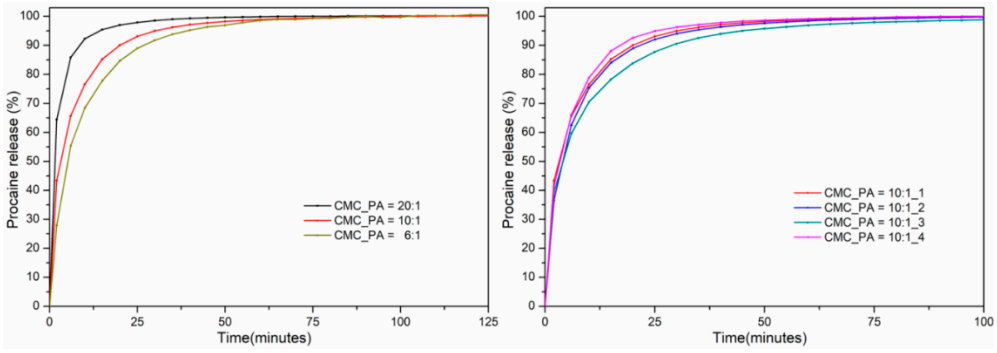

(**a**) (**b**)

Figure 7. Procaine release profiles from the investigated hydrogels with different compositions (**a**) and different drug concentrations (**b**).

The fastest release of procaine, with an equilibrium reached after 65 min, was recorded in the case of the CMC_PA = 20:1 hydrogel. This may be due to the ionic contribution of CMC in the buffer solution at pH 7.4, as well as to the use of a smaller amount of crosslinking agent in the synthesis of this material, which led to the establishing of a low number of crosslinking bonds and implicitly to the obtaining of a more relaxed structure. The drug release equilibrium of the bioactive substance from both hydrogels CMC_PA = 10:1 and CMC_PA = 6:1 was reached after 90–190 min. In the case of CMC_PA = 10:1, this

is attributed to the presence of a larger amount of crosslinking agent in the preparation process that induces an increase in the crosslinking density and the formation of a polymer network with smaller meshes, which maintain the incorporated bioactive compound more firmly through physical bonds. As a consequence, the swelling of the hydrogels decreases, which leads to a delay in the release of the drug.

Figure 7b shows the samples with an optimal ratio of CMC/PA = 10:1 and different amounts of incorporated drug. It can be noted that the sample with the smallest amount of drug, CMC_PA = 10:1_4, releases the fastest. Thus, it can be concluded that with an increase in the drug content, additional intra- and intermolecular interactions between the matrix and the bioactive component appear. The slowest release (k = 0.278 min^{-n}), with a behavior closer to a Fickian release, is shown by the sample CMC_PA = 10:1_3. It can be assumed that at this ratio there is an optimal balance of physical interactions that determines a delayed release.

The value of the release exponent (n) is less than 0.5 (Table 3) for CMC_PA = 20:1 and CMC_PA = 10:1, suggesting a "pseudo-Fickian" diffusion mechanism, caused by a higher rate of polymer relaxation in comparison with the drug diffusion rate. The CMC_PA = 6:1 sample recorded an "n" value of 0.568, which is appropriate for a non-Fickian release behavior. Additionally, it was found that raising the crosslinking agent's concentration causes an increase in the "n" value. The release rate constant (k) values decreased with the increase of the PA content used for the sample preparation. The sample CMC_PA = 20:1 registered the highest value, k = 0.553 min^{-n}, which is correlated to the most accelerated rate of procaine release in comparison with the other samples.

Table 3. Kinetic parameters of procaine release in PBS buffer medium of pH 7.4 at a constant temperature of 37 °C.

Sample Name	n	R^2_n	k [min^{-n}]	R^2_k
CMC_PA = 20:1_1	0.229	0.9689	0.553	0.9976
CMC_PA = 10:1_1	0.338	0.9917	0.347	0.9979
CMC_PA = 10:1_2	0.344	0.9923	0.313	0.9932
CMC_PA = 10:1_3	0.418	0.9814	0.278	0.9979
CMC_PA = 10:1_4	0.381	0.9891	0.321	0.9965
CMC_PA = 6:1_1	0.568	0.9844	0.188	0.9940

n—release exponent; k—release rate constant; R^2_n and R^2_k—correlation coefficients corresponding to the slope obtained for determination of n and k.

2.7. In Vitro Biocompatibility Assay

The biocompatibility of the hydrogels was evaluated in fibroblast cells using an MTS assay to further validate their potential to be applied as skin repair materials. The in vitro experiments were carried out in accordance with the ISO10993-5 standard test method (indirect contact) [35]. Figure 8 illustrates the cell viability after incubation with extracts from CMC/PA hydrogels at different concentrations. The MTS results corresponding to the extracts of all analyzed samples revealed that the cell viability of the fibroblast cells was higher than 96% at all concentrations of the extraction media after 24 h, similar to the reference control condition (100%, within statistical variation). Even though the percentage is very small, the data show that adding a larger amount of PA improves cell viability to some extent, demonstrating once again the advantages of this natural crosslinker. To conclude, all samples demonstrated equivalent cytocompatibility toward fibroblast cells, and this fact can be attributed to the high biocompatibility of CMC and PA. Thereby, these hydrogels have properties and in vitro cytocompatibility suitable for prospective applications in wound healing.

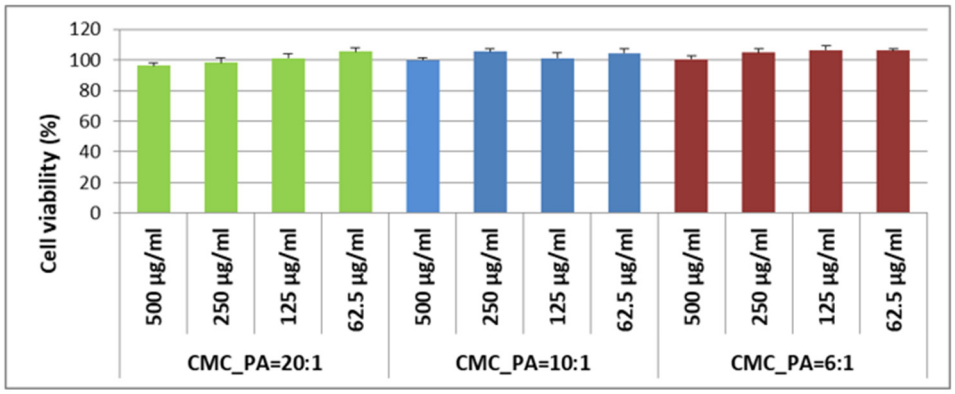

Figure 8. Cell viability of normal human dermal fibroblasts exposed to hydrogel extracts (500/250/125/62, 5 µg/mL) for 24 h; experiments were done in triplicate, and treated cell viability was expressed as percentage of control cells' viability; graphical data were expressed as means ± standard error of the mean.

2.8. Antimicrobial Activity

The antimicrobial activity was evaluated against two different microorganisms using the Kirby–Bauer test, also known as the disk-diffusion method. The diameters of the inhibition zones are presented in Table 4. The hydrogels were effective against both the Gram-positive bacterial strain *S. aureus* and the Gram-negative bacterial strain *E. coli*. These data are in agreement with previous results from the literature reporting that PA exhibits significant inhibitory effects on bacteria and biofilm development when combined with other compounds [36,37]. Additionally, the diameter of the inhibition zone increased slightly with increased amounts of PA in the hydrogel. These results highlighted that PA positively influences the properties of these materials, which could be exploited in biomedical applications where novel strategies to counter antimicrobial resistance are required.

Table 4. Antimicrobial activity of the tested CMC/PA hydrogels against reference strains (mm).

	S. aureus		*E. coli*	
	Inhibition Zone (mm)		**Inhibition Zone (mm)**	
CMC_PA = 20:1	8.80 ± 0.28	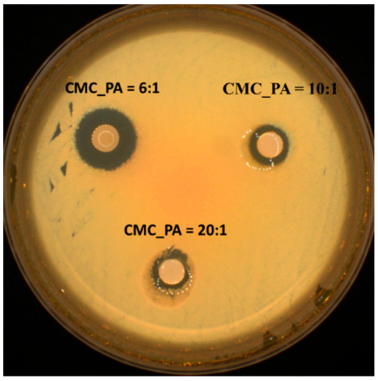	9.10 ± 1.69	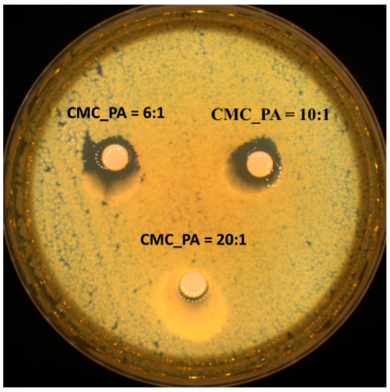
CMC_PA = 10:1	10.60 ± 0.56		10.15 ± 1.06	
CMC_PA = 6:1	12.00 ± 0.42		17.50 ± 0.14	

3. Conclusions

This study focused on the preparation of new hydrogels based on carboxymethyl cellulose and phytic acid through a facile and cost-effective method, as well as their comprehensive characterization for subsequent use as possible skin repair substitutes. The influence of the ratio between the cellulose derivative and the natural and biocompatible crosslinking agent, phytic acid, on the properties of the new compounds was highlighted. The formation of intermolecular bonds between the two compounds was evidenced in the

FTIR spectra by the shifts of the absorption bands characteristic to the hydroxyl groups to lower wavenumbers. Furthermore, these interactions proved to be stronger with the increase of the content of crosslinker agent content in the mixture. These results were also supported by thermal analysis, which indicated a higher stability for the hydrogels compared to pure CMC. Rheological studies showed a gel-like behavior for all tested samples. Moreover, the obtained hydrogels presented a highly porous network, with fine and interconnected pores having the ability to absorb large amounts of water. Procaine was incorporated into hydrogels, and its release properties from the matrix were shown to depend on the polymer/crosslinker mixture ratio. Antimicrobial activity tests showed that the materials have antibacterial activity for both *E. coli* (Gram-negative) and *S. aureus* (Gram-positive) bacteria. Finally, the hydrogels were proved to be cytocompatible, considering the in vitro cell viability responses of over 96% towards fibroblast cells, revealing that the prepared hydrogels could be appropriate options for skin tissue engineering.

4. Materials and Methods

4.1. Materials

All chemicals obtained from commercial suppliers were used without further purification. Carboxymethyl cellulose (CMC), phytic acid (PA, 50 wt.% in water) and procaine hydrochloride (P) were supplied by Sigma Aldrich. In vitro cytocompatibility tests were performed on normal dermal fibroblasts (NHDF, PromoCell, Heidelberg, Germany). The cells were grown in alpha-MEM medium (Lonza, Basel, Switzerland) containing 10% fetal bovine serum (FBS, Gibco, Thermo Fisher Scientific, Waltham, MA, USA) and 1% penicillin–streptomycin–amphotericin B (10 K/10 K/25 µg, Lonza, Basel, Switzerland). An Ultra Clear TWF UV system was used to produce the deionized water that was used for the experiments.

4.2. Sample Preparation

4.2.1. Preparation of CMC/PA Hydrogels

In this study, a series of three hydrogel variants was prepared by varying the feeding of PA into CMC (Table 5). In brief, CMC and deionized water were mixed and mechanically stirred for 24 h to prepare a 2.5% solution. Then, specific amounts of the crosslinking agent (PA, 50% by weight in water) were added dropwise under magnetic stirring to the CMC solution (5 mL). The reaction mixture became increasingly viscous shortly after the addition of PA as a crosslinking agent, and the morphology of the mixture gradually changed from solution to gel approximately 24 h after the start of the reaction. The prepared gel samples were further lyophilized to be characterized and loaded with the therapeutic agent.

Table 5. Chemical composition of the CMC hydrogels in relation with the PA crosslinker content.

Sample Code	CMC, mL	PA, µL
CMC_PA = 20:1	5	250
CMC_PA = 10:1	5	500
CMC_PA = 6:1	5	750
Procaine-Loaded Samples		
Sample Code	**Hydrogel Sample, g**	**Procaine, g**
CMC_PA = 20:1_P_1	0.036	0.0120
CMC_PA = 10:1_P_1	0.036	0.0120
CMC_PA = 10:1_P_2	0.036	0.0090
CMC_PA = 10:1_P_3	0.036	0.0075
CMC_PA = 10:1_P_4	0.036	0.0060
CMC_PA = 6:1_P_1	0.036	0.0120

4.2.2. Preparation of Procaine-Loaded CMC/PA Hydrogels

Previously prepared and lyophilized gels were soaked in an aqueous solution of procaine (0.75% by weight) at a gel/drug mass ratio of 3/1, as presented in Table 5. The

systems were maintained for 24 h under very slow stirring at room temperature (25 °C). In the case of CMC_PA = 10:1, another 3 mass ratios between the hydrogel and drug were taken into consideration: 4:1 (CMC_PA = 10:1_P_2); 5:1 (CMC_PA = 10:1_P_3); and 6:1 (CMC_PA = 10:1_P_4) (Table 5). The procedure allows the entire drug solution to be absorbed by the gel network. The bioactive samples were dried and refrigerated in dark containers until characterization.

4.3. Characterization

4.3.1. FTIR Spectroscopy

The chemical structure of the hydrogels was determined by means of FTIR spectroscopy. The samples, grounded onto KBr disks, were analyzed by using a Bruker spectrometer in vertex mode, with the absorption ranging from 400 cm^{-1} to 4000 cm^{-1}, and the spectra were obtained at a resolution of 4 cm^{-1} as an average of 64 scans.

4.3.2. Swelling Tests

The prepared gels, in the lyophilized state, were tested for their swelling capacity by immersing them in a known amount of phosphate buffer solution (PBS) at pH = 7.4 until equilibrium was reached. Subsequently, the change in gel weight was measured at predetermined time intervals. During the weighing of the samples, PBS was removed from the surface with a filter paper so that only the weight of PBS incorporated in the hydrogel was taken into account. The equilibrium swelling degree (SDE) of the sample was calculated as follows:

$$SDE\ (\%) = [(W_t - W_{d)}/W_d] \cdot 100 \quad (1)$$

where W_d and W_t are the weights of the dry and wet samples, respectively, at time t. Each experiment was performed in triplicate, and the average was obtained.

4.3.3. Rheological Studies

The rheological measurements were carried out at 25 °C with an MCR 302 Anton-Paar rheometer (Graz, Austria) using a plane–plane geometry (diameter of the upper plate of 50 mm, gap of 500 μm).

The oscillatory shear measurements were performed as a function of the oscillation frequency (ω), from 0.1 rad/s to 100 rad/s, for a constant strain of 1%, in the linear range of viscoelasticity that was established for each sample in amplitude sweep tests. The elastic (G′) and viscous (G″) moduli were determined as a measure of the stored energy and dissipated energy during one cycle of deformation, respectively. The loss tangent ($\tan\delta = G''/G'$) provides information on the degree of viscoelasticity of each sample. The shear viscosity (η) was determined in stationary shear flow conditions for shear rate values ($\dot{\gamma}$) in the range 0.01 s^{-1} to 100 s^{-1}.

4.3.4. Scanning Electron Microscopy (SEM) Analysis

Freeze-dried samples fixed in advance by means of colloidal copper supports underwent SEM investigations. A thin layer of gold was spray-coated onto the materials (K Emitech550X). Next, a scanning electron microscope type Quanta 200, which operates at 30 kV with secondary electrons in high-vacuum mode, was used to analyze the covered area.

4.3.5. Thermal Analysis

The thermal behavior of CMC/PA hydrogels was determined on a Netzsch STA 449 F1 Jupiter Simultaneous Thermal Analyzer. This system uses a nitrogen atmosphere and has a heating rate of 10 °C·min^{-1}. Prior to that, the materials were kept in a controlled humidity atmosphere with the inorganic salt $CaCl_2$. Accurate sample amounts (7.5–8 mg samples) were weighed and heated in an open Al_2O_3 crucible under a 50 mL/min^{-1} nitrogen flow

rate. Runs were carried out in dynamic mode with a heating rate of 10 °C/min from room temperature up to 600 °C. Proteus® software was used to collect the data.

4.3.6. In Vitro Studies of Procaine Release

In vitro release studies of the therapeutic agent were carried out in a 708-DS Dissolution Apparatus coupled with a Cary 60 UV-VIS spectrophotometer (Agilent Technologies, Santa Clara, CA, USA) by keeping the procaine-loaded hydrogels (~0.03–0.04 g) in 200 mL of phosphate buffer at pH 7.4 and 37 °C at a rotation speed of 100 rpm. Dissolution tests were performed for 24 h. Aliquots of the medium were withdrawn at predetermined time intervals and were analyzed at λmax = 292 nm by using a UV/VIS spectrophotometer. The polymeric matrix did not interfere with the spectrophotometric reading of the drug. The drug concentration was calculated based on the calibration curves determined at the same wavelengths.

The drug release data up to 60% of total drug release were fitted into the Korsmeyer–Peppas equation to determine the release mechanism (Equation (2)) [38].

$$M_t/M_\infty = k \cdot t^n \quad (2)$$

where M_t/M_∞ represents the fraction of the drug released at time t, while M_t and M_∞ are the absolute cumulative amount of drug released at time t and the maximum amount released in the experimental conditions used, respectively, at the plateau of the release curves, k is a constant incorporating the characteristics of the macromolecular drug-loaded system, and n is the release exponent, which is indicative of the release mechanism.

4.3.7. In Vitro Biocompatibility Assay

The biocompatibility of CMC/PA hydrogel samples was assessed using a CellTiter 96® AQueous One Solution Cell Proliferation Assay (Promega, Madison, WI, USA), according to the manufacturer instructions and ISO 10993–5:2009(E). Normal human dermal fibroblasts (NHDF, PromoCell, Heidelberg, Germany) were seeded at a density of 0.5×10^5 cells/mL into 96-well tissue culture-treated plates. After 24 h, the medium in each well was replaced with 100 µL hydrogel extracts (500 µg/mL, 250 µg/mL, 125 µg/mL, 62.5 µg/mL) or fresh complete medium (control). The extracts were performed in a complete cell culture medium at a concentration of 20 mg/mL for 96 h at 37 °C and then diluted 40× for cell incubation. Cells were incubated with extracts for 24 h, and 20 µL of MTS reagent was then added per well 3 h before reading the absorbance at 490 nm using a FLUOstar® Omega microplate reader (BMG LABTECH, Ortenberg, Germany). Experiments were performed in triplicate, and treated cell viability was expressed as a percentage of the control cells' viability. Graphical data were expressed as means ± standard error of the mean.

4.3.8. Antimicrobial Activity

The antimicrobial activity screening of the samples was determined by disk diffusion assay [39,40] against two different reference strains: *Staphylococcus aureus* ATCC25923 (*S. aureus*) and *Escherichia coli* ATCC25922 (*E. coli*). All microorganisms were stored at −80 °C in 20% glycerol. The bacterial strains were refreshed on trypticase soy agar (TSA) at 37 °C, and the yeast strain was refreshed on Sabouraud dextrose agar (SDA) at 37 °C. Microbial suspensions were prepared with these cultures in sterile solution to obtain turbidity optically comparable to that of 0.5 McFarland standards. Volumes of 0.1 mL from each inoculum were spread onto TSA/SDA plates, and then the sterilized paper disks (6 mm) with an aliquot (50 µL) of the samples were added.

To evaluate the antimicrobial properties, the growth inhibition was measured under standard conditions after 24 h of incubation at 37 °C. All tests were carried out in triplicate to verify the results. After incubation, the samples were analyzed with SCAN1200®, version 8.6.10.0 (Interscience) and were expressed as the mean ± standard deviation (SD), performed with XLSTAT Ecology version 2019.4.1 software [41].

Author Contributions: Conceptualization, A.G. and A.P.C.; methodology, A.G., L.E.N. and A.P.C.; validation, A.G., D.P., N.S., N.T. and D.R.; formal analysis, A.G. and L.E.N.; investigation, A.G., D.P., N.S., N.T., I.R., M.B. and D.R.; resources, L.E.N. and A.P.C.; data curation, A.G., D.P., N.S., N.T., M.B. and D.R.; writing—original draft preparation, A.G. and L.E.N.; writing—review and editing, D.E.C. and A.P.C.; visualization, A.G., D.P., N.S., N.T., D.R. and A.G.R.; supervision, D.E.C.; project administration, L.E.N. and A.P.C.; funding acquisition, L.E.N., D.E.C. and A.P.C. All authors have read and agreed to the published version of the manuscript.

Funding: This work was supported by a grant of the Ministry of Research, Innovation and Digitization, CCCDI-UEFISCDI, project number PN-III-P2-2.1-PED-2021-3003, within PNCDI III, and project number PN-III-P2-2.1-PED-2021-2229, within PNCDI III.

Institutional Review Board Statement: Not applicable.

Data Availability Statement: Not applicable.

Conflicts of Interest: The authors declare no conflict of interest. The funders had no role in the design of the study; in the collection, analyses, or interpretation of data; in the writing of the manuscript; or in the decision to publish the results.

References

1. Rahman, M.S.; Hasan, M.S.; Nitai, A.S.; Nam, S.; Karmakar, A.K.; Ahsan, M.S.; Shiddiky, M.J.A.; Ahmed, M.B. Recent Developments of Carboxymethyl Cellulose. *Polymers* **2021**, *13*, 1345. [CrossRef] [PubMed]
2. Kanikireddy, V.; Varaprasad, K.; Jayaramudu, T.; Karthikeyan, C.; Sadiku, R. Carboxymethyl cellulose-based materials for infection control and wound healing: A review. *Int. J. Biol. Macromol.* **2020**, *164*, 963–975. [CrossRef]
3. Pettignano, A.; Charlot, A.; Fleury, E. Carboxyl-functionalized derivatives of carboxymethyl cellulose: Towards advanced biomedical applications. *Polym. Rev.* **2019**, *59*, 510–560. [CrossRef]
4. Hu, Y.; Hu, S.; Zhang, S. A double-layer hydrogel based on alginate-carboxymethyl cellulose and synthetic polymer as sustained drug delivery system. *Sci. Rep.* **2021**, *11*, 9142. [CrossRef]
5. Verma, N.; Pramanik, K.; Singh, A.K.; Biswas, A. Design of magnesium oxide nanoparticle incorporated carboxy methyl cellulose/poly vinyl alcohol composite film with novel composition for skin tissue engineering. *Adv. Perform. Mater.* **2022**, *37*, 706–716. [CrossRef]
6. Sadeghi, S.; Nourmohammadi, J.; Ghaee, A.; Soleimani, N. Carboxymethyl cellulose-human hair keratin hydrogel with controlled clindamycin release as antibacterial wound dressing. *Int. J. Biol. Macromol.* **2020**, *147*, 1239–1247. [CrossRef] [PubMed]
7. Mansur, A.A.; de Carvalho, F.G.; Mansur, R.L.; Carvalho, S.M.; de Oliveira, L.C.; Mansur, H.S. Carboxymethylcellulose/ZnCdS fluorescent quantum dot nanoconjugates for cancer cell bioimaging. *Int. J. Biol. Macromol.* **2017**, *96*, 675–686. [CrossRef] [PubMed]
8. Priya, G.; Madhan, B.; Narendrakumar, U.; Suresh Kumar, R.V.; Manjubala, I. In Vitro and In Vivo Evaluation of Carboxymethyl Cellulose Scaffolds for Bone Tissue Engineering Applications. *ACS Omega* **2021**, *6*, 1246–1253. [CrossRef]
9. Wang, C.; Fadeev, M.; Zhang, J.; Vázquez-González, M.; Davidson-Rozenfeld, G.; Tian, H.; Willner, I. Shape-memory and self-healing functions of DNA-based carboxymethyl cellulose hydrogels driven by chemical or light triggers. *Chem. Sci.* **2018**, *9*, 7145–7152. [CrossRef]
10. Teti, G.; Salvatore, V.; Focaroli, S. In vitro osteogenic and odontogenic differentiation of human dental pulp stem cells seeded on carboxymethyl cellulose-hydroxyapatite hybrid hydrogel. *Front. Physiol.* **2015**, *6*, 297. [CrossRef] [PubMed]
11. Park, S.; Park, J.; Heo, J.; Lee, S.E.; Shin, J.W.; Chang, M.; Hong, J. Polysaccharide-based superhydrophilic coatings with antibacterial and anti-inflammatory agent-delivering capabilities for ophthalmic applications. *J. Ind. Eng. Chem.* **2018**, *68*, 229–237. [CrossRef]
12. Melilli, G.; Carmagnola, I.; Tonda-Turo, C. DLP 3D Printing Meets Lignocellulosic Biopolymers: Carboxymethyl Cellulose Inks for 3D Biocompatible Hydrogels. *Polymers* **2020**, *12*, 1655. [CrossRef]
13. Ghilan, A.; Chiriac, A.P.; Nita, L.E.; Rusu, A.G.; Neamtu, I.; Chiriac, V.M. Trends in 3D Printing Processes for Biomedical Field: Opportunities and Challenges. *J. Polym. Environ.* **2020**, *28*, 1345–1367. [CrossRef] [PubMed]
14. Memic, A.; Abudula, T.; Mohammed, H.S.; Joshi Navare, K.; Colombani, T.; Bencherif, S.A. Latest progress in electrospun nanofibers for wound healing applications. *ACS Appl. Bio. Mater.* **2019**, *2*, 952–969. [CrossRef]
15. Kaith, B.S.; Singh, A.; Sharma, A.; Sud, D. Synthesis, classification and properties of hydrogels: Their applications in drug delivery and agriculture. *J. Mater. Chem. B* **2022**, *10*, 170–203. [CrossRef]
16. Chirani, N.; Yahia, L.; Gritsch, L.; Motta, F.L.; Chirani, S.; Fare, S. History and Applications of Hydrogels. *J. Biomed. Sci.* **2015**, *4*, 1–23. [CrossRef]
17. Kono, H. Characterization and properties of carboxymethyl cellulose hydrogels crosslinked by polyethylene glycol. *Carbohydr. Polym.* **2014**, *106*, 84–93. [CrossRef]
18. Tashi, Z.; Zare, M.; Parvin, N. Application of phytic-acid as an in-situ crosslinking agent in electrospun gelatin-based scaffolds for skin tissue engineering. *Mater. Lett.* **2020**, *264*, 127275. [CrossRef]

19. Nita, L.E.; Chiriac, A.P.; Ghilan, A.; Rusu, A.G.; Tudorachi, N.; Timpu, D. Alginate enriched with phytic acid for hydrogels preparation. *Int. J. Biol. Macromol.* **2021**, *181*, 561–571. [CrossRef]
20. Liu, G.; Liu, Z.; Li, J.; Zeng, M.; Li, Z.; He, L.; Li, F. Chitosan/phytic acid hydrogel as a platform for facile synthesis of heteroatom-doped porous carbon frameworks for electrocatalytic oxygen reduction. *Carbon.* **2018**, *137*, 68–77. [CrossRef]
21. Han, D.; Zhao, H.; Gao, L.; Qin, Z.; Ma, Z.; Han, Y.; Jiao, T. Preparation of carboxymethyl chitosan/phytic acid composite hydrogels for rapid dye adsorption in wastewater treatment. *Colloids Surf. A Physicochem. Eng. Asp.* **2021**, *628*, 127355. [CrossRef]
22. Zhang, S.; Zhang, Y.; Li, B.; Zhang, P.; Kan, L.; Wang, G.; Wei, H.; Zhang, X.; Ma, N. One-step preparation of highly stretchable, conductive and transparent polyvinyl alcohol-phytic acid hydrogel for casual writing circuits. *ACS Appl. Mater. Interfaces* **2019**, *11*, 32441–32448. [CrossRef] [PubMed]
23. Bui, H.L.; Huang, C.J. Tough Polyelectrolyte Hydrogels with Antimicrobial Property via Incorporation of Natural Multivalent Phytic Acid. *Polymers* **2019**, *11*, 1721. [CrossRef]
24. Zhang, Q.; Liu, X.; Zhang, J.; Duan, L.; Gao, G. A highly conductive hydrogel driven by phytic acid towards a wearable sensor with freezing and dehydration resistance. *J. Mater. Chem. A* **2021**, *9*, 22615–22625. [CrossRef]
25. Pan, L.; Yu, G.; Zhai, D.; Lee, H.R.; Zhao, W.; Liu, N.; Wang, H.; Tee, B.C.; Shi, Y.; Cui, Y.; et al. Hierarchical nanostructured conducting polymer hydrogel with high electrochemical activity. *Proc. Natl. Acad. Sci. USA* **2012**, *109*, 9287–9292. [CrossRef] [PubMed]
26. Narayanaswamy, R.; Wai, L.K.; Esa, N.M. Molecular Docking Analysis of Phytic Acid and 4-hydroxyisoleucine as Cyclooxygenase-2, Microsomal Prostaglandin E Synthase-2, Tyrosinase, Human Neutrophil Elastase, Matrix Metalloproteinase-2 and -9, Xanthine Oxidase, Squalene Synthase, Nitric Oxide Synthase, Human Aldose Reductase, and Lipoxygenase Inhibitors. *Pharmacogn. Mag.* **2017**, *13*, 512–518. [CrossRef]
27. Rodoplu, S.; Celik, B.E.; Kocaaga, B. Dual effect of procaine-loaded pectin hydrogels: Pain management and in vitro wound healing. *Polym. Bull.* **2021**, *78*, 2227–2250. [CrossRef]
28. Capanema, N.S.V.; Mansur, A.A.P.; de Jesus, A.C.; Carvalho, S.M.; de Oliveira, L.C.; Mansur, H.S. Superabsorbent crosslinked carboxymethyl cellulose-PEG hydrogels for potential wound dressing applications. *Int. J. Biol. Macromol.* **2018**, *106*, 1218–1234. [CrossRef] [PubMed]
29. Rosso, N.D. Equilibrium, thermoanalytical and spectroscopic studies to characterize phytic acid complexes with Mn(II) and Co(II). *J. Braz. Chem. Soc.* **2009**, *20*, 1515–1522. [CrossRef]
30. Lee, C.M.; Kubicki, J.D.; Fan, B.F.; Zhong, L.; Jarvis, M.C.; Kim, S.H. Hydrogen-Bonding Network and OH Stretch Vibration of Cellulose:Comparison of Computational Modeling with Polarized IR and SFG Spectra. *J. Phys. Chem. B* **2015**, *119*, 15138–15149. [CrossRef]
31. Rusu, A.G.; Chiriac, A.P.; Nita, L.E.; Bercea, M.; Tudorachi, N.; Ghilan, A.G.; Pamfil, D.; Rusu, D.; Cojocaru, F.D. Interpenetrated polymer network with modified chitosan in composition and self-healing properties. *Int. J. Biol. Macromol.* **2019**, *132*, 374–384. [CrossRef]
32. Tripathy, J.; Mishra, D.K.; Behari, K. Graft copolymerization of N-vinylformamide onto sodium carboxymethylcellulose and study of its swelling, metal ion sorption and flocculation behavior. *Carbohydr. Polym.* **2009**, *75*, 604–611. [CrossRef]
33. Basu, P.; Narendrakumar, U.; Arunachalam, R.; Devi, S.; Manjubala, I. Characterization and evaluation of carboxymethyl cellulose-based films for healing of full-thickness wounds in normal and diabetic rats. *ACS Omega* **2018**, *3*, 12622–12632. [CrossRef]
34. El-Sayed, S.; Mahmoud, K.; Fatah, A.; Hassen, A. DSC, TGA and dielectric properties of carboxymethyl cellulose/polyvinyl alcohol blends. *Phys. B* **2011**, *406*, 4068–4076. [CrossRef]
35. *ISO 10993-5:2009*; Biological Evaluation of Medical Devices—Part 5: Tests for In Vitro Cytotoxicity. International Organization for Standardization: Geneva, Switzerland, 2009.
36. Zhou, Q.; Zhao, Y.; Dang, H.; Tang, Y.; Zhang, B. Antibacterial Effects of Phytic Acid against Foodborne Pathogens and Investigation of Its Mode of Action. *J. Food Prot.* **2018**, *82*, 826–833. [CrossRef]
37. Nassar, R.; Nassar, M.; Vianna, M.E.; Naidoo, N.; Alqutami, F.; Kaklamanos, E.G.; Senok, A.; Williams, D. Antimicrobial Activity of Phytic Acid: An Emerging Agent in Endodontics. *Front. Cell. Infect. Microbiol.* **2021**, *11*, 753649. [CrossRef]
38. Korsmeyer, R.W.; Lustig, S.R.; Peppas, N.A. Solute and penetrant diffusion in swellable polymers. I. Mathematical modeling. *J. Polym. Sci. Part B Polym. Phys.* **1986**, *24*, 395–408. [CrossRef]
39. Bauer, A.W.; Perry, D.M.; Kirby, V.M.M. Single disc antibiotic sensitivity testing of Staphylococci. A.M.A. *Arch. Intern. Med.* **1959**, *104*, 208–216. [CrossRef]
40. Clinical and Laboratory Standards Institute (CLSI). *Performance Standards for Antimicrobial Susceptibility Testing*, 32nd ed.; CLSI supplement M100, ISBN1 978-1-68440-134-5 [Print]. ISBN2 978-1-68440-135-2 [Electronic]. Clinical and Laboratory Standards Institute: Wayne, PA, USA, 2022.
41. XLSTAT | Statistical Software for Excel n.d. Available online: https://www.xlstat.com/en (accessed on 27 September 2022).

gels

MDPI

Article

Tailoring the Structure and Physico-Chemical Features of Cellulose-Based Hydrogels Using Multi-Epoxy Crosslinking Agents

Raluca Nicu [1,*], Gabriela Lisa [2], Raluca Nicoleta Darie-Nita [3], Mihaela Iuliana Avadanei [3], Alexandra Bargan [4], Daniela Rusu [5] and Diana Elena Ciolacu [1,*]

[1] Department of Natural Polymers, Bioactive and Biocompatible Materials, "Petru Poni" Institute of Macromolecular Chemistry, 700487 Iasi, Romania
[2] Department of Chemical Engineering, Faculty of Chemical Engineering and Environmental Protection "Cristofor Simionescu", "Gheorghe Asachi" Technical University, 700050 Iasi, Romania; gabriela.lisa@academic.tuiasi.ro
[3] Department of Physical Chemistry of Polymers, "Petru Poni" Institute of Macromolecular Chemistry, 700487 Iasi, Romania; darier@icmpp.ro (R.N.D.-N.); mavadanei@icmpp.ro (M.I.A.)
[4] Department of Inorganic Polymers, "Petru Poni" Institute of Macromolecular Chemistry, 700487 Iasi, Romania; anistor@icmpp.ro
[5] Department of Physics of Polymers and Polymeric Materials, "Petru Poni" Institute of Macromolecular Chemistry, 700487 Iasi, Romania; rusu.daniela@icmpp.ro
* Correspondence: nicu.raluca@icmpp.ro (R.N.); dciolacu@icmpp.ro (D.E.C.); Tel.: +40-332-880-220 (R.N. & D.E.C.)

Abstract: Hydrogel features can be designed and optimized using different crosslinking agents to meet specific requirements. In this regard, the present work investigates the physico-chemical features of cellulose-based hydrogels, designed by using different epoxy crosslinkers from the same glycidyl family, namely epichlorohydrin (ECH), 1,4-butanediol diglycidyl ether (BDDE), and trimethylolpropane triglycidyl ether (TMPTGE). The effect of the crosslinker's structure (from simple to branched) and functionality (mono-, bi- and tri-epoxy groups) on the hydrogels' features was studied. The performances of the hydrogels were investigated through the gel fraction, as well as by ATR-FTIR, DVS, SEM, DSC, and TG analyses. Also, the swelling and rheological behaviors of the hydrogels were examined. The advantages and limitations of each approach were discussed and a strong correlation between the crosslinker structure and the hydrogel properties was established. The formation of new ether bonds was evidenced by ATR-FTIR spectroscopy. It was emphasized that the pore size is directly influenced by the crosslinker type, namely, it decreases with the increasing number of epoxy groups from the crosslinker molecule, i.e., from 46 ± 11.1 μm (hydrogel CE, with ECH) to 12.3 ± 2.5 μm (hydrogel CB, with BDDE) and 6.7 ± 1.5 μm (hydrogel CT, with TMPTGE). The rheological behavior is consistent with the swelling data and hydrogel morphology, such as CE with the highest Q_{max} and the largest pore size being relatively more elastic than CB and CT. Instead, the denser matrices obtained by using crosslinkers with more complex structures have better thermal stability. The experimental results highlight the possibility of using a specific crosslinking agent, with a defined structure and functionality, in order to establish the main characteristics of hydrogels and, implicitly, to design them for a certain field of application.

Keywords: cellulose; epoxy-based crosslinker; hydrogels; ether bonds; swelling; rheological behavior; thermal degradation

Citation: Nicu, R.; Lisa, G.; Darie-Nita, R.N.; Avadanei, M.I.; Bargan, A.; Rusu, D.; Ciolacu, D.E. Tailoring the Structure and Physico-Chemical Features of Cellulose-Based Hydrogels Using Multi-Epoxy Crosslinking Agents. *Gels* **2024**, *10*, 523. https://doi.org/10.3390/gels10080523

Academic Editor: Junfeng Shi

Received: 20 June 2024
Revised: 2 August 2024
Accepted: 7 August 2024
Published: 9 August 2024

1. Introduction

Cellulose, with many benefits including its abundance and modest cost, along with biodegradability, high functionality, and unique morphology, remains a natural polymer of great interest and is mainly used in the development of new materials for the most varied

and interesting applications [1,2]. These new materials include cellulose-based hydrogels, which are sometimes preferred over other hydrogels due to being highly biocompatible, easily affordable, and designable with fascinating structures and properties on a large scale and at a relatively low cost [3]. The presence of three hydroxy groups on each β-D-anhydroglucopyranose unit (AGU) of cellulose contributes to the formation of intra- and intermolecular hydrogen bonds, which plays a pivotal role in the design of cellulose-based materials. These OH groups can also function as reactive sites to form a variety of covalent linkages, with crosslinking being a feasible option [4].

The crosslinking process is of significant importance in designing permanent three-dimensional (3D) networks established within hydrogels and improving their physical and mechanical properties [5]. Depending on the type of crosslinking mechanism, two main types of hydrogels can be defined, namely physically and chemically crosslinked hydrogels. Physically crosslinked hydrogels are the result of the network involving weak and reversible interactions (i.e., ionic or electrostatic interactions, hydrogen bonds, van der Waals forces, and hydrophobic interactions) that occur between polymer chains and determine molecular entanglements or self-assembly [4]. One of the main advantages of physically crosslinked hydrogels involves the fact that it is not necessary to use chemical agents, possibly toxic, for designing 3D networks. However, physical networks have limited stability, because of the possibility of the established linkages to break relatively easily under stress in aqueous environments, thus restricting their possible applications [5]. This deficiency can be avoided by using chemical crosslinking agents in the preparation of hydrogels, thereby obtaining chemically crosslinked hydrogels with improved properties (i.e., material architecture, porosity, swelling degree, etc.), especially with respect to the control of structural stability and their mechanical properties [3]. Therefore, the choice of the chemical crosslinking agent is extremely important in controlling the physico-chemical characteristics of hydrogels [6–9].

Various types of chemical crosslinkers can be used, depending both on the biopolymer type and the extent of the properties' improvement. In the design of cellulose-based hydrogels, a variety of crosslinking agents can be used, such as epichlorohydrin [1,10], aldehyde-based agents [11], adipic anhydride [12], or multifunctional carboxylic acids [13]. However, epichlorohydrin (ECH), a short epoxy molecule, also known as glycidyl chloride, is one of the most commonly used crosslinking agents. The crosslinking reaction occurs between the epoxy group of ECH and the hydroxyl group of cellulose (at any position) via an ether bond. This reaction takes place under alkaline conditions, using 6–9% NaOH solution, a commercially available low-cost and low-pollution solvent [14], without using a catalyst. The only co-products are NaCl and possible unreacted ECH, which can be easily washed out from the hydrogel once the reaction is complete. Moreover, even though ECH is considered to be toxic, it allows for obtaining materials free from crosslinker residues due to the high efficiency of the washing process [7]. All these facts lead to biocompatible cellulose-based hydrogels, supported by various studies regarding their applications, such as wound dressings in the biomedical field [15,16], as eco-friendly hydrogels with controlled release of fertilizer [17], as sustainable and superabsorbent hydrogels for removing contaminants from water [1], and so on.

The glycidyl ether family includes multi-epoxy compounds with a different number of epoxy groups in their structure (bi-, tri-, or multi-epoxy groups) and with different lengths of aliphatic, linear, or branched chains. The epoxy compounds are preferred when it comes to materials for medical applications due to the fact that they are considered less toxic compared with other crosslinking agents based on the ether bond, such as dialdehydes [18] or divinyl sulfone [19]. 1,4-Butanediol diglycidyl ether (BDDE) is a compound with bi-epoxy functional groups present at the two ends of its molecule, which promotes stable ether linkages with the OH groups of cellulose in alkaline environments [20]. Although unreacted BDDE should be considered as slightly to moderately toxic, the residual BDDE might undergo hydrolysis, leading to diol-ether, which has been proved to be non-toxic and to have limited safety risks [18,19]. For instance, due to its low sensitization and good

biocompatibility, BDDE is widely used in the crosslinking of hyaluronic acid hydrogels in order to produce intradermal fillers and implants, and its clinical safety has been confirmed with a residual content of less than 1 ppm [20,21]. In another work, BDDE was used to crosslink hyaluronic acid and bacterial cellulose to obtain wound dressings with improved surfaces and mechanical properties, and thermal resistance [22]. Also, studies undertaken by Venzhik et al. [23] showed that the gels obtained by crosslinking carboxymethylcellulose with BDDE have reduced cytotoxicity, being proposed as materials suitable for medical use. Trimethylolpropane triglycidyl ether (TMPTGE) is a Y-shaped three-arm epoxy crosslinker, with an epoxy group at the end of each arm. High branching facilitates increased reactivity and crosslinking density. Thus, it is expected by its use to obtain materials with high bonding strength and water resistance [24]. For instance, TMPTGE was used as a crosslinking agent to prepare cellulose-based adhesives with great performance. The covalent bonds established between chains form a dense crosslinking network, which reduces the invasion of water molecules, so that the obtained cellulose-based materials show exceptional lap shear strength and water resistance [25].

Considering the high applicative potential of the cellulose-based hydrogels, as well as the constant search for developing new materials with tuned properties for various applications, we intended to design hydrogels starting from cellulose and three different crosslinking agents, namely epichlorohydrin (ECH), 1,4-butanediol diglycidyl ether (BDDE), and trimethylolpropane triglycidyl ether (TMPTGE), respectively. The crosslinking agents that were chosen for this study present different structures in terms of the number of epoxy groups contained in the compound, as well as in the branching of the structure, from simple to complex.

The aim of the study was to establish the correlation between the crosslinker structure/functionality and the physico-chemical features of their corresponding cellulose-based hydrogels, and to highlight the advantages and limitations of each approach. To the best of our knowledge, no comparative study regarding the use of three different crosslinking agents (ECH, BDDE, and TMPTGE) for the chemical crosslinking of cellulose has been reported in the literature to date. The designed hydrogels were investigated using several characterization methods, such as the gel fraction (GF) and swelling studies, dynamic vapor sorption (DVS), scanning electron microscopy (SEM), attenuated total reflectance Fourier transform infrared (ATR-FTIR) spectroscopy, oscillatory rheology, and thermogravimetric (TG) analysis, in order to cover a wide range of the features and to provide valuable information on the structure–property relationship for the obtained cellulose-based hydrogels.

2. Results and Discussion

There has been a continuous search for crosslinking agents that would allow for obtaining hydrogels with improved mechanical properties, good thermal stability, and adequate porosity while maintaining their high adsorption performance.

In this regard, the current study aims to investigate the features of three chemically crosslinked cellulose-based hydrogels, prepared by using three crosslinkers from the same glycidyl family: glycidyl chloride (ECH), 1,4-butanediol diglycidyl ether (BDDE), and trimethylolpropane triglycidyl ether (TMPTGE). The hydrogels obtained in this work were noted according to the type of crosslinker used, i.e., CE, CB, and CT. The evaluation of the morphology, physico-chemical properties, and rheological and thermal behaviors was performed by comparing the properties of the chemically crosslinked hydrogels both with each other and with those of the physically crosslinked cellulose-based hydrogel (C).

2.1. Interaction between Functional Groups of Cellulose and Epoxy Crosslinkers

Cellulose consists of repeating anhydroglucose units (AGUs), covalently linked between C4 and C1. The epoxy crosslinkers target the OH groups on the AGU, mainly at C2, C6, and C3 [26,27]. In this context, the crosslinking process is determined by the synergy between two processes: on the one hand, the chemical crosslinking processes, which involve the formation of ether linkages –C–O–C– between OH groups of the cellulose and

those of the crosslinker by opening the oxirane ring; and on the other hand, the physical crosslinking process between the OH groups of the cellulose chains in close proximity to each other, with the formation of hydrogen bonds [16].

Under alkaline conditions (pH > 7), most ring structures of epoxy groups either open and covalently link to the most accessible hydroxyl groups in the polymer backbone of cellulose, forming stable ether bonds, or hydrolyze into an alcohol [19]. In addition, it has been demonstrated that a very small portion of the epoxy groups of the crosslinker, on the order of ppm, remain "un-opened" in a strongly alkaline environment [20].

Table 1 shows the structure of the three crosslinking agents used, together with the schematic representation of the most likely chemical crosslinking bond formations between the OH groups of the cellulose side chains and the epoxy groups of the crosslinking agent. As can be seen, the crosslinker can be present in different states: (i) fully reacted, where its molecule is involved in ether bonds with cellulose hydroxyl groups at all ends; (ii) pendant crosslinker, with a molecule that has reacted on one end only; (iii) deactivated or hydrolyzed crosslinker, in which case all the epoxy groups are converted into OH groups; and (iv) a residual crosslinker that has not reacted with cellulose or water (only trace amounts) [19]. These hypotheses are also supported by Ruhr and co-workers [28], in a study on the crosslinking of cellulose with a bifunctional epoxy group crosslinker, where it was stated that only some of the BDDE molecules reacted with the cellulose chains at both ends, establishing chemical crosslinking bonds, while the rest of the BDDE molecules reacted only at one end, and the other end either contained an unreacted epoxy group or was hydrolyzed during the process.

Table 1. Schematic representation of the crosslinking agents' structure and the crosslinked cellulose chains with the corresponding crosslinker: (a) epichlorohydrin (ECH, red color), (b) 1,4-butanediol diglycidyl ether (BDDE, green color), and (c) trimethylolpropane triglycidyl ether (TMPTGE, blue color) (ether bonds are highlighted).

(a)		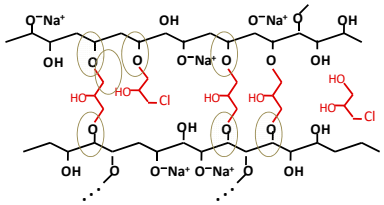
(b)	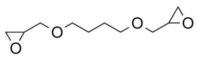	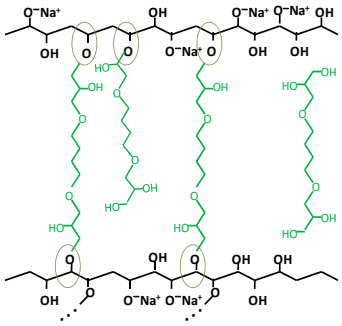
(c)	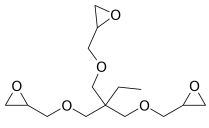	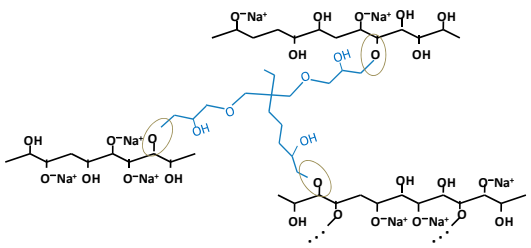

As expected, the more complex the structure of the crosslinker, the more complex the structure of the crosslinked network. In the case of ECH (Table 1a), which is a mono-epoxide molecule and the smallest among the three agents used, the crosslinking reaction is relatively simple regarding the formation of new ether bonds between the available OH groups on the cellulose chains and those formed by the opening of the oxirane ring. Its positioning and binding possibilities are relatively limited. However, with the increase in the number of functional epoxy groups in the structure of the crosslinker, the length of the aliphatic chain, as well as the degree of branching, the crosslinking reaction becomes more complex, increasing the orientation and positioning possibilities of ether bonds. For instance, the presence of the three epoxy groups at each end of the branched chains of TMPTGE (Table 1c) could allow for the formation of a much denser crosslinked network compared with ECH, having a positive effect on the mechanical stability and thermal properties of the hydrogel [25].

2.2. ATR-FTIR Investigations

ATR-FTIR spectroscopy was used as a reliable tool for the general characterization of the crosslinked hydrogels, because it highlights the spectral signatures of functional groups or newly formed bonds through the crosslinking reaction. In this regard, ATR-FTIR was used to establish the realization of the crosslinking reaction and the influence of each crosslinking agent's structure on the cellulose-based hydrogels' network formation.

ATR-FTIR spectra of the physically crosslinked hydrogel (C) and of the three chemically crosslinked hydrogels (CE, CB, and CT, respectively) are shown in Figure 1. All the spectra show the main characteristic bands, such as a broad band attributed to OH stretching vibrations, which are sensitive to inter- and intramolecular interactions (3380–3409 cm^{-1}) [29,30], a C–H stretching band (2800–2960 cm^{-1}) [1], O–H and C–H bending (1400–1300 cm^{-1}) [31], C–O–H, C–O–C asymmetric stretching (1000–1200 cm^{-1}) [18], and the absorption at 895 cm^{-1}, which is characteristic of β-glucan in cellulose [32]. These bands show differences in terms of their intensity and width as a result of the use of the crosslinkers with different epoxy groups (mono-, bi-, and tri-) in the preparation of the hydrogels.

Indeed, the bands from 3200 to 3400 cm^{-1} of the chemically crosslinked hydrogels (CE, CB, and CT) recorded changes in comparison with the physically crosslinked hydrogel (C). More precisely, the band decreases along with the occurrence of a slight shift to the left (i.e., from 3341 cm^{-1} for hydrogel C to 3380 cm^{-1} for CE, 3398 cm^{-1} for CB, or 3409 cm^{-1} for CT, respectively), which might be attributed to the predominant involvement of OH groups in the formation of new ether bonds with the epoxy groups of the crosslinkers [18,33]. In the crosslinking process and, implicitly, in the achievement of the crosslinked network, it is supposed that the OH groups are mainly connected through the opening of the epoxy ring. As the epoxy ring is opened and reacts with OH groups corresponding to the cellulosic chain, the number of free OH groups shows a downward trend [25]. This fact can explain the slight decrease in the intensity of the band at 3341 cm^{-1} for hydrogel CT, in which most of the OH groups are involved in the crosslinking bonds. However, for hydrogel CB, this band shows an increase, being susceptible to an increase in OH groups through the opening of oxirane rings in alkaline medium, without the participation of all OH groups in the formation of ether bonds.

Moreover, significant intensity changes can be observed for the bands in the region from 2800 to 2900 cm^{-1}, associated with the contribution of aliphatic moieties (–CH_2, methylene symmetric, and asymmetric stretching, respectively) [34], especially for hydrogels CB and CT. In these cases, the crosslinkers BDDE and TMPTGE are used, in whose structure long aliphatic chains predominate, compared to the small molecule of ECH, confirming the incorporation of the crosslinker into the cellulose network. The increase is more obvious when TMPTGE is used as a crosslinker, with longer and more branched aliphatic chains.

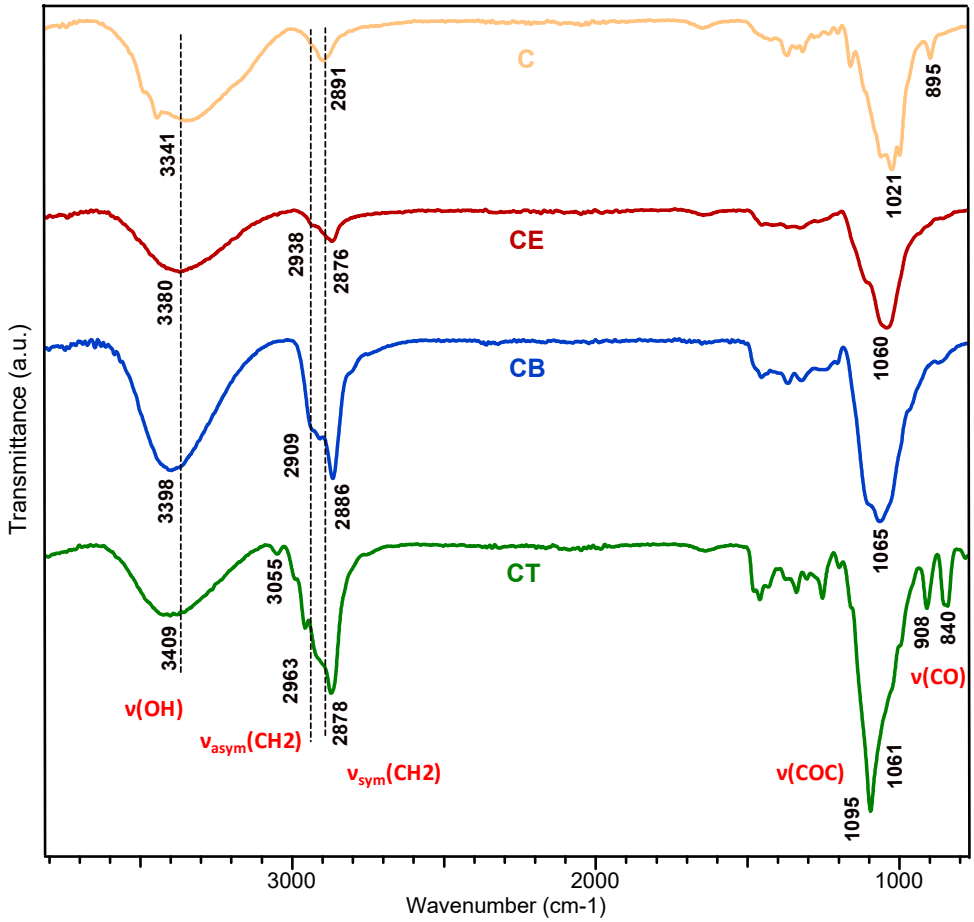

Figure 1. ATR-FTIR spectra of the cellulose-based hydrogels: physically crosslinked hydrogel (C); chemically crosslinked hydrogels with epichlorohydrin (CE), with 1,4-butanediol diglycidyl ether (CB), and with trimethylolpropane triglycidyl ether (CT).

The absorption bands that confirm the achievement of chemical crosslinking by the formation of new ether (C–O–C) bonds are the bands in the 1050–1200 cm^{-1} region [10,17], more exactlyat 1060 cm^{-1} for hydrogel CE, 1065 cm^{-1} for hydrogel CB, and 1061 cm^{-1}, as a shoulder, for hydrogel CT, respectively. However, for hydrogel CT, two small peaks can be observed at 908 cm^{-1} and 840 cm^{-1}, characteristic of the stretching vibration of C–O in glycidyl esters [35], indicating that a small portion of the epoxy ring at the end of TMPEG did not open. This is also suggested by the band at 3055 cm^{-1}, characteristic of the $–CH_2$ stretching vibration of terminal epoxides, which indicates the ring opening did not occur for all the epoxy groups [33].

2.3. Morphological Analysis of Hydrogels

The cross-sectional morphologies of the cellulose-based hydrogels were analyzed by SEM in order to obtain relevant information about the pore geometry, apparent pore size, and heterogeneity of the overall hydrogel's network. It is important to investigate the morphology of the hydrogels before other properties because the pore structure greatly influences essential features, such as interactions with water molecules in the liquid state (i.e., swelling degree) and in vapor state (i.e., adsorption/desorption isotherm and hysteresis), and the rheological behavior.

According to cross-sectional SEM images presented in Figure 2a, the obtained 3D networks have totally different morphologies from each other. Thus, the physically crosslinked hydrogel (C) exhibits an irregular pore structure formed mainly by the entanglement and self-association of the cellulose chains, while the chemically crosslinked hydrogels (CE, CB,

and CT) have different 3D network morphologies and porosities depending on the type of crosslinker used, and implicitly, the established crosslinking bonds. As expected, by using crosslinkers with an increased number of epoxy groups, the pore size decreases and the matrix becomes denser, more compact, and even more uniform. Similar results reported by Luo and coworkers [36] showed that by crosslinking with BDDE, the obtained composites based on bacterial cellulose and hyaluronic acid were much denser and had smaller pores than those from unmodified bacterial cellulose. Moreover, from Figure 2c, it can be seen that the presence of the crosslinker in the system determined the destruction of the self-association and packing of the cellulose chains [37], leading to obtaining more swollen and almost translucent hydrogels (see hydrogel CE), with a more expanded structure.

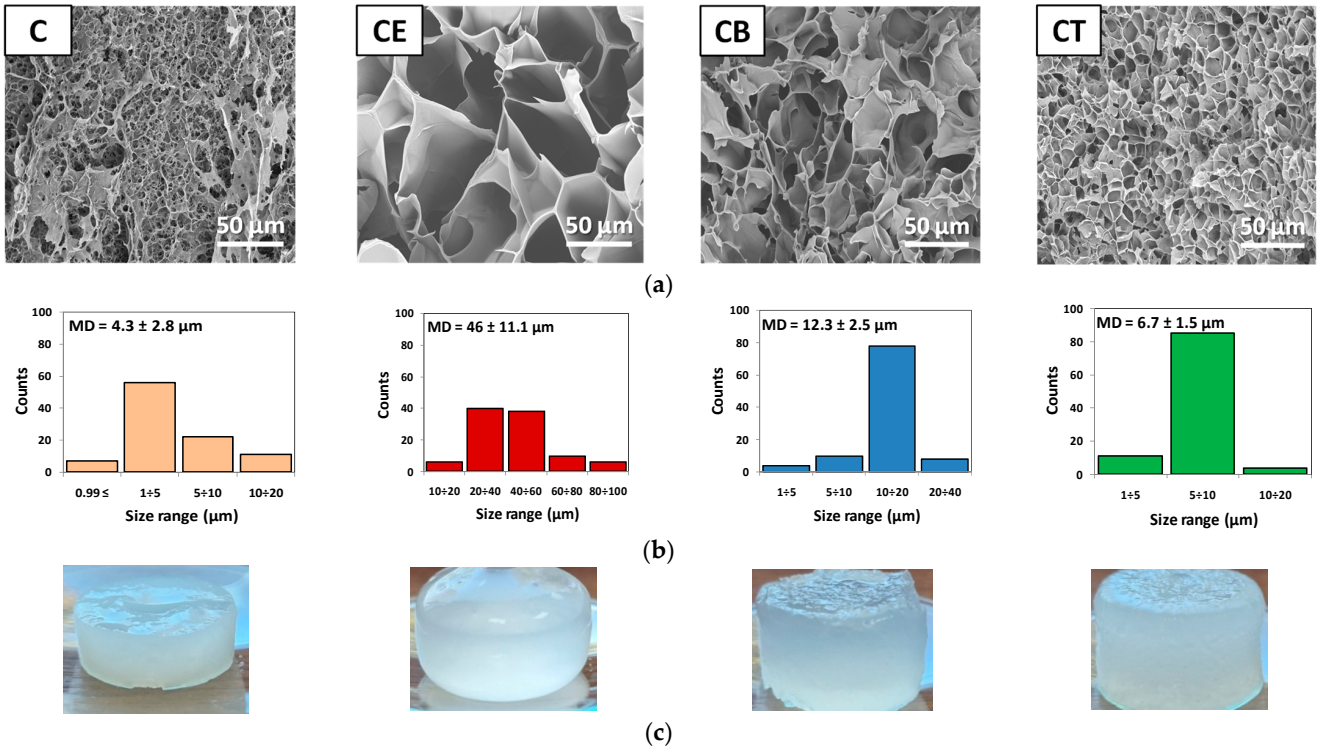

Figure 2. (**a**) Cross-sectional micrographs (mag 500×), (**b**) pore size distribution histogram (MD—mean pore diameter), and (**c**) photographs of never-dried hydrogels.

It was observed that the physically crosslinked hydrogel (C) had a discontinuous porous structure, while the most uniform and compact network, with smaller and regular pore sizes, was obtained for hydrogel CT, where the mean pore diameter (MD) was 6.7 ± 1.5 µm (Figure 2b). This result can be attributed to the TMPTGE crosslinker, with a Y-shaped structure and three arms that permits the formation of new ether bonds with three different cellulose chains at the same time, leading to a more compact structure than that obtained with ECH, for example. Even if ECH is the smallest molecule, this leads to obtaining 3D networks with large, well-defined pores (MD = 46 ± 11.1 µm) with an elongated and irregular shape that are slightly interconnected with visibly thicker walls. For hydrogel CB obtained with the bi-epoxy crosslinker (BDDE), the pores are not as small and uniform as in the case of the CT matrix (MD = 12.3 ± 2.5 µm), but their interconnectivity is much higher than those of the CE and CT hydrogels, which plays a crucial role in the diffusion of the water molecules.

Thus, it can be concluded that the differences between the structure/functionality of the three crosslinking agents are directly reflected both in the pore shape and in the uniformity of pore distribution. With the increase in the number of epoxy groups, pores with an aspect ratio (i.e., the ratio of minor to major pore length) close to unity are obtained, predominantly spherical for hydrogels CB and CT, and the porous structure tends towards

high uniformity (i.e., the majority of the pore size, around 80%, is in the size range of 5–10 μm for CT and 10–20 μm for CB, respectively) (Figure 2b). Instead, hydrogel CE has pores with an aspect ratio less than unity with a predominantly elongated, cylindrical shape, and the hydrogel structure is non-uniform (i.e., the pore size covers a much wider range and the standard deviation has the highest value ±11.1 μm).

2.4. Gel Fraction Measurements

Generally, the formation of a 3D network of hydrogels occurs by chemical or physical crosslinking. To quantify the amount of crosslinking bonds established in the 3D network, the gel fraction (GF) method is used, which is the most effective way to evaluate the degree of crosslinking. Consequently, a hydrogel with a higher gel fraction indicates a higher crosslinking degree.

Table 2 presents the gel fraction (GF, %) and the amount of crosslinker (AC) consumed per unit of anhydroglucose unit (AGU), namely $mole_{AC}/mole_{AGU}$ for the obtained hydrogels. It can be observed that the same amount of crosslinker and cellulose (M_C) leads to different weights of dry hydrogel (M_H) and contributes in a different way to the formation of the 3D network, expressed by the M_H/M_C ratio. For hydrogel C, only 74% from the initial amount of cellulose is converted into a physically crosslinked hydrogel. This result can be explained by the loss of some proportion of the hydrogel through repeated washings with warm distilled water, due to the high susceptibility of intermolecular hydrogen bonds to water. However, after the drying process, the entanglement and self-association of the cellulose chains that occur in hydrogel C become stronger, so that the resultant hydrogel is stiffer, which explains its high GF of 96.3%.

Table 2. Gel fraction and crosslinker consumption per unit of AGU, for the obtained hydrogels.

Sample	M_H (g)	M_H/M_C Ratio	$mole_{AC}/mole_{AGU}$	GF (%)
C	0.37	0.74	-	96.3 ± 4.7
CE	0.75	1.50	0.876	97.3 ± 2.3
CB	1.65	3.30	1.843	94.5 ± 2.0
CT	1.36	2.72	0.915	82.3 ± 2.8

Regarding the chemically crosslinked hydrogels (CE, CB, and CT), the situation is different from that of the physically crosslinked hydrogel. Although the same amount of crosslinker is used for all hydrogels, it is consumed differently depending on the number of epoxy groups located at the ends of the aliphatic, linear, or branched chains. Among the three chemically crosslinked hydrogels, the highest GF is obtained for hydrogel CE, namely 97.3%. This fact demonstrates the high capacity of ECH to form ether bonds with the OH groups of the cellulose chains (only 0.876 mole per mole of AGU is consumed), which allows for the formation of a stronger crosslinked network, with the ability to maintain its physical integrity, without dissolving in an aqueous medium [27]. A GF of over 94% is also obtained for hydrogel CB, which is prepared by using BDDE, with a consumption of 1.843 moles of AC per mole of AGU, double that of ECH. However, the situation is different for hydrogel CT, which has a GF of only 82.3%. In this case, it is assumed that due to the large size of the crosslinker, a "steric effect" is involved to a certain extent in the crosslinking process. Thus, it is possible that the three-arm branched crosslinker (TMPTGE) does not have access to all the OH groups of the cellulose and, implicitly, cannot establish many of the possible ether bonds, remaining partially reacted or even unreacted, and then being removed through the washing process. This hypothesis is also confirmed by the ATR-FTIR investigations (see Figure 1), where the spectrum of the CT hydrogel indicates the fact that a certain proportion of oxirane rings did not open in the alkaline environment, remaining unavailable for crosslinking.

2.5. Swelling Behavior and Swelling Kinetics

The swelling degree is another way to assess the effectiveness of hydrogel crosslinking [5]. Usually, the water content of a fully swollen hydrogel is directly proportional to the crosslinking density, but also to matrix porosity [3]. The swelling ability was measured by the conventional gravimetric method, and the values of the maximum swelling degree (Q_{max}, %), corresponding to the never-dried hydrogels, and the swelling degree (Q_t, %), determined for the hydrogels dried by lyophilization, are presented in Table 3.

Table 3. The swelling degrees of never-dried (Q_{max}) and dried (Q_t) hydrogels, and kinetic parameters of the swelling process.

Sample	Q_{max} (%)	Q_t (%)	n_{sw}	k_{sw}	R^2	Transport Mechanism
C	970 ± 87	710 ± 46	0.038	0.135	0.997	Pseudo Fickian diffusion
CE	1280 ± 54	1030 ± 23	0.094	0.246	0.992	
CB	940 ± 48	580 ± 23	0.111	0.358	0.996	
CT	970 ± 41	470 ± 18	0.104	0.516	0.996	

The swelling degree depends both on the type of crosslinking (physical or chemical) and on the type of crosslinking agent (mono- or multi-epoxy, linear or branched). In terms of swelling ability, it is expected that chemically crosslinked hydrogels will present higher water absorption than physically crosslinked hydrogels, considering that by the crosslinking reaction, the compact chain packing of cellulose chains is disturbed, leading to the enhancement of chain mobility, and implicitly, of hydrophilicity [27]. However, this situation is valid only for CE, but not for hydrogels CB and CT, which have a lower swelling degree (Q_t = 580% and 470%, respectively) than the physically crosslinked hydrogel C (Q_t = 710%). These results can be attributed to the involvement of several factors, such as those related to the network characteristics: the structure and shape of the pores, the thickness of the pore walls, the uniformity of pore distribution, and even the drying process.

Moreover, there is a noticeable difference in terms of swelling degree between the never-dried hydrogels (Q_{max}) and the hydrogels dried by lyophilization (Q_t).

Hydrogel CE has the advantage of a structure with large pores, which explains the higher swelling degree recorded both in the never-dried state (Q_{max} = 1280%) and after drying (Q_t = 1030%). Moreover, the structure of hydrogel CE is characterized by pores with well-defined and thicker walls (see SEM, Figure 2a), so that most of it is preserved after drying, and implicitly, the ability of the hydrogel to absorb water is also maintained (CE loses only 19% of its swelling capacity).

The never-dried C, CB, and CT hydrogels show almost similar swelling degrees, which fall within the range of Q_{max} = 940–970%. However, after drying by lyophilization, the physically crosslinked hydrogel, C, records a loss of swelling capacity of approx. 26%, the chemically crosslinked hydrogel CB of approx. 38%, and the most affected is CT, whose swelling capacity decreases by 50% (from 970% to 470%). An explanation can be the fact that the "never-dried" state of the hydrogels is characterized by a relaxed network and an expanded state. However, through the gradual removal of water during the lyophilization stage, a rearrangement of the network occurs (cornification phenomenon) through the formation of new hydrogen bonds between the polymer chains, and even the collapse of certain pores with very thin walls, which leads to denser networks with lower swelling capacity [6,17].

Regarding the pronounced decrease in the swelling degree of chemically crosslinked hydrogels (CB and CT), a major influence is exerted by the presence in their structure of longer aliphatic chains due to the use of crosslinking agents, such as BDDE and TMPTGE, respectively. During the drying process, they allow for the establishment of a greater

number of hydrogen bonds, and the more complex the structure of the crosslinker, the more noticeable the decrease in swelling degree (Q_t CE > Q_t CB > Q_t CT).

Precious information regarding the phenomenon of water molecule absorption and the behavior of 3D networks in the water uptake process can be provided by studies of swelling kinetics, using empirical Equation (6) [38]. The dynamic swelling behavior of all four hydrogels is presented in Figure 3. The swelling capabilities of all the cellulose-based hydrogels increase with time, so that after a certain period, they reach a steady state, a plateau. As shown in Figure 3, the equilibrium swelling state for all the hydrogels is reached in approximately 30 min, and for the CB and CT hydrogels, reaching the plateau is much slower. For instance, in the first 5 min, almost 80% of the total amount of water is absorbed for C and CE, while in the case of CB and CT, this percentage is much lower, below 50%. This phenomenon can be seen as an advantage of the structures crosslinked with BDDE and TMPTGE, respectively, which present a slower swelling process, controlled more by the diffusion process than by chain relaxation.

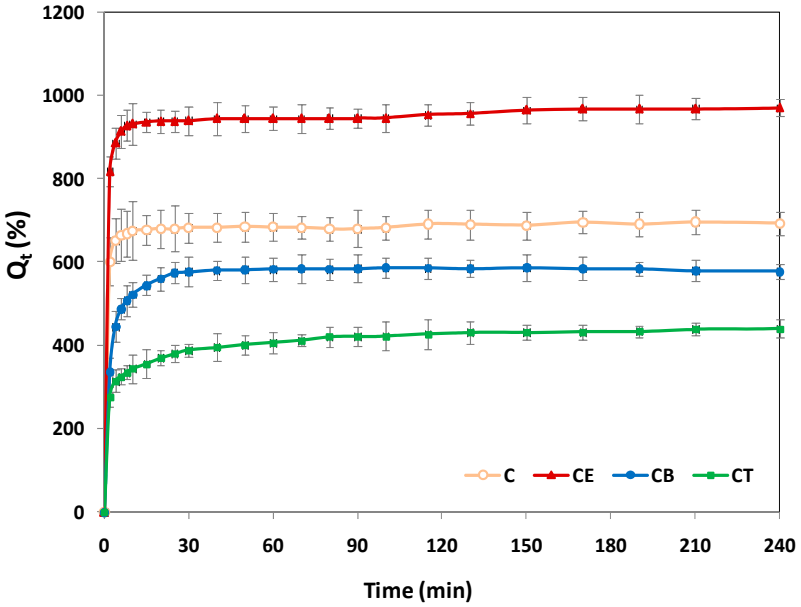

Figure 3. Dynamic swelling behavior of cellulose-based hydrogels: physically crosslinked hydrogel (C) and chemically crosslinked hydrogels with epichlorohydrin (CE), 1,4-butanediol diglycidyl ether (CB), and trimethylolpropane triglycidyl ether (CT).

The kinetic parameters, which are indicative of the water transport mechanism (i.e., the swelling constant, k_{sw}, and the swelling diffusional exponent, n_{sw}) can be found in Table 3 and are in agreement with the results obtained and presented above. The perfect Fickian diffusion process of the water molecules through the porous structure of the hydrogels is characterized by a diffusion coefficient of n_{sw} = 0.45 (i.e., for cylindrical hydrogels) and the relaxation of polymer chains in the swelling process equals the diffusion of water molecules through the porous structure. In the case of the physically crosslinked hydrogel, C, the diffusion coefficient has the lowest value (n_{sw} = 0.038), which indicates that the water transport mechanism is based more on the relaxation phenomenon of the polymer chains and less on the diffusion phenomenon. On the other hand, for chemically crosslinked hydrogels (CE, CB, and CT), in the structure of which there are relatively stable ether chemical bonds, the water diffusion phenomenon prevails to the detriment of the relaxation of the polymer chains, illustrated by the approximately three-fold increase in the diffusion coefficient values (n_{sw} = 0.094–0.111). For all studied hydrogels, the correlation coefficient (R^2) has values greater than 0.99 (between 0.992 and 0.997), which suggests an excellent fit between the experimental data and the chosen model.

2.6. Dynamic Vapor Sorption Measurements

The water adsorption/desorption behavior is important in assessing the porous structure of the materials, establishing their stability in environments with a specific relative humidity (RH), understanding how water molecules migrate within their structure, and determining how they gain or lose water [39]. Furthermore, studies on different types of sorption isotherms provide crucial information regarding the most appropriate mathematical model that the experimental data can be correlated with, and moreover, provide information on the interdependence of physical structure and macroscopic behavior [40]. In our particular case, DVS has been used to study the interaction of the hydrogels with water vapor, to evaluate surface properties, and to highlight the influence of each type of crosslinker on these properties.

The relation between the equilibrium moisture content and the relative humidity, at constant temperature, as well as the hysteresis phenomenon for cellulose-based hydrogels are presented in Figure 4a,b. The adsorption/desorption isotherms (Figure 4a) indicate the dependence between the water content of the hydrogels and the relative humidity (RH). For instance, each value of RH in the sorption isotherm corresponds to a certain value of water content, at a given constant temperature, for a specific type of hydrogel. According to the International Union of Pure and Applied Chemistry (IUPAC) classification, the curves shown in Figure 4a fit on a type V isotherm, characterized by reduced water vapor adsorption at low values of RH (0–10%), moderate adsorption at intermediate values of RH (20–50%), and a sharp increase in water adsorption for RH values higher than 50% [41].

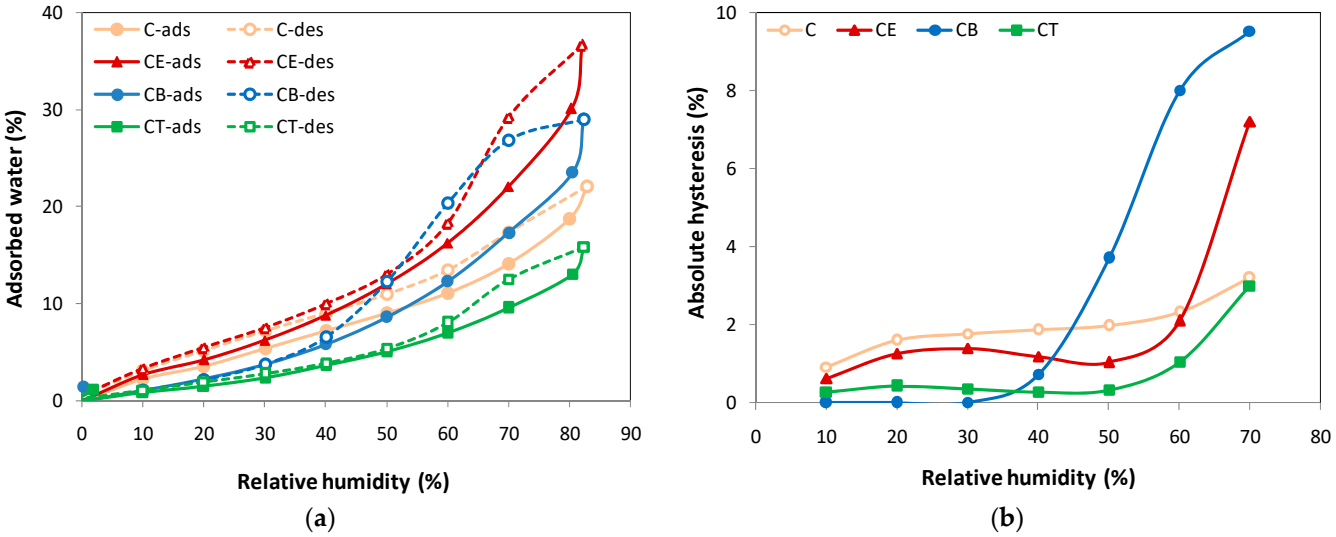

Figure 4. Dynamic vapor sorption data for cellulose-based hydrogels: (**a**) adsorption/desorption isotherms (adsorption—solid line; desorption—dashed line) and (**b**) absolute hysteresis vs. relative humidity.

As shown in Figure 4a, a very low water content (<5%) is recorded for all the hydrogels for a relative humidity of up to 30%, indicating the possibility of the formation of a monomolecular water layer on the surface of the solid (monolayer water adsorbed) [40]. It should be mentioned that with increasing relative humidity, up to 50%, the behavior of the hydrogels in the presence of water vapor is similar to that observed in the case of the swelling degree, where Q_t decreases according to the following series: Q_t CE > Q_t C > Q_t CB > Q_t CT. At this point, a water content of approximately 12% is obtained for CE, 9% for C, 8.6% for CB, and only 5.5% for CT hydrogels, respectively. Above a value of 50% RH, significant changes are recorded in the shape of the vapor adsorption isotherms corresponding to hydrogels and, implicitly, in the interaction between water vapor molecules and the solid material. A more special evolution can be observed for the CB hydrogel, which with a significant increase in RH, adsorbs double the amount of water vapor compared to the CT hydrogel. This fact is also found in the case of the swelling

degree of the hydrogels, when Q_t is higher for CB than for CT. Finally, at approximately 85% RH, the maximum amount registered for adsorbed water vapor (W, %) is 36.6% for CE, 28.9% for CB, 22% for C, and only 15.8% for the CT hydrogel (Table 4).

Table 4. The water content at maximum RH, and surface parameters evaluated based on adsorption/desorption isotherms.

Sample	W (%)	BET Data *	
		Surface Area (m^2/g)	Monolayer (g/g)
C	22.02	237.6	0.0677
CE	36.61	266.4	0.0759
CB	28.97	374.9	0.1068
CT	15.82	114.3	0.0326

* BET data—determined based on the desorption branch of the isotherm (registered up to RH of 40%).

Unlike the swelling process, where the results are due to a combination of factors (nature of the fibers, solvent properties, specific process conditions, etc.), the adsorption/desorption of water vapor, especially for RH > 50%, is overwhelmingly influenced by the pore shape and interconnectivity, namely whether the pores are cylindrical, spherical, open-ended, ink-bottle-shaped, and so on. Experiments show that the large hysteresis loops recorded at high RH (usually at values > 75%) arise either due to differences in condensation/evaporation occurring in "ink bottle" pores or due to differences in the meniscus during adsorption/desorption in cylindrical pores [42,43]. In our case, this can be seen in the isotherms corresponding to the CE and CB hydrogels, shown in Figure 4a. Also, there are notable differences among the four hydrogels, not only in the position of maximum hysteresis, but also in its magnitude (Figure 4b). The lower hysteresis observed for the C and CT hydrogels, at 55–75% RH, may be an indication of the weaker interactions of its active sites with water, and consequently, of the smaller structural changes due to polymer swelling. The highest magnitude of loop hysteresis is observed for the CB hydrogel. It should be mentioned that valuable information can be obtained from the shape of desorption branch, regarding the size and shape of the pores, as well as about the predominant mechanism of filling or emptying the pores. This is the case of "inkbottle" type pores, where wide pores have access to the external surface only through narrow necks. The wide pores remain filled during the desorption process, until vapor pressures are low enough to allow for their emptying through the narrow necks. If the neck diameter is not too small, then the network can empty even at higher relative pressures.

In our particular case, depending on the shape of the adsorption/desorption isotherms and the hysteresis loop size, we can assume that hydrogels C and CT have predominantly spherically shaped pores, hydrogel CE has predominantly cylindrically shaped pores, while hydrogel CB is much more special, containing a large amount of "ink bottle" type pores, which determine the appearance of the largest hysteresis loop. The presence of this type of pore in the porous structure of the CB hydrogel is also confirmed by the higher values obtained both for the specific surface area (approximately 375 m^2/g) and monolayer (0.1068 g/g) (Table 4). This special structural characteristic of the CB hydrogel, although not characterized by a high degree of swelling, can still be seen as an advantage in applications that require high water retention over a long period of time, such as in (i) the field of agriculture, to maintain a certain humidity in the soil in order to ensure the optimal development of plants, or even in (ii) the biomedical field for wound healing, to make wound dressings that maintain a favorable environment for a long time.

2.7. Rheological Behavior

Rheology is an effective tool to characterize the viscoelastic behavior of hydrogels. Rheological properties are evaluated in terms of the storage modulus (G′), which refers to the elastic component of the material, whereas the viscous component is given by the loss

modulus (G″). More specifically, the elastic modulus (G′) describes the solid-like behavior of the gel, whereas the loss or viscous modulus (G″) defines its liquid-like behavior [44]. The first step in the evaluation of the dynamic viscoelastic properties of our developed hydrogels was to perform amplitude sweep tests. Different values of the storage and loss moduli were obtained for the four types of studied hydrogels, by varying the strain from 0.001 to 100%, as shown in Figure 5a, hinting at a clear dependence of the rheological behavior on the crosslinker structure and functionality [6]. As a general remark, the storage modulus of all the hydrogels dominates over the loss modulus up to the crossover point, suggesting that the elastic behavior of all the hydrogels prevails over their viscous behavior, demonstrating a typical gel-like behavior [45,46].

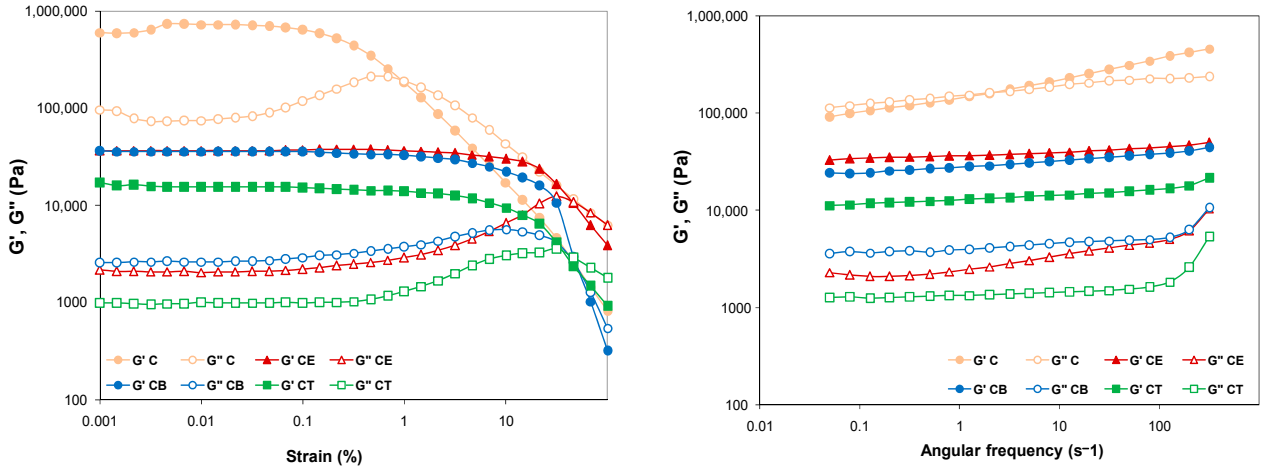

Figure 5. The dependence of dynamic moduli on strain and angular frequency: (**a**) amplitude sweep test results; (**b**) frequency sweep test results (G′—solid symbols; G″—open symbols).

For instance, in the linear viscoelastic region (LVR), where the moduli are strain-independent, values of ~604 kPa (C), 36 kPa (CE, CB), and 17 kPa (CT) are obtained for G′. Although the physically crosslinked hydrogel (C) surprisingly presents the highest value for G′ and exhibits the most enhanced stiffness "at rest" of the network [10], the chemically crosslinked cellulose hydrogels can withstand higher deformation than hydrogel C. Similar results were also reported in previous studies, where the physical hydrogels exhibited a much higher storage modulus, being even 100–200 times greater than that of chemically crosslinked hydrogels. The explanation was based either on the formation of lumps by macromolecules [45] or on the strong development of inter- and intra-molecular hydrogen bonds by the entanglement and self-association of the cellulose chains after the freezing/thawing process, decreasing the free volume [47]. The storage moduli of all the evaluated hydrogels crosslinked with EPC, BDDE, and TMPTGE in LVR are in the range of 17–40 kPa, falling within the value range reported for other chemically crosslinked cellulose-based hydrogels [48,49].

The values of the dynamic moduli (G′ = G″) and strain (γ, %) at the crossover point can be determined from the graph of Figure 5a and are observable in Table 5. All three chemically crosslinked hydrogels (CE, CB, and CT) show the crossover point beyond ~40% strain, reflecting a much higher stability of these hydrogels [6] compared to the physically crosslinked one, where the crossover of G′ and G″ occurs at a very low strain value of less than 1%. Among the chemically crosslinked hydrogels, CT shows the lowest stability during strain deformation. A similar result was obtained by Su Ting and coworkers [24], where the linear crosslinker with two-arms (BDDE) led to a higher storage modulus and a more stable gel than the one with three-arms (TMPTGE).

Table 5. Dynamic moduli (G′ = G″) and strain (γ) at the crossover point (from amplitude sweep tests), and values of G′, G″, and tan δ at 5 s^{-1} (from frequency sweep tests).

Sample	Amplitude Sweep Tests		Frequency Sweep Tests (at 5 s^{-1})		
	G′ = G″ (Pa)	γ (%)	G′ (Pa)	G″ (Pa)	tan δ
C	195,700	0.93	191,000	176,000	0.921
CE	10,920	45.1	38,100	3060	0.080
CB	540	68.4	30,700	4390	0.143
CT	3239	37.5	13,900	1400	0.101

Beyond the value of the crossover point, as can be seen in Figure 5a, the viscous regime dominates (G″ > G′) and all viscoelastic moduli become dependent on the strain amplitude, decreasing as a result of the structural breakdown of the hydrogel network under high deformation [45].

The next step of the dynamic viscoelastic property evaluation was to perform the frequency sweep tests, the corresponding results being summarized in Figures 5b and 6, as well as in Table 5. The physically and chemically crosslinked cellulose hydrogels exhibit G′ moduli greater than G″ moduli, indicating gel-like viscoelastic behavior in the tested frequency range. It is worth noting that, for sample C, both dynamic moduli slightly depend on the frequency in the investigated experimental domain, more obviously for the G′ at higher frequencies. The value of G′ and G″ at the crossover point is 162 kPa at the angular frequency of ω = 2.1 s^{-1}, so this physically crosslinked cellulose hydrogel shows increased stiffness (Figure 5a). In the case of the CE, CT, and CB hydrogels, both dynamic moduli, and especially G′, are nearly independent of the angular frequency. Hence, it can be mentioned that the stability of these hydrogels' network structure is not affected by the applied deformation, with the hydrogels displaying an excellent structured 3D network. Moreover, the lack of a crossover point of viscoelastic moduli suggests permanent chemical crosslinking [10].

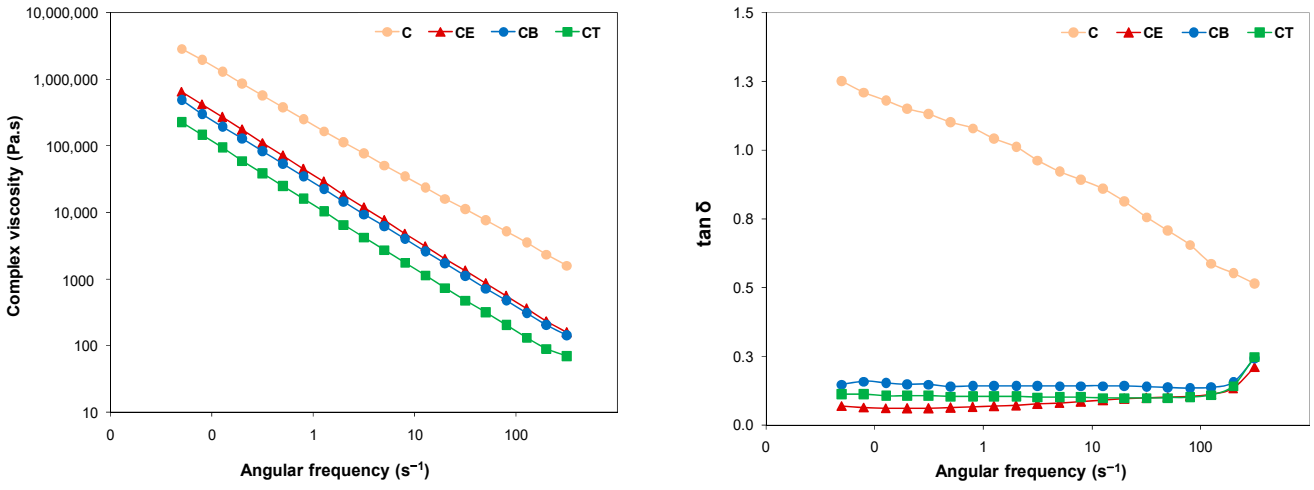

Figure 6. The rheological behavior of cellulose-based hydrogels: (**a**) complex viscosity and (**b**) loss factor dependence on the angular frequency.

The influence of the polymer network structure resulting from chemical crosslinking was revealed by the rheological results as the stiffness of CE, CT, and CB decreased relative to hydrogel C, as also observed by the values of G′ at 5 s^{-1} displayed in Table 5. We have chosen to evaluate the values of G′ and G″ at 5 s^{-1} for a better comparison of the moduli evolution in the middle of the tested frequency range. The decline in G′ values

by crosslinking with EPC, BDDE, and TMPTGE shows a more elastic structure of the resulting materials, which is a highly desired feature for hydrogel applications, especially in the medical field. An observation could be that both G′ and G″ values reduce with the increase in the molecular weight of the crosslinkers used, thus leading to a decline in the entanglement degree, so that the polymer chains move more easily under shear stress [50].

The changes in the hydrogels' network are also reflected in their complex viscosity dependence on angular frequency, lower values being registered for the flexible chemically crosslinked hydrogels compared with the stiffer hydrogel C (Figure 6a).

The relative contribution of the viscous components to rheological properties was evaluated through the loss factor (tan δ), which is defined as the ratio between viscous to elastic response (tan δ = G″/G′) and reflects the damping abilities of the hydrogel. The lower tan δ values for chemically crosslinked hydrogels indicate enhanced elasticity, because tan δ represents the ratio of dissipated to stored energy [48]. Figure 6b presents the loss tangent evolution vs. frequency, and Table 5 shows the values of this parameter at $\omega = 5\ s^{-1}$. As can be seen in Figure 6b, there is a big difference between the physically crosslinked hydrogel and the three chemically crosslinked hydrogels, and that there is no noticeable difference in the loss tangent among the latter. Tan δ values of CE, CB, CT hydrogels are in the range of 0.06–0.3 and are almost constant over the studied frequencies for all the hydrogels, proving that the elastic properties are superior to the viscous properties in terms of the dynamic viscoelastic behavior [51]. Tan δ reflects the superposition of G′ with G″ (tan δ = 1) for hydrogel C, with values decreasing from 1.3 to about 0.5, denoting a gradual shift from a viscous liquid at low frequencies (G″ > G′, tan δ ~ 1) to a soft viscoelastic solid (tan δ ~ 0) at higher frequencies.

As a general conclusion following from these rheological tests, we could say that the viscoelastic properties evaluated by dynamic rheology are correlated with the changes in the structure of the crosslinked hydrogels, especially with respect to their degree of swelling and porosity.

2.8. Differential Scanning Calorimetry and Thermogravimetric Analyses

Generally, DSC is a technique that measures the heat capacity (heat flow) as a function of temperature, in a controlled atmosphere, and can provide information on thermally induced conformational transitions and phase transitions of polymeric materials, which can be associated with the absorption of heat (endothermic: evaporation of water, thermal decomposition of polymers, melting of solids, denaturation of proteins, etc.) or with the release of heat (exothermic: crystallization of polymers, aggregation of proteins, etc.) [13].

Hydrogels, by their nature, are hygroscopic materials that absorb water vapor from the environment until reaching an equilibrium moisture content, which may be present as adsorbed moisture on internal surfaces and as capillary condensed water in pores. This process is closely dependent on the porous structure of the network, but also on the OH groups on the surface of the polymer chains, which are available to bind water molecules [41]. The more OH groups there are, the more difficult it will be to remove water from the hydrogel structure with an increase in temperature (heating).

Figure 7a shows the DSC thermograms corresponding to the water evaporation process, which is highlighted by a single endothermic peak, with a maximum temperature (T_{peak}) located between 70.6–84.6 °C, depending on each type of hydrogel in terms of whether it is physically or chemically crosslinked. As shown in Table 6, the endothermic peaks (T_{peak}) appear at 84.6 °C for hydrogel C, 76.6 °C for CE, 70.6 °C for CB, and at 71.8 °C for CT. For hydrogel C, which presents the largest number of hydroxyl groups available for hydrogen bonds, a broad endothermic peak associated with water loss is recorded at the highest values of T_{peak}.

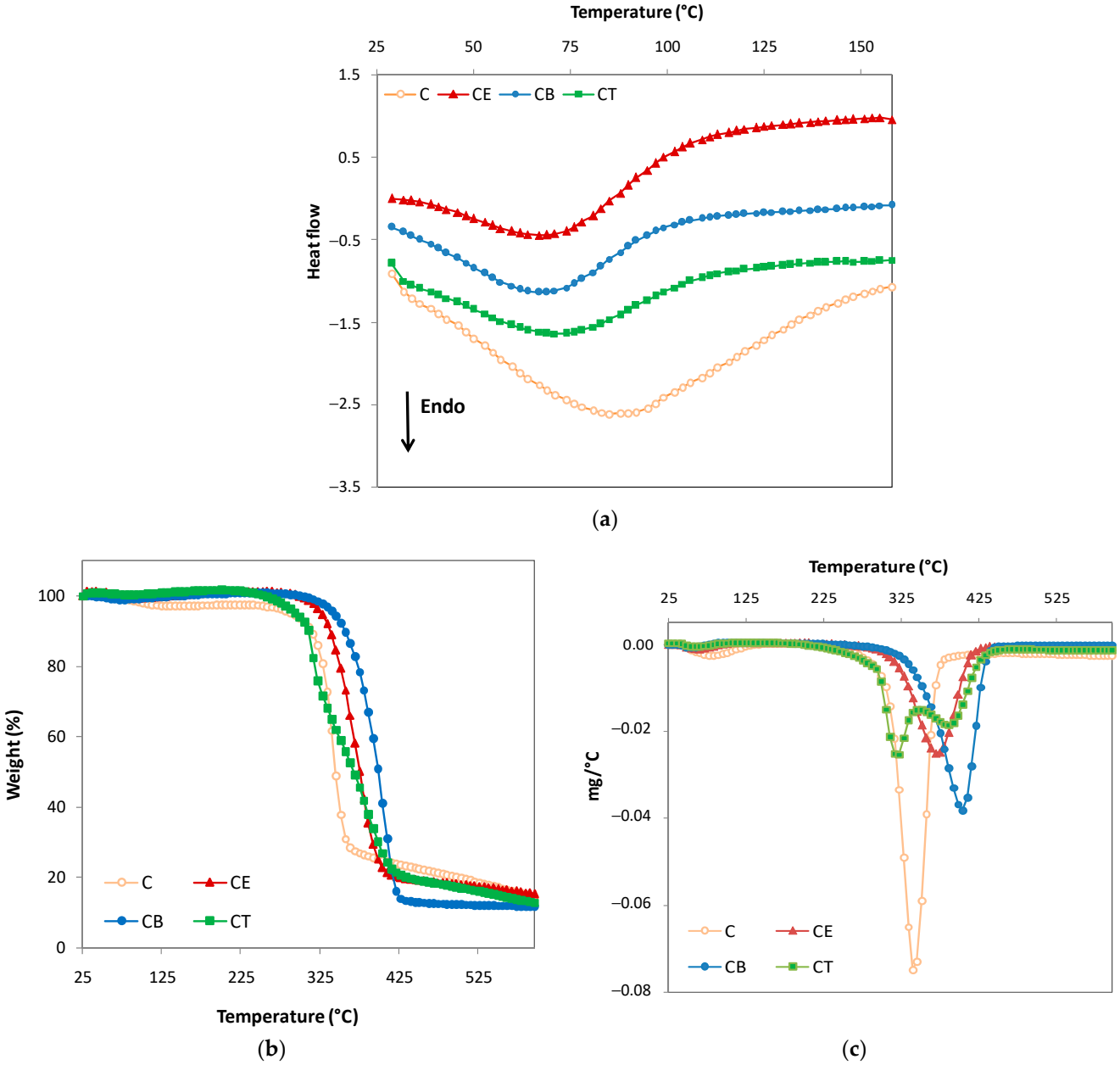

Figure 7. (**a**) DSC, (**b**) TG, and (**c**) DTG curves of cellulose-based hydrogels (physically crosslinked hydrogel—C; chemically crosslinked hydrogels with epichlorohydrin—CE; with 1,4-butanediol diglycidyl ether—CB; with trimethylolpropane triglycidyl ether—CT).

Table 6. DSC data of cellulose-based hydrogels.

Sample	T_{onset} (°C)	T_{peak} (°C)	T_{endset} (°C)	ΔH (J/g)
C	36.3	84.6	178.2	148.5
CE	36.1	76.6	127.7	80.6
CB	31.2	70.6	118.2	51.0
CT	34.2	71.8	122.3	45.1

These results are in agreement with the DVS data, where in the case of hydrogel C, by decreasing the RH from 40% to 10%, a slower water loss is observed, also suggested by the higher value of the absolute hysteresis in this RH range, compared to the other hydrogels (see Figure 4b). Through the chemical crosslinking process, the hydroxyl groups are more

involved in the establishment of ether bonds, thus recording a decrease in the number of water binding sites, which is confirmed in the DSC thermograms of hydrogels CE, CB, and CT by a shift in the maximum temperature of the endothermic peak towards lower temperatures. Dehydration heat values (ΔH, J/g) show the same trend for the chemically crosslinked hydrogels compared to the physically crosslinked ones.

The thermal stability of the hydrogels is closely related to the structure of the network and their crosslinking density. TG analysis was chosen to investigate the thermal stability of the hydrogels, both physically and chemically crosslinked. This technique is a sensitive instrumental technique used to monitor mass changes as a function of temperature and to provide information on degradation processes and thermal stability. Figure 7b,c presents the thermograms (TG, Figure 7b) and derivative thermogravimetric curves (DTG, Figure 7c) of the studied hydrogels. Furthermore, all thermal decomposition parameters, including T_{onset}, T_{peak}, T_{endset}, weight loss at the end of each thermal decomposition stage, and total residue, are presented in Table 7.

Table 7. Thermal degradation of cellulose-based hydrogels.

Sample	Stage I				Stage II				Total Residue (%)
	T_{onset} (°C)	T_{peak} (°C)	T_{endset} (°C)	Mass loss (%)	T_{onset} (°C)	T_{peak} (°C)	T_{endset} (°C)	Mass Loss (%)	
C	60.0	88.8	114.2	3.35	318	342	359	83.2	13.45
CE	55.6	67.5	93.3	1.84	332	372	407	86.2	11.96
CB	45.0	54.1	89.2	0.86	345	403	422	90.1	9.04
CT	47.9	62.0	99.1	0.50	322	388	416	89.0	10.50

As a general observation, the thermal degradation of the cellulose-based hydrogels takes place in two main stages. An exception is highlighted for hydrogel CT, in which an "intermediate" stage corresponding to the "free" TMPTGE crosslinker appears, recorded for the peak with T_{peak} of 319 °C. This result can be explained by a partial consumption of the crosslinking agent during the crosslinking reaction and the fact that "free" TMPTGE could not be removed by repeated washings. This observation is confirmed by ATR-FTIR spectroscopy, where an absorption band characteristic of unopened oxirane rings from TMPTGE is identified in the CT hydrogel spectrum (see Figure 1).

The data obtained from the first stage of weight loss (Stage I, Table 7) are in agreement with those obtained from the DSC analysis, emphasizing the fact that the mass loss in this stage is due to the loss of absorbed moisture from the hydrogel's network. In addition, these data confirm the relatively slower water loss process for the physically crosslinked hydrogel (C) compared to the chemically crosslinked ones.

In the second stage, which represents the thermal degradation stage, there is a substantial loss of mass between 83.2% for C and 90.1% for CB hydrogels. This is related to the cleavages of the ether bonds occurring between cellulose chains (for chemically crosslinked hydrogels CE, CB, and CT), to the breaking of glycosidic linkages of cellulose skeleton (also including the physically crosslinked hydrogel, C) [52], as well as to the complete degradation of the hydrogels, with the formation of gaseous molecules (such as CO, CO_2, H_2O, etc.), into a carbon-rich residue. The physically crosslinked hydrogel has the lowest thermal stability because it starts degrading at T_{onset} = 318 °C, while the CB hydrogel begins degrading at 345 °C, the highest temperature among the studied hydrogels. Moreover, CB has the highest T_{peak} at 403 °C, showing the highest thermal stability (CE, T_{peak} at 372 °C and CT, T_{peak} at 388 °C). However, the thermal behavior of all the three chemically crosslinked hydrogels is relatively similar, indicating that the structure and functionality of the crosslinker has a slight effect on their thermal stability. A notable difference appears only when comparing them with the physically crosslinked hydrogel, revealing a clear indication of the formation of a crosslinked network with a more thermally stable structure.

3. Conclusions

In this study, cellulose-based hydrogels were successfully designed, using physical or chemical crosslinking, in the presence of multi-epoxy crosslinking agents (mono-, bi-, and tri-epoxy). The two-step technique for the preparation of these hydrogels included (i) a dissolution step of cellulose in aqueous NaOH solution to trigger the cellulose gelation process in strong alkaline medium, followed by (ii) a crosslinking step at a relatively low temperature (40 °C) in order to obtain the chemically crosslinked hydrogels. The performances of the engineered hydrogels were systematically investigated through the gel fraction and swelling degree evaluation, the rheological behavior, and SEM, DVS, DSC, and TG analyses.

The obtained results suggest that by using different crosslinking agents such as ECH (mono-epoxy), BDDE (bi-linear epoxy), or TMPTGE (three-branched epoxy), chemically crosslinked hydrogels with relatively different characteristics can be obtained. Significant differences were observed in terms of network morphology and pore size distribution, as well as in gel fraction values, which together synergistically contributed to the design of all other properties (swelling degree, sorption capacity, and rheological and thermal properties). For instance, the CB hydrogels showed the largest hysteresis at values of RH > 50%, followed by the CE hydrogels, mainly due to the predominant shape of the pores, more precisely, the "ink bottle" shape for CB and the cylindrical shape for CE. The gel fraction was greater than 90% for the CE and CB hydrogels, suggesting the obtaining of crosslinked 3D structures that are stable in an aqueous medium at a relatively high temperature (60 °C). Regarding the swelling degree (Q_t) for chemically crosslinked hydrogels, a clear influence of the type of crosslinking agent (mono-, bi-, and tri-epoxy) was observed. Thus, a decrease in Qt was recorded according to the series Qt CE > Qt CB > Qt CT, suggesting the formation of more compact networks as the number of epoxy groups in the structure of the crosslinker increased. These 3D crosslinked structures also led to exceptional rheological properties, especially regarding the elastic component of these hydrogels, where tan δ for the chemically crosslinked hydrogels < tan δ for the physically crosslinked hydrogel. Moreover, the high thermal stability of the CB hydrogel was remarkable with its ability to withstand temperatures close to 400 °C.

As a general conclusion, the results highlight the possibility of using specific crosslinking agents, such as zero-length ECH, dumbbell-shaped linear BDDE, or Y-shaped branched TMPTGE, in order to obtain hydrogels with tailored and guided characteristics to respond to certain requirements of a particular field of application. For example, if hydrogels with high a swelling degree and improved elasticity are required, such as materials for wound dressings, then it is preferable to use crosslinkers with reduced functionality (i.e., mono-epoxy) rather than with multi-epoxy groups. On the other hand, if more rigid hydrogels are necessary, with dense and compact matrices but with a lower swelling degree, then the choice must be directed towards multifunctional crosslinkers (bi-, tri-, or multi-epoxy) and, if possible, with long or branched alkyl chains.

4. Materials and Methods

4.1. Materials

Microcrystalline cellulose was purchased from Sigma-Aldrich (Saint Louis, MO, USA) under the trade name of Avicel PH-101 (~50 μm particle size; DP = 180). Epichlorohydrin (ECH, purity > 98%, M_w = 92.52 g/mol) was purchased from Merck (Hohenbrunn, Germany), 1,4-butanediol diglycidyl ether (BDDE, purity ≤ 100%, M_w = 202.25 g/mol) and trimethylolpropane triglycidyl ether (TMPTGE, purity > 95%, M_w = 302.36 g/mol) were purchased from Sigma-Aldrich (Saint Louis, MO, USA). All three crosslinkers were used without previous purification. Sodium hydroxide (NaOH) in pellets, with a purity ≥ 97%, was supplied by Merck (Hohenbrunn, Germany).

4.2. Methods and Equipment

4.2.1. Hydrogels Preparation

The preparation of hydrogels was carried out by a two-step method, which was adapted from a previously reported method [10].

In the first stage, a suspension of 6% (*w*/*w*) cellulose in NaOH solution was achieved, which was subsequently frozen at −30 °C for 24 h, followed by a thawing stage at room temperature. Starting from this point, the physically crosslinked hydrogel (noted with C) was obtained by keeping the cellulose solution at room temperature for 24 h to undergo physical gelation, and then the obtained gel was carefully washed to coagulate cellulose and remove the NaOH. At the end, the hydrogel was lyophilized in a freeze dryer ALPHA 1-2/LD (Martin Christ Drying Systems GmbH, Osterode, Germany).

In the second stage, for the synthesis of chemically crosslinked hydrogels, 3.2 g of crosslinking agents (ECH, BDDE or TMPTGE) was added to the cellulose solution prepared in the first stage, under strong mechanical stirring for 10 min, until homogeneous solutions were obtained. Chemical crosslinking of the hydrogels was performed at a moderate temperature (40 °C) for 5 h. The obtained hydrogels (CE, CB, and CT) were washed with warm water (at 40 °C) for several days to remove the unreacted crosslinking agent or other impurities, and finally, they were lyophilized.

4.2.2. Gel Fraction

The effectiveness of 3D network formation in hydrogels can be quantitatively evaluated based on gel fraction (GF, %). The stability of a regenerated hydrogel, due to its resistance to dissolution in hot water, is known as gelation degree. First, the hydrogels were oven dried at 40 °C until their weight was constant. The dried hydrogels were then immersed in a distilled water bath at 60 °C for 48 h. The insoluble part corresponding to the hydrogel was dried and weighed. All experiments were performed in triplicate and the data are expressed as the mean ± standard deviation (SD). The gel fraction was calculated using Equation (1) [27].

$$\text{GF}\ (\%) = \frac{\text{M}_\text{g}}{\text{M}_0} \times 100 \quad (1)$$

where M_g is the weight of dried insoluble portion of hydrogel, after immersion(g) and M_0 is the initial weight of the dry hydrogel, before immersion (g).

In order to estimate the amount of the crosslinker (AC, moles) consumed in the crosslinking reaction, we assumed that the cellulose (0.5 g) involved in the chemical crosslinking is found entirely in the mass of the final hydrogel, together with the crosslinking agent. Thus, the amount of crosslinker (AC, moles) consumed was calculated using Equation (2) and its further estimation was carried out referring to the number of moles of anhydroglucose units (m_AGU, moles) resulting from Equation (3).

$$\text{AC}\ (\text{moles}) = \frac{(\text{M}_\text{H} - \text{M}_\text{C})}{\text{M}} \quad (2)$$

$$\text{m}_\text{AGU}(\text{moles}) = \frac{\text{M}_\text{C}}{\text{M}_\text{AGU}} = 0.003086 \quad (3)$$

where M_H is the weight of the final lyophilized hydrogels (g); M_C is the weight of cellulose used in the crosslinking process (0.5 g); M is the molar mass of crosslinker (g/mol); m_AGU is the number of moles of AGUs (moles); M_AGU is the molar mass of one anhydroglucose unit (162 g/mol).

4.2.3. Swelling Degree and Swelling Kinetics

Initially, the maximum swelling degree (Q_{max}, %) of the never-dried hydrogels, after washing for several days with warm distilled water, was determined using Equation (4).

$$Q_{max}(\%) = \frac{(M_{sw} - M_d)}{M_d} \times 100 \quad (4)$$

where M_{sw} is the weight of maximally swollen hydrogel (g); M_d is the weight of dry hydrogel through lyophilization (g). All experiments were performed in triplicate and the data are expressed as the mean ± SD.

Since the drying process is expected to influence the swelling process of the hydrogels, the swelling degree after lyophilization (Q_t, %) was also determined using Equation (5).

$$Q_t(\%) = \frac{(M_t - M_d)}{M_d} \times 100 \quad (5)$$

where M_t is the weight of swollen hydrogel at time t (g); M_d is the weight of dry hydrogel (g). All experiments were performed in triplicate and the data are expressed as the mean ± SD.

At the same time, the study of swelling kinetics was also carried out in order to elucidate the way the water molecules diffuse into the hydrogel matrices over time. In this respect, the lyophilized samples were submerged in distilled water to swell, at 37 ± 1 °C. The samples were taken out of the water at predetermined time intervals, their surface was wiped with filter paper to remove the excess water, and their weights were recorded. The kinetics of the swelling process of the lyophilized hydrogels was carried out using Equation (6) in order to describe the Fickian or non-Fickian behavior of the swelling process [38].

$$\frac{W_t}{W_{eq}} = k_{sw} \times t^{n_{sw}} \quad (6)$$

where W_t is the amount of water absorbed at time t by the hydrogel (g); W_{eq} is the amount of water absorbed by the hydrogel at equilibrium (g); k_{sw} is the swelling constant that incorporates the characteristics of the macromolecular network system (min^{-1}); n_{sw} is the swelling diffusional exponent, which is indicative of the transport mechanism. The constants n_{sw} and k_{sw} were calculated from the slopes and intercepts of the plots of $\ln(W_t/W_{eq})$ vs. ln(t). Usually, Equation (6) is applied in the early stages of the swelling process ($Q_t < 60\%$), where the linearity is observed.

4.2.4. Dynamic Vapor Sorption Measurements

The behavior of the hydrogels in atmosphere with controlled humidity was highlighted by dynamic vapor sorption (DVS) analysis, a gravimetric technique measuring, with an ultra-sensitive microbalance, the changes in sample weight in response to changes in relative humidity. The measurements were made in the test room at a constant temperature. DVS analysis was performed in the dynamic regime using fully automated IGAsorp gravimetric equipment manufactured by Hiden Analytical (Warrington, UK). The determinations were directed by a user-friendly software package, IGAsorp's HIsorp software V6.50.42 (Hiden Analytical, Warrington, UK). The first step involved the placement of the sample in a special container, followed by its drying at 25 °C in flowing nitrogen (250 mL/min) until its weight reached equilibrium at a relative humidity (RH) less than 1% and, after that, followed the isotherm recording. The RH gradually increased from 0 to 90%, in 10% humidity steps, every step having a pre-established equilibrium time until the RH increased again. The amount of water absorbed by the hydrogels (W, %) was calculated using Equation (7). The data are also presented in terms of absolute hysteresis, which is the difference between the weight of adsorbed water under conditions of adsorption (W_{ads}) and desorption (W_{des}), obtained by subtracting W_{ads} from W_{des} at a given RH. Based on the water vapor sorption data, the specific surface area (m^2/g) was also evaluated using

the Brunauer–Emmett–Teller (BET) kinetic model (Equation (7)) [53], which allows for the modeling of sorption isotherms registered under dynamic conditions.

$$W\ (\%) = \frac{W_m cRH}{(1 - RH)(1 - RH + cRH)} \quad (7)$$

where the parameters involved are W—the weight of adsorbed water (%); W_m—the weight of water forming a monolayer (g); c—the sorption constant; RH—the relative humidity (%).

4.2.5. Scanning Electron Microscopy Analysis

SEM was performed in order to thoroughly analyze the internal morphology of the hydrogels and to verify whether the crosslinking process impacted the pore structure. SEM is the most widely employed technique for the investigation of pore shape and pore size distribution of hydrogel networks. Before measurements, the cross-sections of the hydrogels were coated with a platinum layer (6 nm), using a Leica EM ACE200 Sputter coater (Leica Microsystem, Vienna, Austria). SEM analyses were performed on a Verios G4 UC Scanning Electron Microscope (Thermo Scientific, SEM, FEI Company, Brno, Czech Republic), using a secondary electron detector (Everhart–Thornley detector, ETD) with 10 kV accelerating voltage and a beam current of 0.8 nA. The average pore size and the standard deviation (SD) were determined by measuring 100 randomly chosen pores from the SEM micrographs exported into image analysis software (ImageJ software, v1.53k) [15].

4.2.6. Attenuated Total Reflectance Fourier Transform Infrared Spectroscopy

Attenuated total reflectance Fourier transform infrared (ATR-FTIR) spectroscopy measurements were performed using a Bruker Vertex 70 spectrometer (Bruker Optics GMBh, Ettlingen, Germany), with a single-bounce diamond crystal at the incidence angle of 45°. Each spectrum consisted of an average of 128 scans at 2 cm^{-1} resolution in the 4000–600 cm^{-1} wavelength range.

4.2.7. Rheology Measurements

The dynamic rheological behavior of the developed cellulose-based hydrogels was assessed by using an Anton Paar Physica MCR 301 rheometer (Graz, Austria), with plate-plate geometry (25 mm diameter, 4 mm gap), at a constant temperature (25 ± 0.1 °C). Before measurements, the hydrogel samples were swollen in distilled water at room temperature overnight, and the measurements were performed in triplicate at room temperature. A Peltier system for controlling temperature and evaporation was used during measurements. The amplitude sweep tests were performed within 0.001 and 100% strain range with a constant frequency of 1 Hz to determine the linear viscoelastic region (LVR—the region in which the modules are strain-independent) and to characterize the fracture process of the hydrogels. The viscoelastic properties of the hydrogels were also evaluated by performing the oscillatory frequency sweep tests, carried out within the determined LVR, in the frequency range from 0.05 to 500 s^{-1}, at a constant strain of 1%.

4.2.8. Differential Scanning Calorimetry and Thermogravimetric Analyses

Mettler Toledo DSC1 equipment (Columbus, OH, USA) was used to record the DSC curves. The tests were carried out for samples with a mass between 2.5 and 5.7 mg, with a heating rate of 10 °C/min, in an inert atmosphere (nitrogen). The scans were performed in a temperature range of 25–250 °C.

Thermogravimetric (TG) and derivative thermogravimetric (DTG) curves were recorded with Mettler Toledo 851^e equipment (Columbus, OH, USA). Sample mass varying between 2 and 5 mg was used. The measurements were done in nitrogen atmosphere, with a flow rate of 20 L/min and a heating rate of 10 °C/min. TG and DTG curves were recorded in the temperature range of 25–600 °C. After checking the reproducibility of the data obtained by recording three tests under the same conditions, it was found that the uncertainty was less than 1%.

The DSC, TG, and DTG curves were processed using STARe SW 9.10 software from Mettler Toledo in order to obtain the main thermal characteristics.

Author Contributions: Conceptualization, R.N. and D.E.C.; methodology, R.N. and D.E.C.; investigation—SEM, D.R.; investigation—rheology, R.N.D.-N.; investigation—DSC and TG/DTG, G.L.; investigation—ATR-FTIR, M.I.A.; investigation—DVS, A.B.; writing—original draft preparation, R.N. and D.E.C.; writing—review and editing, R.N. and D.E.C.; supervision, R.N. and D.E.C. All authors have read and agreed to the published version of the manuscript.

Funding: This research received no external funding.

Institutional Review Board Statement: Not applicable.

Informed Consent Statement: Not applicable.

Data Availability Statement: The original contributions presented in the study are included in the article, further inquiries can be directed to the corresponding author/s.

Conflicts of Interest: The authors declare no conflicts of interest.

References

1. Udoetok, I.A.; Dimmick, R.M.; Wilson, L.D.; Headley, J.V. Adsorption Properties of Cross-Linked Cellulose-Epichlorohydrin Polymers in Aqueous Solution. *Carbohydr. Polym.* **2016**, *136*, 329–340. [CrossRef]
2. Ciolacu, F. Paper-Based Microfluidic Devices on Fibrous Platforms with Designed Structure. *Cellulose Chem. Technol.* **2018**, *52*, 863–871.
3. Nasution, H.; Harahap, H.; Dalimunthe, N.F.; Ginting, M.H.S.; Jaafar, M.; Tan, O.O.H.; Aruan, H.K.; Herfananda, A.L. Hydrogel and Effects of Crosslinking Agent on Cellulose-Based Hydrogels: A Review. *Gels* **2022**, *8*, 568. [CrossRef]
4. Liang, L.; Bhagia, S.; Li, M.; Huang, C.; Ragauskas, A.J. Cross-Linked Nanocellulosic Materials and Their Applications. *ChemSusChem* **2020**, *13*, 78–87. [CrossRef]
5. Bonetti, L.; DeNardo, L.; Fare, S. Crosslinking Strategies in Modulating Methylcellulose Hydrogel Properties. *Soft Matter* **2023**, *19*, 7869–7884. [CrossRef]
6. Ursini, O.; Grieco, M.; Sappino, C.; Capodilupo, A.L.; Giannitelli, S.M.; Mauri, E.; Bucciarelli, A.; Coricciati, C.; deTurris, V.; Gigli, G.; et al. Modulation of Methacrylated Hyaluronic Acid Hydrogels Enables Their Use as 3D Cultured Model. *Gels* **2023**, *9*, 801. [CrossRef]
7. Mota, L.O.; Gimenez, I.F. Cellulose-Based Materials Crosslinked with Epichlorohydrin: A Mini Review. *Rev. Virtual Quim.* **2022**, *15*, 159–170. [CrossRef]
8. Zyadeh, M.T.; Hamadneh, I.M.K.; Kasrawi, M.A.R.; Saadeh, H.; Shahein, M.H. Synthesis of Cellulose-Based Hydrogel for Regulating the Release of Nitrogen Fertilizer. *Cellul. Chem. Technol.* **2023**, *57*, 71–78. [CrossRef]
9. Truong, T.T.C.; Bam, V.V.; Thi, A.P.L.; Phan, N.T.T.; Kobayashi, T.; Nga, D.T.T.; Nguyen, K.D. Chemically Crosslinked Cellulose-Based Hydrogel Prepared from Rice Straw for the Removal of Aqueous Hexavalent Chromium Ion from Wastewater. *Cellul. Chem. Technol.* **2024**, *58*, 181–193. [CrossRef]
10. Ciolacu, D.E.; Rusu, D.; Darie-Nita, R.N.; Tîmpu, D.; Ciolacu, F. Influence of Gel Stage from Cellulose Dissolution in NaOH-Water System on the Performances of Cellulose Allomorphs-Based Hydrogels. *Gels* **2022**, *8*, 410. [CrossRef]
11. Guo, H.; Lei, B.; Yu, J.; Chen, Y.; Qian, J. Immobilization of Lipase by Dialdehyde Cellulose Crosslinked Magnetic Nanoparticles. *Int. J. Biol. Macromol.* **2021**, *185*, 287–296. [CrossRef]
12. Liu, H.; Kar, N.; Edgar, K.J. Direct Synthesis of Cellulose Adipate Derivatives Using Adipic Anhydride. *Cellulose* **2012**, *19*, 1279–1293. [CrossRef]
13. Priya, G.; Narendrakumar, U.; Manjubala, I. Thermal Behavior of Carboxymethyl Cellulose in the Presence of Polycarboxylic Acid Crosslinkers. *J. Therm. Anal. Calorim.* **2019**, *138*, 89–95. [CrossRef]
14. Korhonen, O.; Budtova, T. Gelation of Cellulose-NaOH Solutions in the Presence of Cellulose Fibers. *Carbohydr. Polym.* **2019**, *224*, 115152–115159. [CrossRef]
15. Nicu, R.; Ciolacu, D.E.; Petrovici, A.R.; Rusu, D.; Avadanei, M.; Mihaila, A.C.; Butoi, E.; Ciolacu, F. 3D Matrices for Enhanced Encapsulation and Controlled Release of Anti-Inflammatory Bioactive Compounds in Wound Healing. *Int. J. Mol. Sci.* **2023**, *24*, 4213. [CrossRef]
16. Ciolacu, D.E.; Nicu, R.; Suflet, D.M.; Rusu, D.; Darie-Nita, R.N.; Simionescu, N.; Cazacu, G.; Ciolacu, F. Multifunctional Hydrogels Based on Cellulose and Modified Lignin for Advanced Wounds Management. *Pharmaceutics* **2023**, *15*, 2588. [CrossRef]
17. Ahmad, D.F.B.A.; Wasli, M.E.; Tan, C.S.Y.; Musa, Z.; Chin, S.F. Eco-friendly Cellulose-Based Hydrogels Derived from Wastepapers as a Controlled-Release Fertilizer. *Chem. Biol. Technol. Agric.* **2023**, *10*, 36–45. [CrossRef]
18. Martucci, J.F.; Espinosa, J.P.; Ruseckaite, R.A. Physicochemical Properties of Films Based on Bovine Gelatin Cross-Linked with 1,4-Butanediol Diglycidyl Ether. *Food Bioprocess Technol.* **2015**, *8*, 1645–1656. [CrossRef]

19. DeBoulle, K.; Glogau, R.; Kono, T.; Nathan, M.; Tezel, A.; Roca-Martinez, J.X.; Paliwal, S.; Stroumpoulis, D. A Review of the Metabolism of 1,4-Butanediol Diglycidyl Ether–Crosslinked Hyaluronic Acid Dermal Fillers. *Dermatol. Surg.* **2013**, *39*, 1758–1766. [CrossRef]
20. Chang, L.; Zhang, J.; Jiang, X. Comparative Properties of Hyaluronic Acid Hydrogel Crosslinked with 1,4-Butanediol Diglycidyl Ether Assayed Using a Marine Hyaluronidase. *IOP Conf. Ser. Mater. Sci. Eng.* **2019**, *493*, 012007–012017. [CrossRef]
21. Wende, F.J.; Gohil, S.; Nord, L.I.; Kenne, A.H.; Sandström, C. 1D NMR Methods for Determination of Degree of Cross-Linking and BDDE Substitution Positions in HA Hydrogels. *Carbohydr. Polym.* **2017**, *157*, 1525–1530. [CrossRef]
22. Tang, S.; Chi, K.; Xu, H.; Yong, Q.; Yang, J.; Catchmark, J.M. A Covalently Cross-Linked Hyaluronic Acid/Bacterial Cellulose Composite Hydrogel for Potential Biological Applications. *Carbohydr. Polym.* **2021**, *252*, 117123–117132. [CrossRef]
23. Venzhik, A.N.; Nikolaev, D.A.; Romanova, I.V. Study of Rheological and Structural Properties of Modified Carboxymethyl Cellulose Solutions Using Crosslinking Agents Based on Substituted Oxyranes. *Inorg. Mater. Appl. Res.* **2022**, *13*, 378–385. [CrossRef]
24. Su, T.; Wu, L.; Zuo, G.; Pan, X.; Shi, M.; Zhang, C.; Qi, X.; Dong, W. Incorporation of Dumbbell-Shaped and Y-shaped Cross-linkers in Adjustable Pullulan/Polydopamine Hydrogels for Selective Adsorption of Cationic Dyes. *Environ. Res.* **2020**, *182*, 109010–109018. [CrossRef]
25. Yuan, J.; Du, G.; Yang, H.; Liu, S.; Wu, Y.; Ni, K.; Ran, X.; Gao, W.; Yang, L.; Li, J. Functionalization of Cellulose with Amine Group and Cross-Linked with Branched Epoxy to Construct High-Performance Wood Adhesive. *Int. J. Biol. Macromol.* **2022**, *222*, 2719–2728. [CrossRef]
26. Ciolacu, D.; Rudaz, C.; Vasilescu, M.; Budtova, T. Physically and Chemically Cross-Linked Cellulose Cryogels: Structure, Properties and Application for Controlled Release. *Carbohydr. Polym.* **2016**, *151*, 392–400. [CrossRef]
27. Salleh, K.M.; Zakaria, S.; Sajab, M.S.; Gan, S.; Chia, C.H.; Jaafar, S.N.S.; Amran, U.A. Chemically Crosslinked Hydrogel and Its Driving Force towards Superabsorbent Behavior. *Int. J. Biol. Macromol.* **2018**, *118*, 1422–1430. [CrossRef]
28. Ruhr, D.; John, M.; Reiche, A. Determination of the Effective Degree of Cross-Linking of Porous Cellulose Membranes Cross-Linked with Bifunctional Epoxides. *Carbohydr. Polym.* **2021**, *251*, 117043–117050. [CrossRef]
29. Lungu, A.; Cernencu, A.I.; Dinescu, S.; Balahura, R.; Mereuta, P.; Costache, M.; Syverud, K.; Stancu, I.C.; Iovu, H. Nanocellulose-Enriched Hydrocolloid-Based Hydrogels Designed Using a Ca^{2+} Free Strategy Based on Citric Acid. *Mater. Des.* **2021**, *197*, 109200–109213. [CrossRef]
30. Amirjani, A.; Salehi, K.; Sadrnezhaad, S.K. Simple SPR-Based Colorimetric Sensor to Differentiate Mg^{2+} and Ca^{2+} in Aqueous Solutions. *Spectrochim. Acta Part A Mol. Biomol. Spectrosc.* **2022**, *268*, 120692–120699. [CrossRef]
31. Ciolacu, F.; Ianus, G.; Marian, G.; Munteanu, C.; Paleu, V.; Nazar, B.; Istrate, B.; Gudîma, A.; Daraduda, N. A Qualitative Assessment of the Specific Woody Biomass of Fruit Trees. *Forests* **2022**, *13*, 405. [CrossRef]
32. Alzorqi, I.; Sudheer, S.; Lu, T.-J.; Manickam, S. Ultrasonically Extracted β-D-Glucan from Artificially Cultivated Mushroom, Characteristic Properties and Antioxidant Activity. *Ultrason. Sonochem.* **2017**, *35*, 531–540. [CrossRef] [PubMed]
33. Luo, H.; Yin, Y.; Wang, Y.; Li, Q.; Tang, A.; Liu, Y. Enhanced Properties of a Soybean Adhesive by Modification with a Cycloaliphatic Epoxy Resin. *Int. J. Adhes. Adhes.* **2022**, *114*, 103026–103032. [CrossRef]
34. Palacios, Y.Y.L.; Khandani, S.; Garcia, E.P.; Chen, A.; Wang, S.; Roy, K.; Knez, D.; Kim, D.A.; Rocha-Mendoza, I.; Potma, E.O. Spectroscopic Analysis of the Sum-Frequency Response of the Carbon–Hydrogen Stretching Modes in Collagen Type I. *J. Chem. Phys.* **2024**, *160*, 185101–185116. [CrossRef] [PubMed]
35. Xu, Y.; Han, Y.; Chen, M.; Li, J.; Li, J.; Luo, J.; Gao, Q. A Soy Protein-Based Film by Mixed Covalent Cross-Linking and Flexibilizing Networks. *Ind. Crop. Prod.* **2022**, *183*, 114952–114961. [CrossRef]
36. Luo, Y.; Li, G.; Chen, L.; Hong, F.F. Preparation and Evaluation of Bacterial Nanocellulose/Hyaluronic Acid Composite Artificial Cornea for Application of Corneal Transplantation. *Biomacromolecules* **2023**, *24*, 201–212. [CrossRef] [PubMed]
37. Zou, P.; Yao, J.; Cui, Y.-N.; Zhao, T.; Che, J.; Yang, M.; Li, Z.; Gao, C. Advances in Cellulose-Based Hydrogels for Biomedical Engineering: A Review Summary. *Gels* **2022**, *8*, 364. [CrossRef]
38. Bruschi, M.L. Mathematical Models of Drug Release. In *Strategies to Modify the Drug Release from Pharmaceutical Systems*, 1st ed.; Bruschi, M.L., Ed.; Woodhead Publishing: Sawston, UK, 2015; Chapter 5, pp. 63–86. [CrossRef]
39. Nistor, A.; Stiubianu, G.; Racles, C.; Cazacu, M. Evaluation of the Water Sorption Capacity of Some Polymeric Materials by Dynamic Vapour Sorption. *Mater. Plast.* **2011**, *48*, 33–37. [CrossRef]
40. Thommes, M.; Kaneko, K.; Neimark, A.V.; Olivier, J.P.; Rodriguez-Reinoso, F.; Rouquerol, J.; Sing, K.S.W. Physisorption of Gases, with Special Reference to the Evaluation of Surface Area and Pore Size Distribution. *Pure Appl. Chem.* **2015**, *87*, 1051–1069. [CrossRef]
41. Uimonen, T.; Hautamäki, S.; Altgen, M.; Kymäläinen, M.; Rautkari, L. Dynamic Vapour Sorption Protocols for the Quantification of Accessible Hydroxyl Groups in Wood. *Holzforschung* **2020**, *74*, 412–419. [CrossRef]
42. Morishige, K. Revisiting the Nature of Adsorption and Desorption Branches: Temperature Dependence of Adsorption Hysteresis in Ordered Mesoporous Silica. *ACS Omega* **2021**, *6*, 15964–15974. [CrossRef] [PubMed]
43. Kachrimanis, K.; Noisternig, M.F.; Griesser, U.J.; Malamataris, S. Dynamic Moisture Sorption and Desorption of Standard and Silicified Microcrystalline Cellulose. *Eur. J. Pharm. Biopharm.* **2006**, *64*, 307–315. [CrossRef] [PubMed]
44. Szymaszek, P.; Tomal, W.; Świergosz, T.; Kamińska-Borek, I.; Popielarz, R.; Ortyl, J. Review of Quantitative and Qualitative Methods for Monitoring Photopolymerization Reactions. *Polym.Chem.* **2023**, *14*, 1690–1717. [CrossRef]

45. Seera, S.D.K.; Kundu, D.; Banerjee, T. Physical and Chemical Crosslinked Microcrystalline Cellulose-Polyvinyl Alcohol Hydrogel: Freeze–Thaw Mediated Synthesis, Characterization and In Vitro Delivery of 5-Fluorouracil. *Cellulose* **2020**, *27*, 6521–6535. [CrossRef]
46. Xu, J.; Boddu, V.M.; Liu, S.X. Rheological Properties of Hydrogels Produced by Cellulose Derivatives Crosslinked with Citric Acid, Succinic Acid and Sebacic Acid. *Cellul. Chem. Technol.* **2022**, *56*, 49–54. [CrossRef]
47. Young, A.T.; White, O.C.; Daniele, M.A. Rheological Properties of Coordinated Physical Gelation and Chemical Crosslinking in Gelatin Methacryloyl (GelMA) Hydrogels. *Macromol. Biosci.* **2020**, *20*, 2000183–2000197. [CrossRef] [PubMed]
48. Blažic, R.; Marušic, K.; Vidovic, E. Swelling and Viscoelastic Properties of Cellulose-Based Hydrogels Prepared by Free Radical Polymerization of Dimethylaminoethyl Methacrylate in Cellulose Solution. *Gels* **2023**, *9*, 94. [CrossRef] [PubMed]
49. Jiang, X.; Yang, X.; Yang, B.; Zhang, L.; Lu, A. Highly Self-Healable and Injectable Cellulose Hydrogels via Rapid Hydrazone Linkage for Drug Delivery and 3D Cell Culture. *Carbohydr. Polym.* **2021**, *273*, 118547–118556. [CrossRef] [PubMed]
50. Bhattacharya, S.; Shunmugam, R. Unraveling the Effect of PEG Chain Length on the Physical Properties and Toxicant Removal Capacities of Cross-Linked Network Synthesized by Thiol–Norbornene Photoclick Chemistry. *ACS Omega* **2020**, *5*, 2800–2810. [CrossRef] [PubMed]
51. Kono, H. Characterization and Properties of Carboxymethyl Cellulose Hydrogels Crosslinked by Polyethylene Glycol. *Carbohydr. Polym.* **2014**, *106*, 84–93. [CrossRef]
52. Cortés-Triviño, E.; Valencia, C.; Delgado, M.A.; Franco, J.M. Rheology of Epoxidized Cellulose Pulp Gel-like Dispersions in Castor Oil: Influence of Epoxidation Degree and the Epoxide Chemical Structure. *Carbohydr. Polym.* **2018**, *199*, 563–571. [CrossRef] [PubMed]
53. Ciolacu, D.; Doroftei, F.; Cazacu, G.; Cazacu, M. Morphological and Surface Aspects of Cellulose-Lignin Hydrogels. *Cellulose Chem. Technol.* **2013**, *47*, 377–386.

gels

MDPI

Article

Influence of Gel Stage from Cellulose Dissolution in NaOH-Water System on the Performances of Cellulose Allomorphs-Based Hydrogels

Diana Elena Ciolacu [1,*], Daniela Rusu [2], Raluca Nicoleta Darie-Niţă [3], Daniel Tîmpu [3] and Florin Ciolacu [4,*]

[1] Department of Natural Polymers, Bioactive and Biocompatible Materials, "Petru Poni" Institute of Macromolecular Chemistry, 700487 Iasi, Romania
[2] Department of Physics of Polymers and Polymeric Materials, "Petru Poni" Institute of Macromolecular Chemistry, 700487 Iasi, Romania; rusu.daniela@icmpp.ro
[3] Department of Physical Chemistry of Polymers, "Petru Poni" Institute of Macromolecular Chemistry, 700487 Iasi, Romania; darier@icmpp.ro (R.N.D.-N.); dtimpu@icmpp.ro (D.T.)
[4] Department of Natural and Synthetic Polymers, "Gheorghe Asachi" Technical University of Iasi, 700050 Iasi, Romania
* Correspondence: dciolacu@icmpp.ro (D.E.C.); florin.ciolacu@academic.tuiasi.ro (F.C.); Tel.: +40-332-880-220 (D.E.C.); +40-232-278-683 (ext. 2200) (F.C.)

Abstract: Novel hydrogels were prepared starting from different cellulose allomorphs (cellulose I, II, and III), through a swelling stage in 8.5% NaOH aqueous solution, followed by freezing at low temperature (−30 °C), for 24 h. After thawing at room temperature, the obtained gels were chemical cross-linked with epichlorohydrin (ECH), at 85 °C. The swelling degrees of the hydrogels were investigated, and a complex dependence on the type of the cellulose allomorph was found. Moreover, the gel stage has been shown to play a key role in the design of hydrogels with different performances, following the series: H-CII > H-CI > H-CIII. The correlations between the allomorph type and the morphological characteristics of hydrogels were established by scanning electron microscopy (SEM). The hydrogel H-CII showed the biggest homogeneous pores, while H-CIII had the most compacted pores network, with small interconnected pores. The rheological studies were performed in similar shear regimes, and a close correlation between the strength of the gel structure and the size of the gel fragments was observed. In the case of hydrogels, it has been shown that H-CII is softer, with a lower resistance of the hydrogel (G′) above the oscillation frequencies tested, but it maintains its stable structure, while H-CIII has the highest modulus of storage and loss compared to H-CI and H-CII, having a stronger and more rigid structure. The X-ray diffraction (XRD) method showed that the crystalline organization of each type of allomorph possesses a distinctive diffraction pattern, and, in addition, the chemically cross-linking reaction has been proved by a strong decrease of the crystallinity. Attenuated total reflectance Fourier transform infrared (ATR-FTIR) spectroscopy provided clear evidence of the chemical cross-linking of cellulose allomorphs with ECH, by the alteration of the crystal structure of cellulose allomorphs and by the formation of new ether bands.

Keywords: cellulose allomorphs; gel stage; gel fracturing; cross-linking; hydrogels; rheology

Citation: Ciolacu, D.E.; Rusu, D.; Darie-Niţă, R.N.; Tîmpu, D.; Ciolacu, F. Influence of Gel Stage from Cellulose Dissolution in NaOH-Water System on the Performances of Cellulose Allomorphs-Based Hydrogels. *Gels* **2022**, *8*, 410. https://doi.org/10.3390/gels8070410

Academic Editor: Yi Cao

Received: 20 May 2022
Accepted: 24 June 2022
Published: 29 June 2022

1. Introduction

Since their development in the late 1960s, hydrogels have distinguished themselves by a network-like three-dimensional (3D) structure, as well as by their unique properties, which gives them competitive advantages compared to the other materials, making them a promising material-platform for various applications [1–3]. The undeniable versatility of hydrogels in terms of their synthesis, composition, and physical and chemical properties has led to a considerable attention from both research and industry and has created wide applicative potential, from the agricultural and industrial to the biomedical field. A key feature of hydrogels is their ability to absorb large quantities of water, which makes

them soft, pliable, and compatible with most of the living tissues and thus of certain interest for the biomedical field [4,5]. In addition, their viscoelastic nature reduces any possible damage to the surrounding tissue, after potential implantation [6]. Moreover, the mechanical properties are comparable to those of soft tissue, a feature which renders them particularly attractive to tissue engineers [7].

Using the natural polymers in the preparation of the hydrogels represents an attractive option over the most of the synthetic counterparts, due to the wide design possibilities of some specific compositions and properties, providing, besides the support function, key features such as biodegradability, biocompatibility, and low latent toxicity [8,9]. Moreover, hydrogels based on natural polymers can be employed either for the sustained and controlled (stimuli-responsive systems) delivery of active pharmaceutical principles (mainly drugs and proteins) to different cultures and tissues, or as scaffolds for tissue engineering [10–14].

In this regard, cellulose, the main constituent of plants fibers and the most abundant natural polymer, with benefits such as low cost, renewability, availability, biodegradability, and non-toxicity, represents one of the most frequently used polymers in the preparation of hydrogels [15]. Cellulose and its derivatives have proven to be versatile polymers, which provide a good platform for the building of 3D networks and various possibilities to design the physico-chemical features of hydrogels, in terms of mechanical behavior, swelling ability, and sensibility to external stimuli [7,9,16].

Cellulose displays a highly ordered crystalline structure, based on extensive intra- and intermolecular hydrogen bonds, and is able to crystallize into various allomorphic forms that differ in unit cell dimensions and chain polarity (cellulose I, II, III, and IV) [17,18]. The structural differences of cellulose allomorphs, in terms of crystalline and amorphous contents and the sizes and shapes of the crystallites corresponding to the allomorphic forms of cellulose, are considered to be important parameters in the realization of functional materials.

Cellulose I (CI), or native cellulose, represents the prevalent form in plants. This contains highly ordered (crystalline) structures, made of tightly packed linear chains, disposed of in a parallel arrangement and held together by inter- and intramolecular hydrogen bonds and also, disordered regions (amorphous) [18]. The natural form of cellulose was found to be a composite of two coexisting crystalline forms, such as cellulose Iα (a triclinic lattice with one chain per unit cell) and cellulose Iβ (a monoclinic lattice with two chains per unit cell) [19]. Cellulose II (CII) is obtained by regeneration from various media or by mercerization in an aqueous NaOH solution [20,21]. CII displays an anti-parallel arrangement of the chains and possesses a superior chemical reactivity, as compared to cellulose I. Moreover, the transition from cellulose I to cellulose II is not reversible, and this implies that cellulose II is a stable form as compared with the metastable cellulose I. Another crystalline form, known as cellulose III (CIII), can be derived from both cellulose I and II, using different treatments [22–24]. Thus, CIII can be prepared either by soaking cellulose samples in anhydrous liquid ammonia at −80 °C or in organic amine.

Each of these three allomorphic forms of cellulose, with the advantages and limitations of their structural architectures, which are reflected in their accessibility and reactivity, present a wide and interesting array of potential applications in different domains.

The variations found between the crystalline and amorphous regions, within the cellulose structure, are the result of both the origin and history of the applied treatments. Many reagents are able to penetrate only the amorphous part of the material, and most of the reactions will take place in this area or at the interface with the crystalline ones. Thus, to increase the chemical reactivity of cellulose it is important to make more accessible the crystalline regions of cellulose to reagents, by swelling and de-crystallization methods.

Due to the fact that important applications of cellulose involve its regeneration in several morphologies such as fibers, films, membranes, nanoparticles, or bulky objects (sponges and aerogels), the dissolution of cellulose is a crucial and challenging step [25,26]. Cellulose is difficult to dissolve in water or most organic solvents due to its characteristic structure with close packing of macromolecular chains and a strong intra- and interchain

bonding network [18,27,28]. More recently, this common concept that cellulose–cellulose hydrogen-bonding is the main obstacle to dissolution and the driving force of aggregation has been questioned and, instead, it was suggested that hydrophobic interactions play a very important role in cellulose (in)solubility [27].

There are a limited number of solvents that can directly dissolve cellulose, and between these, the most important ones are the phosphoric acid-based solvents, LiCl-based solvents, N-methyl morpholine N-oxide/water, ionic liquids, and NaOH–water [29–32]. Nevertheless, most of these solvents are limited to a laboratory scale due to issues such as toxicity, environmental hazard, and limited solvency [33].

One of the most common and attractive solvents of cellulose is the NaOH–water-based system, which has gained attention due to its low cost and of the fact that is easily recyclable and environmentally friendly.

A number of publications have reported that NaOH-water system can be a good solvent for cellulose, if certain conditions are met. These conditions are: (i) the concentration of the alkaline solution, which must be in the range of 7–10% NaOH solution, and (ii) the temperature, which must be low enough, even below 0 °C. As a result of the accomplishment of these conditions, it was proved that the NaOH-water system is able to break the intra- and intermolecular hydrogen bonds [30,34–37].

The dissolution of cellulose in NaOH-water can be achieved to a certain extent depending on factors such as the molecular weight and the dimensions of the crystalline domains [30,33,38,39]. However, most of these alkaline water-based systems allow only for the dissolution of celluloses with a relatively low degree of polymerization, DP < 300.

Isogai and Atalla [39] investigated the possibility of dissolving various types of native cellulose (microcrystalline cellulose, linter cellulose, softwood unbleached, and bleached kraft pulps and softwood groundwood pulp) and of different chemically treated cellulose (mercerized and regenerated). They observed that dissolution is possible only if cellulose is suspended in a solution of 8.5% NaOH, at a low temperature of −20 °C. After the thawing of the frozen mass at room temperature, water is added over the obtained gel, in order to reach a solution containing 2% cellulose in 5% aqueous NaOH.

Considering the above-mentioned dissolution method [39] and the high applicative potential of the hydrogels, the authors intended to obtain hydrogels with controlled densities, porosities, and swelling degrees, starting from the allomorphic forms of cellulose with different crystalline structures.

Thus, the aim of this study is to evaluate the influence of the gel structure obtained from the cellulose-8.5% NaOH system, based on the Isogai and Atalla method, on the performance of their corresponding hydrogels, prepared by chemical crosslinking with epichlorohydrin (ECH).

The hydrogels were obtained starting from three allomorphic forms of cellulose (cellulose I, II, and III) and were investigated by means of swelling measurements, X-ray diffraction (XRD) analysis, scanning electron microscopy (SEM), attenuated total reflectance Fourier transform infrared (ATR-FTIR) spectroscopy, and oscillatory rheology, in order to establish their structure and morphology, as well as the swelling and rheological behaviors.

2. Results and Discussion

2.1. Swelling Behavior of Hydrogels

Novel hydrogels were produced by chemical cross-linking with ECH of different cellulose allomorphs (CI, CII, and CIII), starting from a gel-like mass, obtained as an intermediary stage within the cellulose dissolution process in NaOH-water system, at low temperature (Figure 1a–c). One of the main interests of this study was to evaluate the influence of the cellulose allomorphs' structure upon the swelling capacity of their corresponding hydrogels (Figure 1d–f) since the ability to absorb water represents one of the most important features of these 3D materials.

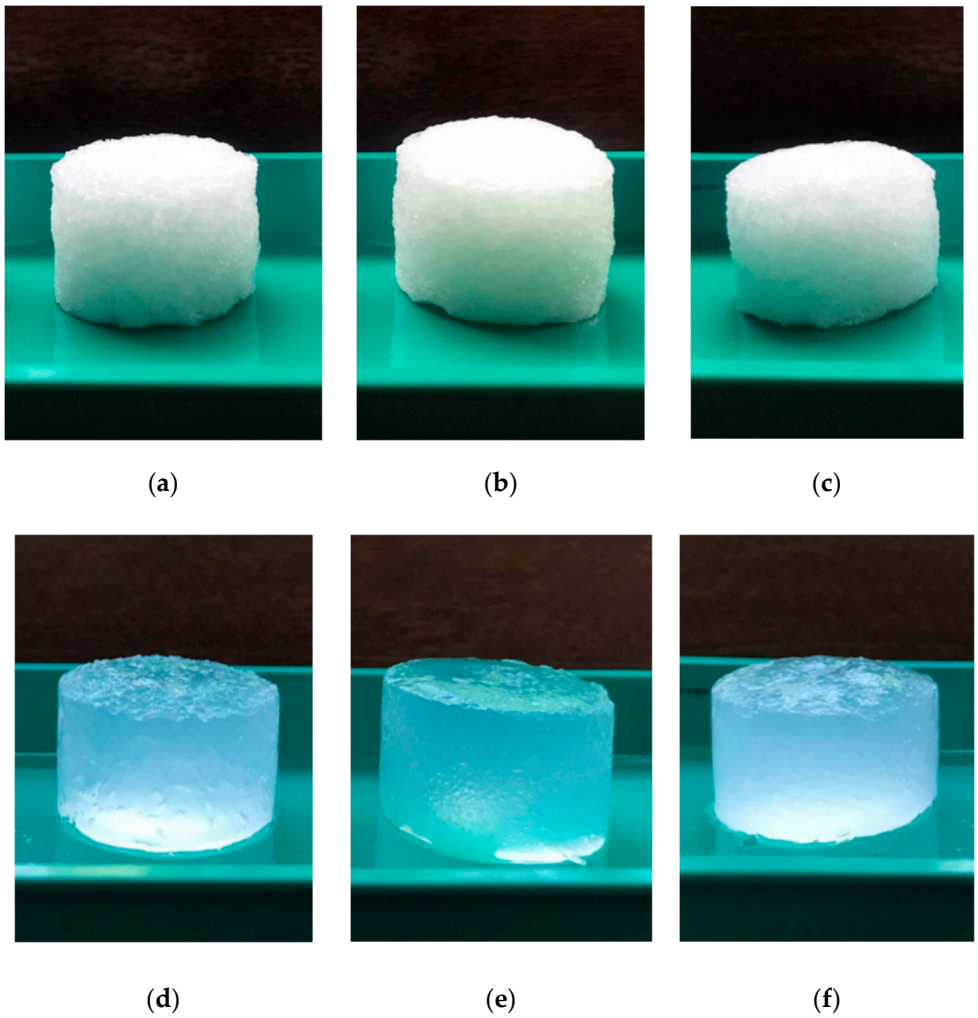

Figure 1. Stages in the investigation of the hydrogels based on cellulose allomorphs: (**a**–**c**) dry state of the hydrogels H-CI, H-CII, and H-CIII, and (**d**–**f**) wet state of the hydrogels H-CI, H-CII, and H-CIII.

The three hydrogels prepared from the cellulose allomorphs H-CI, H-CII, and H-CIII showed different swelling abilities, as reflected by the different values of the maximum swelling degree (Qmax) and equilibrium swelling degree (Qeq) (Table 1).

Table 1. Swelling kinetic parameters of cellulose-allomorphs-based hydrogels.

Sample	Swelling Kinetic Parameters			Qmax (%)	Qeq (%)
	k_{sw}	n_{sw}	R^2		
H-CI	0.291	0.386	0.999	2042	2128
H-CII	0.321	0.377	0.999	2295	2440
H-CIII	0.165	0.614	0.999	1826	1926

The graph displayed in Figure 2 shows that the hydrogel H-CII, obtained from the cellulose II allomorph, exhibited the highest value of the swelling degree (Qmax = 2295%; Qeq = 2440%). A medium value was recorded for the hydrogel prepared from the CI allomorph (H-CI: Qmax = 2042%; Qeq = 2128%), while the lowest swelling values were registered for the CIII allomorph (H-CIII: Qmax = 1826%; Qeq = 1926%). The swelling occurred rapidly in the first 50 min and then slowly reached a constant value (Qmax) for all the samples. The Qeq values of the never-dried hydrogels are higher than that obtained for the Qmax of the freeze-dried hydrogels, due to the well-known hornification

phenomenon [28]. However, the same descending order is maintained for both swelling degrees, such as H-CII > H-CI > H-CIII.

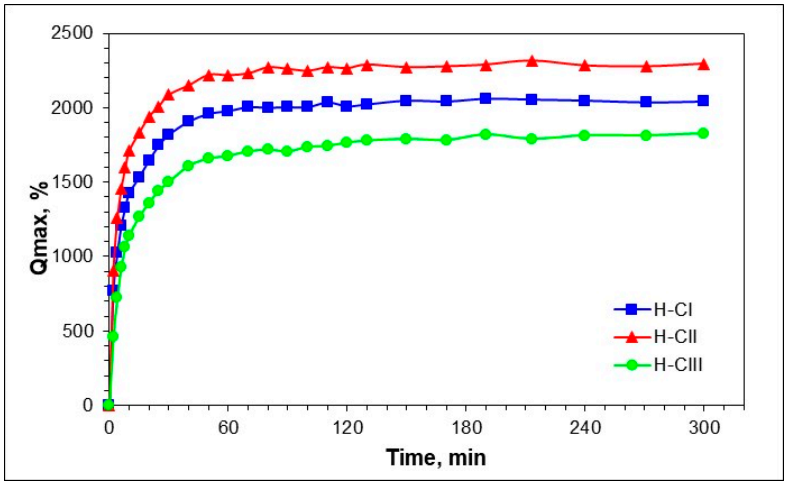

Figure 2. Evolution of the swelling degree (Qmax) for the hydrogels based on cellulose allomorphs H-CI, H-CII, and H-CIII.

The dynamic swelling behavior of the hydrogels is dependent on the relative contribution of polymer relaxation, as well as of the penetrant diffusion [40,41]. In order to study the effect of the hydrogel type (H-CI, H-CII, and H-CIII) on the kinetic of water uptake process, swelling data were fitted using the power-law expression (Equation (3)) [41]. The swelling kinetic parameters of the hydrogels based on the cellulose allomorphs are presented in Table 1.

The parameter n_{sw} is the diffusion exponent that indicates the water transport mechanism, while k_{sw} is the swelling constant, which is related to the structural network. For a hydrogel, (i) n = 0.5 indicates the Fickian diffusion (case I), (ii) n = 1 implies relaxation-controlled transport mechanism (case II), and (iii) 0.5 < n < 1 indicates the non-Fickian or anomalous transport (case III) [42]. The values of n < 0.5 show a pseudo-Fickian (less-Fickian) diffusion [43]. The constants n_{sw} and k_{sw} were calculated from the slopes and intercepts of the plots of ln (M_t/M_0) vs. ln t.

The values of n_{sw} obtained in the case of H-CI and H-CII hydrogels (n_{sw} < 0.5) indicate that the water transport mechanism follows the less Fickian diffusion, in which the rate of diffusion is much smaller than the rate of relaxation ($R_{diffusion} < R_{relaxation}$, system controlled by diffusion) [44]. A slight increase of n_{sw} for H-CI indicated the fact that the swelling is controlled more by the polymer chain relaxation rate then the water diffusion rate. For H-CIII, it was observed that n_{sw} > 0.5 (n_{sw} = 0.614), which indicated a shift from the less-Fickian diffusion (water transport mechanism) to a non-Fickian or anomalous transport (relaxation-controlled transport mechanism). This type of diffusion indicates the fact that the water diffusion and the polymer relaxation rate are about the same order of magnitude ($R_{diffusion} \sim R_{relaxation}$).

The swelling rate constant, k_{sw}, is another important parameter that determines the diffusional characteristics of hydrogels and a slight decrease of this parameter were observed in the case of H-CI and H-CIII hydrogels.

For all the hydrogels, the correlation coefficients R^2 are higher than 0.99, a fact that indicates the high accuracy of the linear regression equations and good agreement between the experimental data and the chosen model.

2.2. Morphological Investigation of the Hydrogels

SEM is a relatively simple morphological analysis technique that requires minimum sample preparation and provides solid and realistic information regarding the spatial arrangement of any given material [28]. Therefore, SEM was used to study the surface features of the hydrogels based on cellulose allomorphs and to collect data with respect

to the appearance, integrity, porosity, and degree of uniformity of the hydrogels. This technique offers essential details regarding the morphological aspects of the hydrogels, which ranged from millimeters down to micrometers.

It is expected that the different types of the allomorph used in the hydrogels will be reflected in different morphologies, as was also observed in the investigations on the swelling behavior (Figure 3).

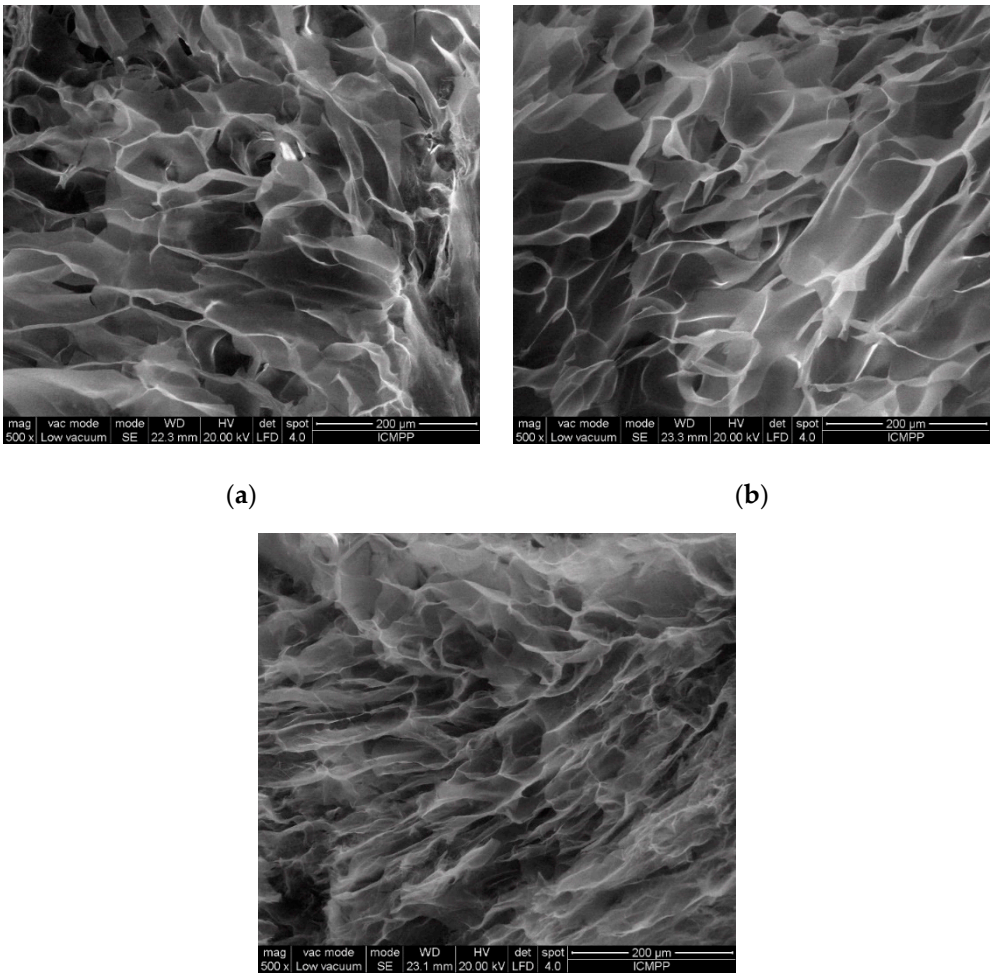

(**a**) (**b**)

(**c**)

Figure 3. SEM micrographs of the hydrogels based on cellulose allomorphs: (**a**) H-CI, (**b**) H-CII, and (**c**) H-CIII.

The analysis of SEM micrographs evidenced the fact that the 3D polymeric matrices with dissimilar homogeneities and had varying porous structures, and they differed from one another in terms of shape, dimension, and distribution of pores. The average pore size was determined from the SEM micrographs, by measuring 50 randomly chosen pores.

The H-CI hydrogel shows interconnected pores of a roughly circular shape, dispersed in a quasi-homogeneous, compact matrix. The average diameter of the pores is 86.2 ± 12.7 µm, confirming a tightly packed morphology, a fact that is explains the relatively small amount of water absorbed by this 3D matrix, as was confirmed by the swelling data.

In comparison, the H-CII hydrogel has bigger, interconnected, and ovoid-pores distributed along a more homogeneous surface. The average diameter of these pores is 108.2 ± 15.3 µm, thus explaining the more relaxed morphology of these hydrogels, which is able to incorporate a larger quantity of water.

The H-CIII hydrogel has the most compacted pores network, with small interconnected pores (an average diameter of 67.5 ± 12.6 µm), information that correlates well

with the swelling data, with H-CIII having the lowest swelling degree compared to the other two hydrogels.

All the observations from the SEM micrographs are consistent with the information data on the swelling behavior, confirming a direct dependence between the pore size and the swelling degree of the hydrogels; thus, the bigger the pore size, the higher the swelling degree.

2.3. Crystallinity in Cellulose Allomorphs and Cellulose-Based Hydrogels

The differences in the swelling behaviors of the hydrogels were initially attributed to the differences in the structural organization of the starting materials (cellulose allomorphs), which is why a complex investigation of the supramolecular structure by XRD of both the starting materials and the hydrogels was performed.

The XRD diffractograms characteristic of cellulose allomorphs (CI, CII, and CIII), as well as those of the corresponding hydrogels (H-CI, H-CII, and H-CIII), are presented in Figure 4. Several structural changes that occur during the mercerization process are highlighted in Figure 4 and consist of a decrease in the degree of crystallinity of CII compared to CI and a complete transformation of CI into the CII allomorph (Figure 4b).

It has been observed that the transition process from CI to CII is accompanied by modifications of the intensities corresponding to different crystallographic planes. The diffraction peaks characteristic of CI are presented in Figure 4a and appear at Bragg angles (2θ) of 14.6°, 16.2°, and 22.5°, which are typical for the crystallographic planes, (110), (1–10), and (200), respectively. In the case of the CII, three characteristic cellulose lattice planes were identified in the XRD diffraction pattern (Figure 4b), and these appear at 12.1° assigned to the (110) plane, at 20.1° for the (1–10) plane, and at 21.8° for (200) plane, respectively. Generally, CII is characterized by a slightly larger peak (1–10) on the left and a slightly smaller (200) on the right, a well-known difference that demonstrates the complete transformation of a crystalline structure of CI to a crystalline structure of CII [17]. This fact was also observed in our study, when it was found that CII contains a (1–10) peak with a much higher intensity than the (200) peak, proving a complete transformation of CI to the lower free energy crystalline pattern, CII. The diffractogram of CIII (Figure 4c) presents one peaks at 11.8° (110 plane) and an overlapping of the planes (1–10) and (200), at 2θ of 21.1°.

It is obvious that the crystalline organization of each type of allomorph has a distinctive diffraction pattern, with specific variations of both the intensities of the diffraction peaks and the positions of the Bragg angles, at which their characteristic maxima are placed.

The diffractograms displayed in Figure 4d–f show a significant decrease of the intensities of all the peaks characteristic of the main crystallographic planes, an overlapping of the planes (1–10) with (200), and a displacement of the plane (110) towards lower values of the angle 2θ. These modifications indicate that the chemical cross-linking has been achieved in all hydrogels, accompanied by the damage of the initial crystalline structure of cellulose.

The synthesis of hydrogels from different types of cellulose allomorphs proceeds with the major impairment of the crystalline organization. All the prepared hydrogels, regardless of the initial allomorph, lead essentially to the same structure specific to a predominantly amorphous cellulose, with peaks that have become wider and weaker. However, the presence of a certain crystallinity was observed, demonstrated by the presence of the peaks corresponding to the characteristic crystallographic planes of CII allomorph.

Thus, the diffraction peaks characteristic of H-CI (Figure 4d) appear at 9.39° for the crystallographic plane (110), while for the crystallographic planes (1–10) and (200) a Bragg angle of 20.1° was recorded. The same transformation was observed also for H-CII (Figure 4e), where the two characteristic peaks were identified at 2θ of 9.21° and 20.1°, while in the case of H-CIII (Figure 4f), the peaks appeared at 2θ of 9.47° and 20.1°.

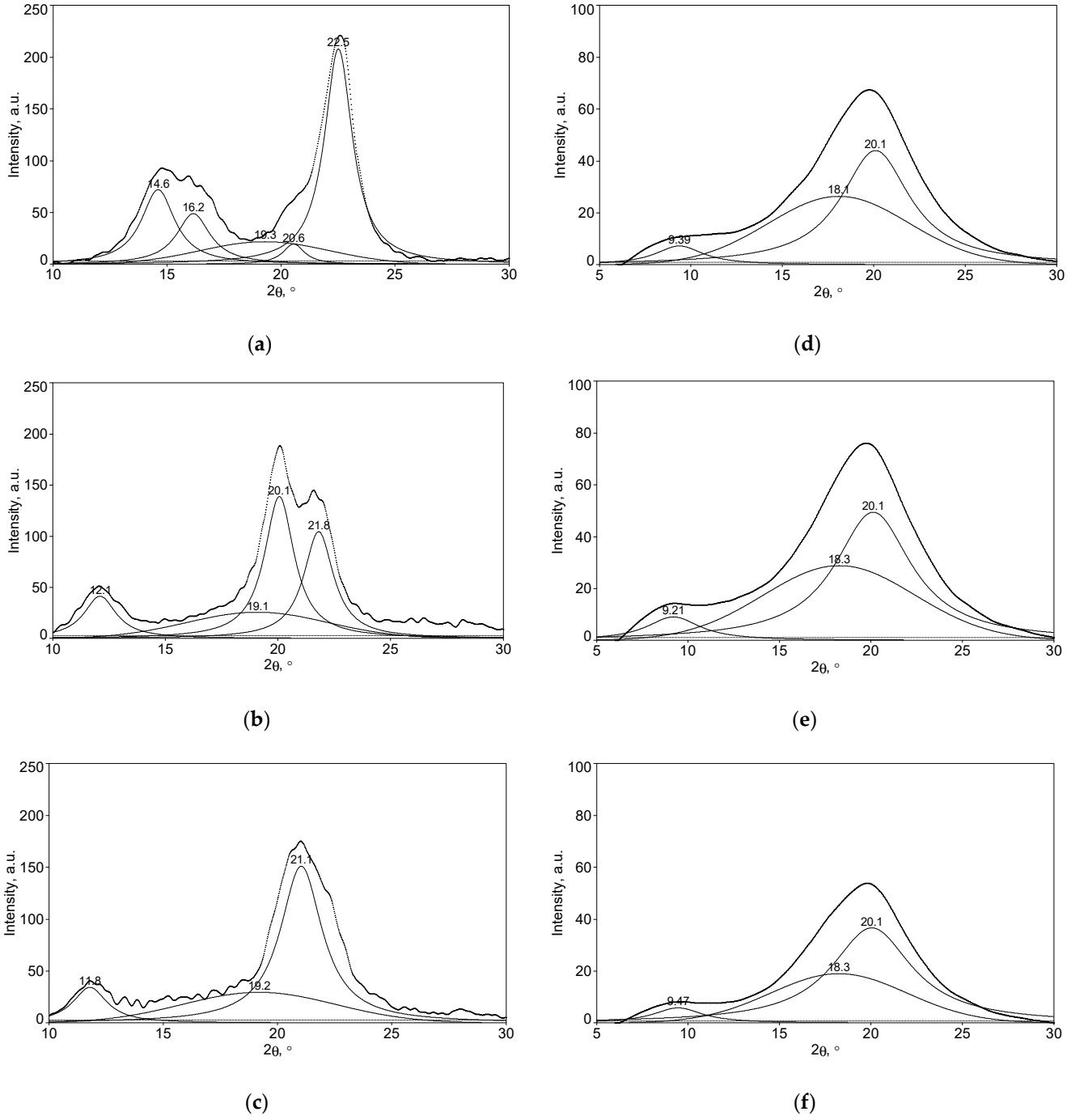

Figure 4. The deconvoluted XRD diffractograms of (**a**–**c**) cellulose allomorphs (CI, CII, and CIII) and (**d**–**f**) hydrogels obtained from the corresponding cellulose allomorphs (H-CI, H-CII, and H-CIII).

XRD studies of cellulose-allomorphs-based hydrogels confirm that chemically cross-linked hydrogels undergo distinct transformations. The sharp reduction of the crystallinity recorded for the case of the chemically cross-linked hydrogels is a fact confirmed also by other authors [28]. In the initial cellulose, the chains are packed in a highly orderly manner with a compact structure, while in the case of hydrogels, the crystalline structure was destroyed by the cross-linking reaction, which disrupts the self-association and the packing of the cellulose chains, consequently leading to an increase of the sample's hydrophilicity [20,28].

The changes recorded by the cellulose-allomorphs-based hydrogels (H-CI, H-CII, and H-CIII), regarding their crystallinity index (CrI) and the crystallite dimension (Dhkl) are presented in Table 2. The crystallinity index was determined by using Equation (4), while the crystallite size (Dhkl) in the direction perpendicular to the analyzed lattice planes with the Miller indices (hkl) was evaluated by using Scherrer's equation (Equation (5)) [41,42].

Table 2. Crystallite size (D) and crystallinity index (CrI) of the cellulose allomorphs and cellulose-based hydrogels.

Samples		$D_{(110)}$ (nm)	$D_{(1–10)}$ (nm)	$D_{(200)}$ (nm)	CrI (%)
Cellulose allomorphs	CI	5.995	5.232	8.330	86.02
	CII	5.492	7.786	8.191	82.20
	CIII	4.821	8.039	8.039	70.72
Cellulose-based hydrogels	H-CI	3.615	2.665		44.99
	H-CII	4.349	3.147		46.62
	H-CIII	3.009	2.636		40.71

Regarding the crystallinity index (CrI) of the allomorphic celluloses, there was a decrease in it when passing from the untreated sample of CI (CrI = 86.02%) to the mercerized CII (CrI = 82.20%) and to CIII (CrI = 70.72%). In the case of the hydrogels, the crystallinity indexes have not varied too much between the samples, with the recorded values being 44.99% for H-CI, 46.62% for H-CII, and 40.71% for H-CIII.

A relationship between the crystallinity index and the crystallite dimensions was observed for the studied samples. Thus, the smaller the dimensions of the crystallites, the lower the CrI of the sample, a fact associated with an increase of the amorphous domains. This aspect was also confirmed by other authors [45,46].

Moreover, the dramatic decrease in the crystalline indexes of cellulose-based hydrogels is a result of chemical crosslinking between the hydroxyl groups of the cellulose chains.

However, XRD investigations have shown the same type of supramolecular organization of hydrogels, regardless of the type of allomorph used as starting material, which does not explain the differences in the swelling behavior of hydrogels resulting from different allomorphs.

2.4. Rheological Evaluation of the Gels and Hydrogels Based on Cellulose Allomorphs

Since the changes in the supramolecular structure do not explain the swelling behavior, the explanation for the differences in the swelling behavior was searched for in the differences recorded during the hydrogel synthesis processes.

Hydrogels were prepared starting from a swelling stage of cellulose in NaOH solutions, at low temperatures, based on a method developed by Isogai and Atalla [39], followed by chemical cross-linking with epichlorohydrin (ECH).

As already known, the first stage in polymer dissolution is swelling (Figure 5—stage I), a phenomenon based on the incorporation into the polymer of a large amount of solvent. The swelling may be limited or unlimited, similar to dissolution. The limited swelling is the process of interaction of the polymer with the solvent, which is stopped when the latter is absorbed by the polymer, without a spontaneous dissolution. The method of dissolving cellulose at low temperatures involves a complete freezing stage by cooling to very low temperatures (Figure 5—stage II), and the thawing of the obtained block allows one to obtain the gel phase. Two phases are specific to the limited swelling process: one represented by the polymeric matrix in which the solvent molecules diffused—*the gel*—and other represented by the pure solvent or diluted solution of polymer in solvent—*the supernatant*. The two phases are delimited by a separation surface and they coexist in an equilibrium, as shown in Figure 5—stage III.

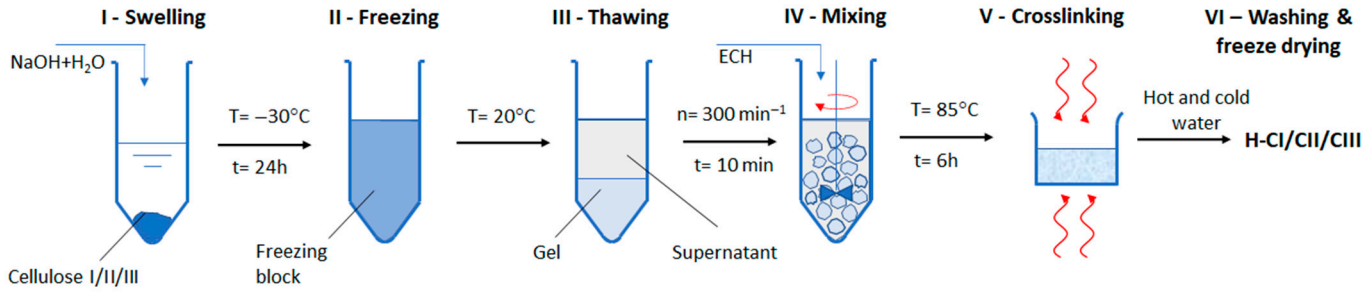

Figure 5. Schematic method for the preparation of hydrogels based on cellulose allomorphs.

The first differences appeared in the aspect of the gel phase resulting from the swelling in NaOH solution of cellulose allomorphs (Figure 6).

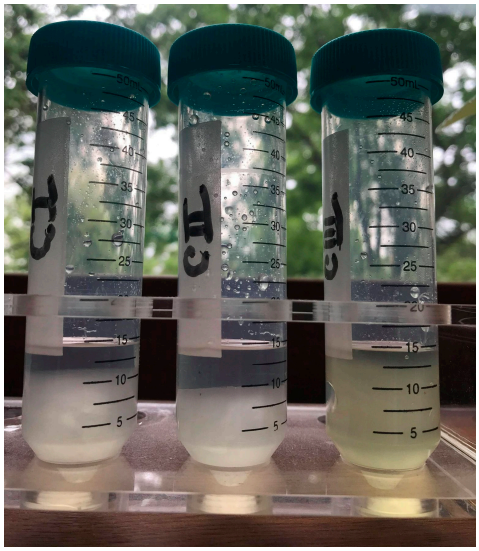

Figure 6. Gel phases corresponding to each type of cellulose allomorphs: CI, CII, and CIII.

The gels have different appearances, volumes, consistencies, and densities. The density and polymerization degree corresponding to the cellulose allomorphs are presented in Table 3.

Table 3. The density and polymerization degree corresponding to the cellulose allomorphs.

Sample	CI	Alkali-Treated CI	CII	Alkali-Treated CII	CIII	Alkali-Treated CIII
DP	183	171	154	149	164	158
Density (g/mL)	1.050	-	1.282	-	0.960	-

The gel resulting from the swelling of the CII allomorph is obviously the most compact, while that of the CIII allomorph is the least dense. These aspects were reflected in their behavior in the next stage, the mixture with the cross-linker under controlled shear regimes.

By mixing with the cross-linking agent in identical shear regimes, the cellulose-NaOH gels are fractured into fragments of sizes correlated with the strength of the gels. The result is a hydrogel with a high cross-linking density if the gel fragments are small in size and with a lower cross-linking density in the case of resistant gels that fracture into large fragments (Figure 7).

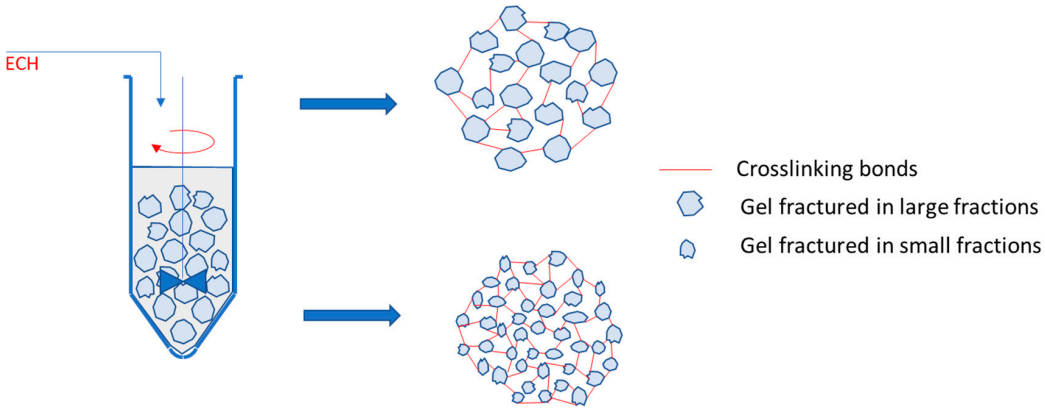

Figure 7. A model for the hydrogels synthesis, as a result of the cross-linking of gels fragmented in large or small fractions.

In order to validate the proposed model, rheological investigations were performed, which were able to explain both the structure and the swelling behavior of the obtained hydrogels.

To highlight the strength of cellulose-NaOH gels, oscillatory amplitude sweeps tests were carried out. The linear viscoelastic region (LVR) was determined, and the brittle fracturing behavior of the gels was evidenced.

The (elastic) storage modulus G′ represents the elastic portion of the viscoelastic behavior, while the (viscous) loss modulus G″ characterizes the viscous portion of the viscoelastic behavior.

The approximate values of G′ within the LVR, which refer to the gel strength, vary between 6350 Pa for CI, 11,500 Pa for CII, and 3500 Pa for CIII, showing enhanced stiffness "at rest" of the network (G′LVR) for cellulose allomorphs CII followed by CI.

When the LVR is exceeded, G′ and G″ are dependent on the strain amplitude, usually decreasing with its enhancement for all gels at large deformations. The amplitude sweep results reveal the network breakdown as the strain increases. All the studied gels of cellulose allomorphs exhibit a "flow point" (crossover G′ = G″) over 14.5%. The stress and strain at the flow points (δ_f) and (γ_f), respectively, were determined at the crossover point (G′ = G″), with the resulting values being presented in Table 4 [47].

Table 4. The values of dynamic moduli at the crossover point (G′ = G″), and the stress and strain at the flow point (δ_f and γ_f).

Sample	G′ = G″ (Pa)	δ_f (Pa)	γ_f (%)
CI	1072	434.9	28.57
CII	1102	491.1	31.52
CIII	1027	211.4	14.54

The experimental results show a lower strength of CIII at the flow point, with the lowest values of the dynamic moduli, δ_f and γ_f, and the maximum structure breakdown of this cellulose allomorph being registered at 14.54% strain deformation.

Figure 8 shows that G′ displays the sharpest downturn starting at γ = 1% for CII, thus indicating a brittle fracturing behavior that led to the inhomogeneous breaking of gel CII under shear into larger pieces [48].

Moreover, Figure 8 displays that the loss modulus G″ follows an almost constant value in the LVE region for all gels, but, unlike G′, the G″ curve rises sharply because initially a few individual bonds in the network are broken, developing micro cracks, keeping the entire surrounding material firmly together. After reaching the maximum peak before breakdown, the gel starts to flow so the G″ curve drops continuously and not as steep as G′. The sharp increase of the viscous modulus G″ is due to the internal viscous friction of

the resulting freely movable fragments around the micro cracks (Figure 8b). The individual micro cracks continue to grow and might lead to the formation of the continuous macro crack through the entire material that starts to flow, with the viscous behavior of the sample dominating in this case (G″ > G′) [49].

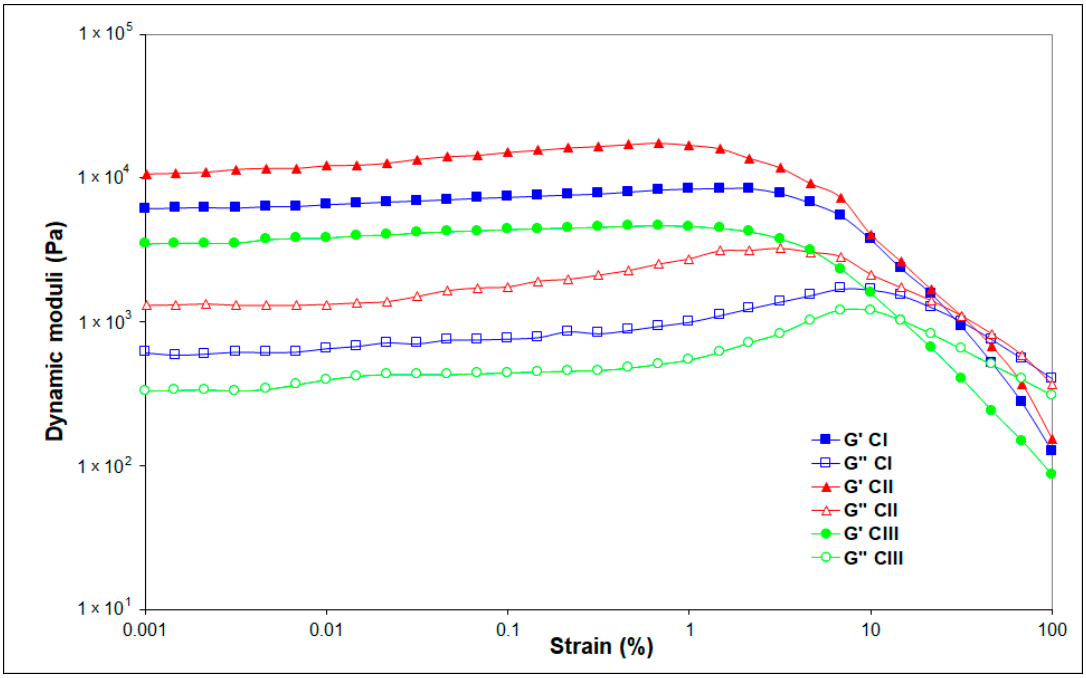

(**a**)

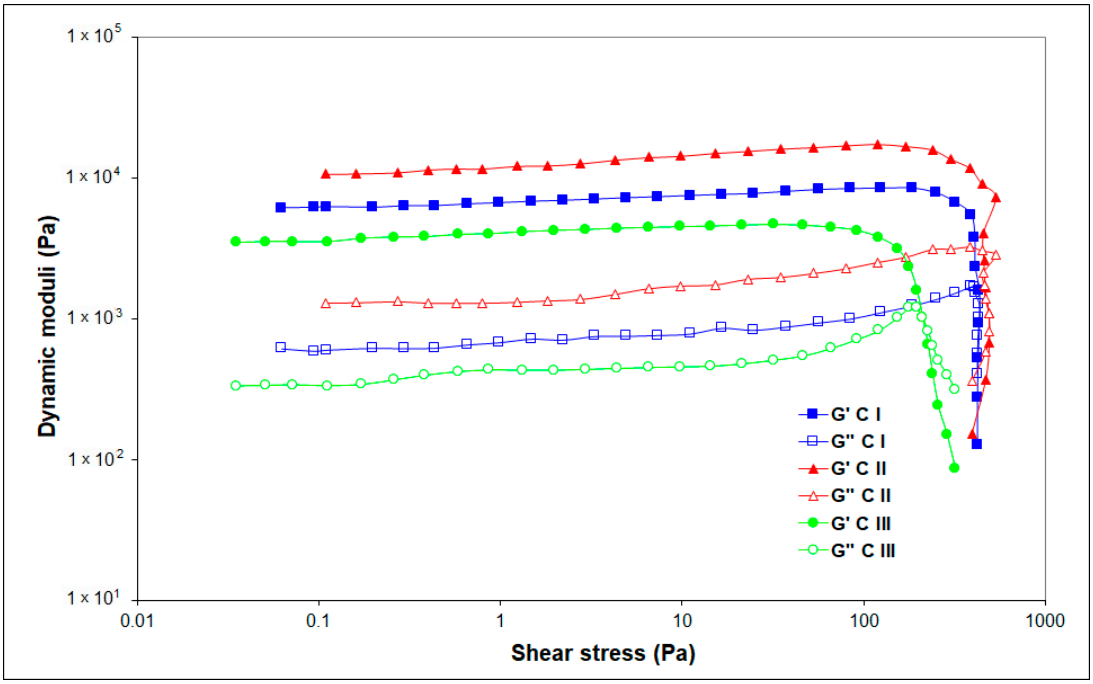

(**b**)

Figure 8. (**a**) Amplitude sweep test results (**a**) G′ and G″ dependence of the oscillatory strain for CI, CII and CIII; and (**b**) G′ and G″ dependence of the shear stress for gels CI, CII, and CIII.

The shape of G″ can be used to distinguish the behavior of the gels. The process of structural breakdown is faster for CII and delayed for CI (and especially CIII).

The rheological measurement results offer information on the structure–property relationship of the hydrogels. The dynamic viscoelastic properties of the formed networks of cellulose-based hydrogels were evaluated by frequency sweep analysis (Figure 9). The elastic features of the matrix were dominant throughout the whole measured angular frequencies, characterized by G′ values higher than G″ values, which demonstrates typical gel-like behavior.

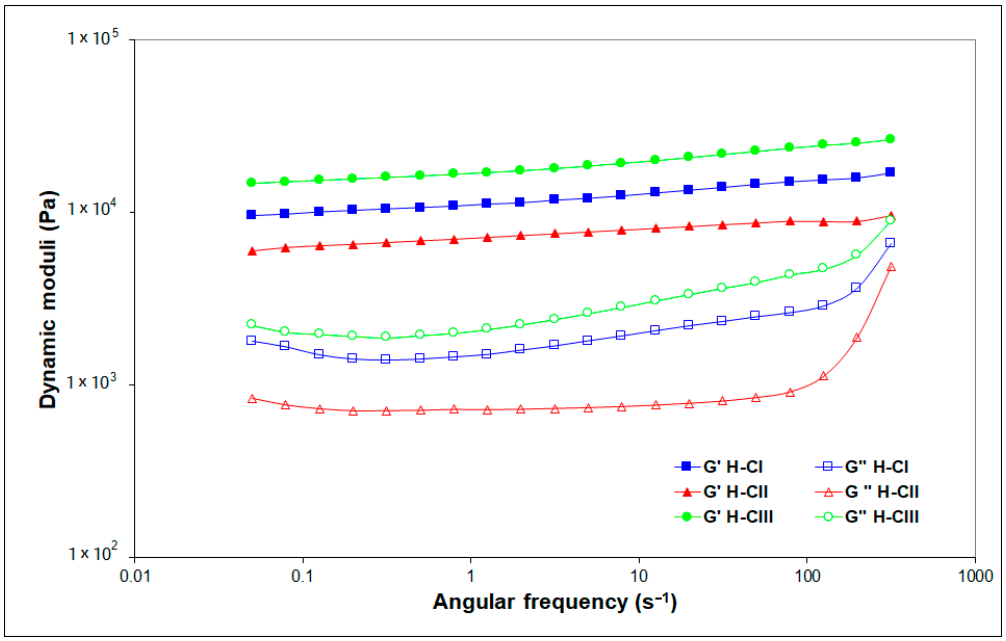

(**a**)

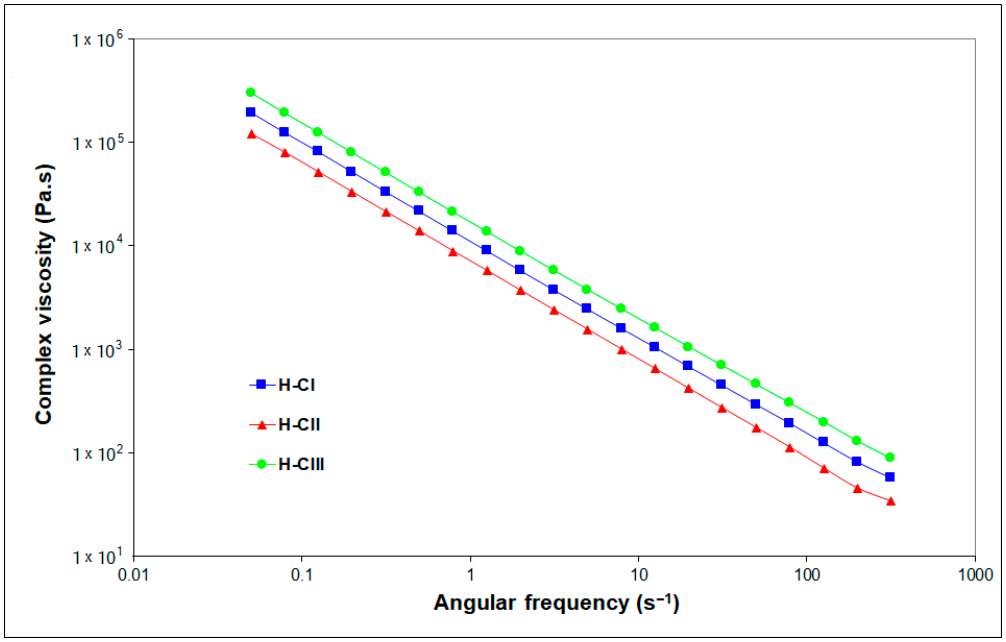

(**b**)

Figure 9. Frequency sweep tests results of hydrogels: (**a**) the dependence of the storage modulus G′ (solid symbols) and loss modulus G″ (open symbols) on the angular frequency; (**b**) the dependence of the complex viscosity on the angular frequency.

All values, especially for G′, are almost independent of the tested angular frequency, proving that the hydrogels display an excellent structured three-dimensional (3D) network,

and the applied deformation does not affect the stability of the studied hydrogels' network structure. The absence of a crossover frequency indicates permanent chemical cross-linking.

The graph shown in Figure 9a reveals that the structure of H-CII is softer, with a lower resistance of the hydrogel (G′) over the tested oscillation frequencies compared with H-CIII, but its stable structure is maintained. At higher angular frequencies (over 100 s^{-1}), the loss (viscous) moduli increase, although not overlapping the storage moduli, maintains the gel-like behavior up to 500 s^{-1}, the highest tested angular frequency.

The hydrogel corresponding to cellulose allomorph III (H-CIII) exhibits a higher storage and loss modulus than hydrogels H-CI and H-CII, showing a stronger and stiffer structure. This mechanical feature is translated also into a higher curve of complex viscosity for H-CIII (Figure 9b). The complex dynamic viscosity decreases with the increasing oscillation frequency for all the evaluated cellulose-based hydrogels.

All the rheological results are in good correlation with the SEM and XRD data and with those obtained for the swelling ability of the hydrogels.

2.5. ATR-FTIR Analysis of the Cellulose Allomorphs and Cellulose-Based Hydrogels

ATR-FTIR spectroscopy was used in order to prove the achievement of the cross-linking reaction between cellulose and EPC, this being a highly effective analytical tool for the evaluation of the surface chemical composition of materials.

The ATR-FTIR spectra of the hydrogels (H-CI, H-CII, and H-CIII) compared with their corresponding cellulose allomorphs (CI, CII, and CIII) are shown in Figure 10.

The spectral modification in the region 1500–800 cm^{-1} is assigned to an alteration of the crystalline structure of cellulose, following the alkaline treatment and, implicitly, the chemical cross-linking of cellulose with ECH [50]. In addition, it can be observed that the band at 1636 cm^{-1}, characteristic of the adsorbed water [51], is more intense in the hydrogel spectra. This observation reflects the higher hydrophilic character of the hydrogels in comparison with their corresponding cellulose allomorphs.

The difference spectrum [H-C_i – C_i] has been calculated in order to highlight the spectral changes resulting from chemical cross-linking (top spectra in Figure 10).

All the three allomorphic forms of cellulose present the decrease of the bands at:

- 994–980 cm^{-1} (ν(CO) at C6) with the counterpart at 3437 cm^{-1} (O2-H···O6 intramolecular H-bonds);
- 1054 cm^{-1} (ν(CO) at C3), 3339 cm^{-1} (O3-H···O5 intramolecular H-bonds), and 3301 cm^{-1} (O6-H···O3′ intermolecular H-bonds);
- 1106 cm^{-1} (ν(CO) at C2) and 3296 cm^{-1} (coupled vibrations of O2-H···O6 and O3-H···O5 intramolecular H-bonds) [51–54].

These changes show that in all three hydrogels, the chemical crosslinking of cellulose with ECH takes place mainly at the secondary alcohol C2 and the primary alcohol C6 and less at the secondary alcohol C3. The same observations were also confirmed by other authors [38,55].

This finding can be explained by the fact that Na^+ breaks the intermolecular hydrogen bonds O2-H···O6′ and that the most probable location of the Na^+ ion is at C2, thus facilitating the realization of the cross-linking reaction on this site [56–59]. In addition, many studies show that C3 carbon is the most resistant to complexation with NaOH [30], which is also observed in our case.

In the case of CI, the large band at 1102 cm^{-1} indicates that the secondary alcohols C2 contributed to the formation of ether-based cross-links. Besides the very clear ν(O2-H···O6) peak at 3437 cm^{-1}, the initial CII cellulose had an additional peak at 3480 cm^{-1}, which belongs to ν(O6-H) weakly H-bonded and to some –OH groups located in the interface and surface regions of crystallites [60]. The disappearance of both peaks upon crosslinking certifies the formation of ether-based linkage in the less organized regions first and also attests to the disruption of intermolecular hydrogen bonds (O6-H···O3′). In the case of H-CIII, the intense negative band at 1160 cm^{-1}, characteristic of ν(COC) of glycosidic

linkage, shows that the network formed through cross-linking reaction has decreased its degrees of freedom.

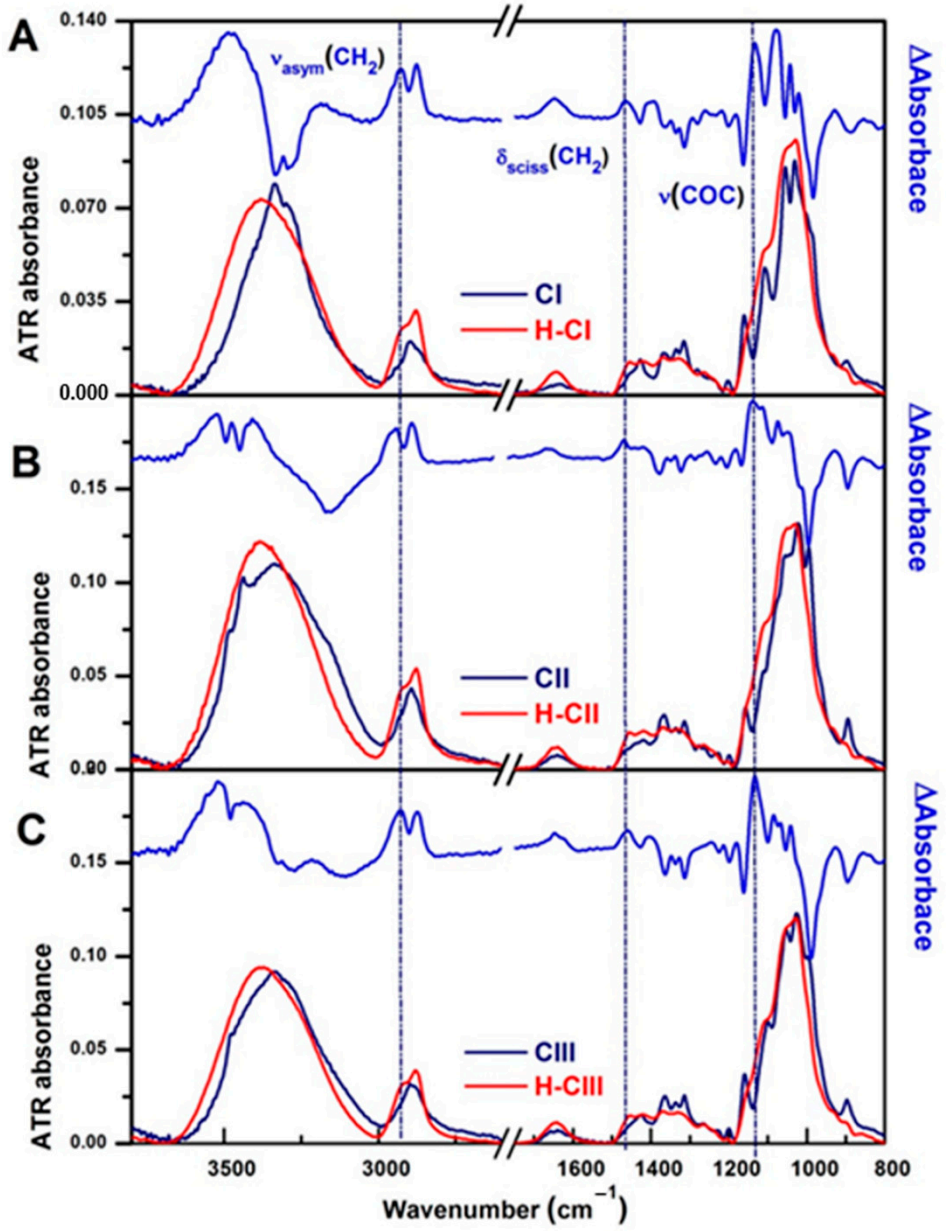

Figure 10. ATR-FTIR spectra comparison of cellulose allomorphs (dark blue line) with those of their corresponding hydrogels (red line): (**A**) CI and H-CI, (**B**) CII and H-CII, and (**C**) CIII and H-CIII. The difference spectrum [H-Ci – Ci] is added to the top of each figure (blue line). The vertical dotted lines mark the position of the characteristic bands of the chemical cross-linking of cellulose with ECH.

In the spectra of the three hydrogels, H-CI, H-CII, and H-CIII, the chemical crosslinking of cellulose with ECH is highlighted by the formation of new bands at 2930 and 2873 $cm^{-1,}$ assigned to $\nu_{asym}(CH_2)$ and $\nu_{sym}(CH_2)$; at 1458 $cm^{-1,}$ given by the $\delta_{sciss}(CH_2)$, and at 1133 $cm^{-1,}$ assigned to ν(COC) of the ether linkages [61].

Because the FTIR spectra of the three hydrogels are very similar and the ν(OH) vibration has the same position and profile in the all three spectra (~3380 cm^{-1}), the network ultimately has the same structure irrespective of the type and number of alcohol groups involved.

3. Conclusions

Cellulose-based hydrogels were prepared from three allomorphic forms of cellulose (CI, CII and CIII) starting from a gel stage, within their dissolution process in NaOH-water system, followed by the chemical cross-linking with ECH. Several correlations have been established by means of the swelling behavior, XRD, SEM, ATR-FTIR, and rheological measurements.

SEM investigations evidenced 3D networks with dissimilar morphologies and homogeneities, depending on each cellulose allomorph, as well as a close correlation between the type of cellulosic allomorph, swelling degree, and morphology of the porous structure.

The method of hydrogel synthesis proceeds with a major impairment of the crystalline organization, even if the dissolution process is partial, being limited only to the swelling phase. All hydrogels prepared regardless of the starting allomorph led to essentially the same supramolecular organization, specific to mostly amorphous cellulose.

The gel stage in the synthesis of hydrogels from cellulose allomorphs plays a key role in obtaining hydrogels with different performances. By swelling in NaOH solutions, at a low temperature, cellulose allomorphs led to gels with different strengths and rheological characteristics. By mixing with the cross-linking agent in identical shear regimes, the cellulose-NaOH gels were fractured into fragments of sizes correlated with the strength of the gels. The result was a hydrogel with a high cross-linking density, if the gel fragments were small in size and with a lower cross-linking density, in the case of resistant gels that fractured into large fragments.

It has been shown that in order to prepare hydrogels with higher characteristics than those obtained from CI, by the method used in this study, a previous conversion of CI to the CII allomorph is necessary. By swelling in NaOH-water, at low temperatures, CII leads to denser gels, which are more difficult to fragment and, implicitly, to less cross-linked hydrogels (H-CII), which have superior swelling capacity. In the case of the CIII allomorph, the obtained hydrogels (H-CIII) demonstrated inferior swelling characteristics to those of native cellulose (H-CI) but superior rheological and resistance properties.

In conclusion, some of the most important features of these hydrogels (controlled porosity and swelling degree) can be tailored by using a certain type of cellulose allomorph (C I, CII or CIII), in order to fulfill a certain set of characteristics requested by a given application (wound dressing or tissue engineering).

4. Materials and Methods

4.1. Materials

Cellulose I (CI), the microcrystalline cellulose, was purchased by Sigma-Aldrich (Saint Louis, MO, US) under the trade name of Avicel PH-101. The cross-linking agent, epichlorohydrin (ECH), was purchased from Merck (Hohenbrunn, Germany) and was used without further purification. Sodium hydroxide (NaOH) in pellets, with a purity $\geq$ 97%, was supplied by Merck (Hohenbrunn, Germany).

4.2. Preparation of Cellulose Allomorphs

Cellulose II (CII), mercerized cellulose, was prepared from cellulose I by soaking in a 17.5% NaOH solution for 24 h at 20 °C, followed by a rigorous rinsing with distilled water and drying in vacuum. Cellulose III (CIII) was prepared by soaking cellulose I in organic amine (100% ethylenediamine) for 24 h, at room temperature. The cellulose amine complex was washed with anhydrous methanol, and finally cellulose III samples were dried in vacuum.

4.3. Preparation of Cellulose Hydrogels

Hydrogels based on cellulose allomorphs were prepared by a patented procedure [62]. One g of cellulose was suspended in 26.9 mL of water, 2.5 g of NaOH was then added, and the mixture was shaken to dissolve the NaOH at room temperature, resulting in a suspension of the cellulose in an 8.5% NaOH solution. The suspension was cooled to −30 °C, up to a frozen solid, and held at that temperature 24 h. The frozen solid was then allowed to thaw at room

temperature and was transformed into a gel-like mass, and the epichlorohydrin was added under controlled stirring, for 10 min. The obtained composition was cross-linked for 6 h at 85 °C. The obtained hydrogels were washed several times with warm water in order to remove the excess of salts and any traces of the cross-linking agent from their structures. The obtained hydrogels were dried in a freeze-dryer and were coded like H-CI for the one obtained from cellulose I and, respectively, H-CII and H-CIII for those obtained from cellulose II and cellulose III.

4.4. Degrees of Polymerization

Degrees of polymerization of cellulose (DP) were measured by the viscosity method in 0.5 mol Cuen [63].

4.5. Swelling Behavior

The swelling studies of the hydrogels were performed by direct immersion in distilled water, at 37 °C. The hydrogels were periodically removed from the solution, gently wiped with a soft tissue in order to remove the excess surface solution, weighed, and then placed back into the vessel. The swelling degree (Q_{max}, %) of the hydrogels in distilled water was determined gravimetrically, using the following relation:

$$Q_{max}\ (\%) = \frac{m_t - m_0}{m_0} \times 100 \quad (1)$$

where m_t—the weight of the swelled hydrogel at time t; and m_0—the weight of dry hydrogel.

The equilibrium swelling degree (Q_{eq}, %) was determined for the never-dried hydrogels and was calculated by using the following equation:

$$Q_{eq}\ (\%) = \frac{m_\infty - m_0}{m_0} \times 100 \quad (2)$$

where: m_∞—the weight of the swelled hydrogel at equilibrium; and m_0—the weight of dry hydrogel.

To determine the kinetics of solvent diffusion into the matrices (swelling), the following equation was used [41]:

$$\frac{W_t}{W_{eq}} = k_{sw} \times t^{n_{sw}} \quad (3)$$

where W_t—the amount of water absorbed by the hydrogel at time t; W_{eq}—the amount of water absorbed by the hydrogel at equilibrium; k_{sw}—the swelling constant incorporating characteristics of the macromolecular network system (min^{-n}); and n_{sw}—the swelling diffusional exponent, which is indicative of the transport mechanism.

The constants n and k were calculated from the slopes and intercepts of the plots of ln (W_t/W_{eq}) vs. lnt. Equation (3) was applied in the early swelling stages (swelling degree less than 60%), and the linearity was observed.

4.6. X-ray Diffraction Analysis (XRD)

XRD investigations were performed by using a Bruker-AXS D8 ADVANCE (Bruker AXS GmbH, Karlsruhe, Germany) apparatus, having a transmission type goniometer based on Ni-filtered, Cu-Kα radiation at 40 kV. The goniometer was scanned stepwise every 10° from 10° to 40° within the 2θ range. The resulting diffraction patterns exhibited peaks that were deconvoluted from a background scattering by using Lorenzian functions, while the diffraction pattern of an artificially amorphized sample was approximated by a Gaussian functions curve fitting analysis [17,23]. The data were obtained using XRD Commander software (Bruker AXS GmbH, Karlsruhe, Germany) and were processed with

DIFFRAC.EVA V1.1 (Bruker AXS GmbH, Karlsruhe, Germany). The crystallinity index (CrI) was calculated by using the following equation [23]:

$$\text{CrI } (\%) = \frac{S_C}{S_C + S_A} \times 100 \quad (4)$$

where S_C and S_A are the surfaces of the crystalline and amorphous areas, respectively.

The crystallite sizes were measured from their respective XRD patterns by using the Scherrer equation [23]:

$$D_{hkl} = \frac{k \times \lambda}{\beta \times \cos\theta} \quad (5)$$

where D_{hkl} is the size of crystallite (nm), k is the Scherrer constant (0.94), λ is the X-ray wavelength (0.15418 nm), β is the full-width at half-maximum of the reflection *hkl*, and θ is the half of the 2θ value for the corresponding Bragg peak.

4.7. Scanning Electron Microscopy (SEM)

A thorough analysis of the internal morphology of the hydrogels was performed by using a scanning electron microscope Quanta 200 (FEI Company, Hillsboro, OR, USA) operating at 20 kV with secondary electrons, in low vacuum mode. SEM investigations were focused on the morphological properties of the hydrogels, including homogeneity, sample shape, surface changes, and porosity. The hydrogels samples were studied at various magnifications, with each magnification being mentioned additionally to the corresponding SEM micrograph.

4.8. Rheological Characterization

A stress-controlled Rheometer Physica MCR-301 (Anton Paar, Graz, Austria) has been used to investigate the rheological properties of cellulose allomorphs gels and their corresponding hydrogels. Specific oscillatory measurements were performed in dynamic mode using parallel plate geometry with 25 mm diameter and a 3 mm gap between the plates. Each swollen sample was placed on the lower plate, the upper plate was lowered to the desired gap height and the sample diameter was cut to fit the used plate geometry, removing the excess sample. In order to prevent the water evaporation, the rheological measurements were conducted at a constant temperature (25 ± 0.1 °C), and a special system for controlling temperature and evaporation was used. Oscillatory amplitude sweeps tests (strain between 0.001% and 100% at 10 rad/s) were carried out to determine the linear viscoelastic region (LVR) and to characterize the gels' microstructure and the fracture process of the gels. The viscoelastic properties of the cellulose-based hydrogels were investigated by frequency sweep tests in the frequency range from 0.05 to 500 s^{-1}, with a constant strain of 1%.

4.9. Attenuated Total Reflectance Fourier Transform Infrared (ATR-FTIR) Spectroscopy

A Vertex 70 spectrometer (Bruker, Hamburg, Germany) was used for the Fourier transform infrared (FTIR) spectra recording in the attenuated total reflection (ATR) configuration. All spectra were collected at 128 scans, at a 2 cm^{-1} resolution, in the mid IR range (4000–600 cm^{-1}). The OPUS 6.5 software was used for the FTIR data processing.

Author Contributions: Conceptualization, D.E.C. and F.C.; investigation—SEM, D.R.; investigation—rheology, R.N.D.-N.; investigation—XRD, D.T. and D.E.C.; writing—original draft preparation, D.E.C. and F.C.; writing—review and editing, D.E.C. and F.C.; and supervision, D.E.C. and F.C. All authors have read and agreed to the published version of the manuscript.

Funding: This research received no external funding.

Institutional Review Board Statement: Not applicable.

Informed Consent Statement: Not applicable.

Data Availability Statement: Not applicable.

Acknowledgments: Mihaela Iuliana Avadanei, affiliated to "Petru Poni" Institute of Macromolecular Chemistry, Iasi, Romania is acknowledged for ATR-FTIR spectroscopy investigations.

Conflicts of Interest: The authors declare no conflict of interest.

References

1. Ho, T.-C.; Chang, C.-C.; Chan, H.-P.; Chung, T.-W.; Shu, C.-W.; Chuang, K.-P.; Duh, T.-H.; Yang, M.-H.; Tyan, Y.-C. Hydrogels: Properties and Applications in Biomedicine. *Molecules* **2022**, *27*, 2902. [CrossRef]
2. Zainal, S.H.; Mohd, N.H.; Suhaili, N.; Anuar, F.H.; Lazim, A.M.; Othaman, R. Preparation of cellulose-based hydrogel: A review. *J. Mater. Res. Technol.* **2021**, *10*, 935–952. [CrossRef]
3. Gebeyehu, E.K.; Sui, X.; Adamu, B.F.; Beyene, K.A.; Tadesse, M.G. Cellulosic-based conductive hydrogels for electro-active tissues: A review summary. *Gels* **2022**, *8*, 140. [CrossRef]
4. Rizwan, M.; Yahya, R.; Hassan, A.; Yar, M.; Azzahari, A.D.; Selvanathan, V.; Sonsudin, F.; Abouloula, C.N. pH sensitive hydrogels in drug delivery: Brief history, properties, swelling, and release mechanism, material selection and applications. *Polymers* **2017**, *9*, 137. [CrossRef] [PubMed]
5. Zhu, T.; Mao, J.; Cheng, Y.; Liu, H.; Lv, L.; Ge, M.; Li, S.; Huang, J.; Chen, Z.; Li, H.; et al. Recent progress of polysaccharide-based hydrogel interfaces for wound healing and tissue engineering. *Adv. Mater. Interfaces* **2019**, *6*, 1900761. [CrossRef]
6. Mantha, S.; Pillai, S.; Khayambashi, P.; Upadhyay, A.; Zhang, Y.; Tao, O.; Pham, H.M.; Tran, S.D. Smart hydrogels in tissue engineering and regenerative medicine. *Materials* **2019**, *12*, 3323. [CrossRef]
7. Kabir, S.M.F.; Sikdar, P.P.; Haque, B.; Bhuiyan, M.A.R.; Ali, A.; Islam, M.N. Cellulose-based hydrogel materials: Chemistry, properties and their prospective applications. *Prog. Biomater.* **2018**, *7*, 153–174. [CrossRef]
8. Loo, S.L.; Vásquez, L.; Athanassiou, A.; Fragouli, D. Polymeric Hydrogels—A promising platform in enhancing water security for a sustainable future. *Adv. Mater. Interfaces* **2021**, *8*, 2100580. [CrossRef]
9. Ciolacu, D.E.; Nicu, R.; Ciolacu, F. Cellulose-based hydrogels as sustained drug-delivery systems. *Materials* **2020**, *13*, 5270. [CrossRef]
10. Hoare, T.R.; Kohane, D.S. Hydrogels in drug delivery: Progress and challenges. *Polymer* **2008**, *49*, 1993–2007. [CrossRef]
11. Kwiecień, I.; Kwiecień, M. Application of polysaccharide-based hydrogels as probiotic delivery systems. *Gels* **2018**, *4*, 47. [CrossRef]
12. Rusu, D.; Ciolacu, D.; Simionescu, B.C. Cellulose-based hydrogels in tissue engineering applications. *Cellul. Chem. Technol.* **2019**, *53*, 907–923. [CrossRef]
13. Gomez-Florit, M.; Pardo, A.; Domingues, R.M.A.; Graça, A.L.; Babo, P.S.; Reis, R.L.; Gomes, M.E. Natural-based hydrogels for tissue engineering applications. *Molecules* **2020**, *25*, 5858. [CrossRef] [PubMed]
14. Ciolacu, D.E.; Nicu, R.; Ciolacu, F. Natural polymers in heart valve tissue engineering: Strategies, advances and challenges. *Biomedicines* **2022**, *10*, 1095. [CrossRef] [PubMed]
15. Kundu, R.; Mahada, P.; Chhirang, B.; Das, B. Cellulose hydrogels: Green and sustainable soft biomaterials. *Curr. Res. Green Sustain. Chem.* **2022**, *5*, 100252. [CrossRef]
16. Onofrei, M.D.; Filimon, A. Cellulose-based hydrogels: Designing concepts, properties, and perspectives for biomedical and environmental applications. In *Polymer Science: Research Advances, Practical Applications and Educational Aspects*; Méndez-Vilas, A., Martín, A.S., Eds.; Formatex Research Center: Badajoz, Spain, 2016; pp. 108–120.
17. Ciolacu, D.; Pitol-Filho, L.; Ciolacu, F. Studies concerning the accessibility of different allomorphic forms of cellulose. *Cellulose* **2012**, *19*, 55–68. [CrossRef]
18. Wohlert, M.; Benselfelt, T.; Wågberg, L.; Furó, I.; Berglund, L.A.; Wohlert, J. Cellulose and the role of hydrogen bonds: Not in charge of everything. *Cellulose* **2022**, *29*, 1–23. [CrossRef]
19. Gautam, S.P.; Bundela, P.S.; Pandey, A.K.; Jamaluddin; Awasthi, M.K.; Sarsaiya, S. A review on systematic study of cellulose. *J. Appl. Nat. Sci.* **2010**, *2*, 330–343. [CrossRef]
20. Chiriac, A.I.; Pastor, F.I.J.; Popa, V.I.; Aflori, M.; Ciolacu, D. The influence of supramolecular structure of cellulose allomorphs on the interactions with cellulose-binding domain, CBD3b from *Paenibacillus barcinonensis*. *Cellulose* **2014**, *21*, 203–219. [CrossRef]
21. Mukarakate, C.; Mittal, A.; Ciesielski, P.N.; Budhi, S.; Thompson, L.; Iisa, K.; Nimlos, M.R.; Donohoe, B.S. Influence of crystal allomorph and crystallinity on the products and behavior of cellulose during fast pyrolysis. *ACS Sustain. Chem. Eng.* **2016**, *4*, 4662–4674. [CrossRef]
22. Ciolacu, D.; Ciolacu, F.; Dumitriu, R.; Vasile, C.; Popa, V.I. Kinetics aspects in the enzymatic hydrolysis of cellulose allomorphs. *Cellulose Chem. Technol.* **2007**, *41*, 37–42.
23. Ciolacu, D.; Gorgieva, S.; Tampu, D.; Kokol, V. Enzymatic hydrolysis of different allomorphic forms of microcrystalline cellulose. *Cellulose* **2011**, *18*, 1527–1541. [CrossRef]
24. Wu, Q.; Xu, J.; Zhu, S.; Kuang, Y.; Wang, B.; Gao, W. Crystalline stability of cellulose III nanocrystals in the hydrothermal treatment and NaOH solution. *Carbohydr. Polym.* **2020**, *249*, 116827. [CrossRef] [PubMed]
25. Klemm, D.; Heublein, B.; Fink, H.P.; Bohn, A. Cellulose: Fascinating biopolymer and sustainable raw material. *Angew. Chem. Int. Ed. Engl.* **2005**, *44*, 3358–3393. [CrossRef] [PubMed]

26. Seddiqi, H.; Oliaei, E.; Honarkar, H.; Jin, J.; Geonzon, L.C.; Bacabac, R.G.; Klein-Nulend, J. Cellulose and its derivatives: Towards biomedical applications. *Cellulose* **2021**, *28*, 1893–1931. [CrossRef]
27. Korhonen, O.; Sawada, D.; Budtova, T. All-cellulose composites via short-fiber dispersion approach using NaOH–water solvent. *Cellulose* **2019**, *26*, 4881–4893. [CrossRef]
28. Lindman, B.; Medronho, B.; Alves, L.; Costa, C.; Edlund, H.; Norgren, M. The relevance of structural features of cellulose and its interactions to dissolution, regeneration, gelation and plasticization phenomena. *Phys. Chem. Chem. Phys.* **2017**, *19*, 23704–23718. [CrossRef]
29. Liebert, T. Cellulose solvents—Remarkable history, bright future. In *Cellulose Solvents: For Analysis, Shaping and Chemical Modification*, 1st ed.; Liebert, T.F., Heinze, T.J., Edgar, K.J., Eds.; ACS Symposium Series; American Chemical Society: Washington, DC, USA, 2010; chapter 1; pp. 3–54.
30. Budtova, T.; Navard, P. Cellulose in NaOH–water based solvents: A review. *Cellulose* **2016**, *23*, 5–55. [CrossRef]
31. Shuai, J.; Wang, X. Novel solvent systems for cellulose dissolution. *BioResources* **2020**, *16*, 2192–2195. [CrossRef]
32. Acharya, S.; Liyanage, S.; Parajuli, P.; Rumi, S.S.; Shamshina, J.L.; Abidi, N. Utilization of cellulose to its full potential: A review on cellulose dissolution, regeneration, and applications. *Polymers* **2021**, *13*, 4344. [CrossRef]
33. Kihlman, M.; Medronho, B.F.; Romano, A.L.; Germgård, U.; Lindman, B. Cellulose dissolution in an alkali based solvent: Influence of additives and pretreatments. *J. Braz. Chem. Soc.* **2013**, *24*, 295–303. [CrossRef]
34. Wang, Y.; Deng, Y. The kinetics of cellulose dissolution in sodium hydroxide solution at low temperature. *Biotechnol. Bioeng.* **2009**, *102*, 1398–1405. [CrossRef] [PubMed]
35. Cai, J.; Zhang, L.; Liu, S.; Liu, Y.; Xu, X.; Chen, X.; Chu, B.; Guo, X.; Xu, J.; Cheng, H.; et al. Dynamic self-assembly induced rapid dissolution of cellulose at low temperatures. *Macromolecules* **2008**, *41*, 9345–9351. [CrossRef]
36. Roy, C.; Budtova, T.; Navard, P.; Bedue, O. Structure of cellulose–soda solutions at low temperatures. *Biomacromolecules* **2001**, *2*, 687–693. [CrossRef]
37. Egal, M.; Budtova, T.; Navard, P. Structure of aqueous solutions of microcrystalline cellulose/sodium hydroxide below 0 °C and the limit of cellulose dissolution. *Biomacromolecules* **2007**, *8*, 2282–2287. [CrossRef]
38. Ciolacu, D.; Rudaz, C.; Vasilescu, M.; Budtova, T. Physically and chemically cross-linked cellulose cryogels: Structure, properties and application for controlled release. *Carbohydr. Polym.* **2016**, *151*, 392–400. [CrossRef]
39. Isogai, A.; Atalla, R.H. Dissolution of Cellulose in Aqueous NaOH Solutions. *Cellulose* **1998**, *5*, 309–319. [CrossRef]
40. Peppas, N.A.; Franson, N.M. The swelling interface number as a criterion for prediction of diffusional solute release mechanisms in swellable polymers. *J. Polym. Sci. Pol. Phys.* **1983**, *21*, 983–997. [CrossRef]
41. Ritger, P.L.; Peppas, N.A. A simple equation for description of solute release. II Fickian and anomalous release from swellable devices. *J. Control Release* **1987**, *5*, 37–42. [CrossRef]
42. Bartil, T.; Bounekhel, M.; Cedric, C.; Jerome, R. Swelling behavior and release properties of pH-sensitive hydrogels based on methacrylic derivatives. *Acta Pharm.* **2007**, *57*, 301–314. [CrossRef]
43. Ostrowska-Czubenko, J.; Gierszewska, M.; Pieróg, M. pH-responsive hydrogel membranes based on modified chitosan: Water transport and kinetics of swelling. *J. Polym. Res.* **2015**, *22*, 1–12. [CrossRef]
44. Gierszewska-Drużyńska, M.; Ostrowska-Czubenko, J. Mechanism of water diffusion into noncrosslinked and ionically crosslinked chitosan membranes. *Prog. Chem. Appl. Chitin Deriv.* **2012**, *17*, 59–66.
45. Poletto, M.; Ornaghi Júnior, H.L.; Zattera, A.J. Native Cellulose: Structure, characterization and thermal properties, materials. *Materials* **2014**, *7*, 6105–6119. [CrossRef] [PubMed]
46. Kim, U.J.; Eom, S.H.; Wada, M. Thermal decomposition of native cel-lulose: Influence on crystallite size. *Polym. Degrad. Stab.* **2010**, *95*, 778–781. [CrossRef]
47. Mezger, T.G. *The Rheology Handbook*, 3rd ed.; Vincentz Network: Hanover, Germany, 2011; pp. 171–173.
48. Available online: https://wiki.anton-paar.com/en/amplitude-sweeps/ (accessed on 16 May 2022).
49. Mendoza, L.; Batchelor, W.; Tabor, R.F.; Garnier, G. Gelation mechanism of cellulose nanofibre gels: A colloids and interfacial perspective. *J. Colloid Interface Sci.* **2018**, *509*, 39–46. [CrossRef]
50. Navarra, M.A.; Dal Bosco, C.; Moreno, J.S.; Vitucci, F.M.; Paolone, A.; Panero, S. Synthesis and characterization of cellulose-based hydrogels to be used as gel electrolytes. *Membranes* **2015**, *5*, 810–823. [CrossRef]
51. Oh, S.Y.; Yoo, D.I.; Shin, Y.; Seo, G. FTIR analysis of cellulose treated with sodium hydroxide and carbon dioxide. *Carbohydr. Res.* **2005**, *340*, 417–428. [CrossRef]
52. Oh, S.Y.; Yoo, D.I.; Shin, Y.; Kim, H.C.; Kim, H.Y.; Chung, Y.S.; Park, W.H.; Youk, J.H. Crystalline structure analysis of cellulose treated with sodium hydroxide and carbon dioxide by means of X-ray diffraction and FTIR spectroscopy. *Carbohydr. Res.* **2005**, *340*, 2376–2391. [CrossRef]
53. Marechal, Y.; Chanzy, H. The hydrogen bond network in Iβ cellulose as observed by infrared spectrometry. *J. Molec. Struct.* **2000**, *523*, 183–196. [CrossRef]
54. Watanabe, A.; Morita, S.; Ozaki, Y. Study on temperature-dependent changes in hydrogen bonds in cellulose Iβ by infrared spectroscopy with perturbation-correlation moving-window two-dimensional correlation spectroscopy. *Biomacromolecules* **2006**, *7*, 3164–3170. [CrossRef]
55. Udoetok, I.A.; Dimmick, R.M.; Wilson, L.D.; Headley, J.V. Adsorption properties of cross-linked cellulose-epichlorohydrin polymers in aqueous solution. *Carbohydr. Polym.* **2016**, *136*, 329–340. [CrossRef] [PubMed]

56. Nishimura, H.; Sarko, A. Mercerization of cellulose. 6. Crystal and molecular structure of Na–cellulose IV. *Macromolecules* **1991**, *24*, 771–778. [CrossRef]
57. Takahashi, M.; Ookubo, M.; Takena, H. Solid state ^{13}C NMR spectra analysis of alkalicellulose. *Polym. J.* **1991**, *23*, 1009–1014. [CrossRef]
58. Fink, H.P.; Walenta, E.; Kunze, J.; Mann, G. Wide angle X-ray and solid state C-NMR studies of cellulose alkalisation. In *Cellulose and cellulose derivatives: Physico-chemical aspects and industrial applications*; Kennedy, J.F., Phillips, G.O., Williams, P.A., Eds.; Woodhead Publishing: Cambridge, UK, 1995; Chapter 66; pp. 523–528.
59. Isogai, A. NMR analysis of cellulose dissolved in aqueous NaOH solutions. *Cellulose* **1997**, *4*, 99–107. [CrossRef]
60. Lee, C.M.; Kubicki, J.D.; Fan, B.; Zhong, L.; Jarvis, M.C.; Kim, S.H. Hydrogen-bonding network and OH stretch vibration of cellulose: Comparison of computational modeling with polarized IR and SFG spectra. *J. Phys. Chem. B* **2015**, *119*, 15138–15149. [CrossRef]
61. Socrates, G. *Infrared and Raman Characteristic Group Frequencies: Tables and Charts*, 3rd ed.; Wiley: Chichester, UK, 2004.
62. Ciolacu, D.E. Process for producing an absorbent material based on cellulose. Patent RO122780; State Office for Inventions and Trademarks (OSIM), Romania, 29 January 2010.
63. *Tappi T230 om-19, Viscosity of Pulp the Partent Owner Is State Office for Inventions and Trademarks (OSIM), Romania. (Capillary Viscometer Method)*; TAPPI Press: Atlanta, GA, USA, 2019.

International Journal of
Molecular Sciences

MDPI

Article

3D Matrices for Enhanced Encapsulation and Controlled Release of Anti-Inflammatory Bioactive Compounds in Wound Healing

Raluca Nicu [1], Diana Elena Ciolacu [1,*], Anca-Roxana Petrovici [2], Daniela Rusu [3], Mihaela Avadanei [4], Andreea Cristina Mihaila [5], Elena Butoi [5] and Florin Ciolacu [6,*]

[1] Department of Natural Polymers, Bioactive and Biocompatible Materials, "Petru Poni" Institute of Macromolecular Chemistry, 700487 Iasi, Romania
[2] Center of Advanced Research in Bionanoconjugates and Biopolymers, "Petru Poni" Institute of Macromolecular Chemistry, 700487 Iasi, Romania
[3] Department of Physics of Polymers and Polymeric Materials, "Petru Poni" Institute of Macromolecular Chemistry, 700487 Iasi, Romania
[4] Department of Physical Chemistry of Polymers, "Petru Poni" Institute of Macromolecular Chemistry, 700487 Iasi, Romania
[5] Biopathology and Therapy of Inflammation, Institute of Cellular Biology and Pathology "Nicolae Simionescu", 050568 Bucuresti, Romania
[6] Department of Natural and Synthetic Polymers, "Gheorghe Asachi" Technical University of Iasi, 700050 Iasi, Romania
* Correspondence: dciolacu@icmpp.ro (D.E.C.); fciolacu@tuiasi.ro (F.C.); Tel.: +40-332-880-220 (D.E.C.); +40-232-278-683 (ext. 2200) (F.C.)

Abstract: Current trends in the development of wound dressings are oriented towards the use of biopolymer-based materials, due to their unique properties such as non-toxicity, hydrophilicity, biocompatibility and biodegradability, properties that have advantageous therapeutic characteristics. In this regard, the present study aims to develop hydrogels based on cellulose and dextran (CD) and to reveal their anti-inflammatory performance. This purpose is achieved by incorporating plant bioactive polyphenols (PFs) in CD hydrogels. The assessments include establishing the structural characteristics using attenuated total reflection Fourier transformed infrared (ATR-FTIR) spectroscopy, the morphology by scanning electron microscopy (SEM), the swelling degree of hydrogels, the PFs incorporation/release kinetics and the hydrogels' cytotoxicity, together with evaluation of the anti-inflammatory properties of PFs-loaded hydrogels. The results show that the presence of dextran has a positive impact on the hydrogel's structure by decreasing the pore size at the same time as increasing the uniformity and interconnectivity of the pores. In addition, there is an increased degree of swelling and of the encapsulation capacity of PFs, with the increase of the dextran content in hydrogels. The kinetics of PFs released by hydrogels was studied according to the Korsmeyer–Peppas model, and it was observed that the transport mechanisms depend on hydrogels' composition and morphology. Furthermore, CD hydrogels have been shown to promote cell proliferation without cytotoxicity, by successfully culturing fibroblasts and endothelial cells on CD hydrogels (over 80% viability). The anti-inflammatory tests performed in the presence of lipopolysaccharides demonstrate the anti-inflammatory properties of the PFs-loaded hydrogels. All these results provide conclusive evidence on the acceleration of wound healing by inhibiting the inflammation process and support the use of these hydrogels encapsulated with PFs in wound healing applications.

Keywords: cellulose; dextran; polyphenols; hydrogels; controlled release; wound healing

Citation: Nicu, R.; Ciolacu, D.E.; Petrovici, A.-R.; Rusu, D.; Avadanei, M.; Mihaila, A.C.; Butoi, E.; Ciolacu, F. 3D Matrices for Enhanced Encapsulation and Controlled Release of Anti-Inflammatory Bioactive Compounds in Wound Healing. *Int. J. Mol. Sci.* **2023**, *24*, 4213. https://doi.org/10.3390/ijms24044213

Academic Editor: Shujun Li

Received: 20 January 2023
Revised: 13 February 2023
Accepted: 17 February 2023
Published: 20 February 2023

1. Introduction

Wound healing consists of four partially overlapping stages, namely hemostasis, inflammation, proliferation, and remodeling, which determine whether the wound will

heal normally or will undergo an aberrant healing process that will finally lead to fibrosis [1]. Thus, the inflammation is one of the key stages of the wound healing process, extending over a period of 3 to 7 days. Its rigorous control is crucial so that this process does not become pathogenic, with bacterial colonization and excessive formation of pathological scar tissue [2].

For this reason, the choice of an appropriate dressing for wounds is of crucial importance, and it must present some special characteristics, such as: (i) an adequate water retention, to be able to absorb exudates; (ii) adequate mechanical stability to support skin lesions; (iii) resistance to breaking; (iv) antibacterial properties, to prevent biofilm formation, and (v) promoting healing, by releasing a long-term drug and growth factors [3]. Thus, the role of wound dressings is to cover, clean and protect the wound from the external environment.

Among the wound dressings, hydrogel dressings have become the main focus in wound healing research, because they can maintain a moist environment at the wound interface, allow gaseous exchange, act as a barrier against the invasion and proliferation of microorganisms, remove excess exudates, have excellent biocompatibility and be easily removed without trauma [4,5]. By incorporating different anti-inflammatory agents, they can also demonstrate anti-inflammatory capabilities [6].

In recent decades, research has focused on wound-healing applications of hydrogels based on natural polymers, because these are abundantly available and inexpensive, and are considered to have great potential for large-scale production. However, in many cases, the use of a single type of natural polymer cannot meet the various requirements of an ideal wound dressing, and therefore binary, ternary or multicomponent polymeric mixtures, that have synergistic interactions, are generally used [7–10].

In the present study, an attempt was made to develop a binary mixture of polysaccharides, using cellulose and dextran. These polysaccharides are both composed of D-glucose units, but differs in the way the units are arranged and connected by linear and side-chain links (Figure 1) [11,12].

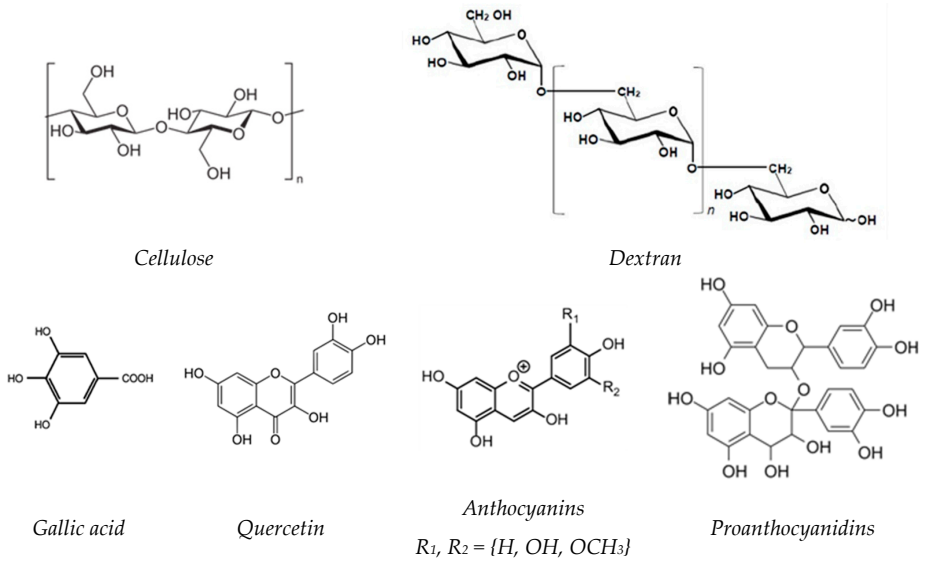

Figure 1. Chemical structure of cellulose, dextran and the major phenolic compounds identified in grape seeds.

Cellulose-based hydrogels are especially distinguished by their excellent mechanical properties and thermal stability, while dextran-based hydrogels are highly hydrophilic and have a great ability to support cell adhesion and proliferation, but exhibit poor mechanical properties [13–18]. Thus, the combination of the unique properties of these two polysaccharide-based hydrogels can result in obtaining a perfect wound dressing material.

In the literature, there are only a few studies related to the hydrogels based on cellulose and dextran, and these refer either to (i) dextran and bacterial cellulose (BC) [5], or to (ii) dextran sulfate (DS) and carboxymethyl cellulose (CMC) [19], (iii) amino dextran and CMC [20] and (iv) cellulose nanocrystals (CNC), oxidized dextran and gelatin [21]. The performance in wound healing applications of the dextran/BC hydrogel reveals that the addition of dextran affected the network structure of BC, resulting in the decrease of the water content; cell-based experiments showed that these hydrogels promoted enhanced cell proliferation, without cytotoxicity compared to unmodified BC, while in vivo wound healing tests demonstrated that the hydrogels can accelerate the wound healing process [5]. Hydrogel composite beads based on CMC and DS were prepared using ionotropic gelation, in presence of sodium n-dodecyl sulfate. By increasing the DS content, a remarkably improvement of the adsorption performances was observed, as well as a good reusability after five adsorption/desorption cycles [19]. Another example of composite hydrogel is that obtained by conjugation of CMC with amino dextran (DEX), in order to formulate piroxicam loaded CMC-DEX hydrogels for topical application. The entrapment efficiency was observed as being 87.36 ± 1.23% for CMC-DEX and 72.35 ± 2.35% in the case of CMC hydrogels, respectively. The piroxicam deposited from CMC hydrogels was 15.61 ± 1.5 mg/mL (epidermis) and 6.24 ± 1.2% (dermis) in 12 h, while in the case of CMC-DEX hydrogels, the piroxicam retention was 5.21 ± 1.19 mg/mL (epidermis) and 26.34 ± 0.5 mg/mL (dermis), in 12 h. This fact proved that when there was a cross-linking reaction between DEX and CMC, it increased the penetration of piroxicam [20]. The hydrogels obtained from cellulose nanocrystals (CNC), oxidized dextran and gelatin were fabricated by 3D printing [21].

No study has reported the preparation of chemically cross-linked hydrogels based on cellulose and dextran by a two-step method, dissolution in alkaline solutions followed by cross-linking in the presence of epichlorohydrin.

Numerous pharmacological agents can significantly reduce or completely inhibit the inflammation process, thus promoting wound healing [22,23].

In the last few years, there has been a growing interest in compounds from natural sources with anti-inflammatory properties, among them polyphenols (PFs) which have attracted significant attention. PFs are a large group of organic compounds distributed in various plants and marine organisms, covering a wide range of complex structures (Figure 1) [24,25]. They are classified according to their chemical structures into flavonoids such as flavones, flavonols, isoflavones, neoflavonoids, chalcones, anthocyanidins, and proanthocyanidins and non-flavonoids, such as phenolic acids, stilbenoids and phenolic amides [26].

PFs have been the subject of numerous studies, being tested for their unique antioxidant [27,28] and anti-inflammatory properties [26,29,30]. The ability of these PFs to modify the expression of several pro-inflammatory genes including those encoding cytokines, lipoxygenase, nitric oxide synthases cyclooxygenase, in addition to their antioxidant characteristics, such as reactive oxygen species scavenging (ROS), contributes to the regulation of inflammatory signaling [26]. Moreover, the incorporation of these polyphenolic compounds as therapeutic agents in wound dressings makes it possible to repair wounds faster and better [27,31].

In this regard, the present study aims to prepare new 3D matrices based on cellulose and dextran with anti-inflammatory activity, capable of encapsulation/controlled release of PFs, considering the applications in wound healing. Lipopolysaccharides (LPS), the major component of Gram-negative bacteria cell walls that can cause an acute inflammatory response, were used as a pro-inflammatory model to reveal the protective mechanism of PFs in LPS-induced inflammation.

2. Results and Discussion

2.1. Swelling Behavior of Hydrogels

One of the most important characteristics of hydrogels is the degree of swelling because all the other properties of hydrogels are related to this value. The hydrogel's

polymeric network can absorb 10 to 1000 times its dry weight in water, due to the hydration of the hydrophilic groups and the penetration of the water molecules into the pores of the 3D matrices [32].

In our particular case, the equilibrium swelling degree (Q_{eq}, %) of never-dried hydrogels varies from 1640% for cellulose hydrogels (C) up to 5310% for dextran hydrogel (D). Regarding the cellulose-dextran (CD) hydrogels it was observed that even by adding the lowest dextran content (CD75/25 hydrogel, namely, a dextran content of 25%) there was almost a doubling of the swelling degree compared to C hydrogel (more precisely, from 1640% to 2980%). The swelling degrees of CD hydrogels gradually increase with the increase of the dextran content in the 3D network, but not higher than that of the D hydrogel. The Q_{eq} data obtained for CD hydrogels demonstrate their superabsorbent character.

The composition and Q_{eq} of the hydrogels, as well as the gel fraction yield are presented in Table 1.

Table 1. The composition of cellulose-dextran hydrogels and their main features.

Samples	Hydrogels Composition		Hydrogels Features	
	Cellulose, %	Dextran, %	Gel Fraction Yield, %	Q_{eq}, %
C	100	0	99.9	1640
CD75/25	75	25	99.9	2980
CD63/37	63	37	95.2	3530
CD50/50	50	50	90.4	4430
CD37/63	37	63	87.8	4460
CD25/75	25	75	84.9	4520
D	0	100	76.3	5310

The maximum swelling degree (Q_{max}, %) of the freeze-dried hydrogels increases from approximately 1060% for C hydrogel up to 3740% for D hydrogel (Table 2). For the other five CD hydrogel formulations, which contain different proportions of cellulose and dextran, Q_{max} is between 1485 and 2367%, with the observation that it increases with the increase of the dextran content in the hydrogels' matrix.

Table 2. Swelling kinetic parameters for different hydrogel formulations.

Samples	Swelling Kinetic Parameters			Q_{max}, %
	n_{sw}	k_{sw}	R^2	
C	0.192	0.712	0.993	1064
CD 75/25	0.079	0.544	0.995	1485
CD 63/37	0.087	0.436	0.997	1363
CD 50/50	0.183	0.869	0.999	1607
CD 37/63	0.205	1.226	0.997	1873
CD 25/75	0.269	1.417	0.992	2367
D	0.369	2.207	0.993	3745

The evolution in time of the Q_{max} of the C, D and CD hydrogels, as a function of composition, is presented in Figure 2.

As a general observation for all hydrogels, there was a sharp increase of Q_{max} at the beginning of the swelling process, after which the increase continued until reaching a plateau. This behavior depends on the hydrogel's composition, more exactly on the content of dextran in the 3D matrix. Thus, if the equilibrium appears quite quickly in the case of C hydrogel, approximately 20 min, the time to reach the Q_{max} increased with increasing of the content of dextran in the matrix. Unlike C hydrogel, the Q_{max} of D hydrogel is reached after approximately 300 min. This different swelling behavior is obviously due to the different morphology of these 3D matrices, a major influence in this regard being the dimensions of the pores and their interconnectivity in the porous network of the hydrogels (see Figure 3).

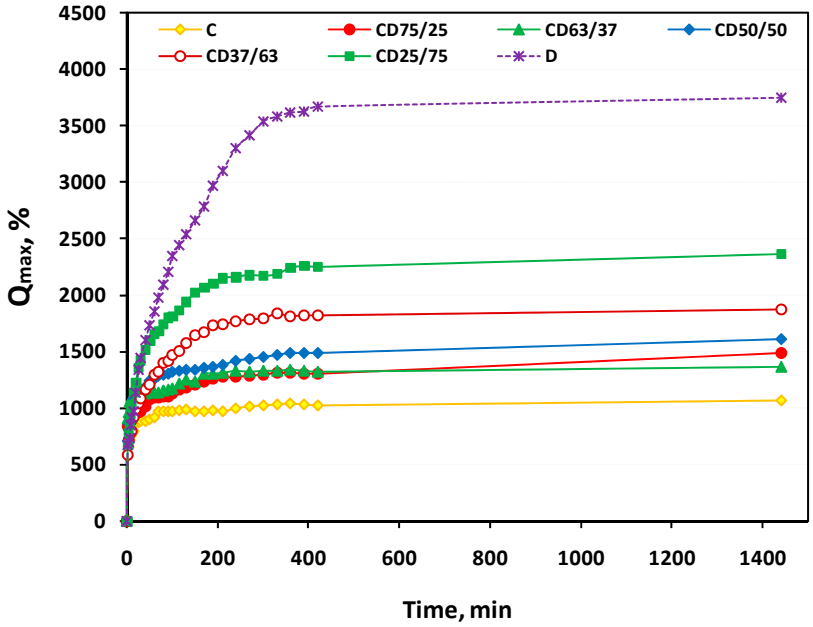

Figure 2. Swelling kinetics curves of the hydrogels, as a function of composition.

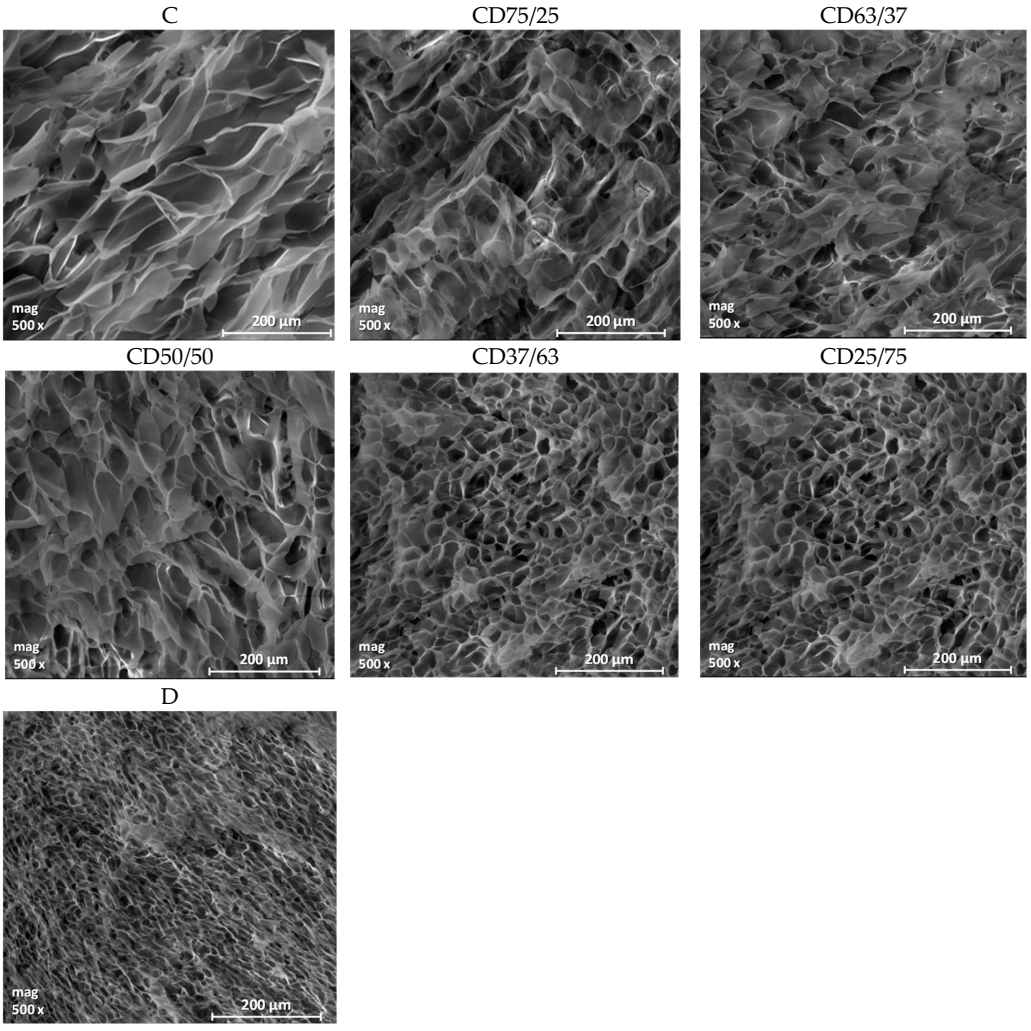

Figure 3. SEM images of the hydrogels obtained from cellulose (C), dextran (D) and their binary mixtures, in different gravimetric ratios (CD).

In order to study the effect of the hydrogel composition on the kinetics of the water uptake process, the empirical Equation (3) [33] was used and the swelling kinetic parameters of C, D and CD hydrogels are presented in Table 2.

The swelling process of the hydrogels is a complex process involving three successive steps: (i) the water molecules diffuse into the polymer network, followed by (ii) the relaxation of hydrated polymer chains, and then, in the final stage, (iii) the expansion of the polymer network into the surrounding aqueous solution [34]. Depending on the value of the diffusional exponent (n) and the geometry of the hydrogels (i.e., thin films, cylinders or spheres), the water transport mechanism in the hydrogel network can be established [35].

In our particular case of cylinder hydrogels, the values of the diffusional exponent (n_{sw}) are lower than 0.45, indicating the fact that the water transport mechanism follows the pseudo (less) Fickian diffusion, characterized by a diffusion rate lower than the relaxation rate of the polymer network. However, with the increase of the dextran content in the hydrogel formulations, a slight increase of the n_{sw} value is observed, showing a tendency towards the perfectly Fickian diffusion mechanism (n_{sw} = 0.45), where the polymer chains have a higher mobility that allows easier penetration of the solvent [34].

The swelling rate constant, k_{sw}, is an important parameter that characterizes the diffusion rate in a hydrogel network. It can be seen that this constant varies with the hydrogel's composition; more precisely, this parameter slightly increases with the increase of dextran content in hydrogel matrices.

For all hydrogels, the correlation coefficients R^2 are higher than 0.99, indicating a good fitting between experimental data and the chosen model.

2.2. Hydrogels Morphology

The cross-sectional morphologies of the cellulose-dextran hydrogels were analyzed by using scanning electron microscopy (SEM), which offers information regarding the pores' appearance and the structural uniformity of the hydrogels.

As expected, considering the various swelling degrees of the hydrogel formulations, the analysis of SEM micrographs evidenced different morphologies, depending on the matrix composition (Figure 3). Thus, if the cellulose-based hydrogel (C) has a discontinuous structure with large, irregular pores, in the case of the dextran-based hydrogel (D) a homogeneous structure with small, interconnected pores is observed. Related to CD hydrogels, it was observed that by increasing the dextran content in the hydrogels' 3D network, the size and unevenness of the pores decreases. The average pore size decreases from 66 µm for C hydrogels, to 41.6 µm for CD50/50 hydrogel and to 13.5 µm for D hydrogel (Table 3).

Table 3. The average pore size of the obtained hydrogels.

Samples	Average Pore Size, µm
C	66.1 ± 12.0
CD 75/25	44.4 ± 9.2
CD 63/37	44.0 ± 9.8
CD 50/50	41.6 ± 8.6
CD 37/63	34.8 ± 7.8
CD 25/75	27.1 ± 7.0
D	13.5 ± 3.1

Regarding the pore size homogeneity, this increases with increasing dextran content in the hydrogels, a fact which is also reflected by the standard deviation (SD). Thus, the less homogenous structure was recorded for C hydrogel, with the highest SD value (±12) and by increasing the dextran content, this value gradually decreased to that for the D hydrogel (±3), which has the most uniform structure. In addition, although the network of the D hydrogel has small pores, compared to those of C hydrogel, its pores are uniformly distributed within the 3D network of hydrogels and are interconnected. This fact is shown

by the high swelling degree of this hydrogel, which further influences its capacity for encapsulation and release of bioactive compounds, respectively. The only disadvantage of D hydrogel is the low gel fraction yield, but this can be controlled by its combination with cellulose, thus obtaining materials with optimal properties in wound healing.

2.3. ATR-FTIR Measurements

The ATR-FTIR spectroscopy technique was used to analyze the structural changes of the CD hydrogels, obtained after chemical cross-linking the two polysaccharides in different proportions, but also to confirm the incorporation of polyphenolic compounds in the hydrogel matrix.

2.3.1. ATR-FTIR Measurements for CD Hydrogels

The ATR-FTIR spectra of cellulose and dextran hydrogels, as well as the spectra of two of the bicomponent CD hydrogels (CD50/50 and CD25/75, respectively) are presented in Figure 4 (to simplify the figure, we chose only two bicomponent hydrogels). The two polysaccharides, cellulose and dextran, show quite similar spectra, but each one is still distinguished by their characteristic absorption bands. Generally, the absorption bands for polysaccharides are grouped in two main wavenumber regions, namely the region of 3700–2700 cm^{-1} and 1800–400 cm^{-1}, respectively.

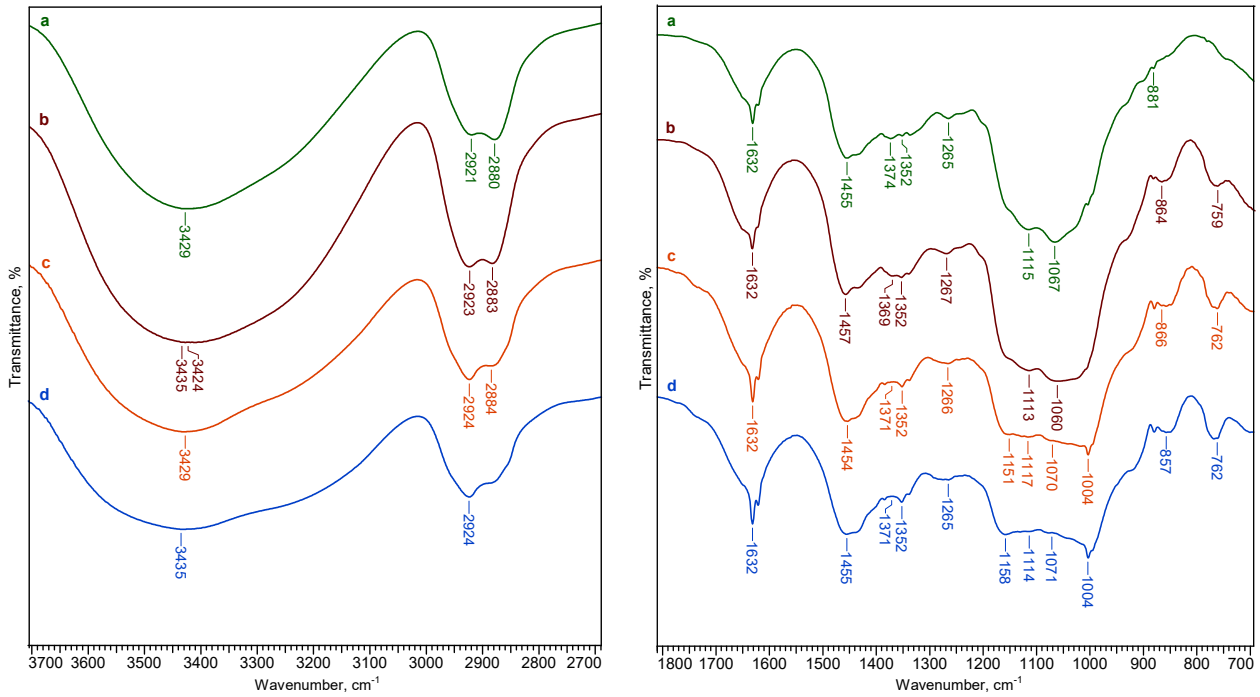

(**A**) (**B**)

Figure 4. ATR-FTIR spectra in the regions of (**A**) 3700–2700 cm^{-1} and (**B**) 1800–700 cm^{-1}, for the hydrogels based on cellulose (a), dextran (d), and cellulose-dextran hydrogels: CD50/50 (b) and CD25/75 (c).

In the range of 3660–2700 cm^{-1} are presented the broad band at 3429–3435 cm^{-1} characteristic for O-H stretching vibrations of the OH groups and the band at 2921 cm^{-1}, attributed to skeletal C-H stretching vibration in polysaccharides [36]. The bands located at 1631 cm^{-1} correspond to the O-H bending of adsorbed water.

In the ATR-FTIR spectrum of cellulose, there is a particular region between 1550 cm^{-1} and 800 cm^{-1} called "fingerprint" region, where the main absorption bands are: 1455 cm^{-1} assigned to CH_2 bending vibration, 1374 cm^{-1} and 1352 cm^{-1} to C-H bending and in-plane OH bending, 1265 cm^{-1} to C-O-H in plane bending, 1114 cm^{-1} to C–O–C anhydroglucose

ring asymmetric stretching, 1066 cm^{-1} to C-O stretching and the band at 881 cm^{-1} assigned to C-O-C stretching at the β-(1–4)-glycosidic linkage [37–39].

The main absorption bands that characterize the dextran were found at 1158 cm^{-1}, being related to the vibrations of the glycosidic linkage C-O-C of α-D-glucopyranoses, while the band at 1003 cm^{-1} is assigned to the vibration of the C-O bond of α-D-glucoses and chain flexibility around the α-(1→6) glycosidic bond [40,41]. The shoulder around 912 cm^{-1} along with the band at 857 cm^{-1} indicate the existence of glycosidic links, a branched chain in α-(1→3) anomeric configuration [12,42]. Moreover, in the case of dextran, the band at 761 cm^{-1} is considered a reference band, against which the structural changes that take place following the reaction can be determined [43].

In order to quantitatively characterize the changes produced in the cellulose matrix after mixing with dextran in different proportions, some absorption ratios of the characteristic bands were used and listed in Table 4. For instance, the hydrogen bond intensity (HBI) is correlated with the high ordered phase (crystalline) and degree of intermolecular regularity [36,44]. This parameter was determined from the ratio A_{3429}/A_{1336}, where the band at 3429 cm^{-1} is assigned to O–H stretching vibrations, while the band at 1336 cm^{-1} is due to C–O-H in-plane bending vibration [33,39].

Table 4. ATR-FTIR spectral characteristics for cellulose (C), dextran (D) and CD hydrogels.

Samples	HBI	A_{1630}/A_{2900}	A_{1116}/A_{2900}	A_{1066}/A_{2900}	A_{1116}/A_{761}	A_{1066}/A_{761}
C	2.426	0.695	2.253	2.536	19.86	22.36
CD 75/25	2.537	0.588	2.250	2.544	13.27	15.00
CD 63/37	2.267	0.694	2.119	2.362	10.43	11.63
CD 50/50	2.515	0.631	2.138	2.404	9.45	10.62
CD 37/63	2.216	0.675	1.906	2.098	8.00	8.80
CD 25/75	1.976	1.169	1.495	1.557	5.71	5.95
D	1.694	1.379	1.358	1.379	4.27	4.34

Increasing the dextran content in the cellulosic matrix led to a decrease in the HBI values, indicating a decrease in the samples' crystallinity. This fact is also confirmed by a gradual decrease of the maximum absorbance of OH stretching from the spectra of cellulose hydrogel to that of dextran hydrogel and implicitly of the total area of these peaks (Figure 4A).

The proof of the chemical cross-linking reaction in hydrogels is illustrated in the FTIR spectra by the presence of absorption bands at 1116 cm^{-1} (deformation vibration of ether linkages) and 1066 cm^{-1} (primary and aliphatic ethers groups), corresponding to the stretching vibrations of the C-O and C-O-C ether bonds [33]. In order to highlight the crosslinking capacity of the cellulose (FTIR internal standard: 2900 cm^{-1}) and dextran (FTIR internal standard: 761 cm^{-1}), the following ratios were established: A_{1116}/A_{2900}, A_{1066}/A_{2900}, A_{1116}/A_{761} and A_{1066}/A_{761}. The hydrogels' crosslinking capacity obviously decreases with the increase of the dextran content in the hydrogel's matrix, confirming the increased ability of cellulose to crosslink in the presence of EPC, compared to dextran. The obtaining of a more relaxed 3D network of the hydrogels with increasing dextran content was also confirmed by the data obtained from the hydrogels' gel fraction yield (from 99.9% for cellulose to 76.3% for dextran) and the swelling data (Tables 1 and 2).

Table 4 also includes the A_{1630}/A_{2900} ratios, associated with the ability of polysaccharides to bond water molecules into their network. These ratios increase with the increasing of dextran content in the hydrogel matrix, reflecting the higher hydrophilic character of dextran hydrogels compared to cellulose ones. This observation is also confirmed by the data on the swelling degrees of the hydrogels.

2.3.2. ATR-FTIR Measurements for PFs-Loaded Hydrogels

Figure 5 shows the ATR-FTIR spectra of CD50/50 hydrogel loaded with PFs (CD50/50 + PFs) compared with the spectrum of PFs alone and CD50/50 hydrogel without PFs, respectively.

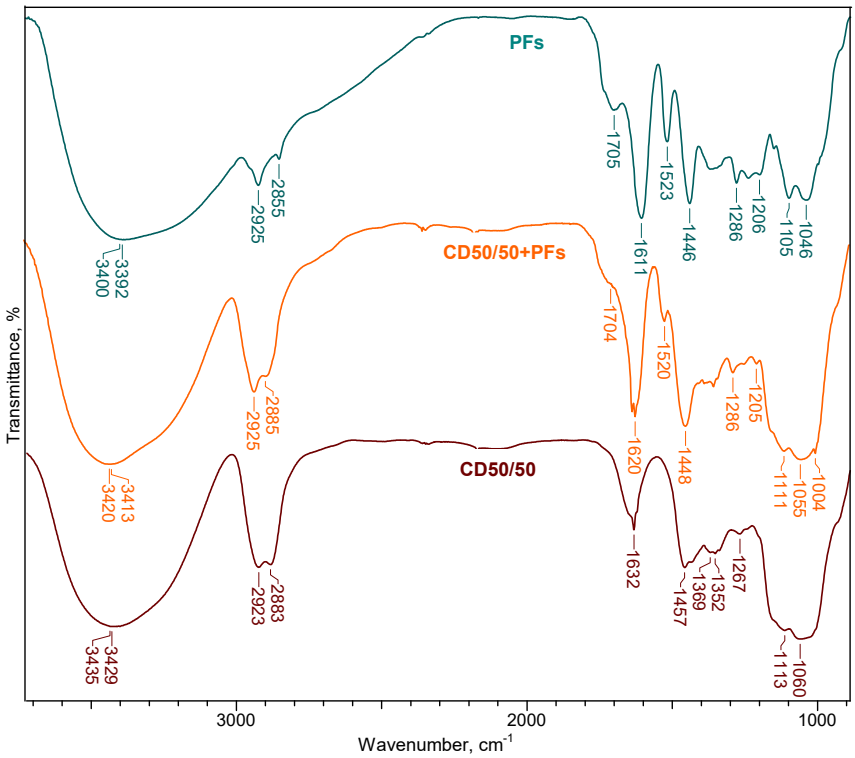

Figure 5. ATR-FTIR spectra of PFs, CD50/50 hydrogel and PFs-loaded hydrogel: CD50/50 + PFs.

The main characteristic ATR-FTIR absorption bands of PFs are: 3391 cm^{-1} for OH stretching vibration, 2924 cm^{-1} for CH stretching vibration, 1705 cm^{-1} for C-O stretching vibration, 1611 cm^{-1} for C-C stretching vibration, 1445 cm^{-1} for CH_2 bending vibrations, 1285 cm^{-1} and 1206 cm^{-1} for C-O stretching vibration (aryl ether band), 1105 cm^{-1} for C-O-C stretching vibration (alkyl ether band) and 1046 cm^{-1} for C-O stretching vibration (alkyl substituted ether) [33].

It is observed that, in addition to the characteristic absorption bands of CD50/50 hydrogel, the CD50/50 + PFs spectra contain also the specific bands of polyphenolic compound, proving their successful incorporation in the hydrogel's network.

For instance, the absorption band at 1705 cm^{-1} in PFs, assigned to C=O stretching vibrations of carbonyl double bond, is shifted to 1704 cm^{-1} for the PFs-loaded hydrogel. The band at 1522 cm^{-1}, corresponding to in-plane CH bending vibration from the phenyl rings, is shifted to lower wavenumbers, 1519 cm^{-1}, after PFs incorporation in CD50/50 hydrogel. The absorption bands at 1285 cm^{-1} and 1206 cm^{-1} from the FTIR spectrum of PFs are also found in the spectrum of CD50/50 + PFs, but with lower intensities. Regarding the bands 1105 cm^{-1} and 1046 cm^{-1} from PFs spectrum, they are also found in the CD50/50 + PFs spectrum, but are shifted to higher wavenumbers (1110 cm^{-1} and 1055 cm^{-1}) and overlapped by the characteristic bands of CD hydrogel (1112 cm^{-1} and 1059 cm^{-1}).

Two ratios of the characteristic absorption bands intensity of PFs, namely A_{1522}/A_{2900} and A_{1705}/A_{2900}, were used to quantitatively evaluate the incorporation of PFs in the hydrogels' matrix (Table 5). Both ratios increase with increase in the PFs content in the hydrogels and the obtained data are in good correlation with the incorporation degree (I_d).

Table 5. ATR-FTIR spectral characteristic for CD hydrogels, with or without PFs.

PFs-Loaded Hydrogels	A_{1522}/A_{2900}	A_{1705}/A_{2900}	I_d, %
C + PFs	0.591	0.337	13.6
CD75/25 + PFs	0.612	0.366	22.1
CD50/50 + PFs	0.637	0.418	24.5
CD25/75 + PFs	0.705	0.459	33.7
D + PFs	0.710	0.469	41.9
PFs	0.789	0.544	-

2.4. In Vitro Release of the Polyphenolic Compound from Hydrogels

The release profiles of PFs indicate a prolonged release of them from CD hydrogels (over a period of 3 days), a release that depends on the composition of the hydrogels (Figure 6). As can be seen, all CD hydrogels show a sustained PFs release which constantly increases until about 1400 min (24 h), after which it stabilizes on a plateau. The PFs release is presented for two different time periods, (i) the first 12 h, where the clear influence of the hydrogels' composition on the PFs release rate can be observed (Figure 6A), and (ii) the release up to 72 h, in order to highlight the plateau phase (Figure 6B). The initial release can be explained as the release of PFs trapped on the surface and in the pores in its immediate vicinity, during the incorporation process.

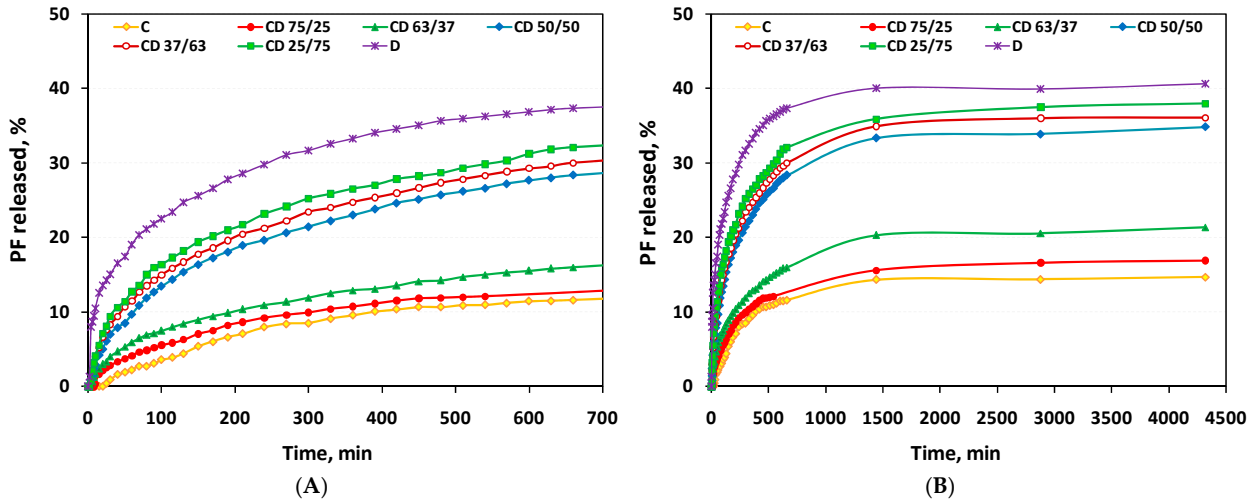

Figure 6. The release profiles of PFs from C, D and CD hydrogels, for (**A**) 12 h and (**B**) 72 h.

The PFs release is higher with increased dextran content in the matrix. For instance, for the first 30 min, the PFs release was only 6.3% (relative to the total PFs released) for cellulose hydrogels, while for CD50/50 hydrogels the release was 20.2% and for CD25/75 it was 24.7%, respectively. As expected, a higher swelling degree of dextran hydrogel (D) leads to more uptake of the drug during loading and furthermore, to a higher PFs release after only 30 min, of 37.2%.

Related to the time necessary to reach the maximum percentage of PFs released (72 h), the highest amount of PFs release is registered for the D hydrogel, reaching up to 40.6% (relative to the total incorporated amount of PFs), while for C hydrogel, this is only 14.7%. The sustained release of PFs continues even after 72 h, up to 14 days (results not shown), reaching for D hydrogels up to 45.01% and for C hydrogels up to 20.9%, respectively.

To understand the release behavior for PFs and to evaluate the possible release mechanism of PFs from the hydrogels, the experimental release data were investigated by fitting the Korsmeyer–Peppas model using the empirical Equation (5) [35]. This equation was used for the linearization of the release data and n and k values were calculated from the slope and intercept of the plot of $\ln(M_t/M_\infty)$ against ln(t) [45]. Their values are presented

in Table 6, along with the regression coefficients, R^2. The diffusional exponent, n, is used as an indicator for the release mechanism and the kinetic constant, k, is used to describe the structural and geometrical parameters of the hydrogels. For cylindrical hydrogels, if the exponent $n < 0.45$, the drug release mechanism is a Fickian diffusion, while if $0.45 < n < 0.89$, then it is a non-Fickian or anomalous diffusion; when $n > 0.89$, the release is a Case II transport mechanism [35].

Table 6. Kinetic parameters of PFs release for C, D and CD hydrogels.

PFs Loaded-Hydrogels	*n*	*k*	R^2	Transport Mechanism
C	1.004	1.009	0.984	Case II
CD 75/25	0.573	1.205	0.993	Anomalous
CD 63/37	0.563	1.369	0.990	Anomalous
CD 50/50	0.558	1.369	0.993	Anomalous
CD 37/63	0.537	1.535	0.992	Anomalous
CD 25/75	0.504	1.761	0.993	Anomalous
D	0.329	2.630	0.994	Pseudo Fickian diffusion

By using this model, the regression coefficient was found very close to unity ($R^2 = 0.984-0.994$), suggesting that the release data best fit to the Korsmeyer–Peppas model. The n value of the Korsmeyer–Peppas model was further used to examine the PFs release mechanism. Thus, the n values range from 0.329 for D hydrogel to 1.004 for C hydrogel, while for CD hydrogels n falls between these two values, more exactly to $0.504 < n < 0.573$, depending on the hydrogel's composition. The different values obtained for the diffusional exponent, n, indicate different diffusion mechanisms for PFs-loaded hydrogels. For instance, for PFs-loaded D hydrogel, the $n < 0.45$ indicates a pseudo (less) Fickian mechanism that is diffusion-controlled and is characterized by a high diffusion rate and a low rate of polymer chain relaxation [46]. Instead, the n value obtained for C hydrogel ($n = 1.004$) indicates a non-Fickian mechanism (Case II) that is controlled by polymer relaxation and the release rate is constant. The PFs loaded CD hydrogels ($0.45 < n < 0.89$) exhibit an anomalous (non-Fickian) transport mechanism, when the solvent diffusion rate and the rate of polymer chain relaxation are comparable [35].

Based on these results, it can be concluded that PFs release is usually controlled by a diffusion process and so, the release profile can be easily modified by changing the material properties, including the pore size or pore connectivity, which are very closely correlated with the hydrogels composition.

2.5. Cytocompatibility and Anti-Inflammatory Tests

2.5.1. Cytocompatibility of CD Hydrogels with Human Cells

The safety of the wound dressing is the top priority for its clinical efficiency [5]. Recent data showed that endothelial cells and fibroblasts are involved in the closure of three-dimensional wounds, which results in the repopulation of the wound with the cell-derived extracellular matrix [47]. Therefore, we went further with our research study and tested whether hydrogel formulations with incorporated PFs have a cytotoxic effect on the proliferation of human fibroblasts and endothelial cells. The cell viability was determined for cells grown on all hydrogels formulation and compared to the control group—cells grown in conventional tissue culture plate (CTRL) (Figure 7).

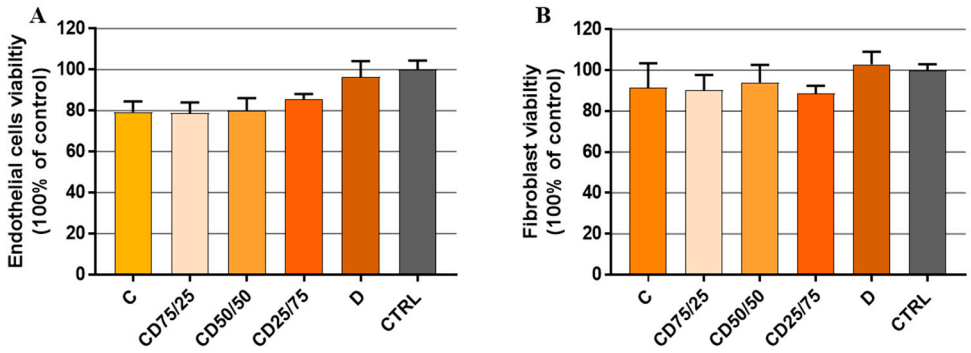

Figure 7. The viability of endothelial cells (**A**) and fibroblasts (**B**), after cultivation on different CD hydrogels, was determined by XTT assay. Cells were seeded for 72 h on the hydrogels or in a normal TPC culture plate (CTRL). Results are expressed as a mean ± standard deviation (SD) ($n = 3$).

The biocompatibility tests for the two cell types (fibroblasts and endothelial cells, respectively) showed that CD hydrogels are non-toxic, with cell viability being over 80% (% of CTRL TCP) in all cases, which means that CD hydrogels do not cause cell death. No significant difference regarding the influence of the hydrogels' composition on cell proliferation was observed. However, a slight increase in cell viability of endothelial cells can be observed with an increase of the dextran content in the hydrogel matrix, sustained by the biological function of dextran to help cell adhesion and growth [5]. In addition, one can add the contribution of the high interconnectivity of pores, as well as their size and uniformity.

Since in the case of fibroblast cells, the least influence of the hydrogels' composition on cell viability was observed (Figure 7B), it was decided to perform the following tests only with this type of cells.

2.5.2. Anti-Inflammatory Effect of PFs on Human Cells Exposed to LPS

Before testing the anti-inflammatory capacity of PFs-loaded hydrogels, we investigated the effect of three different concentrations of PFs (25, 50 and 100 µg/mL, respectively) on inflammatory cytokine IL-6 released by cells grown in conventional culture, in the presence or absence of LPS (100 ng/mL). For this, human fibroblasts were grown in conventional tissue culture plates and next activated for 18h with LPS in the presence or absence of PFs. The anti-inflammatory effect of PFs was investigated by quantification of IL-6 released by cells in the culture media using ELISA assay (Figure 8).

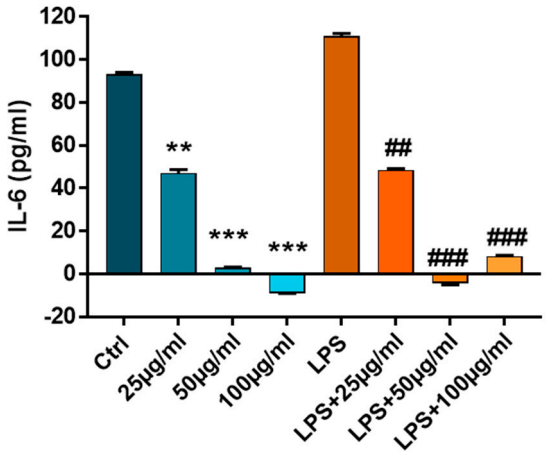

Figure 8. The protein expression of IL-6 released in the conditioned medium from control cells or cells activated with LPS (100 ng/mL) and treated with PFs (25, 50 and 100 µg/mL). $n = 3$, ** $p < 0.01$, *** $p < 0.001$, PFs versus control cells and ## $p < 0.01$, ### $p < 0.001$ PFs versus LPS.

The results show that PFs exhibit potent anti-inflammatory properties on both control cells and cells exposed to LPS, which are evident even at low concentrations of PF solutions (25 μg/mL), where the reduction of cell inflammation is almost 50% (related to control or LPS). After doubling the concentration of the PFs solution from 25 μg/mL to 50 μg/mL, the reduction of inflammation is almost 100%, so the increase of PFs concentration above this value is not justified.

The concentration of 50 μg/mL of PFs was considered optimal for the anti-inflammatory protective character of PFs in the LPS-induced inflammation process and was further used for encapsulation in hydrogels. Considering this, for the next stage, taking also into account the swelling degree of each type of hydrogel, the CD matrices were embedded with a solution of PFs, so that at the end, they contain approximately the optimal amount of bioactive compound, 50 μg/mL.

2.5.3. Cytocompatibility and Anti-Inflammatory Tests for PFs-Loaded Hydrogel

The PFs were embedded in different CD hydrogels and before testing the anti-inflammatory effects, the biocompatibility of PFs-functionalized hydrogels was quantified. For this, the fibroblasts were cultured on PFs-embedded hydrogels in the presence or absence of LPS for 72h and cell cytotoxicity was quantified by LDH (Figure 9A).

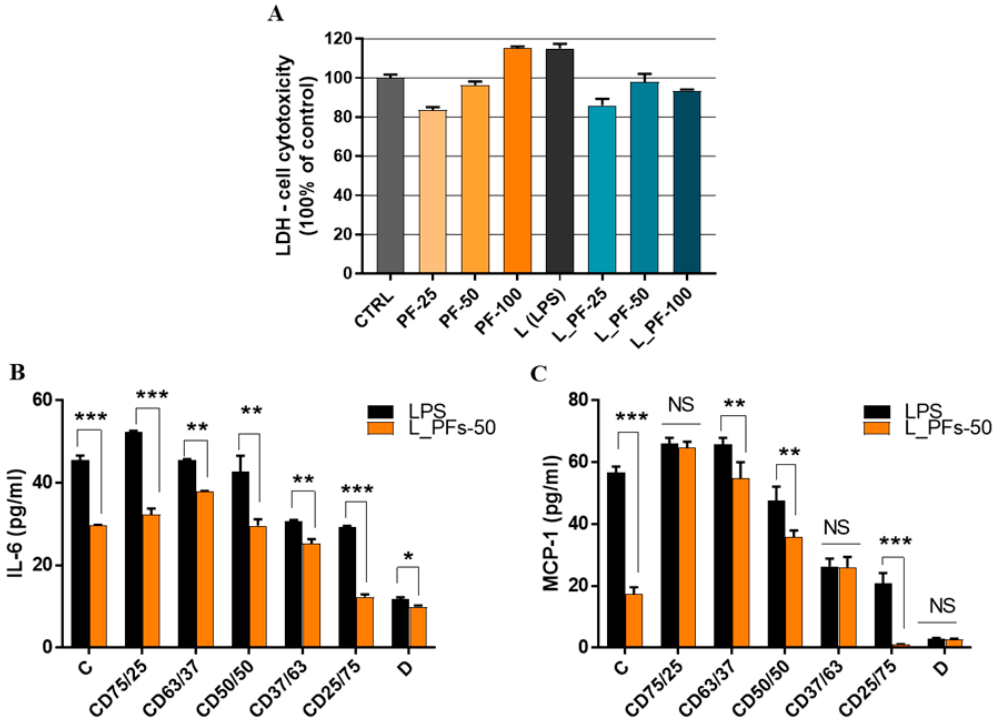

Figure 9. PFs-loaded hydrogels are biocompatible (**A**) and significantly reduce secretion of pro-inflammatory cytokines IL-6 and MCP-1 in human fibroblasts: (**A**) Quantitative evaluation of the cytotoxicity released by fibroblasts cultured on functionalized hydrogels, after 72 h of culture, using LDH assay; (**B**,**C**) IL-6 and MCP-1 concentration released in condition media from cells grown on PFs-hydrogels tested with ELISA assay. Data are presented as a mean ± SD ($n = 3$). An unpaired t-test was performed with GraphPad Prism. * $p \leq 0.05$, ** $p \leq 0.01$, *** $p \leq 0.001$, NS–nonsignificant.

The biocompatibility results that quantified the level of LDH enzyme released in the cell culture media revealed that after 3 days of culture, PFs-loaded hydrogels exhibited similar cytotoxicity compared to the control (Figure 9A), or even lower, for hydrogels loaded with 25 μg/mL PFs. No statistically significant difference was found between the LDH levels released by the tested hydrogels, indicating that the encapsulation of PFs in hydrogels does not exert an important cytotoxic effect on the cellular component.

To further evaluate anti-inflammatory effects of PFs embedded in hydrogels, the cells were cultured on hydrogels with or without PFs (50 μg/mL), in presence of LPS—to induce an inflammatory status of cells. The ELISA results (Figure 9B,C) showed that the levels of both investigated inflammatory molecules released by cells were reduced when the cells were grown on PFs-functionalized hydrogels. Therefore, the interleukin IL-6 was significantly reduced by all hydrogel formulations with encapsulated PFs (Figure 9B) and the chemokine MCP-1 was significantly reduced by C, CD63/37, CD50/50 and CD25/75 formulations (Figure 9C). All these data reveal that PFs embedded into the hydrogel exhibit anti-inflammatory effects on human cells.

Moreover, from the obtained data it was possible to highlight the anti-inflammatory character of dextran from the hydrogel formulations that do not contain PF, by decreasing the level of the two inflammatory molecules, IL-6 and MCP-1 (Figure 9B,C—black bars). The ability of dextran to reduce the inflammatory response of cytokines is also supported by previous literature [48–50]. In our case, by increasing the amount of dextran in the hydrogel formulations, its anti-inflammatory effect overlaps the anti-inflammatory effect of PF. Thus, for the cellulose hydrogel (C), a decrease in the IL-6 level of approximately 35% was observed, due to the effect of the encapsulated PFs, while for the dextran hydrogel (D) this decrease is only 8%, confirming the major anti-inflammatory influence of dextran.

3. Materials and Methods

3.1. Materials

Microcrystalline cellulose (C) was purchased from Sigma-Aldrich (Saint Louis, MO, USA) under the trade name of Avicel PH-101 (~50 μm particle size; DP = 180). Dextran (D) was obtained by biotechnological methods, using a lactic acid bacteria (LAB) strain identified by 16S rDNA sequence as *Weissella confusa*, isolated in the laboratories of Centre of Advanced Research in Bionanoconjugates and Biopolymers (IntelCentru) of the "Petru Poni" Institute of Macromolecular Chemistry, Iasi [12,40,42]. Polyphenols (PFs) were obtained by extraction from grape seeds of Chambourcin type, according to the procedure described in detail by Ciolacu and coworkers [33]. The identification of the major phenolic compounds from grape seeds led to the following composition: 34.3% gallic acid, 30.8% quercetin, 18.3% monomers anthocyanin, and 9.3% proanthocyanidins. The chemical structures of the phenolic compounds identified in grape seeds are presented in Figure 1. Epichlorohydrin (EPC) was purchased from Merck (Darmstadt, Germany) (purity > 99 %; d = 1.18 g/cm^3) and was used without further purification. Sodium hydroxide (NaOH) in pellets, with a purity $\geq$ 97%, was supplied by Merck (Hohenbrunn, Germany).

Cytotoxicity of the hydrogels was tested using a LDH detection kit (ThermoFischer, Rockford, IL, USA), while viability and proliferation of human cells seeded on the hydrogels were quantified using a XTT assay (ThermoFischer, Rockford, IL, USA). Anti-inflammatory effects of hydrogels enriched with polyphenolic compounds on human cells stimulated with lipopolysaccharide (LPS, Sigma-Aldrich) were tested by quantification of inflammatory molecules MCP-I and IL-6 using Enzyme-Linked Immunosorbent Assays (DuoSet ELISA Kits, R&D Systems, Minneapolis, MN, USA).

3.2. Methods

3.2.1. Preparation of the Hydrogels

3D matrices were prepared from cellulose (C) and from dextran (D), but also from the mixture of these two polysaccharides, in different gravimetric ratios (CD), C/D: 75/25, 63/37, 50/50, 37/63 and 25/75 (Table 1). The hydrogels were prepared as follows: 0.25 g polymer was added to 3.67 mL 8.5% NaOH solution and frozen at low temperature (−30 °C). After thawing, 1.45 mL EPC was added under continuous stirring. The obtained composition was maintained for 5 h at 84 °C. The hydrogels were washed with warm distilled water (60 °C), for 15 days, in order to remove the excess of NaOH, any EPC traces and NaCl, followed by drying by lyophilization.

3.2.2. Swelling Measurements

Swelling studies were performed for all hydrogels in distilled water, at 37 °C. The samples were periodically removed from the swelling medium, gently wiped with a soft tissue to remove the surface solution, quickly weighed and then placed back into the vessel. The swelling degree (Q_{max}, %) of the hydrogels was determined gravimetrically and calculated according to Equation (1):

$$Q_{max} = \frac{M_s - M_d}{M_d} \cdot 100\% \quad (1)$$

where: M_s—the weight, at time t, of swollen hydrogel (g); M_d—the weight of dry hydrogel (g).

The equilibrium swelling degree (Q_{eq}, %) was determined for the never-dried hydrogels (hydrogels just after synthesis) using Equation (2):

$$Q_{eq} = \frac{M_\infty - M_d}{M_d} \cdot 100\% \quad (2)$$

where: M_∞—the weight of swollen hydrogel, at equilibrium (g); M_d—the weight of dry hydrogel (g).

In order to determine the kinetics of solvent diffusion into the hydrogels matrices, Equation (3) was used to describe the Fickian or non-Fickian behavior of swelling-controlled release systems [33]:

$$\frac{W_t}{W_{eq}} = k_{sw} \cdot t^{n_{sw}} \quad (3)$$

where: W_t—the amount, at time t, of water absorbed by the hydrogel (g); W_{eq}—the amount of water absorbed by the hydrogel at equilibrium (g); k_{sw}—the swelling constant that incorporates the characteristics of the macromolecular network system (min^{-1}); n_{sw}—the swelling diffusional exponent, which is indicative of the transport mechanism. The constants n and k were calculated from the slopes and intercepts of the plots of $\ln(W_t/W_{eq})$ vs. ln(t). Equation (3) was applied in the early swelling stages (swelling degree less than 60%) where the linearity was observed.

3.2.3. Incorporation of the PFs

0.1 g dried hydrogel was immersed in 25 mL solution of 4 g/L PFs in water:ethanol (19:1, *v*/*v*) and left to swell at room temperature for 72 h, while the PFs penetrated and/or attached to matrices. Finally, the PFs-loaded samples were dried by lyophilization. In order to establish the amount of PFs incorporated in the hydrogels, the remaining solutions were analyzed by UV-VIS spectroscopy, measuring the absorbance at 280 nm. The calibration curve (Figure 10) was obtained according to different concentrations of PFs in water-ethanol (19:1, *v*/*v*), in the range of 0.025 ÷ 0.25 g/L. The unknown concentrations of the remaining solutions after PFs incorporation were determined using the equation obtained from the calibration curve, y = 15.39x + 0.049, with a correlation coefficient of $R^2 = 0.998$.

The incorporation degree (I_d) of PFs into hydrogel matrices was calculated using Equation (4):

$$I_d = \frac{c_0 V_0 - cV}{M} \cdot 100\% \quad (4)$$

where: c_0—the initial concentration of the PFs solution (g/mL); V_0—the volume of initial PFs solution (mL); c—the concentration of remained PFs in solution, determined from the calibration curve (g/mL); V—the volume of the PFs solution remaining after incorporation (mL); M—the weight of dry PFs loaded-hydrogel (g).

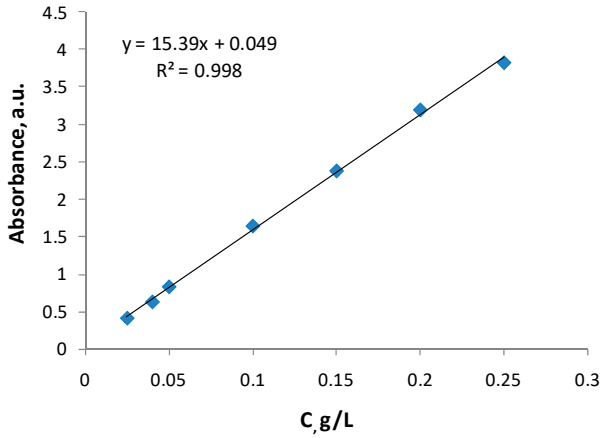

Figure 10. Calibration curve of PFs (water:ethanol = 19:1, 37 °C).

3.2.4. In Vitro Release of the PFs

In vitro release studies have been conducted by a standard dissolution procedure using the water:ethanol (19:1, *v*/*v*) mixture as release medium, at 37 °C [33]. 1 mL samples of release medium were withdrawn periodically, at predetermined time intervals, and the absorbance at 280 nm was measured. In order to maintain the solution concentration, the sample was reintroduced in the system after analyzing. The PFs concentration in release medium was calculated based on the PFs calibration curve (see Figure 10).

In order to kinetically analyze the release data of PFs from hydrogel matrices with different compositions, a semi-empirical equation (Equation (5) of Korsmeyer–Peppas release model was used and applied at the earlier stages of PFs release (between 5% and 60% fractional release) [35]:

$$\frac{M_t}{M_\infty} = k \cdot t^n \quad (5)$$

where: M_t—the amount of PFs released at time t (g); M_∞—the amount of PFs at the equilibrium state (g); *k*—the rate constant, characteristic to the PFs-polymers system, incorporating its structural and geometric character (min^{-1}); *n*—the diffusional exponent, which suggests the nature of the release mechanism. The value of *n* depends on the hydrogel shape. Thus, for a cylinder shape, if: (i) $n < 0.45$ then a Fickian diffusion release mechanism is implied, (ii) $0.45 < n < 0.89$, the release mechanism follows an anomalous transport mechanism and (iii) *n* is above 0.89 then Case II release mechanism takes place [32,35].

3.2.5. Cell Isolation and Culture

Endothelial cells: human valvular endothelial cells isolated from non-calcified cusps of human aortic valves as we previously described [51]. Endothelial cells were cultured in endothelial cell growth medium with 20% FBS (Gibco) and 100 U/mL Penicillin, 100 µg/mL Streptomycin and 50 µg/mL Neomycin (Sigma-Aldrich, Schnelldorf, Germany).

Fibroblasts: human valvular interstitial cells—fibroblast-like cells—purchased from Innoprot (no. P10462), and cultured in Dulbecco's Modified Eagle Medium (DMEM, Gibco), supplemented with 10% Fetal Bovine Serum (FBS, Gibco) and 1% Antibiotics (Penicillin/Streptomycin, Sigma-Aldrich, Germany), according to manufacturer's protocols.

3.2.6. XTT—Cell Viability Assay

The dried hydrogels composed of different amounts of cellulose and dextran, with or without PFs were sectioned and UV sterilized for 30 min on both sides. Once sterilized, they were hydrated with complete medium (DMEM or M200, 10% FBS and 1% P/S) in a 96-well plate for 3 h, at 37 °C, 5% CO_2. After hydrogel hydration, human fibroblasts and endothelial cells were seeded at a density of 7500 cells/hydrogel in a 96-well plate. After 72 h, the biocompatibility of the hydrogels was determined by XTT assay and the viability of cells from the hydrogels was compared to the viability of cells that were grown

in normal culture conditions, in a conventional tissue culture plastic 96-well plate (control group—Ctrl TCP). Live cells reduce the yellow tetrazolium salt to water-soluble orange colored formazan, which is spectrophotometrically measured at 450 nm.

3.2.7. LDH—Cytotoxicity Assay

To test the cytotoxicity of PFs extracted from grape seeds, cells were cultured at a density of 7500 cells/well in a 96-well plate and exposed to different concentrations of PFs (25–100 μg/mL), in the presence or absence of LPS (100 ng/mL). After 24 h, the medium was collected and the lactate dehydrogenase enzyme (LDH) activity—an enzyme that is released into the culture medium when the cell membrane is damaged—was quantified according to the manufacturer's protocol.

3.2.8. ELISA Assay

To test the anti-inflammatory properties of PFs extracted from grape seeds, the human cells were cultured in conventional culture or on the hydrogels and exposed to different concentrations of PFs (25–100 μg/mL), in the presence or absence of LPS (100 ng/mL). After 24 h, the medium was collected and the levels of inflammatory cytokine MCP-1 and IL-6 released by cells were quantified using ELISA DuoSet kits (R&D systems, Abingdon, UK), following manufacturer's instructions.

3.3. Equipment

UV–VIS absorption spectra were recorded at room temperature on a Hewlett Packard 8540A UV–VIS spectrophotometer, in 10 mm quartz cells, using water:ethanol mixture as a solvent.

Attenuated Total Reflection Fourier Transformed Infrared (ATR-FTIR) spectroscopy was carried out on silicon single-crystal parallelepiped internal reflection elements (IRE; 55 × 5 × 2 mm, 45° incident angle), using a Bruker Vertex 70 instrument. All the spectra were the results of 256 scans at a resolution of 4 cm^{-1}, frequency range 4000–400 cm^{-1}.

The morphology of the samples was investigated by using a Scanning electron microscope (SEM) type Quanta 200, operating at 30 kV with secondary electrons, in low vacuum mode.

The average pore size and the standard deviation (SD) were determined using the SEM images exported in the image analysis software—ImageJ, measuring 20 randomly chosen pores and following the steps presented in the procedure described in the literature [52,53].

The cytotoxicity and cytocompatibility experiments of hydrogels, PFS and PFs loaded-hydrogels were carried out by Tecan Infinite M200 Pro spectrophotometer measurements.

4. Conclusions

New 3D bicomponent matrices based on cellulose and dextran, for the encapsulation and controlled release of anti-inflammatory bioactive compounds have been obtained. The properties of the hydrogels were found to be dependent on their composition. Thus, the presence of dextran in different proportions has a positive impact on the hydrogel's morphology, by increasing the uniformity and interconnectivity of the pores. In addition, the hydrogels CD50/50, CD37/63 and CD25/75, respectively, show a high swelling degree and an encapsulation capacity of PFs clearly superior to cellulose hydrogel. The PFs release kinetics indicate different transport mechanisms depending on hydrogels' composition and morphology. For instance, the PFs release from D hydrogel follows a Fickian diffusion mechanism, while the diffusional coefficient value obtained for C hydrogel indicates a non-Fickian mechanism Case II based on the swelling or relaxation of polymeric chains. Related to CD hydrogels, these exhibit a non-Fickian model with anomalous transport mechanism governed by diffusion and swelling processes with comparable rates.

The cell-based experiments showed that fibroblasts and endothelial cells were successfully cultured on the CD hydrogels with a high viability, of over 80% for all formulations, a fact which demonstrates their good cytocompatibility. Moreover, the encapsulation of PFs

as a bioactive principle gives to hydrogels anti-inflammatory properties, sustained by the anti-inflammatory tests in the presence of LPS, used as a pro-inflammatory model.

Considering the results obtained, it can be concluded that PFs-loaded CD hydrogels have the potential to facilitate and accelerate wound healing by inhibiting the inflammation process through a controlled and sustained release of the anti-inflammatory bioactive compounds in skin wound applications.

Author Contributions: Conceptualization, R.N. and D.E.C.; methodology, R.N., D.E.C. and F.C.; validation, A.-R.P., D.R., M.A., A.C.M. and E.B.; formal analysis, R.N. and D.E.C.; investigation, R.N., D.E.C., A.-R.P., D.R., M.A., A.C.M. and E.B.; resources, R.N. and D.E.C.; data curation, R.N., D.E.C., A.-R.P., D.R., M.A., A.C.M. and E.B.; writing—original draft preparation, R.N. and D.E.C.; writing—review and editing, R.N., D.E.C. and F.C.; visualization, A.-R.P., D.R., M.A., A.C.M. and E.B.; supervision, D.E.C. and F.C.; project administration, D.E.C.; funding acquisition, R.N., D.E.C. and F.C. All authors have read and agreed to the published version of the manuscript.

Funding: This work was supported by a grant of the Romanian Ministry of Research and Innovation, CCCDI—UEFISCDI, project number PN-III-P1-1.2-PCCDI-2017-0697/13PCCDI/2018, within PNCDI III.

Institutional Review Board Statement: Not applicable.

Informed Consent Statement: Not applicable.

Data Availability Statement: Data are contained within the article.

Acknowledgments: The authors would like to thank Narcis Anghel, affiliated to "Petru Poni" Institute of Macromolecular Chemistry, Iasi, Romania, for providing the polyphenols extracted from grape seeds of Chambourcin type.

Conflicts of Interest: The authors declare no conflict of interest.

References

1. Hinz, B. The role of myofibroblasts in wound healing. *Curr. Res. Transl. Med.* **2016**, *64*, 171–177. [CrossRef] [PubMed]
2. Karppinen, S.M.; Heljasvaara, R.; Gullberg, D.; Tasanen, K.; Pihlajaniemi, T. Toward understanding scarless skin wound healing and pathological scarring. *F1000Research* **2019**, *5*, 787–797. [CrossRef] [PubMed]
3. D'Amora, U.; Dacrory, S.; Hasanin, M.S.; Longo, A.; Soriente, A.; Kamel, S.; Raucci, M.G.; Ambrosio, L.; Scialla, S. Advances in the physico-chemical, antimicrobial and angiogenic properties of graphene-oxide/cellulose nanocomposites for wound healing. *Pharmaceutics* **2023**, *15*, 338. [CrossRef]
4. Ciolacu, D.E.; Nicu, R.; Ciolacu, F. Cellulose-based hydrogels as sustained drug-delivery systems. *Materials* **2020**, *13*, 5270–5306. [CrossRef]
5. Lin, S.P.; Kung, H.N.; Tsai, Y.S.; Tseng, T.N.; Hsu, K.D.; Cheng, K.C. Novel dextran modified bacterial cellulose hydrogel accelerating cutaneous wound healing. *Cellulose* **2017**, *24*, 4927–4937. [CrossRef]
6. Hu, H.; Xu, F.-J. Rational design and latest advances of polysaccharide-based hydrogels for wound healing. *Biomater. Sci.* **2020**, *8*, 2084–2101. [CrossRef]
7. Cui, R.; Zhang, L.; Ou, R.; Xu, Y.; Xu, L.; Zhan, X.-Y.; Li, D. Polysaccharide-based hydrogels for wound dressing: Design considerations and clinical applications. *Front. Bioeng. Biotechnol.* **2022**, *10*, 845735. [CrossRef]
8. Abou-Yousef, H.; Dacrory, S.; Hasanin, M.; Saber, E.; Kamel, S. Biocompatible hydrogel based on aldehyde-functionalized cellulose and chitosan for potential control drug release. *Sustain. Chem. Pharm.* **2021**, *21*, 100419. [CrossRef]
9. Attasgah, R.B.; Velasco-Rodríguez, B.; Pardo, A.; Fernández-Vega, J.; Arellano-Galindo, L.; Rosales-Rivera, L.C.; Prieto, G.; Barbosa, S.; Soltero, J.F.A.; Mahmoudi, M.; et al. Development of functional hybrid scaffolds for wound healing applications. *iScience* **2022**, *25*, 104019. [CrossRef]
10. Rial, R.; Liu, Z.; Ruso, J.M. Soft actuated hybrid hydrogel with bioinspired complexity to control mechanical flexure behavior for tissue engineering. *Nanomaterials* **2020**, *10*, 1302. [CrossRef]
11. Tabernero, A.; Cardea, S. Microbial exopolysaccharides as drug carriers. *Polymers* **2020**, *12*, 2142–2172. [CrossRef] [PubMed]
12. Petrovici, A.R.; Nicolescu, A.; Silion, M.; Rosca, I.; Ciolacu, D. Biopolymer biosynthesis by lactic acid bacteria strain in four different culture media. *Rev. Roum. Chim.* **2018**, *63*, 637–642.
13. Kaur, J.; Mankoo, R.K.; Dudeja, I.; Kapil, S. Recent approaches to the synthesis of hydrogels from lignocellulosic biomass: A review. *Cellulose Chem. Technol.* **2022**, *56*, 891–906. [CrossRef]
14. De Andrade Peixoto, M.; Reis, E.M.D.; Cesca, K.; Porto, L.M. Study of melanoma cell behaviorin vitroin collagen functionalized bacterial nanocellulose hydrogels. *Cellulose Chem. Technol.* **2020**, *54*, 669–677. [CrossRef]

15. Rusu, D.; Ciolacu, D.; Simionescu, B.C. Cellulose-based hydrogels in tissue engineering applications. *Cellul. Chem. Technol.* **2019**, *53*, 907–923. [CrossRef]
16. O'Connor, N.A.; Jitianu, M.; Nunez, G.; Picard, Q.; Wong, M.; Akpatsu, D.; Negrin, A.; Gharbaran, R.; Lugo, D.; Shaker, S.; et al. Dextran hydrogels by crosslinking with amino acid diamines and their viscoelastic properties. *Int. J. Biol. Macromol.* **2018**, *111*, 370–378. [CrossRef]
17. Salimi-Kenari, H.; Mollaie, F.; Dashtimoghadam, E.; Imani, M.; Nyström, B. Effects of chain length of the cross-linking agent on rheological and swelling characteristics of dextran hydrogels. *Carbohydr. Polym.* **2018**, *181*, 141–149. [CrossRef] [PubMed]
18. Ciolacu, D.; Rudaz, C.; Vasilescu, M.; Budtova, T. Physically and chemically cross-linked cellulose cryogels: Structure, properties and application for controlled release. *Carbohydr. Polym.* **2016**, *151*, 392–400. [CrossRef]
19. Benhalima, T.; Ferfera-Harrar, H. Eco-friendly porous carboxymethyl cellulose/dextran sulfate composite beads as reusable and efficient adsorbents of cationic dye methylene blue. *Int. J. Biol. Macromol.* **2019**, *132*, 126–141. [CrossRef]
20. Garg, A.; Garg, S.; Pandey, P.; Shukla, A.K.; Janadri, S.; Kori, M.L.; Lodhi, S. Fabrication and evaluation of carboxy methyl cellulose anchored dextran bioinspired hydrogel for effective delivery of piroxicam. *Indian J. Pharm. Sci.* **2022**, *84*, 821–831. [CrossRef]
21. Jiang, Y.; Zhou, J.; Shi, H.; Zhao, G.; Zhang, Q.; Feng, C.; Xv, X. Preparation of cellulose nanocrystal/oxidized dextran/gelatin (CNC/OD/GEL) hydrogels and fabrication of a CNC/OD/GEL scaffold by 3D printing. *J. Mater. Sci.* **2020**, *55*, 2618–2635. [CrossRef]
22. Stupin, V.; Manturova, N.; Silina, E.; Litvitskiy, P.; Vasin, V.; Artyushkova, E.; Ivanov, A.; Gladchenko, M.; Aliev, S. The effect of inflammation on the healing process of acute skin wounds under the treatment of wounds with injections in rats. *J. Exp. Pharmacol.* **2020**, *30*, 409–422. [CrossRef] [PubMed]
23. Li, Z.; Chen, Z.; Chen, H.; Chen, K.; Tao, W.; Ouyang, X.; Mei, L.; Zeng, X. Polyphenol-based hydrogels: Pyramid evolution from crosslinked structures to biomedical applications and the reverse design. *Bioact. Mater.* **2022**, *17*, 49–70. [CrossRef]
24. Zhang, X.; Li, Z.; Yang, P.; Duan, G.; Liu, X.; Gu, Z.; Li, Y. Polyphenol scaffolds in tissue engineering. *Mater. Horiz.* **2021**, *8*, 145–167. [CrossRef] [PubMed]
25. Shavandi, A.; Bekhit, A.E.D.A.; Saeedi, P.; Izadifar, Z.; Bekhit, A.A.; Khademhosseini, A. Polyphenol uses in biomaterials engineering. *Biomaterials* **2018**, *167*, 91–106. [CrossRef] [PubMed]
26. Yahfoufi, N.; Alsadi, N.; Jambi, M.; Matar, C. The immunomodulatory and anti-inflammatory role of polyphenols. *Nutrients* **2018**, *10*, 1618. [CrossRef] [PubMed]
27. Ćorković, I.; Pichler, A.; Šimunović, J.; Kopjar, M. Hydrogels: Characteristics and application as delivery systems of phenolic and aroma compounds. *Foods* **2021**, *10*, 1252–1274. [CrossRef]
28. Brza, M.A.; Aziz, S.B.; Anuar, H.; Ali, F.; Dannoun, E.M.A.; Mohammed, S.J.; Abdulwahid, R.T.; Al-Zangana, S. Tea from the drinking to the synthesis of metal complexes and fabrication of PVA based polymer composites with controlled optical band gap. *Sci. Rep.* **2020**, *10*, 18108. [CrossRef]
29. Kaczmarek, B. Tannic acid with antiviral and antibacterial activity as a promising component of biomaterials—A mini review. *Materials* **2020**, *13*, 3224–3236. [CrossRef]
30. Tong, W.; Chen, X.; Song, X.; Chen, Y.; Jia, R.; Zou, Y.; Li, L.; Yin, L.; He, C.; Liang, X.; et al. Resveratrol inhibits LPS-induced inflammation through suppressing the signaling cascades of TLR4-NF-κB/MAPKs/IRF3. *Exp. Ther. Med.* **2020**, *19*, 1824–1834. [CrossRef]
31. Dhivya, S.; Padma, V.V.; Santhini, E. Wound dressings—A review. *BioMedicine* **2015**, *5*, 22–28. [CrossRef]
32. Supramaniam, J.; Adnan, R.; Kaus, N.H.M.; Bushra, R. Magnetic nanocellulose alginate hydrogel beads as potential drug delivery system. *Int. J. Biol. Macromol. A* **2018**, *118*, 640–648. [CrossRef]
33. Ciolacu, D.; Oprea, A.M.; Anghel, N.; Cazacu, G.; Cazacu, M. New cellulose–lignin hydrogels and their application in controlled release of polyphenols. *Mater. Sci. Eng. C* **2012**, *32*, 452–463. [CrossRef]
34. Ostrowska-Czubenko, J.; Gierszewska, M.; Pieróg, M. PH-responsive hydrogel membranes based on modified chitosan: Water transport and kinetics of swelling. *J. Polym. Res.* **2015**, *22*, 153–164. [CrossRef]
35. Bruschi, M.L. Mathematical models of drug release. In *Strategies to Modify the Drug Release from Pharmaceutical Systems*, 1st ed.; Bruschi, M.L., Ed.; Woodhead Publishing: Sawston, UK, 2015; Chapter 5; pp. 63–86. [CrossRef]
36. Hong, T.; Yin, J.-Y.; Nie, S.-P.; Xie, M.-Y. Applications of infrared spectroscopy in polysaccharide structural analysis: Progress, challenge and perspective. *Food Chem. X* **2021**, *12*, 100168. [CrossRef] [PubMed]
37. Hospodarova, V.; Singovszka, E.; Stevulova, N. Characterization of cellulosic fibers by FTIR spectroscopy for their further implementation to building materials. *Am. J. Anal. Chem.* **2018**, *9*, 303–310. [CrossRef]
38. Polleto, M.; Pistor, V.; Zattera, A.J. Structural characteristics and thermal properties of native cellulose. In *Cellulose—Fundamental Aspects*; Van De Ven, T.G.M., Ed.; IntechOpen Limited: London, UK, 2013; Chapter 2; pp. 45–68. [CrossRef]
39. Oh, S.Y.; Yoo, D.I.; Shin, Y.; Gon Seo, G. FTIR analysis of cellulose treated with sodium hydroxide and carbon dioxide. *Carbohydr. Res.* **2005**, *340*, 417–428. [CrossRef] [PubMed]
40. Rosca, I.; Petrovici, A.R.; Peptanariu, D.; Nicolescu, A.; Dodi, G.; Avadanei, M.; Ivanov, I.C.; Bostanaru, A.C.; Mares, M.; Ciolacu, D. Biosynthesis of dextran by *Weissella confusa* and its in vitro functional characteristics. *Int. J. Biol. Macromol. B* **2018**, *107*, 1765–1772. [CrossRef]

41. Siddiqui, N.N.; Aman, A.; Silipo, A.; Qader, S.A.U.; Molinaro, A. Structural analysis and characterization of dextran produced by wild and mutant strains of *Leuconostoc mesenteroides*. *Carbohydr. Polym.* **2014**, *99*, 331–338. [CrossRef]
42. Petrovici, A.R.; Rosca, I.; Dodi, G.; Nicolescu, A.; Avadanei, M.; Varganici, C.D.; Ciolacu, D. Effects of culture medium composition on biosynthesis of exopolysaccharides. *Cellulose Chem. Technol.* **2017**, *51*, 821–830.
43. Ferreira, L.; Gil, M.H.; Dordick, J.S. Enzymatic synthesis of dextran-containing hydrogels. *Biomaterials* **2002**, *23*, 3957–3967. [CrossRef] [PubMed]
44. Anghel, N.; Dinu, M.V.; Zaltariov, M.; Pamfil, D.; Spiridon, I. New cellulose-collagen-alginate materials incorporated with quercetin, anthocyanins and lipoic acid. *Int. J. Biol. Macromol.* **2021**, *181*, 30–40. [CrossRef] [PubMed]
45. Orasugh, J.T.; Saha, N.R.; Rana, D.; Sarkar, G.; Mollick, M.M.R.; Chattoapadhyay, A.; Mitra, B.C.; Mondal, D.; Ghosh, S.K.; Chattopadhyay, D. Jute cellulose nano-fibrils/hydroxypropylmethylcellulose nanocomposite: A novel material with potential for application in packaging and transdermal drug delivery system. *Ind. Crops Prod.* **2018**, *112*, 633–643. [CrossRef]
46. Gunathilake, T.M.S.U.; Ching, Y.C.; Chuah, C.H. Enhancement of curcumin bioavailability using nanocellulose reinforced chitosan hydrogel. *Polymers* **2017**, *9*, 64–82. [CrossRef]
47. Tefft, J.B.; Chen, C.S.; Eyckmans, J. Reconstituting the dynamics of endothelial cells and fibroblasts in wound closure. *APL Bioeng.* **2021**, *5*, 016102. [CrossRef]
48. Lee, S.; Stubelius, A. Inflammation-responsive drug-conjugated dextran nanoparticles enhance anti-inflammatory drug efficacy. *ACS Appl. Mater. Interfaces* **2018**, *10*, 40378–40387. [CrossRef]
49. Sun, G.; Mao, J.J. Engineering dextran-based scaffolds for drug delivery and tissue repair. *Nanomedicine* **2012**, *7*, 1771–1784. [CrossRef]
50. Gombocz, K.; Beledi, Á.; Alotti, N.; Kecskés, G.; Gábor, V.; Bogár, L.; Kőszegi, T.; Garai, J. Influence of dextran-70 on systemic inflammatory response and myocardial ischaemia-reperfusion following cardiac operations. *Crit. Care* **2007**, *11*, R87–R96. [CrossRef]
51. Vadana, M.; Cecoltan, S.; Ciortan, L.; Macarie, R.D.; Tucureanu, M.M.; Mihaila, A.C.; Droc, I.; Butoi, E. Molecular mechanisms involved in high glucose-induced valve calcification in a 3D valve model with human valvular cells. *J. Cell. Mol. Med.* **2020**, *24*, 6350–6361. [CrossRef]
52. Aston, R.; Sewell, K.; Klein, T.; Lawrie, G.; Grøndahl, L. Evaluation of the impact of freezing preparation techniques on the characterisation of alginate hydrogels by cryo-SEM. *Eur. Polym. J.* **2016**, *82*, 1–15. [CrossRef]
53. Jayawardena, I.; Turunen, P.; Garms, B.C.; Alan Rowan, A.; Simon Corrie, S.; Grøndahl, L. Evaluation of techniques used for visualisation of hydrogel morphology and determination of pore size distributions. *Mater. Adv.* **2023**, *4*, 669–682. [CrossRef]

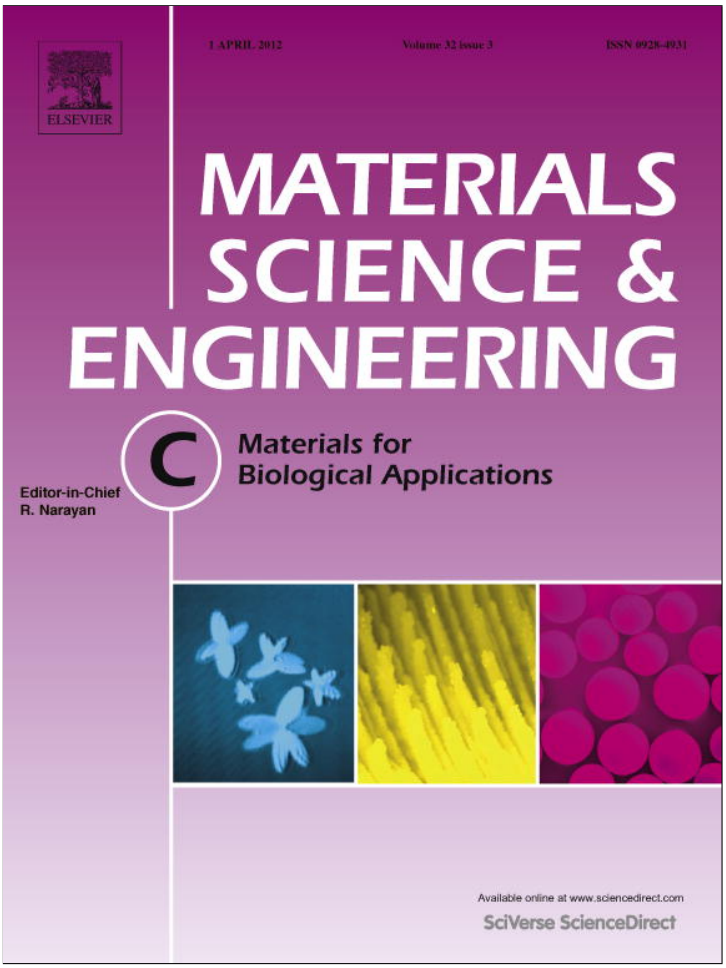

Materials Science and Engineering C 32 (2012) 452–463

Contents lists available at SciVerse ScienceDirect

Materials Science and Engineering C

journal homepage: www.elsevier.com/locate/msec

New cellulose–lignin hydrogels and their application in controlled release of polyphenols

Diana Ciolacu *, Ana Maria Oprea, Narcis Anghel, Georgeta Cazacu, Maria Cazacu

"Petru Poni" Institute of Macromolecular Chemistry, 41A, Grigore Ghica Voda Alley, 700487, Iasi, Romania

ARTICLE INFO

Article history:
Received 23 February 2011
Received in revised form 19 August 2011
Accepted 28 November 2011
Available online 3 December 2011

Keywords:
Cellulose
Lignin
Hydrogels
Polyphenols
Swelling
Controlled release

ABSTRACT

Novel superabsorbant cellulose–lignin hydrogels (CL) were prepared by a new two-step procedure consisting in dissolving cellulose in an alkaline solution with further mixing with lignin, followed by the chemical crosslinking with epichlorohydrin. The crosslinking occurrence was verified by Fourier Transform Infrared spectroscopy (FT-IR). The effect of the structure features of cellulose–lignin hydrogels on their dehydration heat was evaluated by Differential Scanning Calorimetry (DSC). The Scanning Electron Microscopy (SEM) images reveal some morphological aspects of the hydrogels. The degree as well as the rate of swelling in a mixture of water:ethanol = 19:1 were estimated. The possible application of these hydrogels as controlled release systems was tested. Polyphenols known as having a wide range of biological effects were selected to be incorporated in such hydrogels by an optimal procedure. The extract of grapes seeds from the *Chambourcin* type was used as a source of polyphenols (PF). The amount of the incorporated polyphenols was estimated by UV–VIS measurements. Characterization of the hydrogels containing polyphenols was performed by FTIR spectroscopy. Some parameters were estimated based on the registered spectra, as H-bond energy (E_H), the asymmetric index (a/b) and the enthalpy of H-bond formation (ΔH). The modifications of the thermal behavior and morphology induced by the presence of the polyphenols in hydrogels were highlighted by DSC and SEM, respectively. The release of polyphenols from CL hydrogels depended on the lignin content from matrices, as assessed by spectral studies. Both loading with polyphenols and their release can be controlled by the composition of the hydrogels. The kinetic of polyphenols release was studied.

1. Introduction

Hydrogels are polymeric networks that can absorb large amounts of water while remain insoluble in aqueous solutions due to chemical or physical crosslinking of individual polymer chains. These can be prepared from natural or synthetic polymers [1].

Innovative hydrogel products have been developed either as water absorbents for specific applications (e.g., personal hygiene products, underwater devices, water reservoirs for dry soils) [2,3] or as biomedical devices, including soft contact lenses, lubricating surface coatings, controlled drug release devices, wound healing dressings, cell immobilization islets, three-dimensional cell culture substrates, and bioactive scaffolds for regenerative medicine [4–7]. Among these applications, hydrogel-based drug delivery devices have become a major area of research interest with several commercial products already developed [8].

Although hydrogels made from natural polymers may not provide sufficient mechanical properties and may contain pathogens or evoke immune/inflammatory responses, they do offer several advantageous properties such as inherent biocompatibility, biodegradability, and biologically recognizable moieties that support cellular activities [8]. The growth of hydrogel based on natural polysaccharides technologies helped to improve many fields ranging from food industry and cosmetics to pharmaceuticals and biomedical implants [9–12].

Cellulose is the most common organic polymer, and is considered an almost inexhaustible source of raw material for the increasing demand for environment friendly and biocompatible products [13]. The interest on cellulose-based superabsorbent hydrogels is increasing both in the scientific and the industrial field due to their biodegradable character and their high swelling capacity [14,15]. These hydrogels are obtained by cross-linking of cellulose derivatives using difunctional molecules as cross-linkers, which covalently bind different polymer molecules in a three-dimensional hydrophilic network. Epichlorhydrin, aldehydes and aldehyde-based reagents, urea derivatives, carbodiimides and multifunctional carboxylic acids are the most widely used crosslinkers for cellulose [7,16–18].

Lignin is a natural phenolic polymer occurring in higher plant tissues and is the second most abundant polymer after cellulose. It is usually obtained as waste products of pulp and paper industry and often used as fuel for the energy balance of the pulping process. Due to their very complex structure, lignin has rather limited industrial

* Corresponding author. Tel.: +40 232 217454; fax: +40 232 211299.
E-mail address: dciolacu@icmpp.ro (D. Ciolacu).

0928-4931/$ – see front matter © 2011 Elsevier B.V. All rights reserved.
doi:10.1016/j.msec.2011.11.018

use. Hence, the great challenge is to find novel applications for lignin. Recently, there is an increasing interest in the potential health applications of lignin. Many researchers have attributed potential health benefits to lignin such as high activity in binding sodium salt of cholic acid and antitumoral, antiviral and immunopotentiating activity, as well as, antibacterial and antiparasite action [19–21]. It is known that lignin is an effective free radical scavenger that stabilizes the reactions induced by oxygen and its free-radical species [22]. As a major component in dietary fiber, lignin can inhibit the activity of enzymes related to the generation of superoxide anion radicals and obstruct the growth and viability of cancer cells [23]. Lignin displayed potent antiviral activity by directly interacting with the virus. Anti-HIV activity of lignin was significantly higher than that of tannins and flavonoids [24].

In order to create novel hydrogels with unique physical and functional properties, lignin was incorporated in the matrix of cellulose, to bring to materials the potential in human health of this bioactive compound and for a regulation of the rate of release. There are only a few studies related with the hydrogels obtained from lignin and these reports on the derivatives of lignin, as lignin–phenol–resorcinol resin cross-linked with glutaraldehyde [25] and to lignin/synthetic polymers gels synthesized by graft copolymerization between acrylamide (AM), poly(vinyl alcohol) (PVA) with alkaline or kraft lignin (AM–PVA–g-lignin) [26].

By combining the biocompatibility with tissues and blood, nontoxicity and low price of cellulose with the antioxidant and free radical scavenger properties of lignin, in this paper we obtained new cellulose–lignin hydrogels with the aim to be tested in cosmetic and pharmaceutical applications.

The best approach for such tests consists in the immobilization of different active principles (drugs, enzymes or proteins, etc.) and their release in controlled conditions. It is well known that the morphology and the transport characteristics of such systems highly depend on their components and the way of preparation them.

The polyphenols constitute one of the most numerous groups of chemicals found in higher plants and are presented in many products of vegetable origin that are used as human foods or animal feeds.

In this paper we used grapes-derived polyphenols as active principles to be incorporated in the hydrogels. Grapes and their products have been consumed for a long time. The health benefits of grapes are thought to arise mainly from bioactivities of their polyphenols. The phenolic compounds from grapes exhibit a wide range of biological effects linking to human health benefits and new research indicates that may have extremely important properties as antioxidant, cardioprotective, anti-carcinogenic, antiviral, anti-inflammatory, anti-aging and antimicrobial properties [27–32].

The aim of this work is to present the preparation of novel cellulose–lignin hydrogels and to demonstrate their ability to function as systems for incorporation and controlled release of active principles, taking the specific case of the polyphenols from grapes. The obtained structures were investigated by FT-IR and UV–VIS spectroscopy, differential scanning calorimetry (DSC) and scanning electron microscopy (SEM).

2. Experimental

2.1. Materials

Microcrystalline cellulose — Avicel HP-101 (C), purchased from Fluka was dissolved in 8.5% NaOH solution, at −30 °C. The sample was allowed to stand for 24 h at this temperature. The frozen solid was then thawing at room temperature and water was added until a clear cellulose solution was obtained [33,34].

Steam explosion lignin from aspen wood (L) was supplied by ENEA, Italy. Epichlorohydrin (ECH) supplied by Fluka, purity ≥99.5%, b.p 115–117 °C was used without further purification.

Polyphenols (PF) were obtained by extraction from grape seeds of *Chambourcin* type. Firstly, the seeds were separated from the marc, dried and sorted at dimension between 1 and 2 mm, then were ground and at the end a brown-red powder resulted. This powder was extracted in a device for continuous extraction (Soxhlet) with ethyl-ether to degrease vegetal material. The obtained residue was treated with ethanol for the extraction of polyphenolic compounds, at the optimum ratio between the vegetal material and the solvent 1:3.5 and the extraction was conducted until the complete extraction of vegetal material. The alcoholic extract was concentrated on a rotary evaporator system until the solvent complete evaporation. The final product as dark red powder resulted in 2.74% yield. The obtained residue contains 97.32% organic substance and 2.68% anorganic compounds. The identification of the major phenolic compounds from grape seeds made according to the literature methods [35–37] led to the following composition: 34.3% total polyphenols, as gallic acid, 30.8% total polyphenols, as quercetin, 18.3% monomers anthocyanin, and 9.3% proanthocyanidins.

2.2. Preparation of the hydrogels

Cellulose hydrogel (C) — 0.5 g microcrystalline cellulose was dissolved in 6.7 mL solution 8.5% NaOH by freezing at low temperature (−30 °C). After thawing, 2.14 mL ECH was added in the clear cellulose solution under continuously stirring. The obtained composition was maintained for 8 h at 80 °C. The hydrogels were washed with warm and cold distilled water, during one week, in order to remove the NaOH in excess and NaCl formed. Then, for the limitation of the ECH traces, the hydrogels were washed with acetone. The samples were dried in vacuum, at the room temperature.

Cellulose–lignin hydrogels (CL). For the preparation of cellulose/lignin hydrogels, the cellulose was firstly dissolved as described above, in alkaline solution at low temperature (−30 °C). After thawing, in the obtained cellulose solution, different amounts of lignin (Table 1) and then 2.14 mL ECH were added, under continuously stirring. The obtained composition was carefully transferred into device and the cross-linking reaction was allowed to proceed for 8 h, at 80 °C. The hydrogel was washed thoroughly with warm and cold water, with acetone and then the sample was dried in vacuum, at room temperature and weighted, the yields being presented in Table 1.

2.3. Swelling measurements

Swelling studies were performed for all hydrogels in a medium of water:ethanol = 19:1, during 24 h at 37 °C. The samples were periodically removed, gently wiped with a soft tissue to remove

Table 1
The feed amounts used to prepare cellulose/lignin hydrogels and the main characteristics of these.

Sample	Reaction mixture composition		Hydrogel features	
	Cellulose, g	Lignin, g	Yield, %	Q_{max},[a] %
C	0.500	0.000	99.90	1145
CL1	0.375	0.125	99.91	2358
CL2	0.335	0.165	99.52	2446
CL3	0.250	0.250	92.34	2642
CL4	0.165	0.335	78.28	2737
CL5	0.125	0.375	71.70	3061

[a] Maximum swelling degree in mixture water:ethanol = 19:1.

surface solution and then quickly weighed. The swelling degree at equilibrium was calculated according to the equation:

$$Q_{max} = \frac{W_s - W_d}{W_d} \times 100(\%) \quad (1)$$

where:

W_d dry hydrogel weight (g);
W_s swollen hydrogel weight (g).

The maximum swelling degrees are presented in Table 1.

To determine the kinetics of solvent diffusion into the matrices (swelling) the following equation was used [38]:

$$\frac{W_t}{W_{eq}} = k_{sw} \times t^{n_{sw}} \quad (2)$$

where:

W_t the amount of water:ethanol (19:1) solution, absorbed by the matrices at time *t*;
W_{eq} the amount of water:ethanol (19:1) solution, absorbed by the matrices at equilibrium;
k_{sw} the swelling rate constant characteristic of the system;
n_{sw} the power law diffusion exponent, which describe the mode of the penetrant transport mechanism.

The constants n and k were calculated from the slopes and intercepts of the plots of ln (W_t/W_{eq}) vs ln t [39].

Eq. (2) was applied in the early swelling stages (swelling degree less than 60%) and was represented log Ft as a function of log t when the linearity was observed.

2.4. Incorporation of the polyphenols in cellulose–lignin hydrogels (CLa)

0.1 g Dried hydrogel in powder form was immersed in 2.5 mL solution of 5% polyphenols in water:ethanol = 19:1 and left to swell at room temperature for 24 h, while the PF penetrates and/or attached into matrices. At the end, the polyphenols-loaded samples were dried in vacuum, at room temperature. UV spectrum was registered for the remained solution in order to establish the incorporated polyphenol concentration. The calibration curve (Fig. 1) was drawn in this aim for the solution of polyphenols by registering UV–VIS spectra of different PF/water–ethanol solutions having standard concentrations of polyphenols in range of 10^{-4}–10^{-2} g/mL.

The UV absorbance at 278 nm was measured at every concentration. The unknown concentrations of the remained solutions after PF incorporation were determined using the equation obtained from the calibration curve, y = 107.46145x + 0.04522, with a correlation coefficient of $R^2 = 0.99$. The concentration of the incorporated polyphenols in polymers matrix was determined as the difference from the initial concentration of PF of the above determined parameter.

The incorporation degree (Id_1) was calculated based on UV studies by using the following equation:

$$Id_1 = \frac{(V_1 \times c_1) - (V \times c)}{m_1} \times 100(\%) \quad (3)$$

where:

V_1 the volume of initial PF solution (mL);
c_1 the initial concentration of the PF (g/mL);
V the remained volume of the PF solution (mL);
c the concentration of remained PF in solution, determined from the equation of calibration curve (g/mL);
m_1 the amount of dry hydrogel (g).

The second method used to establish the loaded PF quantity was the gravimetrical method, which establishes the PF incorporation degree (Id_2) by equation:

$$Id_2 = \frac{m_2 - m_1}{m_2} \times 100(\%) \quad (4)$$

where:

m_1 the initial dry hydrogel weight (g);
m_2 the PF incorporated hydrogel weight (g).

2.5. The encapsulation efficiency (EE)

The CL hydrogels loaded with polyphenols were rinsed with an water:ethanol mixture and the amount of PF rinsed out into the released medium was determined by measuring the UV absorption at 278 nm and determining the concentration based on the calibration curve. The Eq. (5) was used for EE calculation is:

$$EE = \frac{L_1 - L_2}{L_1} \times 100(\%) \quad (5)$$

where:

L_1 the total amount of PF incorporated, g;
L_2 the amount of PF released in medium, g.

2.6. The release of the polyphenols from hydrogels

In vitro release studies have been conducted by a standard dissolution set-up [40]. The dissolution medium was water:ethanol = 19:1. During dissolution testing, the media was maintained at 37 ± 0.5 °C. 1 mL aliquots of medium were withdrawn periodically at predetermined time intervals and the absorbance was measured at the λ_{max} value of 278 nm. In order to maintain the solution concentration, the sample is reintroduced in the system after analyzing. The concentrations of the polyphenols in solution were calculated based on calibration curves determined for the active ingredient at the specific maximum absorption wavelengths (278 nm).

A semi-empirical equation using Korsmeyer and Peppas model was used to kinetically analyze the data regarding the polyphenols release

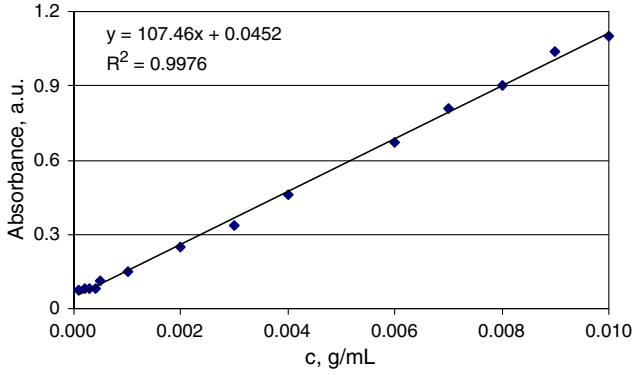

Fig. 1. Calibration curve of PF in water:ethanol mixture (19:1), at 37 °C.

from the systems which is applied at the earlier stages (approximately 60% fractional release) [41]:

$$\frac{M_t}{M_\infty} = k_r \times t^{n_r} \quad (6)$$

where:

M_t/M_α the fraction of polyphenols released at time t;
M_t the amount of polyphenols released at time t;
M_∞ the amount of polyphenols released at infinite time;
k_r the rate constant, characteristic to the polyphenols–polymers system;
n_r the diffusional exponent, which suggests the nature of the release mechanism.

As for swelling process, in case of the above equation, a value of $n_r = 0.5$ indicates a Fickian diffusion mechanism of the active principle from matrix, while a value $0.5 < n_r < 1$ indicates an anomalous or non-Fickian behavior. When $n_r = 1$ a case II transport mechanism is involved while $n_r > 1$ indicates a special case II transport mechanism [42,43].

The corresponding polyphenols-release profiles were represented through plots of the cumulative percentage of polyphenols released versus time.

2.7. Equipments

UV–VIS absorption spectra were recorded at room temperature on a Hewlett Packard 8540A UV–VIS spectrophotometer, in 10 mm quartz cells, using water:ethanol mixture as a solvent.

FT-IR/ATR experiments were carried out on silicon single-crystal parallelepiped internal reflection elements (IRE; 55×5×2 mm, 45° incident angle), using a Bruker Vertex 70 instrument. All the spectra were the results of 256 scans at a resolution of 4 cm^{-1}, frequency range 4000–400 cm^{-1}.

The morphology of the samples was investigated by using a Scanning electron microscope (SEM) type Quanta 200, operating at 30 kV with secondary electrons, in low vacuum mode. For a better observation of the pores, the hydrogels were previously freeze-dried in an ALPHA 1-2/LD device (Martin Christ GmbH, Germany), for 15 h, at −65 °C. The cross-sections were prepared by cutting the dry hydrogels with a sharp razor blade, in order to expose the internal structures.

The DSC curves were recorded on a Mettler DSC 12E with a heating rate of 20 °C/min. The samples were conditioned at the constant relative humidity of 65% and temperature of 25 °C, until constant weights.

3. Results and discussion

3.1. Incorporation of polyphenols in hydrogels matrix

New hydrogels have been prepared based on cellulose and lignin. The two natural polymers were together homogenized into an alkaline solution. Epichlorohydrin (ECH) was added as a crosslinker. The mixture was heated during 8 h, at 80 °C to form the network that subsequently was purified by washing with water and acetone and then dried in vacuum, at room temperature. The hydrogels are uniform and the intensity of color varied from light to dark brown with increasing lignin quantity.

ECH is a convenient base-catalyzed cross-linking agent and it has been widely used for the cross-linking of carbohydrates in polysaccharide chemistry [44–46]. In alkaline conditions, the epoxy cycle from ECH opens and then binds to cellulose or lignin by their OH groups. After the chloride displacement, new epoxy groups can

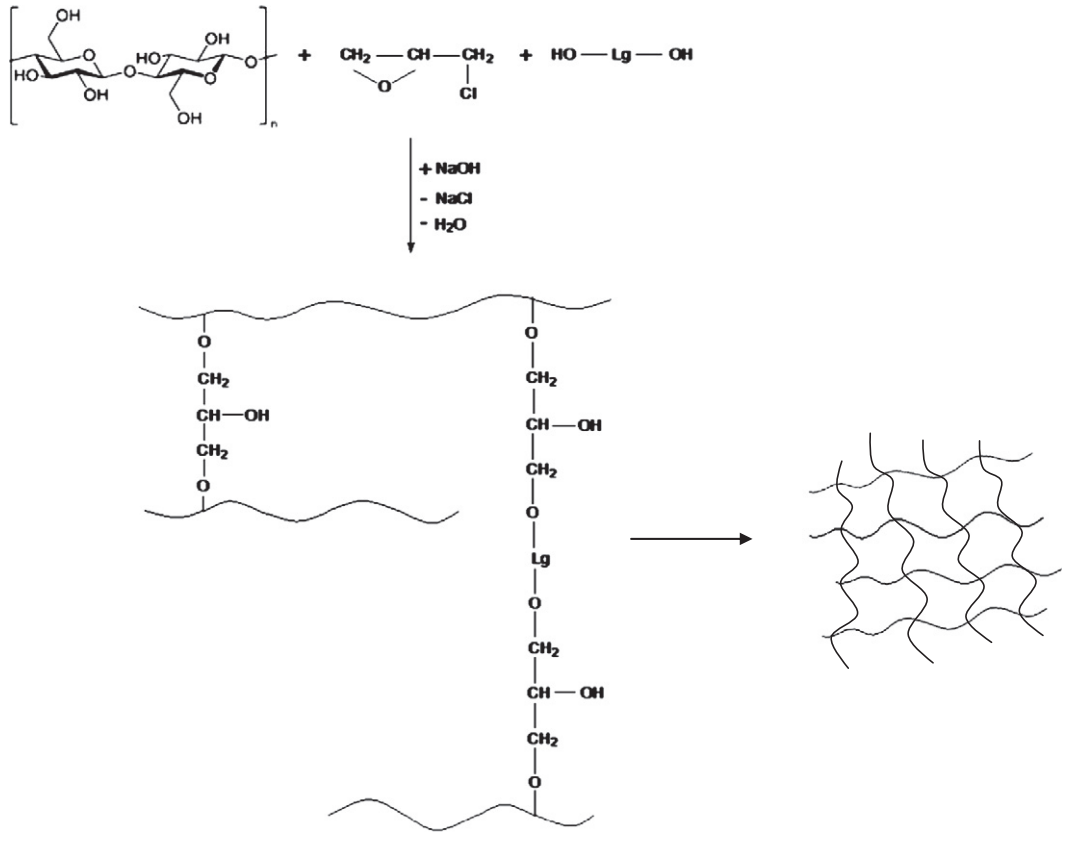

Fig. 2. The presumed reaction pathway for the formation of CL hydrogels with ECH as cross-linker.

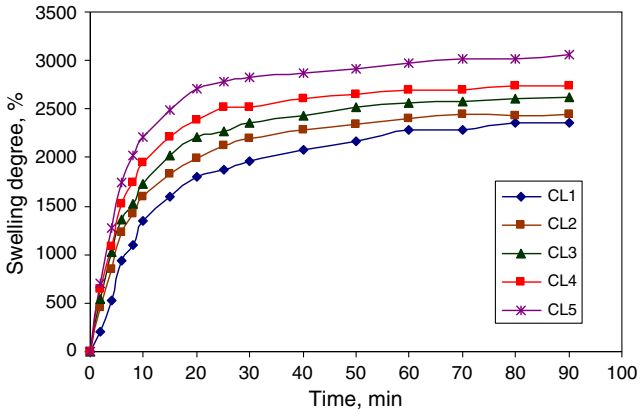

Fig. 3. Variation of the hydrogels swelling degrees as a function of time and composition.

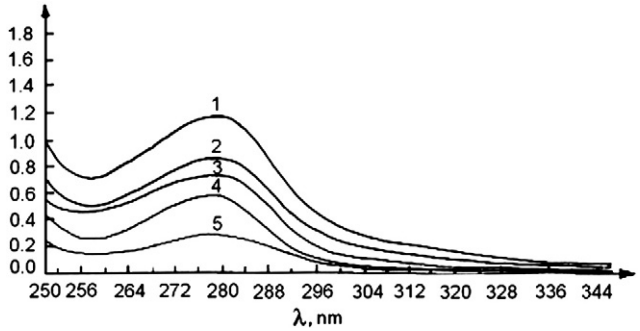

Fig. 4. UV spectra of the remained solutions after PF incorporation in different CL hydrogels: 1 — CL1a; 2 — CL2a; 3 — CL3a; 4 — CL4a; 5 — CL5a.

form, which react further with the hydroxyl groups from other cellulose or lignin chains and thus the cross-linking between C and L occurs, as shown in Fig. 2.

The crosslinking reaction could involve two structural units that may or may not belong to the same cellulosic chain, or could be accomplish without involvement of the lignin. Moreover, some side reactions could occur. For example, some ECH molecules may react only with one hydroxyl group of cellulose or lignin, or some unreacted ECH hydrolyzes to glycerol.

It was found that cellulose–lignin ratio is a critical parameter in CL network formation and has a strong influence on the hydrogel properties, particularly on water retention capacity.

These networks were prepared to be tested for controlled release of polyphenols, which are soluble in fluids with physiological pH. In order to mimic the aqueous composition of physiological fluids, the active principle was dissolved in 19:1 water:ethanol medium. The swelling studies were led in water–alcohol mixture having the same composition as presented above and revealed values of the maximum swelling degree (Q_{max}) situated in range of 2300–3000 wt.% (Table 1), fact which demonstrates the superabsorbant character of these types of hydrogels. Fig. 3 shows that the swelling capacity of hydrogels increases by increasing lignin content, the sample CL5 based on 25% cellulose and 75% lignin having the highest value.

This behavior is explained by the chemical uniqueness of lignin. Lignin contains a high number of polar groups (aromatic and aliphatic hydroxyls, carbonyls, ethers). By involving itself in crosslinking reactions, some hydroxyl groups are blocked by forming C – O – C linkages but many other remain free, conferring hydrophilicity to the resulted three-dimensional matrix. Simultaneously, pores with different structures and polarities could be formed. Thus, an increase in lignin content in CL hydrogels produces a more relaxed network with higher swelling capacity.

The high values of the swelling degree for CL hydrogels demonstrate the enhanced diffusion of a large volume of liquid. As a result, it is expected as a large amount of polyphenols to be also accommodated into the matrix. In order to determine the loading capacity of polyphenols in CL hydrogels, the swelling studies were performed in media where polyphenols have a good solubility, as water:ethanol (19:1) solution. From the obtained swelling profiles, the diffusion exponent, n, was calculated according to Eq. (2). The swelling kinetic parameters for various cellulose/lignin-based hydrogels are presented in Table 2.

Table 2
Kinetic parameters of swelling in water:ethanol (19:1) solution for CL hydrogels.

Compositions	k_{sw} (min^{-n})	n_{sw}	R^2
CL1	0.11	0.63	0.99
CL2	0.15	0.61	0.99
CL3	0.21	0.47	0.99
CL4	0.27	0.41	0.99
CL5	0.31	0.33	0.99

The values of diffusion parameter – n_s – obtained in the case of cellulose/lignin-based hydrogels indicate the presence of both diffusion and erosion mechanisms, resulting in a so called anomalous swelling mechanism for all formulations. This fact suggests that more than one process control the polyphenols release [39]. In the case of the swelling rate constant, k, the values increase by raising the lignin content in hydrogels composition, fact which indicates that hydrogels with a smallest quantity of lignin exhibited the slowest release rate.

The incorporation of polyphenols in cellulose–lignin matrices led to new samples labeled as CLa, respectively, CL1a, CL2a, CL3a, CL4a and CL5a, depending on hydrogel composition.

Two pathways were followed to estimate the PF quantity absorbed by the natural polymers systems, as spectroscopy (Id_1) and gravimetrical (Id_2) measurements, respectively.

The first procedure consisted in recording of UV spectra for the polyphenols aqueous solutions remained after the PF incorporation process. It was observed a decreasing of the absorption band at 278 nm from CL1 to CL5 proving the increasing of polyphenols amounts loaded in matrix (Fig. 4).

The obtained values for Id_1 and Id_2 as well as for encapsulation efficiency are presented in Table 3.

By examining the data from Table 3 it can be seen that, although different due to the procedure used for their measurements, the Id_1 and Id_2 as well as EE values follow the same increasing trend in the series C-CL5.

Based on these considerations, the amount of loaded polyphenols depends on the hydrogel composition and on the implicit swelling properties of cellulose–lignin hydrogels. Thus, the highest polyphenols incorporation degree ($Id_1 = 30.3\%$, $Id_2 = 43.8\%$) was obtained for the CL5 hydrogel, that showed the highest swelling capacity ($Q_{max} = 3061\%$) (Table 3). The PF encapsulation efficiency (EE)

Table 3
Some relevant parameters for the incorporation of the polyphenols in CL hydrogels.

Sample	PF Incorporation degree, %wt.		EE [c], %
	Id_1 [a]	Id_2 [b]	
C	12.5	21.8	61.9
CL1a	20.5	24.7	82.6
CL2a	22.8	30.9	88.4
CL3a	25.8	32.1	91.1
CL4a	27.5	36.5	95.0
CL5a	30.3	43.8	96.2

[a] Determined based on UV–vis spectra.
[b] Determined by gravimetrical method.
[c] Encapsulation efficiency.

increases with increase of lignin content in matrices, as well, the highest value for this parameter being also obtained for the sample CL5. Thus, the variation of CL hydrogels composition permits a control of PF incorporation and its efficiency.

3.2. FT-IR/ATR measurements

3.2.1. Cellulose–lignin hydrogels

The first evidence for the crosslinking is the insolubility of the resulted materials. In order to confirm the achievement of the cross-linking reaction between cellulose and lignin, FT-IR spectroscopy was used, this being a highly effective analytical tool to study the interactions between polymers. The hydrogen bonding formation and the interpolymer miscibility can be studied.

The spectra of cellulose (C), lignin (L) as well as hydrogel based on 50% cellulose and 50% lignin (CL3) are shown in Fig. 5. The changes of many FT-IR bands characteristic of cellulose reflect the occurrence of the cross-linking reaction with lignin.

The broad band between 3700 and 3000 cm^{-1} is assigned to the OH-stretching vibration. CL3 spectrum shows a strong wide band at 3436 cm^{-1}, caused by the presence of alcoholic and phenolic hydroxyl groups involved in hydrogen bonds. However, the peak is weaker than the corresponding peaks from C spectrum (3350 cm^{-1}) and also from L spectrum (3429 cm^{-1}), fact which could indicate that the cross-linking reaction between cellulose and lignin has occurred. The modifications which take place during cross-linking of cellulose with lignin can be further confirmed by the presence of the absorption band at 2877 cm^{-1} from CL3 spectrum, corresponding to the C–H stretching vibration. The intensity of this band is visible increased and is situated between the bands 2899 cm^{-1} from cellulose spectrum (C–H stretching vibration) and 2844 cm^{-1}, assigned to C–H stretching vibration of the methoxyl group, characteristic to lignin. Also, in CL3 spectrum a peak at 2912 cm^{-1} appears, probably by shifting from 2938 cm^{-1} (L spectrum) which could indicate the presence of lignin in the matrix.

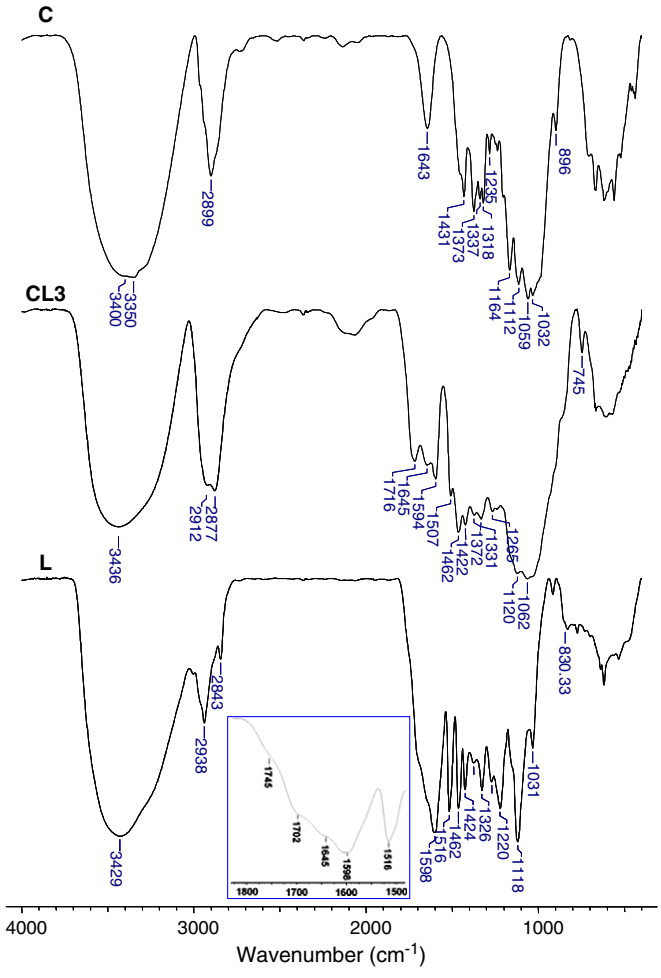

Fig. 5. FT-IR spectra for cellulose (C), lignin (L) and cellulose–lignin hydrogel (CL3).

The spectrum of CL3 shows absorption bands caused to the stretching vibrations of carbonyl groups which are located in the 1765–1615 cm^{-1} wavenumber range indicating the presence of lignin in hydrogel. In case of lignin, according to Herbert [47], the absorption band located at 1716 cm^{-1} can be assigned to ketone group located at β-position and that one located at 1645 cm^{-1} to ketone group located at α-position. The absorption band at 1594 cm^{-1} is related to the vibration of aromatic rings present in lignin. In case of C spectrum in the discussed region appears only one peak assigned to absorbed water, at 1643 cm^{-1} which is associated with the OH stretching.

Referring to the band at 1463 cm^{-1}, this is a characteristic to lignin spectrum and is assigned to deformation vibrations of CH_2 groups [48]. In CL3 spectrum, this band is maintained at the same wavenumber, but a strong decrease of its intensity was recorded.

The FT-IR absorption band at 1431 cm^{-1} from cellulose spectrum, assigned to a symmetric CH_2 bending vibration, is shifted to a lower wavenumber, 1422 cm^{-1}, as a result of the cross-linking reaction and the intensity of this peak is decreased. This shift indicates the development of new inter- and intramolecular hydrogen bonds [49,50]. Moreover, this band is known as the 'crystallinity band' and a decrease in its intensity reflects a decrease of the crystallinity degree of cellulose. This is the same with the band at 1373 cm^{-1} assigned as CH_2 bending, which, in the spectrum of CL3, is shifted at 1372 cm^{-1} with a visible decrease in intensity.

The band at 1337 cm^{-1}, assigned as C–OH bending in plane at C-2 or C-3, is decreased and is moved to 1331 cm^{-1} after cross-linking reaction, while the band from 1318 cm^{-1} that is assigned to CH_2 wagging, disappears from CL3 spectrum. Also, the band at 1236 cm^{-1} from C spectrum, corresponding to C–OH bending in plane at C-6, disappears as a result of the cross-linking process.

Direct evidence of the cross-linking reaction is the formation of ether bonds between cellulose and lignin which are shown in FT-IR spectrum of CL3 hydrogel by an increase of aryl ether band (C–O–C stretching) at 1265 cm^{-1} and of alkyl ether band at 1120 cm^{-1} (C–O–C stretching) and 1062 cm^{-1} (C–O stretch from alkyl substituted ether). The absorption band at 1265 cm^{-1} is assigned to asymmetric vibration of the C–O–C linkages in phenolic ether bonds, the band at 1062 cm^{-1} is caused by primary and aliphatic ethers groups and the band at 1120 cm^{-1} to deformation vibration of ether linkages (Fig. 6). These bands were also reported by Duri in a study related FT-IR investigation of different modified lignin [51].

In the spectrum of lignin, the band at 1270 cm^{-1} and 1220 cm^{-1} is caused by stretching of CH bonds in guaiacyl rings, while the band at 1031 cm^{-1} and 1118 cm^{-1} to the stretching vibration of syringyl rings. The last one, if still present in CL3 spectrum, is overlapped by the large band of alkyl ether groups.

In the region 900–780 cm^{-1} of lignin spectrum, the absorption bands caused by deformation vibrations of C–H bonds on the benzene ring are located (830 cm^{-1} and 781 cm^{-1}) [48]. In cellulose spectrum, the absorption band at 897 cm^{-1} is assigned to C–O–C stretching at β-(1→4)-glycosidic linkages. All these bands are not present in FT-IR spectrum of CL3, but instead a new and sharp band appears at 745 cm^{-1}, assigned to the residual C–Cl stretching vibration [52]. In FT-IR spectrum of ECH (not shown) at the same wavenumber (745 cm^{-1}) is present the band with the biggest intensity from the spectrum. The strong decrease of this band in CL3 spectrum confirms the occurrence of the cross-linking.

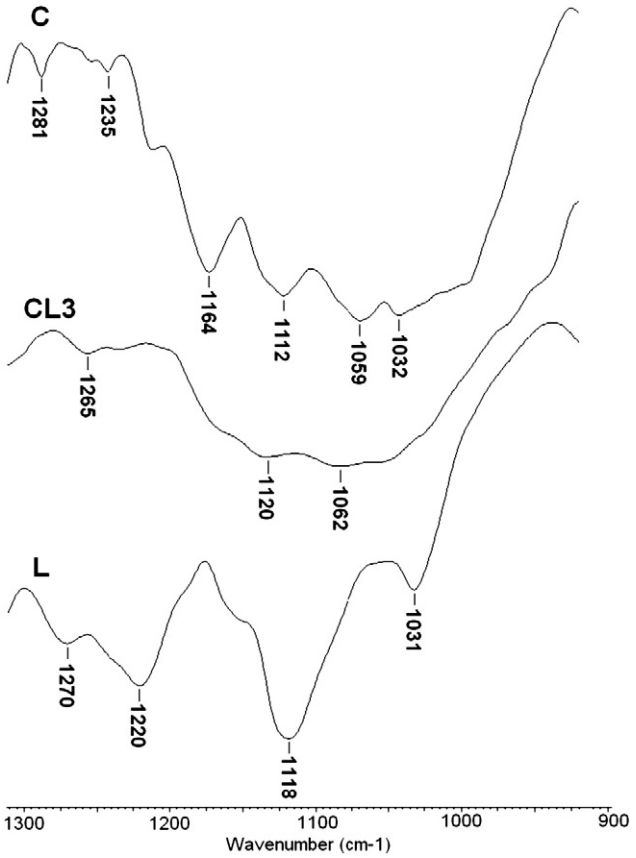

Fig. 6. FT-IR spectra of cellulose (C), lignin (L) and cellulose–lignin hydrogel (CL3) in 1300–1000 cm^{-1} region.

FT-IR spectroscopy was also used as an alternative approach to quantify the formation of the cross-linking bonds. In Fig. 7a is shown the decrease of the absorption peaks assigned to OH groups stretching vibration from CL1 to CL5. During cross-linking reaction, the OH bands are split and O is involved in new ether linkages, thus decreasing the amount of OH groups and their intensity in IR spectrum. This is an indirect measure of the crosslinking degree (Fig. 2).

In the 1500–900 cm^{-1} wavenumber range (Fig. 7b), the intensities of the aryl and alkyl ether bands appear as a function of hydrogels compositions. An increase of intensities of the absorption bands characteristic to ether bonds with the increase of the lignin amount in hydrogels composition was recorded. This fact proves the incorporation of a higher amount of lignin in cellulose matrix, which contributes to an increase of ether linkages and implicitly to an increase of the swelling degree of the hydrogels, owing to its bulky and branched structure, consisting of phenolic hydroxyl, carboxylate and aliphatic hydroxyl groups.

The structural modification of the cellulose structure after cross-linking with lignin, in the presence of ECH, can be established from the ratio between the intensities of ether band (1300–1000 cm^{-1}) and that at 2900 cm^{-1} selected as an internal standard. Fig. 8 presented the variations determined by incorporation of lignin in cellulose matrix related to the ether absorption bands from CL hydrogels.

It can be seen that the intensities of aryl and alkyl ether groups proving the formation of cross-links between the polymeric components increase from CL1 to CL5.

3.2.2. Cellulose–lignin hydrogels incorporating PF

By the incorporation of polyphenols in CL hydrogels, the OH band is shifted to lower wavenumbers. In the same time a slight decrease of this peak with the increasing of the concentration of absorbed polyphenols in hydrogel can be observed, probably because of the new hydrogen bonds established between PF and CL hydrogels. This is exemplified in Fig. 7a for sample CL3a.

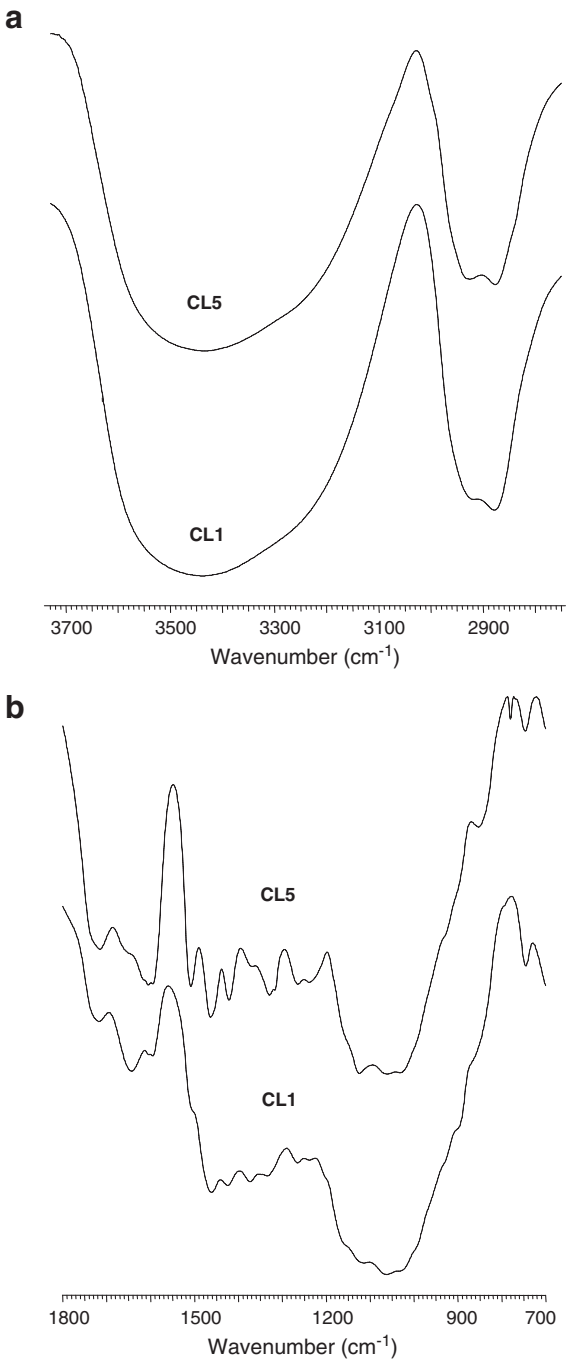

Fig. 7. FT-IR spectra of CL1 and CL5 hydrogels in the 3700–2700 cm^{-1} (a) and 1800–700 cm^{-1} (b) wavenumber ranges.

In FT-IR spectrum of polyphenols obtained from grapes seed (Fig. 9), the following characteristic bands can be identified: OH-stretching vibration at 3391 cm^{-1}, CH-stretching vibration at 2926 cm^{-1}, stretching vibration of C═O at 1709 cm^{-1}, stretching vibration of C–C at 1610 cm^{-1}, deformation vibrations of CH at 1369 cm^{-1}, stretching vibration of C–O at 1284 cm^{-1} and 1245 cm^{-1}, stretching vibration of C–O–C at 1156 cm^{-1} and 1105 cm^{-1} and stretching vibration of C–O at 1046 cm^{-1}. Some of these bands can also be found in the system CL/PF, and their intensities increase with the polyphenols content. In Fig. 9b, the arrows

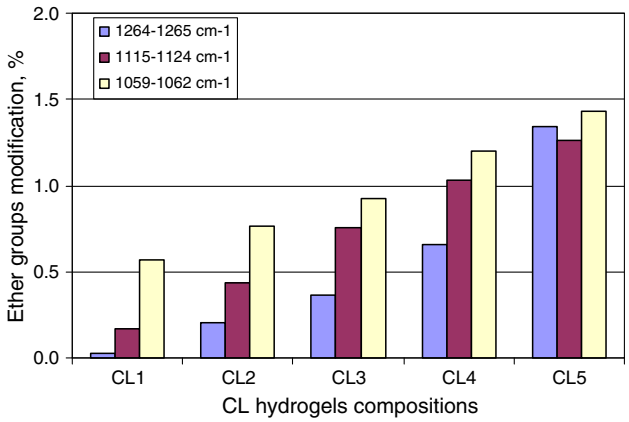

Fig. 8. Changes in FT-IR aryl and alkyl ether bands intensities depending on CL hydrogels composition.

indicate the bands for sample CL3 and the modifications occurring as a result of polyphenols incorporation in matrix (CL3a) can be observed.

Based on FT-IR spectra of the CL hydrogels and polyphenols/hydrogel systems, the energy of the H-bonds (E_H), the asymmetric index (a/b), the enthalpy of H-bond formation (ΔH) and the bond distance (R) were calculated.

The *energy of the H-bonds* (E_H, kJ) has been calculated using the following equation [53]:

$$E_H = \frac{1}{k} \times \frac{(\nu_0 - \nu)}{\nu_0} \quad (7)$$

where:

ν_0 the standard frequency corresponding to free –OH groups (3600 cm^{-1}),

ν the frequency of the bonded –OH groups (cm^{-1}), $k = 1.68 \times 10^{-2}$ $kcal^{-1}$.

The increase of the H-bonds energy values (E_H) involves the increase of the number of hydrogen bonds in the supramolecular structure of the natural polymers matrices/polyphenols (Table 4). This behavior can be observed for the sample loaded with polyphenols, where the increase of the value for energy of the H-bonds demonstrates an increase of the number of hydrogen bonds established between components.

The *asymmetric index* (a/b) is the ratio between the segments established as widths of the OH absorption band determined at the half of peak intensity [54]. The highest values for asymmetric index (a/b) are distinguished in the case of cellulose/lignin hydrogels (Table 4). For the systems incorporating polyphenols, a decrease of a/b ratio can be observed, which indicates a diminution of the sample uniformity.

The *enthalpy of H-bond formation* (ΔH, J/g) was determined using the following equation [55]:

$$-\Delta H = 0.016\Delta_{OH} + 0.63 \quad (8)$$

The wavenumber shift $\Delta\nu_{OH}$ between the free hydroxyl-stretching vibration and that of hydrogen-bonded species yields a measure of the average strength of the intermolecular interactions.

For polyphenols, $\Delta\nu_{OH}$ is 258 cm^{-1}, while for CLa hydrogels, the values are situated in the range of 218–250 cm^{-1}, as a function of the hydrogel's composition. The obtained ΔH values suggest that the average hydrogen-bond from CLa hydrogels is bigger than those established between the hydroxyl groups from CL hydrogels, fact also confirmed by the data obtained for the energy of the H-bonds.

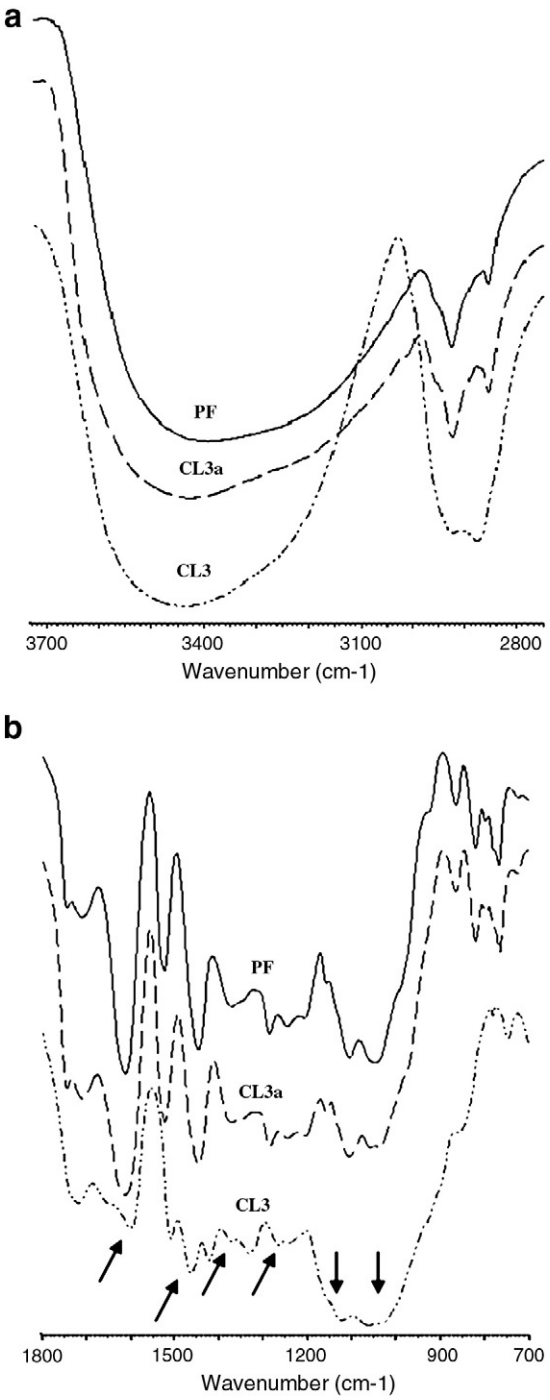

Fig. 9. Differences in the FT-IR spectra of PF, CL3 and CL3a hydrogels in the 3700–2700 cm^{-1} (a) and 1800–700 cm^{-1} (b) wavenumber ranges.

Pimentel and Sederholm have found linear relationships between *the bond distance* (R) for O–H…O and the frequency shift ($\Delta\nu$) of the OH absorption band caused by hydrogen bonding, and expressed it as follows [56]:

$$\Delta\nu = 4.43 \times 10^3 (2.84 - R) \quad (9)$$

As it can be observed from the results collected in Table 4, the hydrogen bond length (R) values obtained for all cellulose–lignin based hydrogels having incorporated polyphenols (CLa) are smaller than the ones reported for CL hydrogels, fact which evidences that the domains are packed in a highly ordered arrangement; note that shorter

Table 4
FT-IR spectral characteristic for CL hydrogels with or without polyphenols.

Sample	$\Delta\nu_{OH}$, cm^{-1}	ΔH, J/g	E_H, kJ	a/b	R, nm
PF	258	122.89	4.42	0.53	2.782
CL1	212	103.88	3.63	0.62	2.792
CL1a	218	106.36	3.73	0.49	2.791
CL2	213	104.29	3.65	0.58	2.792
CL2a	221	107.60	3.78	0.44	2.790
CL3	214	104.70	3.66	0.53	2.792
CL3a	225	109.25	3.85	0.40	2.789
CL4	214	104.70	3.66	0.50	2.792
CL4a	228	110.49	3.90	0.39	2.789
CL5	215	105.12	3.68	0.43	2.791
CL-5a	250	119.58	4.28	0.41	2.784

hydrogen bonds are generally stronger [57]. The shortest bond distance appears at polyphenols.

3.3. DSC studies

DSC is an excellent technique to assess the miscibility of the components within a hydrogel network and to prove the intermolecular interactions that may exist between the components.

In Fig. 10a the DSC thermograms of cellulose (C), lignin (L) and the hydrogel based on 50% cellulose and 50% lignin (CL3) are presented.

As can be seen, lignin exhibits a sharp endothermic peak at 80 °C while cellulose has a smaller and broad peak at 63 °C, which is caused by the evaporation of the solvent traces. The cross-linking of these two natural polymers determines a shift of the endothermic peak between the temperatures of the initial samples. This behavior certifies the formation of the cross-links within CL hydrogel.

In the case of CL3 hydrogel loaded with polyphenols (CL3a) it was recorded an increase of the endothermic peak and the maximum temperature shifted to higher temperature (Fig. 10b).

Fig. 11 presents the DSC curves of various compositions of cellulose–lignin based hydrogels. Endothermic peak intensity increases with increasing lignin content in the sample. This is due to the very

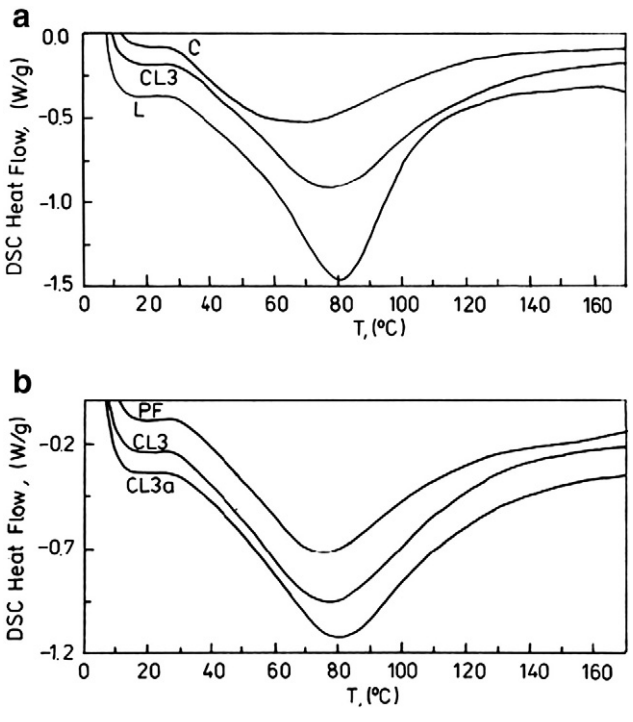

Fig. 10. DSC curves of: a) C, L and CL3 hydrogel; and b) polyphenol (PF), CL3 hydrogel and loaded CL3 hydrogel (CL3a).

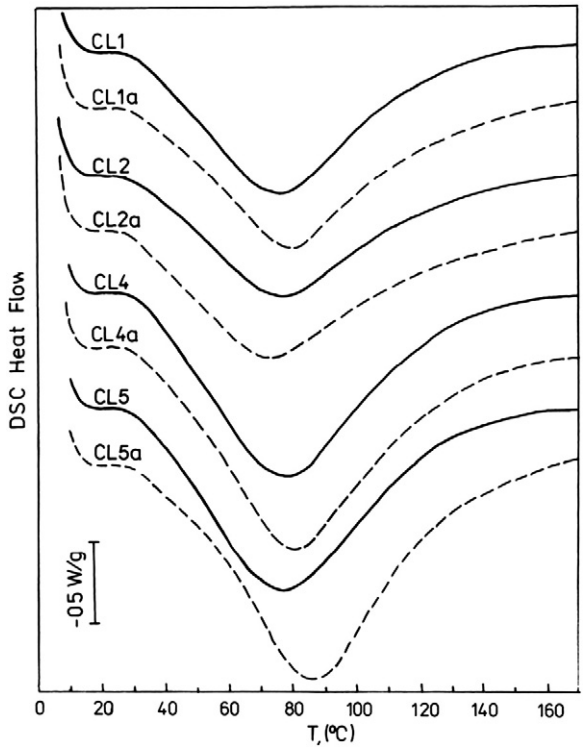

Fig. 11. Comparative DSC thermograms of unloaded (CL) and loaded (CLa) hydrogels.

broad molecular weight distribution of lignin and the phenolic OH-functionality which induces strong hydrogen bonding effects. The areas of endothermic peaks detected in the DSC curves alongside the increase of the dehydration heat (Table 5) are in a good relationship with the percent of water uptaken by hydrogels, implicit with the data obtained for swelling degrees (Table 1). Also, the movement of the peak temperature (Tmax) to higher values indicates an enhancement of the thermal stability, fact which exhibits a strong intermolecular interaction existing in hydrogels. These results indicate that Tmax value increases when lignin amount increases due to the enhancement of crosslinking density.

In the case of CL/PF systems (CLa), the peaks increased significantly from CL1a to CL5a and a shift of the maximum temperature to higher values, from 78 °C (CL1a) to 86 °C (CL5a), was also recorded.

The dehydration heat recorded for cellulose is 160.8 J/g, while for lignin is 291.2 J/g. From the data presented in Table 5 regarding the values of ΔH for CL hydrogels is evident that the obtained values range between those of the initial samples, which confirm the achievement of cross-linking.

Polyphenols present a heat of dehydration of 196.0 J/g. The values established for the dehydration heat of CLa hydrogels are increased from CL1a to CL5a, as a result of PF incorporation. The obtained data are in good correlation with the enthalpy of H-bond formation determined from FT-IR spectra.

Table 5
Dehydration heat for CL and CLa hydrogels.

Sample	ΔH, J/g	
	Hydrogels without PF (CL)	PF loaded hydrogels (CLa)
CL1	250.5	270
CL2	252.3	271
CL3	254.5	282
CL4	256.9	312
CL5	295.8	321

3.4. Scanning electron microscopy (SEM) analysis

The SEM micrographs of hydrogels obtained from cellulose (C) and from cellulose and lignin (CL) are presented in Fig. 12. The cross-section of the cellulose hydrogels indicates a macro-porous structure with the pore sizes between 169 (C) and 431 μm (CL5). It can be observed that the average pore size of the hydrogels increased with the rise of the lignin content, which suggests that a higher quantity of water can be uptaken, this assumption being in good agreement with the data obtained for swelling degree of the hydrogels.

Moreover, the hydrogel structure is strongly influenced by the lignin content in the sample, this leading to a more homogenous and less dense structure.

3.5. Controlled release of polyphenols from hydrogels matrix

One of the factors which control the release from cellulose–lignin matrices is the amount of incorporated polyphenols. The various compositions of CL hydrogels affect the release mechanism by the formation of networks with different pore structures and cross-link density. Thus, the amount of polyphenols released in a given period of time can be controlled by selecting the conditions to obtain the cross-linked hydrogels and the degree of loading of polyphenols.

The release profiles for all cellulose–lignin based hydrogels are presented in Fig. 13.

The results showed that the release of polyphenols from CL hydrogels depends on the lignin content. Thus, an increase in lignin content

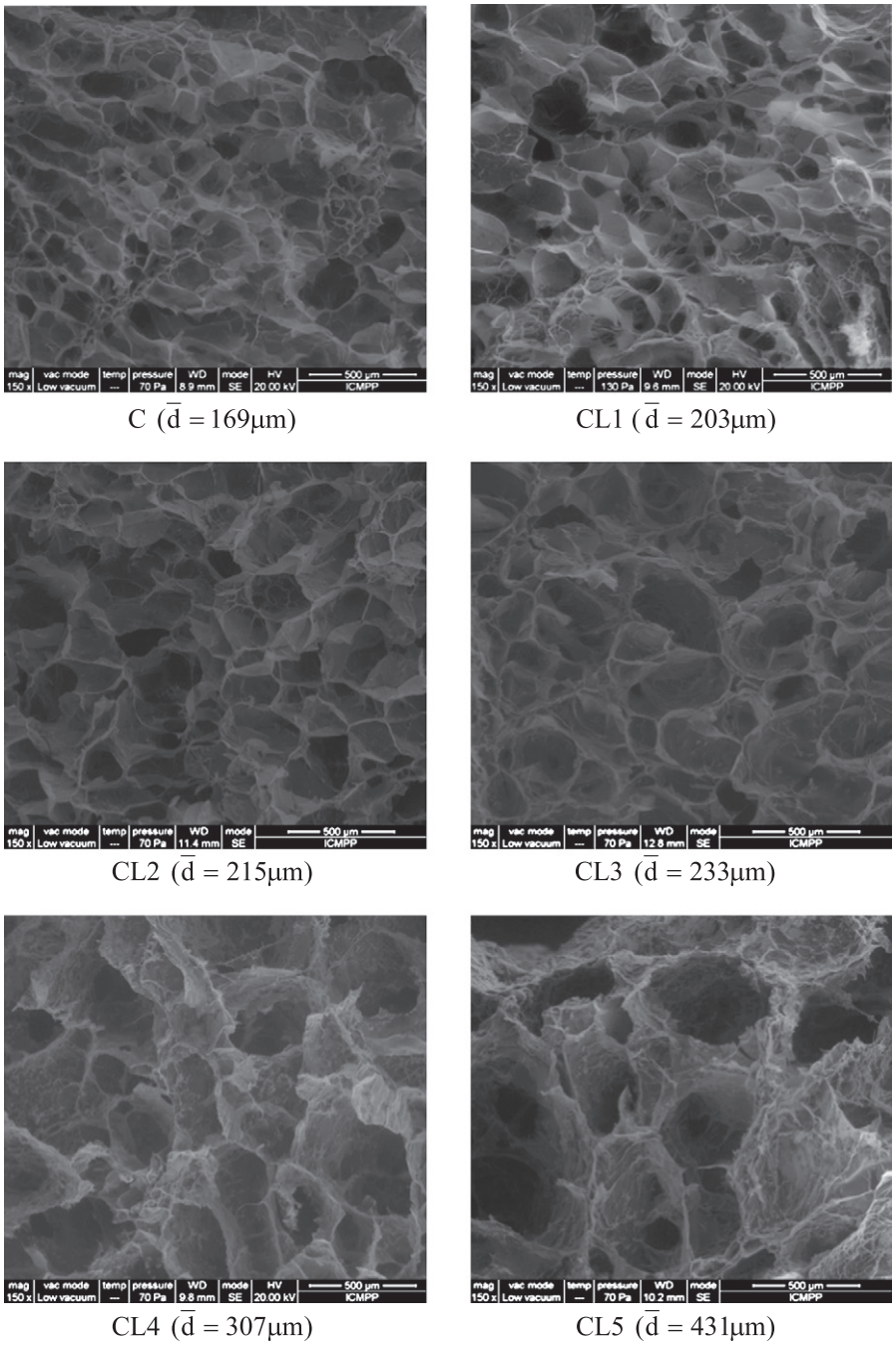

Fig. 12. SEM images of unloaded (CL) and loaded (CLa) hydrogels.

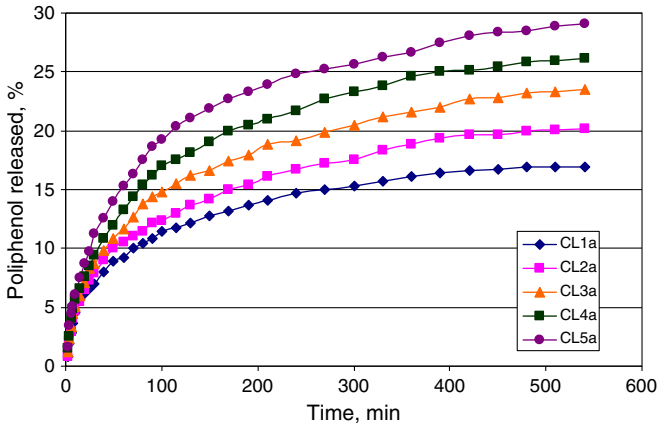

Fig. 13. Release profiles of polyphenols from CL hydrogels in water:ethanol medium, at 37 °C.

leads to an increase of polyphenol percent released, so, for CL5a composition the percent released is approximately 29% while for CL1a composition the percent released is 17%.

The kinetic parameters for polyphenol release in water:ethanol (19:1) solution from cellulose–lignin hydrogels with various compositions are shown in Table 6.

The diffusion exponent (n_r) obtained for polyphenols released from cellulose–lignin hydrogels indicates a case II transport mechanism for CL1a and CL2a compositions. The reason behind such mechanism is the network relaxation as the gels swell. On the other hand, for CL3a, CL4a and CL5a hydrogels, an anomalous transport mechanism is preferred, which appeared by coupling Fickian diffusion with relaxation of hydrogel network.

The lignin content from CL hydrogels and the release rate constants (k_r) are correlated, so, an increase in lignin content leads to an increase of the release rate constants.

4. Conclusions

New hydrogels have been prepared from lignin and cellulose, by a freezing method in order to dissolve cellulose in NaOH aqueous solution. By chemical crosslinking of the cellulose–lignin mixtures in the presence of ECH, hydrogels with high swelling capacities were obtained. Structure and properties of the hydrogels were analyzed by UV–VIS and FT-IR spectroscopy, DSC and SEM. These hydrogels proved to be suitable to incorporate polyphenols from aqueous solutions. The amount of the incorporated PF increased as a function of swelling capacity of the hydrogel.

From FT-IR spectroscopy the cross-linking reaction between the two natural polymers was confirmed by appearance of new ether adsorption band. The characteristic bands of hydrogels may be influenced by the change of intra- and intermolecular hydrogen bonds established during the polyphenols loading. This observation was highlighted by the determination of the energy of the H-bonds and the asymmetric index for studied samples. The enthalpy of H-bond formation and the bond length were also established from FT-IR spectrum.

The effect of the structure features of cellulose–lignin hydrogels on their dehydration heat was evaluated by DSC. It was confirmed the obtaining of hydrogel structures by correlation the composition of hydrogels with obtained data from DSC thermograms. The incorporation of polyphenols in hydrogels determined an increase of the values established for the dehydration heat of CLa hydrogels.

The SEM micrographs reveal the changes in morphological aspects of the obtained cellulose–lignin hydrogels depending of the CL composition.

The study regarding the release of polyphenols from CL hydrogels showed the dependence on the lignin content from matrices. Thus, an increase in lignin content leads to an increase of polyphenol released percent. Both the swelling process and drug release from hydrogels can be controlled by the composition of the hydrogels. The prepared hydrogels may be potential candidates for biomedical applications.

Table 6
Kinetic parameters for PF release from CLa hydrogels.

Samples	Korsmeyer–Peppas equation			Transport mechanism
	$k_r\ 10^3\ (min^{-n})$	n_r	R^2	
CL1a	4.12	1.05	0.99	Case II
CL2a	3.88	1.11	0.99	Case II special
CL3a	6.72	0.91	0.99	Anomalous
CL4a	8.56	0.83	0.99	Anomalous
CL5a	11.17	0.69	0.98	Anomalous

Acknowledgments

This research was financially supported by the European Social Fund — "Cristofor I. Simionescu" Postdoctoral Fellowship Programme (ID POSDRU/89/1.5/S/55216), Sectoral Operational Programme Human Resources Development 2007–2013.

References

[1] K.A. Davis, K.S. Anseth, Crit. Rev. Ther. Drug Carrier Syst. 19 (2002) 385–423.
[2] M.J. Smith, T.H. Flowers, M.J. Cowling, H.J. Duncan, J. Environ. Monit. 5 (2003) 359–362.
[3] J. Berger, M. Reist, J.M. Mayer, O. Felt, N.A. Peppas, R. Gurny, Eur. J. Pharm. Biopharm. 57 (2004) 19–34.
[4] J. Wang, C. Gao, Y. Zhang, Y. Wan, Mater. Sci. Eng., C 30 (2010) 214–218.
[5] C. Demitri, A. Sannino, F. Conversano, S. Casciaro, A. Distante, A. Maffezzoli, J. Biomed. Mater. Res. Part B Appl. Biomater. 87 (2008) 338–345.
[6] A. Sannino, C. Demitri, M. Madaghiele, Materials 2 (2009) 353–373.
[7] C. Tsioptsias, I. Tsivintzelis, L. Papadopoulou, C. Panayiotou, Mater. Sci. Eng., C 29 (2009) 159–164.
[8] C.-C. Lin, A.T. Metters, Adv. Drug Delivery Rev. 58 (2006) 1379–1408.
[9] N. Kashyap, N. Kumar, M. Kumar, Crit. Rev. Ther. Drug Carrier Syst. 22 (2005) 107–149.
[10] M. Prabaharan, J.F. Mano, Macromol. Biosci. 6 (2006) 991–1008.
[11] C. Chang, B. Duan, J. Cai, L. Zhang, Eur. Polym. J. 46 (2010) 92–100.
[12] D.O.S. Recouvreux, C.R. Rambo, F.V. Berti, C.A. Carminatti, R.V. Antônio, L.M. Porto, Mater. Sci. Eng., C 31 (2011) 151–157.
[13] D. Klemm, B. Heubletin, H.-P. Fink, A. Bohn, Angew. Chem. Int. Ed. 44 (2005) 3358–3393.
[14] J. Li, Y. Wan, L. Li, H. Liang, J. Wang, Mater. Sci. Eng., C 29 (2009) 1635–1642.
[15] S. Trombino, R. Cassano, E. Bloise, R. Muzzalupo, L. Tavano, N. Picci, Carbohydr. Polym. 75 (2009) 184–188.
[16] C. Demitri, R. Del Sole, F. Scalera, A. Sannino, G. Vasapollo, A. Maffezzoli, L. Ambrosio, L. Nicolais, J. Appl. Polym. Sci. 110 (2008) 2453–2460.
[17] A. Sannino, G. Mensitieri, L. Nicolais, J. Appl. Polym. Sci. 91 (2004) 3791–3796.
[18] V. Coma, I. Sebti, P. Pardon, F.H. Pichavant, A. Deschamps, Carbohydr. Polym. 51 (2003) 265–271.
[19] M. Mitjans, M.P. Vinardell, Trends Comp. Biochem. Physiol. 11 (2005) 55–62.
[20] V. Ugartondo, M. Mitjans, M.P. Vinardell, Ind. Crop. Prod. 30 (2009) 184–187.
[21] K. Toh, H. Yokoyama, H. Noda, Y. Yuguchi, J. Food Biochem. 34 (2010) 192–206.
[22] T. Dizhbite, G. Telysheva, V. Jurkjane, U. Viesturs, Bioresour. Technol. 95 (2004) 309–317.
[23] A. Belicová, J. Krajčovič, L. Križková, L. Ebringer, B. Košíková, World J. Microbiol. Biotechnol. 16 (2001) 91–93.
[24] J.N. Thakkar, V. Tiwari, U.R. Desai, Biomacromolecules 11 (2010) 1412–1416.
[25] H. Yamamoto, M. Amaike, H. Saitoh, Y. Sano, Mater. Sci. Eng. C7 (7) (2000) 143–147.
[26] W.K. El-Zawawy, Polym. Adv. Technol. 16 (2004) 48–54.
[27] R.W. Hemingway, P.E. Laks (Eds.), Plant Polyphenols: Synthesis, Properties, Significance, Basic Life Sciences, vol. 59, Plenum Publishing Corporation, New York, 2003, pp. 523–827.
[28] I.C. Arts, P.C. Hollman, Am. J. Clin. Nutr. 81 (2005) 317S–325S.
[29] G.G. Gross, R.W. Hemingway, T. Yoshida (Eds.), Basic Life Sciences, vol. 66, Plenum Publishing Corporation, New York, 2007.
[30] E.-Q. Xia, G.-F. Deng, Y.-J. Guo, H.-B. Li, Int. J. Mol. Sci. 11 (2010) 622–646.
[31] A.J. Shrikhande, Food Res. Int. 33 (2000) 469–474.
[32] M. Wada, H. Kido, K. Ohyama, T. Ichibangas, N. Kishikaw, Y. Ohba, M.N. Nakashima, N. Kurod, K. Nakashima, Food Chem. 101 (2007) 980–986.
[33] A. Isogai, R.H. Atalla, Cellulose 5 (1998) 309–319.
[34] D. Ciolacu, V.I. Popa, Cellul. Chem. Technol. 39 (2005) 179–188.

[35] B. Mozetič, I. Tomažič, A. Škvarč, P. Trebše, Acta Chim. Slov. 53 (2006) 58–64.
[36] J.A. Kennedy, Cien. Inv. Agr. 35 (2008) 107–120.
[37] A. Hernandez-Jimenez, E. Gomez-Plaza, A. Martinez-Cutillas, J.A. Kennedy, J. Agric. Food Chem. 57 (2009) 10798–10803.
[38] A.R. Berens, H.B. Hopfenberg, Polymer 19 (1978) 489–496.
[39] P.L. Rittger, N.A. Peppas, J. Controlled Release 5 (1987) 37–42.
[40] J.-M. Oh, C.-S. Cho, H.-K. Choi, J. Appl. Polym. Sci. 94 (2004) 327–331.
[41] N.A. Peppas, R.W. Korsmeyer, in: N.A. Peppas (Ed.), Hydrogels in Medicine and Pharmacy, Vol. 3, CRC Press, Boca Raton, Florida, Properties and Applications, 1987, pp. 109–136.
[42] R.W. Korsmeyer, N.A. Peppas, J. Controlled Release 1 (1984) 89–98.
[43] L. Serra, J. Domenechc, N.A. Peppas, Biomaterials 27 (2006) 5440–5451.
[44] Y.X. Bai, Y.F. Li, Carbohydr. Polym. 64 (2006) 402–407.
[45] C. Chang, A. Lue, L. Zhang, Macromol. Chem. Phys. 209 (2008) 1266–1273.
[46] B.K. Denizli, H.K. Can, Z.M.O. Rzaev, A. Guner, Polymer 45 (2004) 6431–6435.
[47] H.L. Hergert, J. Org. Chem. 25 (1960) 405–413.
[48] K.V. Sarkanen, H.-M. Chang, B. Erricsson, Tappi J. 50 (1967) 572–575.
[49] S.Y. Oh, D.I. Yoo, Y. Shin, G. Seo, Carbohydr. Res. 340 (2005) 417–428.
[50] D. Ciolacu, J. Kovac, V. Kokol, Carbohydr. Res. 345 (2010) 621–630.
[51] R.A. Duri, B.M. Lynch, S. Sternhell, Aust. J. Chem. 13 (1960) 156–168.
[52] G. Socrates, Organic Halogen Compounds, in: Infrared and Raman Characteristic Group Frequencies: Tables and Charts, 3rd edition John Wiley & Sons Ltd., Chichester, 2004 pp. 198–208.
[53] M.L. Rabinovich, M.S. Melnick, A.V. Bolobova, Biochemistry 67 (2002) 850–871.
[54] N.W. Alcock, Bonding and Structure: Structural Principles in Inorganic and Organic Chemistry, Ellis Horwood, New York, 1990 pp. 40–42.
[55] J.F. Kadla, S. Kubo, Compos. A 35 (2004) 395–400.
[56] G.C. Pimentel, C.H. Sederholm, J. Chem. Phys. 24 (1956) 639–641.
[57] L. Salmén, M. Åkertholm, B. Hinterstoisser, in: S. Dumitriu (Ed.), Polyssaccharides: Structural Diversity and Functional Versatility, CRC Press, 2004, pp. 159–189.

pharmaceutics

MDPI

Article

Multifunctional Hydrogels Based on Cellulose and Modified Lignin for Advanced Wounds Management

Diana Elena Ciolacu [1,*], Raluca Nicu [1], Dana Mihaela Suflet [1], Daniela Rusu [2], Raluca Nicoleta Darie-Nita [3], Natalia Simionescu [4], Georgeta Cazacu [3] and Florin Ciolacu [5,*]

[1] Department of Natural Polymers, Bioactive and Biocompatible Materials, "Petru Poni" Institute of Macromolecular Chemistry, 700487 Iasi, Romania; nicu.raluca@icmpp.ro (R.N.); dsuflet@icmpp.ro (D.M.S.)
[2] Department of Physics of Polymers and Polymeric Materials, "Petru Poni" Institute of Macromolecular Chemistry, 700487 Iasi, Romania; rusu.daniela@icmpp.ro
[3] Department of Physical Chemistry of Polymers, "Petru Poni" Institute of Macromolecular Chemistry, 700487 Iasi, Romania; darier@icmpp.ro (R.N.D.-N.); gcazacu@icmpp.ro (G.C.)
[4] Center of Advanced Research in Bionanoconjugates and Biopolymers, "Petru Poni" Institute of Macromolecular Chemistry, 700487 Iasi, Romania; natalia.simionescu@icmpp.ro
[5] Department of Natural and Synthetic Polymers, "Gheorghe Asachi" Technical University of Iasi, 700050 Iasi, Romania
* Correspondence: dciolacu@icmpp.ro (D.E.C.); fciolacu@tuiasi.ro (F.C.); Tel.: +40-332-880-220 (D.E.C.); +40-232-278-683 (ext. 2200) (F.C.)

Abstract: Considering the complex process of wound healing, it is expected that an optimal wound dressing should be able to overcome the multiple obstacles that can be encountered in the wound healing process. An ideal dressing should be biocompatible, biodegradable and able to maintain moisture, as well as allow the removal of exudate, have antibacterial properties, protect the wound from pathogens and promote wound healing. Starting from this desideratum, we intended to design a multifunctional hydrogel that would present good biocompatibility, the ability to provide a favorable environment for wound healing, antibacterial properties, and also, the capacity to release drugs in a controlled manner. In the preparation of hydrogels, two natural polymers were used, cellulose (C) and chemically modified lignin (LE), which were chemically cross-linked in the presence of epichlorohydrin. The structural and morphological characterization of CLE hydrogels was performed by ATR-FTIR spectroscopy and scanning electron microscopy (SEM), respectively. In addition, the degree of swelling of CLE hydrogels, the incorporation/release kinetics of procaine hydrochloride (PrHy), and their cytotoxicity and antibacterial properties were investigated. The rheological characterization, mechanical properties and mucoadhesion assessment completed the study of CLE hydrogels. The obtained results show that CLE hydrogels have an increased degree of swelling compared to cellulose-based hydrogel, a better capacity to encapsulate PrHy and to control the release of the drug, as well as antibacterial properties and improved mucoadhesion. All these characteristics highlight that the addition of LE to the cellulose matrix has a positive impact on the properties of CLE hydrogels, confirming that these hydrogels can be considered as potential candidates for applications as oral wound dressings.

Keywords: cellulose; modified lignin; hydrogel; controlled drug release; antibacterial activity; biocompatibility; wound dressing

Citation: Ciolacu, D.E.; Nicu, R.; Suflet, D.M.; Rusu, D.; Darie-Nita, R.N.; Simionescu, N.; Cazacu, G.; Ciolacu, F. Multifunctional Hydrogels Based on Cellulose and Modified Lignin for Advanced Wounds Management. *Pharmaceutics* **2023**, *15*, 2588. https://doi.org/10.3390/pharmaceutics15112588

Academic Editors: Peter Foot, Pietro Matricardi, Elena Polycarpou and Federico Buonocore

Received: 17 September 2023
Revised: 20 October 2023
Accepted: 2 November 2023
Published: 4 November 2023

1. Introduction

Wound healing is a complicated process that is affected by local and systemic factors, requiring a longer period of time to reach maximum healing capacity and an appropriate environment [1]. Wound management must take into account the wound complexity and collaborative processes, which include wound pre-cleaning, wound healing, infection

prevention, germ treatment and the treatment strategy [2,3]. The advanced wound management strategies must achieve the non-invasive monitoring of healing, manage pain and allow the controlled release of substances capable of promoting wound regeneration [4].

Medical dressings are essential devices in healthcare and play critical roles in wound treatments. A dressing that can be used for wound healing must meet several conditions, including maintaining moisture on the wound surface, protecting the wound from infection, absorbing exudates, and reducing pain in the wounds [5,6]. Furthermore, an oral wound dressing must overcome all the challenges brought by the oral environment, which consist of (i) changes in temperature and pH caused by the presence of saliva and (ii) the formation of biofilms due to the presence of different types of bacteria [7]. In order to fulfill all these goals, different multifunctional wound dressing materials have been designed, which are able to act at the same time on various aspects of the wound healing process. Moreover, wound dressing materials that would present a reasonable cost, fast-healing capacity and minimal inconvenience for the patients have been sought. In recent years, numerous wound dressings with excellent properties, such as antibacterial properties and self-healing ability, have been successfully developed to speed up wound healing [8]. Among these biomaterials, hydrogels are the most promising interactive dressings due to their active intervention in the wound healing process, through the controlled delivery of drugs, growth factors or other therapeutic agents. Hydrogels present essential characteristics in promoting wound healing, such as: (i) a calming effect—due to their moisture content, an optimal microclimate develops between the wound bed and the dressing; (ii) they reduce the pain associated with dressing changes; (iii) their limited adhesion allows for easy removal from the wound without causing additional trauma to the healing tissue; (iv) their transparent nature allows for the clinical assessment of the healing process without the removal of the dressing [4]. Hydrogels based on natural polymers have gained attention due to their significant potential in the regeneration process, highlighted also by the possibility of encapsulating active substances that give them antibacterial, anti-inflammatory and antioxidant properties.

A cellulose-based hydrogel has water-absorbing properties; in this particular case, it can absorb tissue exudates, contribute to the removal of bacteria from wounds and provide excellent moisture conditions for the wound healing process [9]. Many studies have focused on the use of cellulose in the development of wound dressings, due to its excellent properties, such as: biocompatibility, biodegradability, non-toxicity, hydrophilicity, abundance and cost-effectiveness. Cellulose derivatives have been the most widely studied for this purpose, as they have suitable applicability to the development of hydrogel-based dressings that can contribute to wound healing [10]. Cellulose can be used in combination with different natural or synthetic polymers to obtain hydrogels with three-dimensional (3D) networks, presenting improved properties and combining the performance of each individual component. This is the case for hydrogels prepared from cellulose and linseed gum, wherein it was confirmed that the presence of linseed gum improves the mechanical properties of hydrogels and their thermal stability (TG and DSC) [11]. Moreover, an example where the presence of cellulose contributes to improving the mechanical properties of hydrogels is hydrogels based on cellulose and dextran [12]. These hydrogels have demonstrated their ability to facilitate and accelerate wound healing by inhibiting the inflammation process through the controlled and sustained release of the anti-inflammatory bioactive compounds (polyphenols, PFs).

Lignin, considered the second most abundant biopolymer, is an attractive candidate in the preparation of hydrogels used in biomedical applications. Due to its antibacterial and antioxidant properties, lignin has drawn increased attention for its application in wound healing [13]. Lignin used in combination with natural (chitosan, gelatin, agarose, carrageenan) or synthetic (polyvinyl alcohol) polymers in hydrogel preparation has provided new opportunities for effective wound care and management [14–16]. It was shown that the introduction of lignin into cellulose-based hydrogels effectively improved the adsorption capacity and contributed to the controlled release of drugs (polyphenols, PFs) [17]. Hy-

drogels made from bacterial cellulose and lignin enzymatically synthesized from coniferyl alcohol were designed to have an inhibitory/bactericidal effect against clinically isolated biofilm-forming bacteria (*P. aeruginosa*, *S. aureus* and *Serratia* sp.) and laboratory strains (*S. aureus*, *L. monocytogenes* and *S. typhimurium*), and to be used in wound healing [18].

In this context, this study aims to report the preparation and characterization of new multifunctional hydrogels based on cellulose and lignin chemically modified with epoxy groups. To our knowledge, there are no up-to-date studies reporting the preparation of this type of bicomponent hydrogel. The expected outcome of this study is to obtain improved properties in these hydrogels compared to cellulose–lignin hydrogels from our previous work [17], in terms of their swelling capacity and controlled drug release. Moreover, the multifunctional hydrogels thus obtained are intended to have the ability to reduce pain by releasing procaine in a controlled manner, antibacterial properties induced by the components of the 3D network, and biocompatibility, all these with a view to their possible application in oral wound management.

2. Materials and Methods

2.1. Materials

Microcrystalline cellulose (C) was purchased from Sigma-Aldrich (Avicel PH-101, DP = 180; Sigma-Aldrich GmbH, Darmstadt, Germany).

The chemical modification of steam explosion lignin (L; produced by the steam explosion of aspen wood (*Populus tremuloides*); ENEA, Italy) was achieved in the presence of 20% NaOH solution, with epichlorohydrin (ECH) at a molar ratio of L:ECH = 1:10, for 5 h at 75 °C. Two fractions of modified lignin were obtained: a solid fraction, which was separated from the mixture by filtration, and a liquid fraction, which was dissolved in absolute methanol, filtrated and then concentrated. This concentrated fraction of chemically modified lignin (LE) has a brown color, high viscosity, and is soluble in water and methanol. The obtained LE has an epoxy equivalent of 0.2% and a dynamic viscosity of 18,000 cP.

Epichlorohydrin (ECH) was purchased from Sigma-Aldrich (purity > 99%; d = 1.18 g/cm^3; Darmstadt, Germany) and was used without further purification. Sodium hydroxide (NaOH) in pellets (purity $\geq$ 97%) was supplied by Merck (Merck KGaA, Darmstadt, Germany). Procaine hydrochloride (PrHy), with m.p. 155–156 °C and purity $\geq$ 97%, was also supplied by Sigma-Aldrich (Darmstadt, Germany).

2.1.1. Preparation of CLE Hydrogels

CLE hydrogels were prepared in different gravimetric ratios of cellulose (C) and modified lignin (LE), through the following procedure: 0.5 g polymer was added into a 6.7 mL 8.5% NaOH solution and frozen at low temperature (−30 °C). After thawing, 2.14 mL of ECH was added under continuous stirring. The obtained composition was maintained for 5 h at 80 °C. The hydrogels were washed with warm distilled water (60 °C) for 15 days in order to remove the excess NaOH, any ECH traces, and NaCl, followed by lyophilization.

2.1.2. Preparation of PrHy-Loaded CLE Hydrogels

CLE hydrogels were immersed in 50 mL of 4 g/L PrHy solution for 72 h at room temperature to allow the PrHy to diffuse into the hydrogels, and finally lyophilized in a freeze dryer ALPHA 1-2/LD (Martin Christ Drying Systems GmbH, Osterode, Germany) for 48 h. CLE hydrogels loaded with PrHy are denoted as P-CLE.

2.2. Methods

2.2.1. Swelling Measurements

Swelling studies of CLE hydrogels were performed in distilled water, at 37 °C. The samples were periodically taken out and gently wiped with a soft tissue to remove the

excess water, weighed, and then returned into the vessel. The swelling degree (Q_{max}, %) of the hydrogels was calculated according to Equation (1):

$$Q_{max} = \frac{M_s - M_d}{M_d} \cdot 100\% \quad (1)$$

where M_s—the weight of swollen hydrogel at time t, (g); M_d—the weight of dry hydrogel (g).

The equilibrium swelling degree (Q_{eq}, %) was determined for the never-dried hydrogels (initial hydrogels immediately after synthesis) using Equation (2):

$$Q_{eq} = \frac{M_\infty - M_d}{M_d} \cdot 100\% \quad (2)$$

where M_∞—the weight of swollen hydrogel at equilibrium (g); M_d—the weight of dry hydrogel (g).

In order to determine the kinetic parameters of the water diffusion process, Equation (3) was used to describe the Fickian or non-Fickian behavior of swelling-controlled release systems:

$$\frac{W_t}{W_{eq}} = k_{sw} \cdot t^{n_{sw}} \quad (3)$$

where W_t—the amount of water absorbed by the hydrogel at time t, (g); W_{eq}—the amount of water absorbed by the hydrogel at equilibrium (g); k_{sw}—the swelling rate constant, characteristic of the 3D network; n_{sw}—the swelling diffusional exponent, which is dependent on the geometry of the device and indicates the transport mechanism. The constants n_{sw} and k_{sw} were calculated from the slopes and intercepts of the plots of $\ln(W_t/W_{eq})$ vs. ln(t). Equation (3) was applied in the early swelling stages (swelling degree less than 60%), where linearity was observed.

2.2.2. Scanning Electron Microscopy (SEM)

Scanning electron microscopy (SEM) analyses were performed on a Verios G4 UC Scanning Electron Microscope (Thermo Scientific, SEM, FEI Company, Brno, Czech Republic). Cross-sections of the CLE hydrogels were coated with a platinum layer (6 nm) prior to examination, using a Leica EM ACE200 Sputter coater (Leica Microsystem, Vienna, Austria). SEM analyses were conducted using a secondary electron detector (Everhart–Thornley detector, ETD) with 10 kV accelerating voltage and a beam current of 0.8 nA. The average pore size ± standard deviation (SD) was determined for each sample, by measuring 100 randomly chosen pores from the SEM micrographs exported into an image analysis software (ImageJ software, v1.53k).

2.2.3. ATR-FTIR Spectroscopy (ATR-FTIR)

ATR-FTIR investigations were carried out on silicon single-crystal parallelepiped internal reflection elements (IRE; 55 mm × 5 mm × 2 mm, 45° incident angle), using a Bruker Vertex 70 spectrometer (Bruker Optics, Ettlingen, Germany). All the ATR-FTIR spectra were the results of 256 scans at a resolution of 4 cm^{-1}, in the frequency range of 4000–400 cm^{-1}.

2.2.4. Rheological Characterization

The rheological properties of the cellulose-based hydrogels were investigated on a Physica MCR-301 Rheometer (Anton Paar, Graz, Austria) at 25 °C, using parallel plate geometry with 25 mm diameter and a 3 mm gap between the plates. Each hydrated hydrogel was placed on the lower plate, the excess sample being removed after the upper plate descended to the desired gap height. A Peltier device was used for temperature control and the prevention of water evaporation. Amplitude sweep tests were performed in the strain range of 0.001–100% at 10 rad/s to determine the linear viscoelasticity region, LVR (stable values for G′ and G″). Frequency sweep measurements were carried out in the

frequency range from 0.05 to 500 s^{-1}, with a constant strain of 1% (determined from LVR) to evaluate the viscoelastic properties of the cellulose-based hydrogels, such as storage (G′) and loss (G″) moduli, and complex viscosity (η*) as a function of angular frequency.

2.2.5. Mechanical Properties

The mechanical tests were performed using a Brookfield Texture PRO CT3(R) Analyser (Brookfield Engineering Laboratories Inc., Middleboro, MA, USA).

The compressive test was performed with CLE hydrogels of rectangular shape (20 mm length, 11 mm width, and 9 mm high) at room temperature. The samples were saturated with PBS of pH 5.5 for two hours, then placed between two parallel plates and tested under uniaxial compression till 70% deformation, using a 4500 g load cell and 0.2 mm/s test speed.

The compressive strength was measured at the 60% strain level, while the elastic modulus (E) was calculated from the linear part of the stress–strain curves, between 3 and 10% compression, using Equation (4):

$$E = \frac{\sigma}{\varepsilon} = \frac{\frac{F}{A}}{\frac{\Delta l}{l_0}} \quad (4)$$

where σ—compressive stress; ε—strain; F—force (N); A—cross-sectional area of the hydrogel (m^2); Δl—change in length; l_0—original length.

2.2.6. Mucoadhesion Capacity

In order to investigate the mucoadhesion ability of the obtained hydrogels, chicken skin mucosa was used as the model surface. This device (TA-MA kit) consists of a membrane holder, where the mucosal tissue was fixed between two plates. The hydrogel discs (10 mm diameter and 3 mm height) were attached with double-sided adhesive to the lower end of a cylindrical probe (TA5, 10 mm diameter). The skin and the sample were kept in contact for 60 s with 1N force applied during this time. After 60 s, the sample was moved upward (0.5 mm/s) until complete separation between the surfaces occurred, and the mucoadhesive force (Fmax, N) was measured using TexturePro CT Software (TA-CT-PRO-AY). The mechanical measurements were performed in triplicate, and the average of three determinations was used to estimate the elastic modulus and the adhesiveness.

2.2.7. Hydrolytic Degradation

The hydrolytic degradation of the CLE hydrogels was studied in phosphate-buffered saline (PBS, pH 7.4) solution, the most common buffer used in studies for biomedical applications, due to its similarity to bodily fluids. Samples of about 100 mg were immersed in 80 mL PBS and placed in a thermostatic water bath at 37 ± 0.2 °C. The hydrolytic degradation in PBS was monitored for 14 days, when the samples were weighed after removing the excess liquid from their surface. The CLE hydrogels were left to swell under these conditions for 24 h, and then weighed—this was considered the initial swollen weight (SW_0), and the recorded weight over time was noted as SW. The weight change of the hydrogel over time (WC) was determined using Equation (5):

$$WC = \frac{SW - SW_0}{SW_0} \quad (5)$$

where WC—weight change of the hydrogel over time (%); SW_0—the initial swollen weight of the hydrogel (g); SW—the swollen weight at a specific time (g).

It should be mentioned that, in this study, only the hydrogels CLE 1 to CLE 6 were chosen, because the hydrogel CLE 7 started to disintegrate after 24 h of swelling. In addition, the pH of the solutions was measured immediately after weighing the samples.

2.2.8. Incorporation of PrHy Release

In total, 0.1 g dried hydrogel was immersed in 50 mL solution of 4 g/L PrHy and left to swell at room temperature for 72 h, while the PrHy penetrated the 3D network. Then, the PrHy-loaded hydrogels (P-CLE) were dried by lyophilization. In order to establish the amount of PrHy incorporated into the hydrogels, the remaining solutions were analyzed by UV-VIS spectroscopy (Shimadzu UV-1900i, Kyoto, Japan), measuring the absorbance at 290 nm. The calibration curve, y = 71.337x, with a correlation coefficient of R^2 = 0.999, was established using different PrHy solutions with concentrations between 10^{-4}–10^{-2} g/mL. The unknown concentrations of the solutions of PrHy remaining after hydrogel loading were determined using the equation obtained from the calibration curve.

The incorporation degree (Id) of PrHy into hydrogel matrices was calculated using Equation (6):

$$I_d = \frac{c_0 \cdot V_0 - c \cdot V}{M} \cdot 100\% \quad (6)$$

where c_0—the initial concentration of the PrHy solution (g/mL); V_0—the volume of initial PrHy solution (mL); c—the concentration of PrHy solution after hydrogels loading, determined from the calibration curve (g/mL); V—the volume of the PrHy solution remaining after incorporation (mL); M—the weight of the dry PrHy-loaded hydrogel (g).

2.2.9. In Vitro Release of PrHy

In vitro release studies were performed in distilled water, at 37 °C, using a standard dissolution procedure. Here, 3 mL samples of release medium were withdrawn periodically, at predetermined time intervals, and the absorbance at 290 nm was measured. In order to maintain the solution's concentration, the sample was reintroduced into the system after analyzing. The PrHy concentration in the release medium was calculated based on the calibration curve.

A semi-empirical equation using the Korsmeyer and Peppas model was used to kinetically analyze the data in terms of the PrHy release, such as in Equation (7):

$$\frac{M_t}{M_\infty} = k_r \cdot t^{n_r} \quad (7)$$

where M_t—the amount of PrHy released at time t (g); M_∞—the amount of PrHy at the equilibrium state (g); k_r—structural/geometric constant for a particular system; n_r—the diffusional exponent, representing the release mechanism.

2.2.10. Antimicrobial Tests

The antimicrobial activity of the hydrogels was considered against two different strains: *Escherichia coli* (Gram-negative bacteria, ATCC 25922) and *Staphyilococcus aureus* (Gram-positive bacteria, ATCC 25923). This was established by following the standardized methods of bacteriological procedures, according to ISO 16649-2:2001 [19] (*Escherichia coli*) and ISO 6888-3:2003 [20] (*Staphyilococcus aureus*): (i) sterilization of samples in an autoclave for 20 min, at 110 °C and 0.5 bars; (ii) the seeding of the pre-inoculated culture medium, American Type Culture Collection (ATCC) culture bacteria, and incubation for 24 h at 37 °C; (iii) the counting of colonies in 0.1 mL culture by selective culture medium separation; (iv) 0.1 mL of bacterial culture ATCC was inoculated with sterile swabs on the surface of the samples; (v) incubation of samples contaminated with ATCC for 24 h at 25 °C in the dark, in sterilized glass Petri dishes, repeated for another 24 h; (vi) identification of the target germs.

2.2.11. In Vitro Biocompatibility Assessment (MTS Assay)

Human gingival fibroblasts (HGF, CLS Cell Lines Service GmbH, Eppelheim, Germany) were seeded (0.5×10^5 cells/mL) into 96-well plates. The biocompatibility of the samples was assessed using the CellTiter 96®AQueous One Solution Cell Proliferation Assay (Promega, Madison, WI USA), according to manufacturer's instructions and ISO

10993-5:2009 [21] (extract dilution method). Samples (4 mg/mL) were extracted over 24 h, at 37 °C, in complete cell culture medium: MEM α medium with 10% fetal bovine serum (FBS, both from Gibco, Thermo Fisher Scientific, Waltham, MA USA) and 1% Penicillin–Streptomycin–Amphotericin B mixture (10 K/10 K/25 µg, Lonza, Basel, Switzerland). The cells were incubated with fresh complete medium (Control) or different concentrations of sample extracts (1 mg/mL, 2 mg/mL, 3 mg/mL, 4 mg/mL) for 24 h. MTS absorbance readings were taken at 490 nm on a FLUOstar®Omega microplate reader (BMG LABTECH, Ortenberg, Germany). Experiments were done in triplicate, and the treated cells' viability was expressed as a percentage of the control cells' viability (means ± standard deviation).

2.2.12. Statistical Analysis

GraphPad Prism 8 software (GraphPad Software Inc., San Diego, CA, USA) was used for statistical analyses. Data were expressed as mean ± SD and analyzed by independent two-tailed (Student's) *t*-test, considering $p < 0.05$ as statistically significant.

3. Results and Discussion

3.1. Preparation of CLE Hydrogels

Lignin is an excellent candidate for chemical modifications, due to its high functionality (the presence of phenolic and aliphatic hydroxyl groups), which gives the possibility of developing new biomaterials [13]. It is expected that the incorporation of LE with high contents of ether bonds would provide higher structural flexibility of the hydrogels, an improved swelling capacity, and also antimicrobial properties [22].

Thus, starting from the idea of designing a hydrogel with significantly improved properties and performance, hydrogels containing C and LE were made by the cross-linking reaction in the presence of ECH. ECH is widely used in the cross-linking process of biopolymers, and more importantly, it allows for obtaining polymers free from crosslinker residues, due to the high efficiency of the washing process [23]. Our previous study on the in vitro cytocompatibility of cellulose–dextran hydrogels (CD) provided evidence in favor of ECH and of the safety of materials prepared by chemical cross-linking with ECH. The cell-based experiments showed that human fibroblasts and endothelial cells were successfully cultured on the CD hydrogels with high viability of over 80% for all formulations [12]. Safe and noncytotoxic cellulose-based hydrogels were constructed via chemical cross-linking with ECH for potential applications in biological imaging, when the viability of L02 cells was demonstrated to exceed 90% for all hydrogels [24].

Related to LE preparation, it has been noted that, under the conditions of an alkaline environment (NaOH), the epoxy groups in ECH open, and the cross-linking reaction with the OH groups from lignin takes place. Moreover, after the removal of chlorine, new epoxy groups can be formed, which further react with other OH groups within lignin, achieving the cross-linking of the lignin (LE) [25]. The obtained LEs have an epoxy equivalent of 0.2%, a value confirmed by other authors as well [26,27].

Generally, the cross-linking process with ECH that takes place in various alkaline media is controlled by the synergy between the chemical and physical cross-linking processes of the polymer chains, and more precisely by (i) the chemical cross-linking processes, through the etherification reaction between the OH groups of ECH and those of the cellulose chains, as well as by (ii) the physical cross-linking process between the OH groups of the polymeric chains, with the reconstruction of hydrogen bonds [28].

In our particular case of CLE hydrogels, the OH groups of cellulose and those of LE are covalently linked to the reactive groups of ECH, and covalent bonds are established either between two functional groups belonging to the same macromolecular chain, or with the groups of a neighboring polymeric chain.

The proposed mechanism for the cross-linking process between cellulose and LE with ECH, in alkaline medium, is presented in Figure 1.

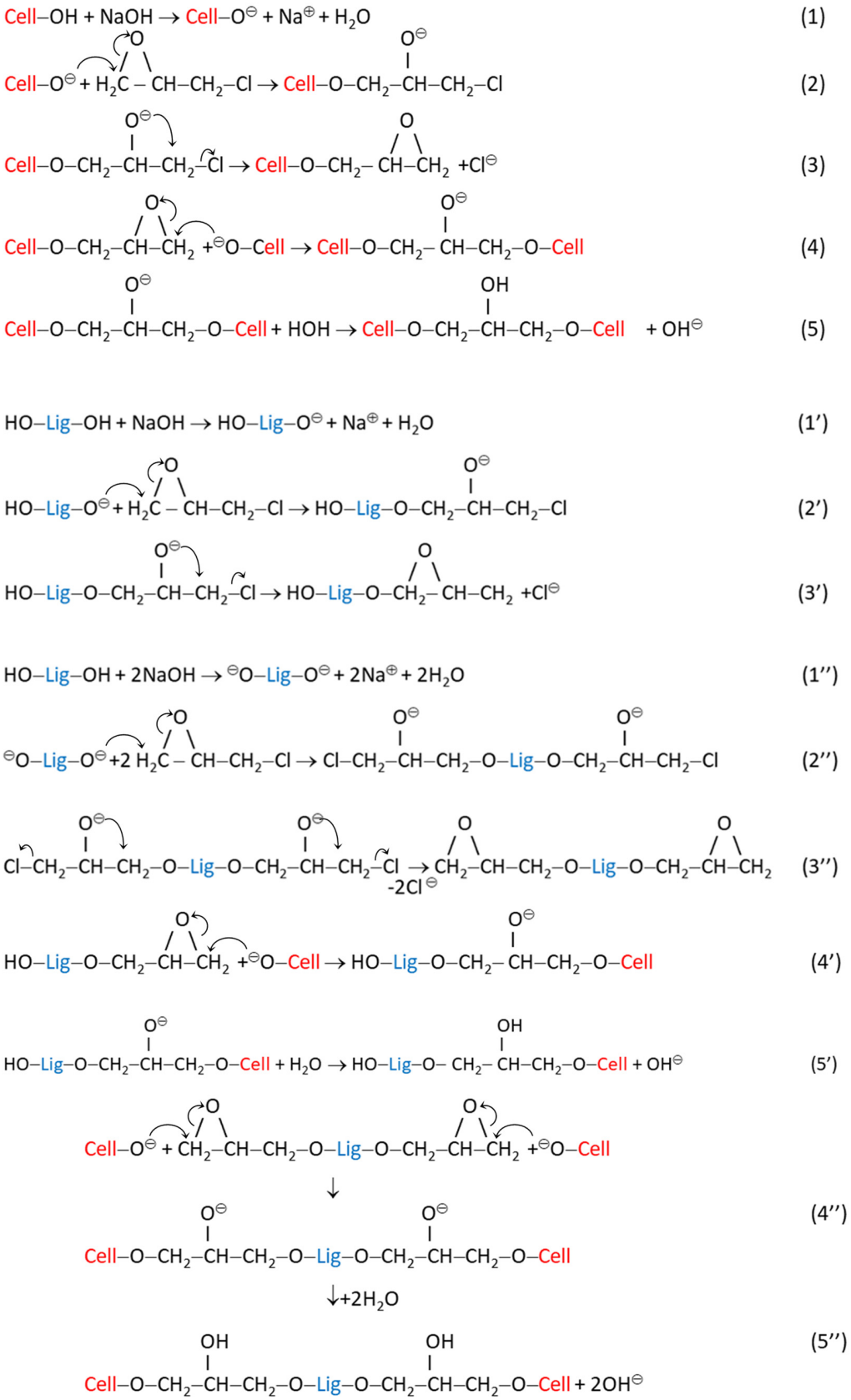

Figure 1. The proposed mechanism of the cross-linking reaction of cellulose with LE, in the presence of ECH: (1)–(5)—possible cross-linking reactions between cellulose (Cell) and ECH; (1′)–(3′) and (1″)–(3″)—chemical reactions between lignin (Lig) and ECH; (4′)–(5′) and (4″)–(5″)—possible cross-linking reactions between and Cell, LE and ECH.

Chemical reactions (1)–(5) illustrate the cross-linking mechanism of cellulose (Cell) with ECH, highlighting the formation of ether bonds between the cellulose chains.

The next reactions, (1′)–(3′) and (1″)–(3″), prove the chemical modification of lignin macromolecules (Lig) by introducing multiple epoxy groups, but also by preserving some unreacted OH groups.

The last group of chemical reactions, (4′)–(5′) and (4″)–(5″), exemplify the possible interactions between the active species based on Cell and Lig in the reaction medium.

In addition, some secondary reactions may occur, in which the groups in ECH could interact only with an OH group from cellulose or lignin, and there is also the possibility of hydrolyzing some ECH. It is worth mentioning that the gravimetric ratio between C and LE is an important factor in the formation of the 3D network of CLE hydrogels, with a strong impact on the characteristics of the hydrogels, especially on their swelling capacity.

3.2. Swelling Behavior of CLE Hydrogels

The color of CLE hydrogels depends on the LE content within the 3D network (Figure 2). Importantly, it has been remarked that, in comparison with the cellulose–lignin (CL) hydrogels, which have a color from light brown to dark brown [17], CLE hydrogels are semitransparent and turn from white to slightly yellowish, with an increase in the LE content in the matrix.

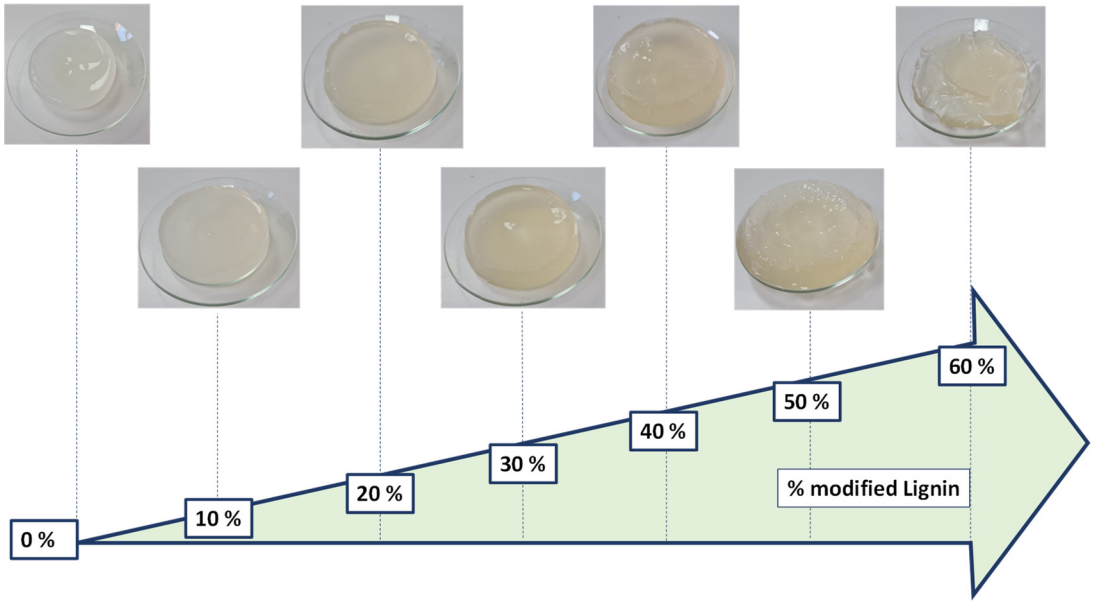

Figure 2. Changes in the appearance of CLE hydrogels with increasing LE content in the matrix.

Moreover, an obvious increase in the volume of CLE hydrogels is observed, along with the increase in the content of LE in the system, accompanied by a gradual increase in samples' Q_{max}.

The evolution in time of Q_{max} as a function of the composition of CLE hydrogels is presented in Figure 3.

It is observed that the swelling properties of CLE hydrogels are influenced by the presence of LE within the hydrogels; thus, a higher content of LE determines a higher swelling capacity. This behavior can be explained by the presence of a large number of polar groups (aromatic and aliphatic hydroxyls, carbonyls) in LE, which are partially involved in C–O–C bonds, but with most hydroxyl groups remaining free and conferring hydrophilicity to the matrix. Also, a contribution to the increase in Q_{max} is made by the voluminous structure of the LE, which allows for the formation of a more relaxed 3D network and, implicitly, a higher swelling capacity.

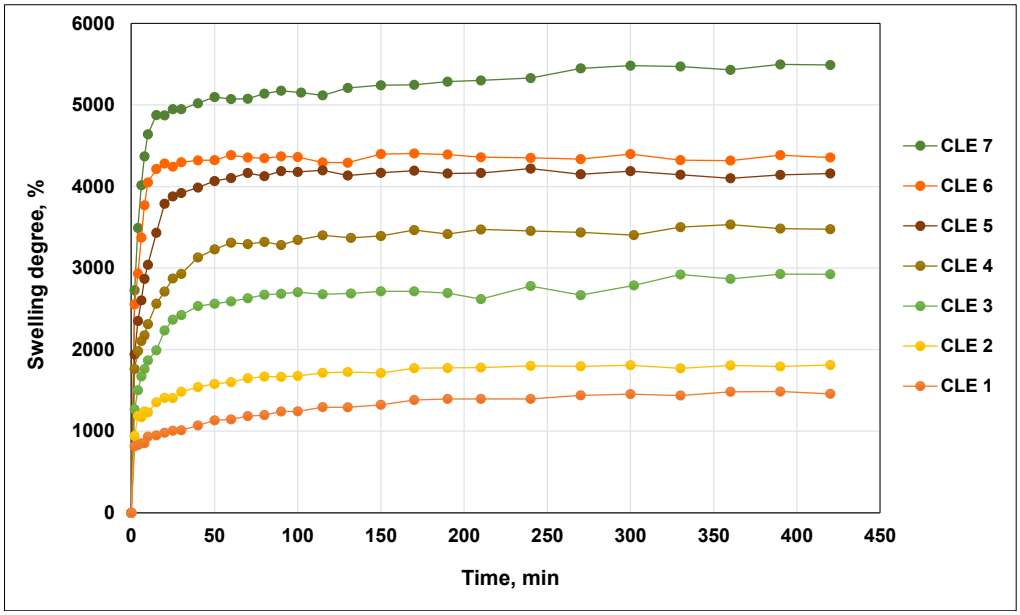

Figure 3. Swelling kinetics of CLE hydrogels as a function of time and composition.

The composition of CLE hydrogels, the gel fraction yield and the Q_{eq} of the hydrogels are presented in Table 1.

Table 1. Composition and main characteristics of CLE hydrogels.

Samples	Hydrogels Composition		Hydrogels Features		
	Cellulose, %	LE, %	Gel Fraction Yield, %	Q_{eq}, %	Q_{max}, %
CLE 1	100	0	99.9	1920	1460
CLE 2	90	10	95.7	3250	1810
CLE 3	80	20	92.5	3550	2050
CLE 4	70	30	80.8	4010	3480
CLE 5	60	40	78.5	5750	4360
CLE 6	50	50	76.0	7310	4160
CLE 7	40	60	54.8	10,265	5490

The Q_{eq} determined for never-dried hydrogels varies from 1920% for CLE 1 up to 10.265% for CLE 7. In addition, the Q_{max} is improved from 1460% for CLE 1 up to 5490% for CLE 7. It should be noted that CLE hydrogels exhibited a significantly higher swelling capacity than the CL hydrogels reported earlier in the literature [17], suggesting that the use of LE in the preparation of CLE hydrogels greatly improves the capacity for water absorption. Furthermore, if LE is used in the preparation of hydrogels together with poly(vinyl alcohol) (PVA), the same tendency of increasing an Q_{max} with increasing LE content within the hydrogel is observed, but the Q_{max} values recorded for LE hydrogels–PVA are significantly lower than those obtained in this study [27].

The kinetic parameters of the swelling of CLE hydrogels are presented in Table 2, where the influence of the hydrogel's composition on the kinetics of the water uptake process can be observed.

Table 2. Swelling kinetic parameters for CLE hydrogels.

Samples	Swelling Kinetic Parameters		
	n_{sw}	k_{sw}	R^2
CLE 1	0.080	0.636	0.994
CLE 2	0.140	0.672	0.996
CLE 3	0.147	0.818	0.997
CLE 4	0.201	0.853	0.996
CLE 5	0.255	0.889	0.999
CLE 6	0.265	0.936	0.994
CLE 7	0.352	0.943	0.999

The values of the diffusional exponent (n_{sw}) are lower than 0.45, indicating that the water diffusion rate is lower than the polymer chains relaxation rate, which shows that the water transport mechanism is defined by the less Fickian diffusion. With the increase in the LE content in the hydrogel formulations, an increase in the n_{sw} value is observed, showing a tendency towards the Fickian diffusion process, as characterized by n_{sw} = 0.45.

The swelling rate constant (k_{sw}), which characterizes the diffusion rate in the hydrogels network, varies with the composition; more precisely, it increases with the increase in the LE content in hydrogel matrices.

For all hydrogels, the correlation coefficients R^2 are higher than 0.99, indicating a good fitting between experimental data and the chosen model.

3.3. Scanning Electron Microscopy (SEM)

The morphological details of all CLE hydrogels were assessed using SEM micrographs, as presented in Figure 4. The cross-section SEM images reveal that all prepared hydrogels formed a macroporous heterogenic structure, with interconnected pores of various sizes.

It can be observed that a higher content of LE in the CLE hydrogels determines evident changes in pores size and pore distribution within the 3D matrices, which are critical factors in the control of swelling capacity and drug release behavior. It is easy to observe that an increase in the LE content results in hydrogels with lower pore density and higher average pore size, namely, hydrogels CLE 4–CLE 7 having larger, more irregular pores, as compared to hydrogels CLE 1–CLE 3. Thus, the presence of LE in the hydrogels determines the formation of a more heterogeneous, loosely packed porous architecture, compared with CLE 1, where the porous architecture seems to be denser. Moreover, by increasing the LE content, it is observed that the walls between the pores become thinner, leading to the formation of a more relaxed porous network, capable of retaining a larger amount of water, observations that are confirmed by the data regarding the swelling degree of the CLE hydrogels.

The average pore sizes increased gradually from CL1 to CL7 and range from 38.2 ± 15.2 μm (CLE 1) to 63.3 ± 25.2 μm (CLE 2), 71.0 ± 28.1 μm (CLE 3), 129.3 ± 52.5 μm (CLE 4), 131.4 ± 41.9 μm (CLE 5), 137.4 ± 45.4 μm (CLE 6) and 148.0 ± 43.0 μm (CLE 7), respectively. The difference between the diameters of pores in CLE 1 (without LE) and CLE 7 (with the greatest amount of LE) is noticeable.

Figure 5 shows the pore size distribution for CLE hydrogels. It can be observed that, as the LE content increased in the CLE hydrogels, a wider distribution of the pore size was registered (CLE 4–CLE 7), compared to those containing a smaller amount of LE (CLE 1 and CLE 2). For example, if, for CLE 1, the pore size frequency is concentrated in a small size range, between 20 and 75 μm, in the case of sample CLE 7, this range widens, starting from 75 μm and continuing up to approximately 275 μm, with a maximum size located in the range of 175–200 μm. In fact, with the increase in the LE content in the hydrogel,

the size range moves to the right with the greater pore frequency, to larger sizes, with approximately 25 µm for every 5% addition of LE in the formula.

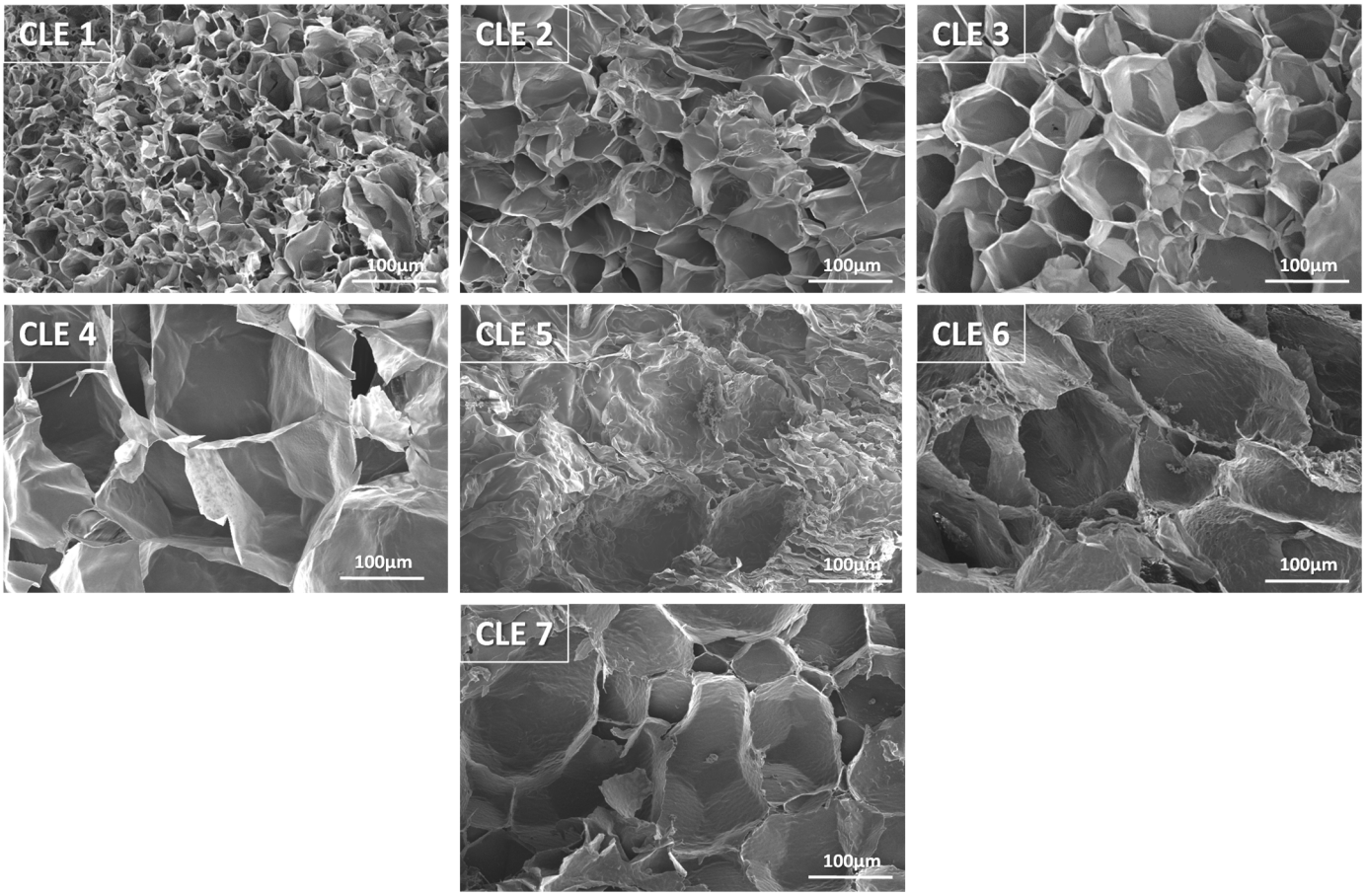

Figure 4. SEM micrographs of CLE hydrogels (magnification 250×).

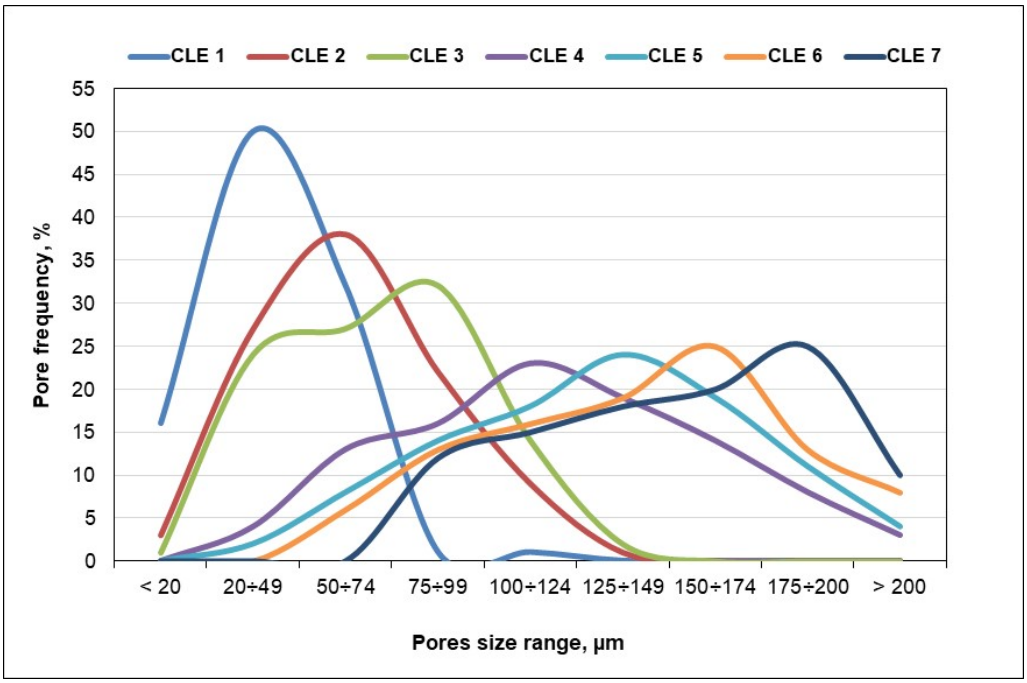

Figure 5. Pore size distribution of CLE hydrogels.

In this way, by changing the LE content in the hydrogel formula, the size and frequency of the pores in the matrix can be easily controlled, and implicitly, all the properties of the hydrogel that are directly influenced by these parameters.

3.4. ATR-FTIR Spectroscopy

The structural changes of the CLE hydrogels following the incorporation of different amounts of epoxidized lignin in the 3D network were investigated by ATR-FTIR spectroscopy.

Due to their complexity, the spectra are presented into two regions, such as: (i) 3700–2600 cm^{-1}, the region of the OH and CH stretching vibrations (Figure 6a), and (ii) 1700–700 cm^{-1}, the "fingerprint" region, assigned to the stretching vibrations of different groups (Figure 6b). From all the spectra, only three have been selected to be presented, namely, the spectra of CLE 1 (C:LE = 100:0), CLE 4 (C:LE = 70:30) and CLE 7 (C:LE = 40:60).

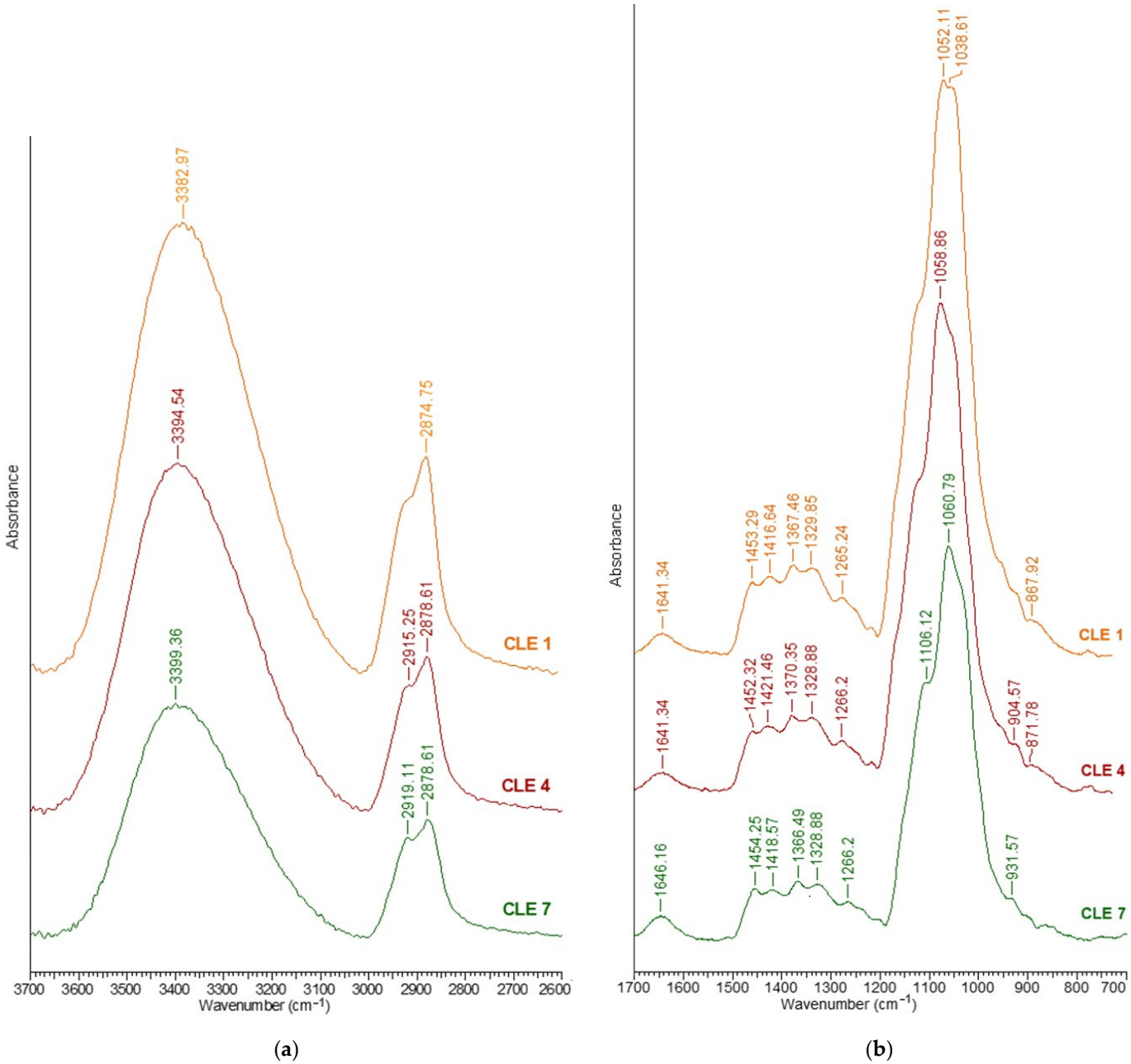

Figure 6. ATR-FTIR spectra of CLE hydrogels in (**a**) 3700–2500 cm^{-1} region and (**b**) 1700–700 cm^{-1} region.

A broad band assigned to OH stretching at 3700–3000 cm^{-1} is observed for all the spectra (Figure 6a), and also, a shift of the maximum absorbance to higher wavenumbers, from 3382 cm^{-1} (CLE 1) to 3399 cm^{-1} (CLE 7), was recorded. This band is more prominent for the CLE 1 sample than for the other samples, which is due to the presence of a large number of hydroxyl groups being involved in an increased number of hydrogen bonds, considered to be the cause of this broad OH band. By increasing the amount of LE in the matrix, the absorbance of OH stretching decreases progressively, proving the lower involvement of -OH groups in new hydrogen bonds, or perhaps even the scission of the already formed intra- and inter-molecular hydrogen bonds.

In the region of 3000–2800 cm^{-1}, two strong bands can be observed for CLE 1 at 2912 cm^{-1} and 2874 cm^{-1}, respectively, which can be attributed to the stretching of symmetric and asymmetric methyl and methylene groups. The appearance of the band at 2892 cm^{-1}, attributed to CH stretching, demonstrates the modification of the cellulose crystal system following the process of obtaining the hydrogel; more precisely, the transition from cellulose I to cellulose II in the presence of the NaOH aqueous solution [29]. The two bands that appeared in the samples with different LE contents (CLE 2 to CLE 7), namely, 2919 cm^{-1} (symmetric) and 2879 cm^{-1} (asymmetric) for CLE 7, can also be attributed to the CH stretching vibration in the aromatic methoxyl group and the methyl and methylene groups [30].

Moreover, it was observed that, by increasing the content of LE within the hydrogels, obvious decreases in the band at 2919 cm^{-1}, characteristic of asymmetric CH stretching vibrations, and in the band at 2879 cm^{-1} were recorded.

In the 1700–700 cm^{-1} region, a complex region of the ATR-FTIR spectrum of the hydrogels, several characteristic bands can be identified, among which we might mention: (i) the band at 1635 cm^{-1}, which is attributed to adsorbed water; (ii) the absorption band at 1419 cm^{-1} (characteristic of cellulose II [29], attributed to the symmetric CH_2 bending vibration—this band is also known as the "crystallinity band" [17] and a decrease in its intensity, as can be seen in Figure 6b, indicates a reduction in the crystallinity degree of the samples; (iii) the band at 1453 cm^{-1} attributed to the CH_2 and CH groups of cellulose; (iv) the band at 1367 cm^{-1} attributed to the symmetric CH_2 bending vibration; (v) the band at 1266 cm^{-1} attributed to the CH bending vibration; (vi) the band at 1162 cm^{-1} attributed to C–O–C groups at the β-glycosidic linkage; (vii) the band at 1053 cm^{-1} attributed to the CO bending vibration at C3; (viii) the band at 1038 cm^{-1} attributed to the CO bending vibration at C-6 and (ix) the band at 867 cm^{-1} attributed to C–O–C stretching at the β-(1→4)-glycosidic linkages.

In the "fingerprint" region, the bands characteristic of cellulose overlap with those characteristic of LE, and therefore, it is difficult to distinguish between them.

However, it should be mentioned that the bands at 1454 cm^{-1} and 1508 cm^{-1}, characteristic of CLE hydrogels, are attributed to asymmetric CH deformations in the methyl, methylene and methoxyl groups, and to the aromatic vibrations of the skeleton coupled with CH in plane strains, respectively [30]. Also, the bands at 1329 cm^{-1} can be due to the C=O stretch of the syringyl ring, at 1266 cm^{-1} to the C=O stretching of the syringyl ring and at 1217 cm^{-1} to the C=O stretching of the guaiacyl ring. The characteristic bands of LE, where the presence of epoxy groups is highlighted, appear at 1230 cm^{-1}, 910 cm^{-1} and 830 cm^{-1} [26].

The broad band at 3400 cm^{-1} of the samples with an increased content of LE is also attributed to the stretching vibrations of phenolic and aliphatic hydroxyl groups involved in hydrogen bonds, while the bands at 2919 cm^{-1} and 2879 cm^{-1} are attributed to the CH stretching in methyl of aromatic and methylene groups of side chains and aromatic methoxyl groups.

As can be seen in Figure 6a, there is a decrease in the band at 3400 cm^{-1}, related to OH stretching, which is due to the decrease in the number of newly formed hydrogen bonds, as a result of the increasing amounts of LE within the matrix. To prove this observation, several structural parameters were inferred from the ATR-FTIR spectra, such as the hydrogen bond

intensity (HBI), hydrogen bond energy (E_H), the enthalpy of the *H*-bond formation (ΔH) and the asymmetric index (a/b), data that are presented in Table 3.

Table 3. Cellulose infrared crystallinity –atios and hydrogen bond intensity.

Samples	IR Crystallinity Ratio		HBI	E_H, kJ	ΔH, J/g	a/b
	TCI	LOI				
	A_{1375}/A_{2892}	A_{1420}/A_{893}	A_{3400}/A_{1320}			
CLE 1	0.55	0.96	5.28	4.57	126.60	0.92
CLE 2	0.53	1.21	4.59	4.54	125.37	0.92
CLE 3	0.52	1.23	4.49	4.52	125.78	0.92
CLE 4	0.53	1.36	4.36	4.37	121.65	0.92
CLE 5	0.51	1.48	4.08	4.35	121.23	0.89
CLE 6	0.51	1.52	4.01	4.33	120.82	0.85
CLE 7	0.48	2.06	3.96	4.30	119.99	0.81

To establish the hydrogen bond intensity (HBI), the ratio between the absorption bands at 3400 cm^{-1} and 1320 cm^{-1} is used [31]. This parameter is an indicator of the mobility of the chains, and more precisely, of the structure's ordering degree (crystallinity), and also of the amount of bound water [29]. From the data presented in Table 3, it can be inferred that the HBI value for CLE 1 (5.28) is the highest, which demonstrates the presence of a large number of intra- and intermolecular hydrogen bonds, which determine a more compact structure, with better organization and greater crystallinity of the sample. This intensity gradually decreases from 5.28 (CLE 1) to 4.36 (CLE 4), until 3.95 for CLE 7, indicating that the introduction of LE leads to a distortion of the sample's organization, and implicitly to a decrease in the number of hydrogen bonds and the crystallinity of the sample.

To confirm this assumption, the energy of the *H*-bonds (E_H, kJ) has been determined. This parameter is calculated using Equation (8) [17]:

$$E_H = \frac{1}{k} \cdot \frac{\nu_0 - \nu}{\nu_0} \quad (8)$$

where ν_0—the standard frequency corresponding to free -OH groups (cm^{-1}); ν—the frequency of the bonded -OH groups (cm^{-1}); $k = 1.68 \times 10^{-2}$ $kcal^{-1}$.

The values obtained for E_H follow the same trend as those of HBI, which confirms the reduction in the number of hydrogen bonds in the supramolecular structure of the hydrogels—a gradual decrease from CLE 1 to CLE 7 with the increase in the addition of LE.

The LE addition in the 3D networks causes a decrease in the a/b index values, a fact that confirms the information obtained when determining the other parameters (HBI and E_H), namely, that the uniformity of the sample decreases from CLE 1 to CLE 7.

The enthalpy of *H*-bond formation (ΔH, J/g) was calculated with Equation (9) [17]:

$$-\Delta H = 0.016 \cdot \Delta\nu_{OH} + 0.63 \quad (9)$$

where $\Delta\nu_{OH}$—the difference between the frequency corresponding to free -OH groups (cm^{-1}) and the frequency of the bonded -OH groups (cm^{-1}).

The obtained ΔH values (Table 3) indicate that the number of hydrogen bonds established between the -OH groups in CLE 1 is greater than those established between the -OH groups in CLE 7—data that confirm the previously presented assumptions.

For a supplementary investigation of the hydrogels' crystalline structure, we went further and determined the two relative absorbance ratios usually applied to study crystallinity changes, which are total crystalline index (TCI) and lateral order index (LOI) (Table 3). The total crystalline index (TCI) was calculated from the ratio between the absorption bands at

1375 cm^{-1} (CH_2 bending vibration) and 2892 cm^{-1} (CH stretching vibration). This ratio is proportional to the crystallinity of the samples, and its decrease indicates a decrease in the crystallinity degree of the samples. In our case, the highest crystallinity ratio was recorded for CLE 1 (0.55), and then the crystallinity ratio of the hydrogels consistently decreased to 0.53 (CLE 4) and 0.48 (CLE 7).

Another important ratio is the lateral order index (LOI), which was established as the ratio between the absorption bands at 1420 cm^{-1} (symmetric CH_2 bending vibration) and 893 cm^{-1} (β-1,4-glycosidic bonds in cellulose). For the prepared cellulose-based hydrogels, which presented the crystalline structure of cellulose II, the ratio with the band at 893 cm^{-1} was used, because this is the band used for the samples predominantly composed of cellulose II [32,33]. This index is correlated to the overall degree of order in the sample, and, for the special case of cellulose II, a lower value reflects a more ordered structure [32,34]. It was observed that the LOI values increase with the decrease in the TCI, which is proportional to the crystallinity degree of the hydrogels. More exactly, CLE 1 has the highest TCI index and the lowest LOI index in comparison with CLE 7, which has the highest LOI index and the lowest TCI index.

The formation of etheric bonds in the hydrogels, following the cross-linking reaction between C and LE, was highlighted by the aryl ether band (C–O–C stretching) at 1266 cm^{-1} and the alkyl ether bands at 1106 cm^{-1} (C–O–C stretching) and 1060 cm^{-1} (C–O stretch from alkyl substituted ether). In order to highlight the structural changes that occur when the LE content increases in the CLE hydrogels, the ratio between the ether bands mentioned above and a band considered an internal standard for cellulose II, the band at 2892 cm^{-1}, was determined (Table 4). The formation of etheric cross-linking bonds was highlighted for all CLE hydrogels. It is worth mentioning that the number of these bands decreases with the increase in the LE content. A possible explanation for this behavior lies in the fact that, following the chemical modification of lignin, some free -OH groups are blocked with epoxy groups, which prevents the formation of new cross-linking bonds.

Table 4. Absorbance ratios used for the evaluation of structural modifications in CLE hydrogels.

Samples	A_{1266}/A_{2892}	A_{1106}/A_{2892}	A_{1060}/A_{2892}	A_{1508}/A_{2892}	A_{931}/A_{2892}
CLE 1	0.66	4.13	6.65	-	1.08
CLE 2	0.59	3.79	6.07	0.06	0.83
CLE 3	0.41	2.58	4.06	0.12	0.53
CLE 4	0.31	1.89	3.06	0.13	0.53
CLE 5	0.28	1.98	2.36	0.18	0.49
CLE 6	0.27	1.61	2.50	0.19	0.47
CLE 7	0.23	1.52	2.32	0.22	0.25

The characteristic band of lignin, at 1508 cm^{-1}, attributed to aromatic skeletal vibrations, is independent of the ones related to cellulose. Thus, in order to establish the LE content within the CLE hydrogels, a ratio between this band and the one at 2892 cm^{-1} was used [35]. Notably, the treatment with NaOH solution decreases the intensities of the band at 1508 cm^{-1}, and this is why it is significantly diminished in the ATR-FTIR spectrum of the CLE hydrogels. However, the values obtained for the A_{1508}/A_{2892} ratio confirm the presence of LE in the structure of the hydrogels and, in addition, it is observed that the ratio increases as the LE content increases in the CLE samples.

3.5. Rheological Investigations

The rheological properties of the CLE hydrogels were evaluated by amplitude and frequency sweep tests. The values of the storage modulus (G′) were greater than those of the loss modulus (G″), revealing the gel-like behavior of the CLE hydrogels, which can be thus considered viscoelastic solid materials (Figure 7). An enhanced stiffness “at rest”

(G′LVR) has been observed for CLE 1, or the samples containing less LE, as the mean values of G′ within the LVR were found to be of 13,500 Pa for CLE 1, 2560 Pa for CLE 4 and 750 Pa for CLE 7 [36].

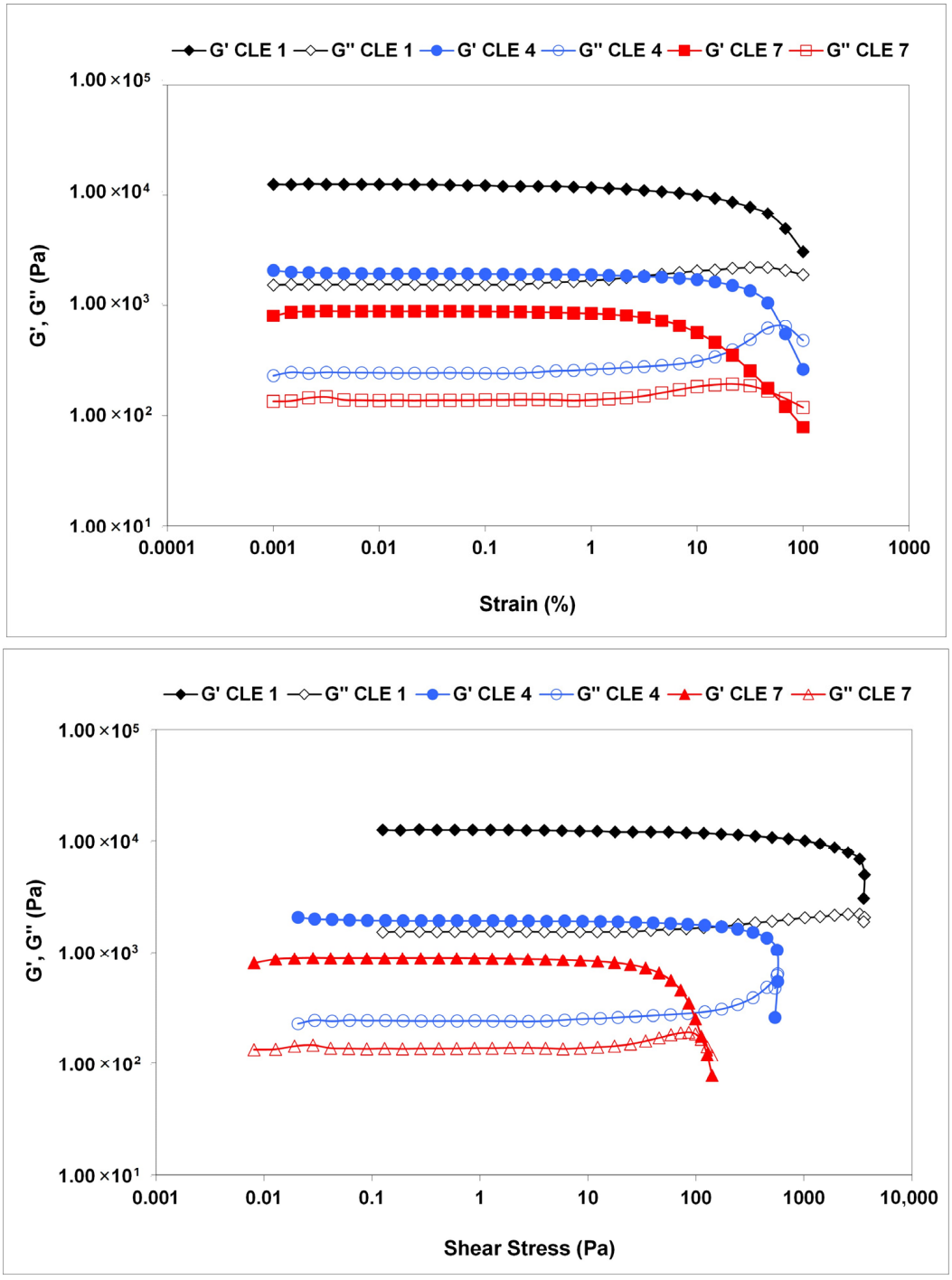

Figure 7. Amplitude sweep test results for CLE 1, CLE 4 and CLE 7 hydrogels: (**a**) G′ and G′′ dependence on the oscillatory strain; (**b**) G′ and G′′ dependence on the shear stress.

The curves plotted in Figure 7 show that the dynamic moduli G′ and G" depend on the strain amplitude at values exceeding LVE, the decrease in G′ and G" indicating material breakdown at large deformations. While G′ decreases sharply, G′′ increases before reaching a maximum peak, followed by a sudden drop. The rise in G′′ is associated with

the occurrence of micro-cracks, while the overall structural integrity is maintained as G′ remains constant and dominant over G″ (Figure 7a) [37,38].

The value of shear stress at the limit of the LVE region is considered the yield point (or linearity limit), while the flow point is represented as the value of shear stress at the crossover point of G′ and G″ (where G′ = G″). Between the yield stress and the flow point, with G′ still having higher values than G″, the initial structural strength of the hydrogel is modified, but it still exhibits the properties of a solid material. Above the flow point, G″ becomes greater than G′, and any further increase in shear stress leads to material flow, with the sample acquiring liquid-like properties [39]. The hydrogel CLE 1 did not show a flow point, maintaining its viscoelastic solid properties. The yield stress, stress and strain at the flow point were extracted from amplitude sweep measurements, the resulting values being presented in Table 5. The studied CLE hydrogels showed a flow point over 115 Pa (CLE 7). Increasing the LE concentration led to a decrease in yield stress and flow point values, respectively, with the samples becoming softer, changing their solid network structure.

Table 5. Values of yield stress, dynamic moduli at the crossover point (G′ = G″), and the stress and strain at the flow point (δf and γf).

Sample	Yield Stress, Pa	G′ = G″, Pa	δ_f, Pa	γ_f, %
CLE 1	118.0	-	-	-
CLE 4	19.0	631.9	569.7	62.5
CLE 7	8.5	159.5	115.6	51.1

The results of the frequency sweep tests carried out in the linear viscoelastic region also suggest the gel-like behavior of the CLE hydrogels, as the G′ values exceed those of G″ (Figure 8). A very small variation in G′ was observed in the whole range of investigated oscillation frequencies, in the absence of crossover frequency, demonstrating that the CLE hydrogels display a structured 3D network.

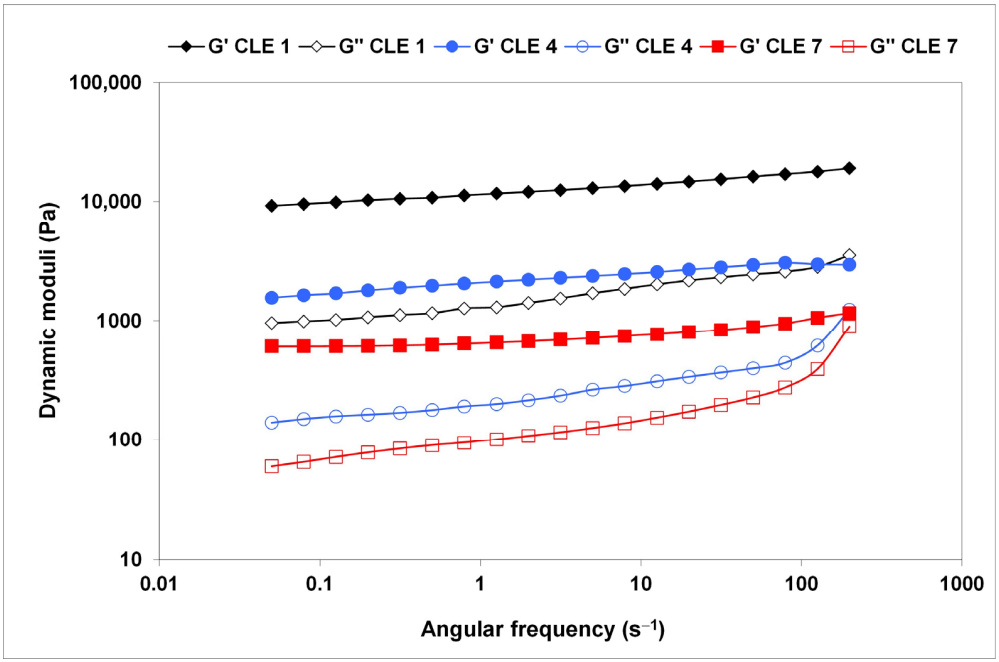

Figure 8. Variation of storage modulus G′ (solid symbols) and loss modulus G″ (open symbols) as a function of oscillatory frequency, ω, at 25 °C.

However, a higher dependency has been registered for G″, with the lowest values of dynamic moduli being recorded for CLE 7, which proved to be the softest material, although maintaining its stable structure. Similar behavior, typical of soft glassy materials, was reported for oxidized pullulan–dopamine cryogels [40].

A stronger and stiffer structure of CLE 1 is revealed by the highest values of G′ and G″ at the tested oscillation frequencies, with about one order of magnitude increase compared to CLE 7.

3.6. Mechanical Properties of CLE Hydrogels

The mechanical properties of CLE hydrogels were determined by a compression test, and the response of CLE hydrogels to compressive stress is an important indicator for their medical applications.

Figure 9a presents the compressive stress–strain curves of the CLE measured by a dynamic mechanical analyzer (DMA) with 60% strain in compression. All CLE hydrogels have a compressive strength up to 42% of the original height without fracture. The values of the elastic modulus were calculated at between 3 and 10% compression, where the stress–strain curves are linear (detail in Figure 9a), and the values obtained for the elastic modulus are presented in Figure 9b.

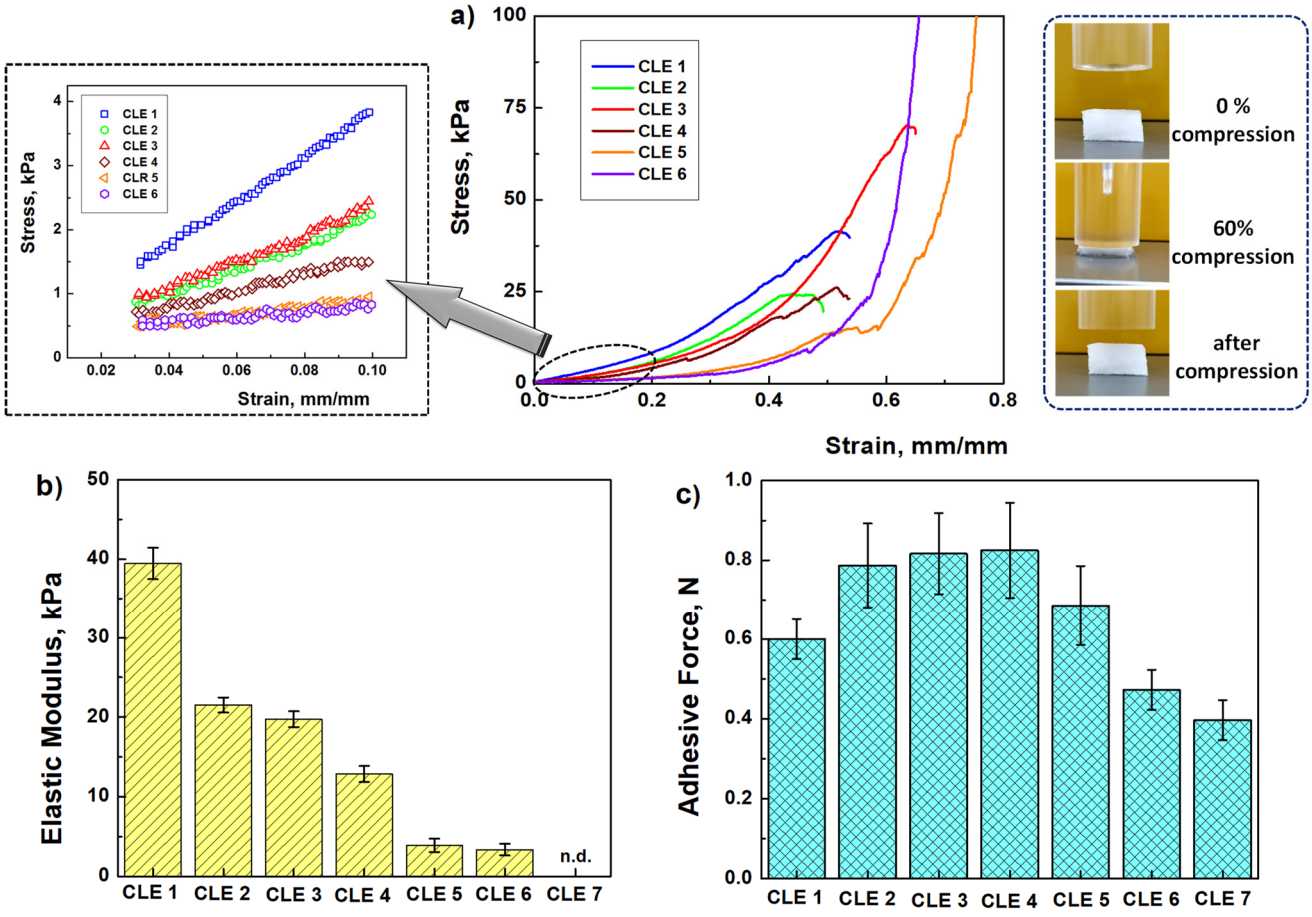

Figure 9. Mechanical properties of CLE hydrogels: (**a**) stress–strain profiles (in detail, linear dependence of stress–strain curves from which the elastic modulus of hydrogel samples was calculated), (**b**) the elastic modulus values as a function of hydrogel's composition, and (**c**) mucoadhesion force of CLE hydrogels.

As expected, the maximum value of the elastic modulus of 39.46 kPa was obtained in the case of the CLE 1 hydrogel, when the structure of the hydrogel was based only on covalent bonds between cellulose chains. Increasing the LE content in the hydrogel's structure, from 10% (CLE 2) to 30% (CLE 4), caused a decrease in the compressive modulus from 21.52 kPa to 12.86 kPa, respectively, due to the fact that the presence of LE hinders the formation of covalent bonds between cellulose chains. As a result, the elastic modulus of the hydrogels also decreases. In addition, by increasing the LE content to 40–50% (CLE 5 and CLE 6), the elastic modulus value significantly decreases to 3.34 kPa. A higher LE content (CLE 7) resulted in a very soft hydrogel, which did not allow the compression behavior to be recorded on the apparatus.

It is known that values of the modulus of elasticity between 3 and 20 kPa are ideal for oral wound dressings, which need to be soft and flexible [41,42]. This observation suggests CLE hydrogels with a higher LE content be applied as wound healing dressings.

3.7. Mucoadhesive Properties

For topical administration to the oral mucosa, polymer hydrogels must adhere to the mucosa, and in this respect adequate mucoadherence is essential. Figure 9c shows the values obtained for the adhesive force of CLE hydrogels, and it can be seen that all the samples fall within the necessary range allowed for the adhesion process (0.3–1.3 N) of oral dressings [43].

As a conclusion, the results obtained for the mechanical tests suggest the CLE hydrogels that have in their composition an LE amount of 10–30%, such as the CLE 2, CLE 3 and CLE 4 hydrogels, as ideal materials for applications as oral wound dressings.

3.8. Hydrolytic Degradation of CLE Hydrogels

Figure 10 shows the weight change recorded for wet hydrogels, as a function of immersion time. It is observed that, in the first 5–6 days, all CLE hydrogels go through a swelling phase, and after that CLE 5 and CLE 6 begin to degrade, a phenomenon illustrated by the mass decrease. At this point, due to the increase in water content inside the hydrogel, the ether bonds undergo hydrolysis and could be more easily cleaved [44], leading eventually to the detachment of small fragments from the hydrogel matrix. This phenomenon is more accentuated as the LE percentage in the hydrogel increases. Thus, the first hydrogels that start to degrade on the 6th day are those with 40% and 50% LE, respectively—CLE 5 (with 2.8%) and CLE 6 (with approximately 5%). The percentage of mass loss increased with the increasing the immersion time. Thus, the degradation process continues in the following days, reaching on the 14th day a decrease of 7.3% for CLE 4, of 8.7% for CLE 5 and 11.3% for CLE 6, respectively. However, for the other three hydrogels, CLE 1–CLE 3, this hydrolytic degradation does not occur, and in their case only the swelling phase is recorded. This is possible because, in the case of hydrogels with lower LE contents, the swelling process occurs more slowly, and thus the ether bonds are not yet completely hydrolyzed enough to be broken. So, it can be said that the hydrolytic degradation speed of CLE hydrogels is affected by the swelling ratio.

On the other hand, the pH of the immersion solutions does not vary much during the 14 days; there is only a slight, almost negligible, increasing tendency with the increase in the immersion time.

In conclusion, the hydrolytic degradation study indicates that the CLE hydrogel undergoes small in vitro degradation in the PBS buffer solution over 14 days (i.e., between 7.3 and 11.3%), significantly depending on the LE percentage within the hydrogel, which, in turn, directly influences its swelling behavior. Thus, considering the reduced hydrolytic degradation and their capacity to release drugs in a controlled manner, we can conclude that the proposed hydrogels are suitable for use as oral wound dressings.

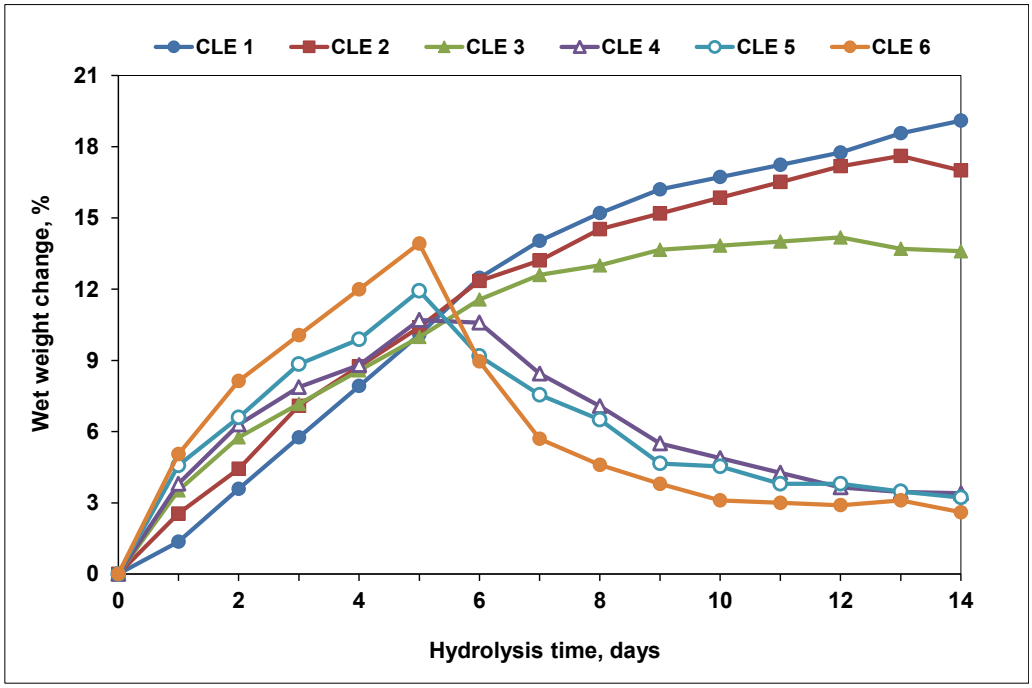

Figure 10. Wet weight change of CLE hydrogels in PBS solution (pH 7.4, 37 °C), over 14 days.

3.9. In Vitro Release of PrHy from P-CLE Hydrogels

The degree of incorporation (Id, %) of procaine hydrochloride (PrHy) in CLE hydrogels was studied by UV-VIS spectroscopy. In order to establish the amount of incorporated PrHy in each CLE hydrogel, the UV-VIS spectra of the aqueous solutions of PrHy remaining after the incorporation were recorded at 290 nm. A decrease in the absorption band was observed, which demonstrates an increase in the PrHy content in the P-CLE hydrogels. Moreover, it was found that the amount of incorporated PrHy depends on the composition of the hydrogel and, implicitly, on the Q_{max} of the CLE hydrogels. Thus, an increase in the LE content in the hydrogel's composition determines an increase in the Id of PrHy, which can be correlated with the data obtained for the swelling capacity of the CLE hydrogels (Table 6).

Table 6. Degree of incorporation (Id) and kinetic parameters of PrHy released from P-CLE hydrogels.

Sample	Kinetic Parameters of PrHy Release			Id, %
	n_r	k_r	R^2	
P-CLE 1	0.602	1.942	0.995	11.50
P-CLE 2	0.579	1.975	0.997	13.89
P-CLE 3	0.576	2.036	0.999	16.19
P-CLE 4	0.576	2.231	0.997	19.31
P-CLE 5	0.535	2.343	0.995	21.93
P-CLE 6	0.515	2.486	0.996	27.20
P-CLE 7	0.503	2.630	0.995	29.51

The release profiles of PrHy in distilled water at 37 °C from P-CLE hydrogels are presented in Figure 11. As expected, an increase in the swelling degree of the CLE hydrogels leads to a greater uptake of PrHy during the incorporation process and, implicitly, to the release of a greater amount of PrHy.

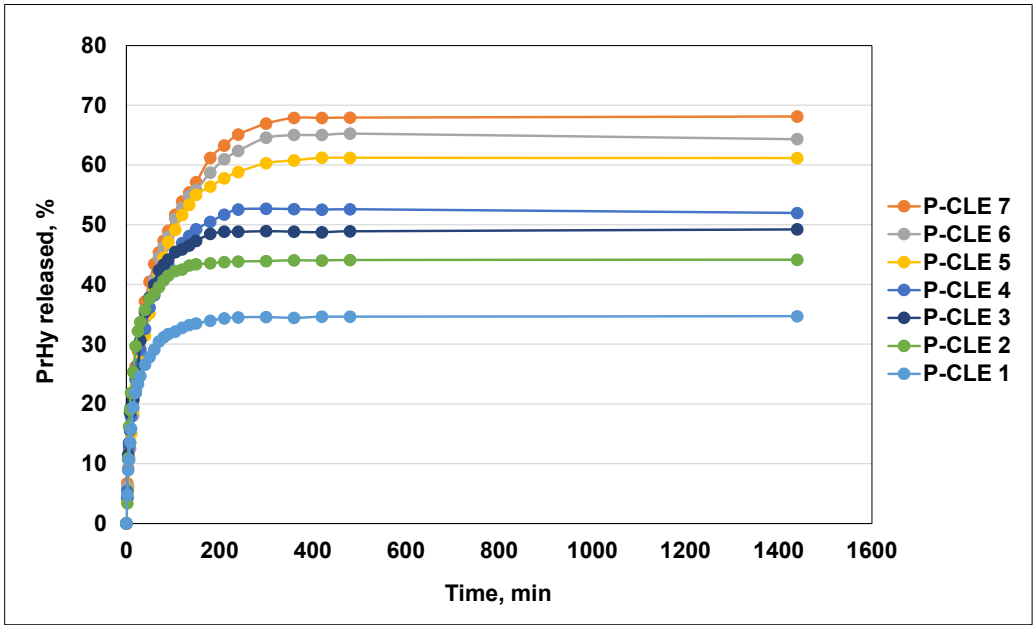

Figure 11. Release profiles of PrHy in distilled water at 37 °C from CLE hydrogels.

It is known that drugs are released from the polymer network only by a diffusion mechanism, and in this sense, the type of porous structure of the hydrogels is particularly important [45]. Depending on the pore size of the 3D network of the CLE hydrogels, which are between 38 μm (CLE 1) and 148 μm (CLE 7), it can be concluded that the CLE hydrogels have a macroporous structure, and that the release mechanism of PrHy is governed by the porosity of the matrix and the diffusion coefficient of the drug. It is observed that the release rate of PrHy is higher for the hydrogel CLE 7, with the highest content of LE, compared to CLE 1, which does not contain LE. Lower hydrogel density and larger pores are the reasons for the faster release.

The PrHy release profiles indicate for all P-CLE hydrogels a prolonged release of the drug, which increases gradually until about 400 min, where a plateau is reached. The drug is constantly released until 1440 min. There is an obvious influence of the LE content of P-CLE hydrogels on the PrHY release process; more precisely, the increase in the LE content within the matrix determines an increase in the amount of PrHy released. In this regard, it is observed that 68% PrHy is released from the P-CLE 7 hydrogel (with the highest amount of LE), in comparison with 34% PrHy released from the P-CLE 1 hydrogel, whose composition is based only on cellulose.

To evaluate the possible release mechanism of PrHy from the P-CLE hydrogels and the kinetic parameters of the release process, the experimental release data were investigated by fitting to the Korsmeyer–Peppas model. The kinetic parameters of the release process of PrHy (in distilled water, at 37 °C) from the P-CLE hydrogels are presented in Table 6.

Thus, the diffusion exponent, n, which is an indicator of the release mechanism, and the kinetic constant, k, which describes the structural and geometric parameters of the hydrogels, were determined. It is known that, for the hydrogels (cylindrical geometry), the exponent $n < 0.45$ indicates a release mechanism designed as Fickian diffusion, while if $0.45 < n < 0.89$, the mechanism is defined by non-Fickian diffusion or anomalous transport; when n = 0.89, the release is Case II transport, and for $n > 0.89$, the release mechanism is super Case II transport [46,47].

As can be seen from Table 6, in our case, all P-CLE hydrogels are governed by non-Fickian transport, where both the water diffusion rate and the polymer chain relaxation rate control the overall drug release process, because n_r has values between 0.503 (P-CLE 7) and 0.602 (P-CLE 1).

It can be concluded that the amount of PrHy released in a given period of time from the CLE hydrogels can be controlled by selecting specific preparation conditions of the hydrogels, such as a certain pore size or cross-linking density, a particular swelling degree and, implicitly, a certain degree of drug incorporation.

3.10. Antibacterial Properties of CLE and P-CLE Hydrogels

The oral flora is continuously changing due to the fact that the oral cavity comes into direct contact with the external environment. The species that we can find in the oral cavity, under normal conditions, belong to the genera Streptococcus, Lactobacillus, Lactococcus, Enterococcus, Staphylococcus, Corynebacterium, Veillonella and Bacteroids [48]. Both Gram-positive and Gram-negative bacteria produce bacteriocins, which consist of long peptide chains produced by bacterial ribosomes, used to inhibit or kill another bacterium, in the competition for nutrients within this ecosystem. Gram-negative bacteria have been observed to be more resistant to the bacteriocins produced by Gram-positive bacteria, due to their outer membrane, which acts as an effective barrier [49]. This is the reason why, in the oral cavity, Enterobacteriaceae is the overall predominant family (19.36%), and within this family, the most prevalent species is *Escherichia coli* (53.06%) [50].

Under specific conditions, these oral bacteria can cause numerous systemic infections, including bacterial endocarditis, respiratory pneumonia, osteomyelitis, and even cardiovascular diseases [48].

In order to test the antimicrobial activity of the CLE and P-CLE hydrogels, two different strains were considered: *Escherichia coli*, as the model Gram-negative bacteria, and *Staphyilococcus aureus*, as the model Gram-positive bacteria (Table 7).

Table 7. Antibacterial activity of CLE and P-CLE hydrogels.

Sample	Growth Inhibition, %	
	Escherichia coli	***Staphylococcus aureus***
CLE 1	20	14
CLE 2	70	59
CLE 4	81	65
CLE 6	91	85
P-CLE 1	36	16
P-CLE 2	80	43
P-CLE 4	85	64
P-CLE 6	96	88

The antibacterial activities of the CLE hydrogels were found to be dependent on the amount of LE within the matrix; more exactly, it is higher with the increase in LE content. The same observation was made by El-Nemr and coworkers [51], who explained that the presence of lignin induces the antimicrobial activity of PVA/gelatin–lignin blends due to the content of hydroxyl groups and methoxyl groups that interact with the bacterial cell membrane, causing the disruption and rupture of the cell membrane structure, and finally causing the infiltration of the cell component and the release of the bacterial cell contents. Moreover, the antibacterial effect of lignin modified with epoxy groups was highlighted by Kaur and colleagues, who showed that it is the most effective compared to unmodified or variously modified lignin, against both Gram-negative and Gram-positive bacteria [52].

In addition, CLE hydrogels were found to be more active against *Escherichia coli* than against *Staphylococcus aureus*. The same behavior was stated by Medina et al. [53], who showed that the inhibition effect of lignin on the Gram-positive bacteria was remarkable, compared to that on Gram-negative bacteria. This behavior was explained by the absence of the secondary cell wall of Gram-positive bacteria.

Furthermore, by testing the P-CLE hydrogels against *Escherichia coli* and *Staphylococcus aureus*, an improvement in the antimicrobial properties of the CLE hydrogels induced by the presence of PrHy in the matrix was observed. When increasing the concentration of PrHy in the hydrogels, from P-CLE 1 to P-CLE 6, the inhibitory effect is more obvious. Also, it was observed that PrHy was more active against *Escherichia coli* than against *Staphylococcus aureus*.

Based on the obtained results, it can be concluded that the hydrogels CLE 4 and CLE 6 are more effective against *Escherichia coli* and *Staphylococcus aureus* than the other hydrogels, which evidences the real potential of these materials to be used as antibacterial wound dressings for administering medical treatments.

3.11. In Vitro Biocompatibility of CLE and P-CLE Hydrogels (MTS Assay)

Human gingival fibroblasts (hGFs) are the main cells of the gingival tissue that play an important role in wound healing, being much more efficient at remodeling connective tissue than dermal fibroblasts. They play an important role in the synthesis of extracellular matrix (ECM) components (collagen, fibronectin, hyaluronan and elastin) and in maintaining tissue integrity [54].

To investigate the influence of the amount of LE within CLE hydrogels on their cytocompatibility, hGFs were used. In addition, the cytocompatibility of P-CLE hydrogels was also investigated.

The in vitro biocompatibility of CLE and P-CLE hydrogels was evaluated by the MTS assay, after incubation for 24 h (extract dilution method: extracts at different concentrations of 1 mg/mL, 2 mg/mL, 3 mg/mL and 4 mg/mL), using hGFs (Figure 12).

As already reported, cellulose hydrogels have excellent cytocompatibility for fibroblast cells [12,55]. In our study, the results show that the cellulose hydrogel (CLE 1) has good cell viability, with more than 100% cell viability, regardless of the concentration of the extract used. An increase in the cell viability for the CLE hydrogels is observed through the gradual increase in the percentage of LE in the hydrogel composition, and moreover, this increase in LE also causes the stimulation of fibroblast proliferation up to a maximum value, as recorded for the CLE 7 hydrogel (Figure 12a). Also, increasing the concentration of the extracts up to 4 mg/mL, for each sample, led to an increase in the viability of the fibroblast for each individual sample.

P-CLE hydrogels were also evaluated regarding their level of safety, by incubating extracts of different concentrations, for 24 h in the presence of fibroblast cells (Figure 12b). It was demonstrated that the presence of PrHy in the P-CLE hydrogels did not significantly change their biocompatibility; thus, cell viabilities of over 99% were obtained. However, a decrease in cell viability was observed for P-CLE hydrogels, compared to CLE hydrogels. In addition, for P-CLE hydrogels, a slight decrease in cell viability was observed, with the increase in the amount of LE in the samples and, implicitly, with the increase in the drug concentration within the 3D networks.

Considering that none of the tested extract dilutions decreased the cell viability to below 99%, according to the international standard ISO 10993-5:2009 [21], it can be concluded that all CLE and P-CLE hydrogels can be regarded as non-cytotoxic materials.

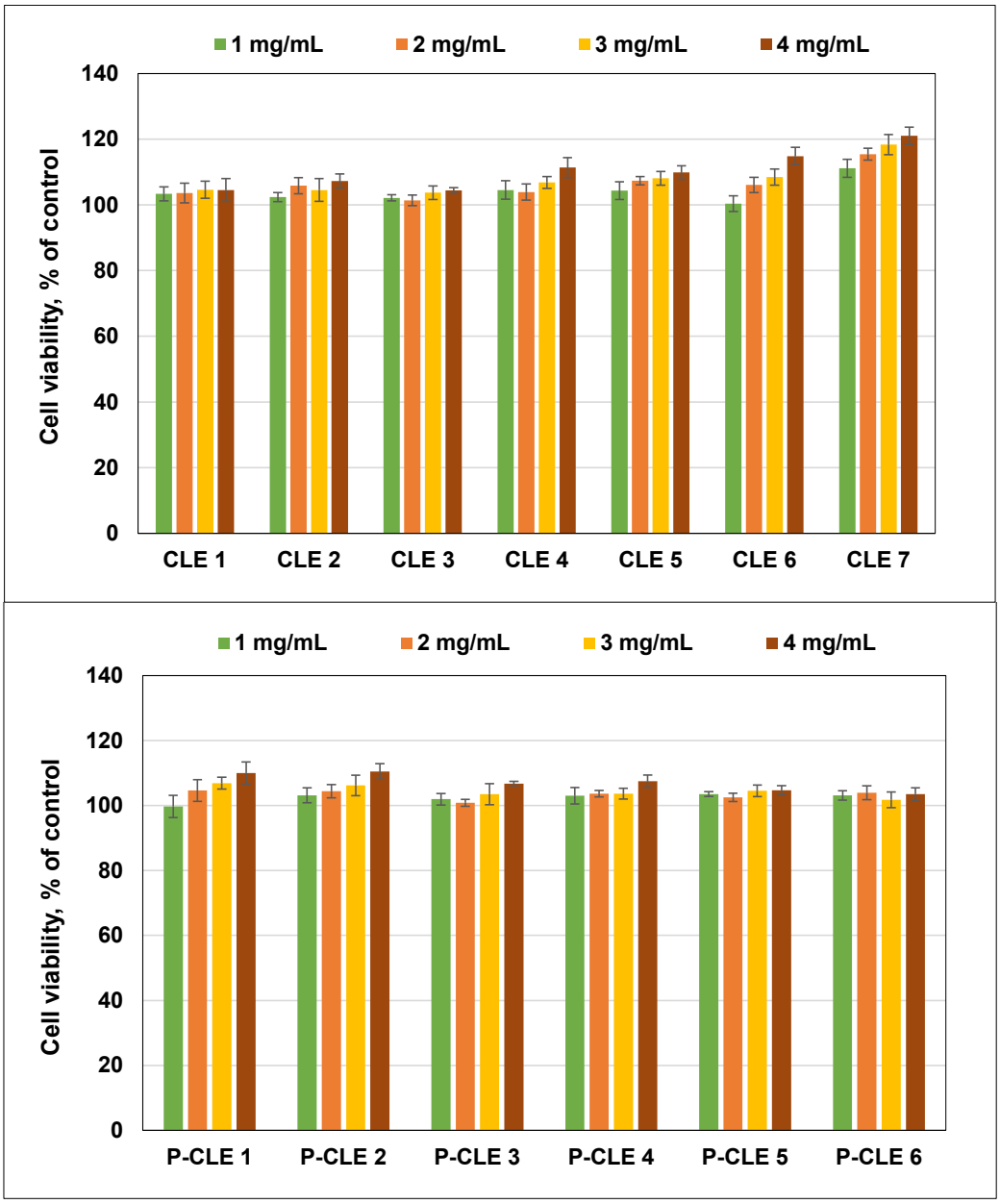

Figure 12. Biocompatibility on human gingival fibroblast cells of (**a**) CLE hydrogels and (**b**) P-CLE hydrogels. Experiments were done in triplicate and treated cell viability was expressed as percentage of control cells' viability. Graphical data were expressed as means ± standard deviation.

4. Conclusions

New multifunctional hydrogels based on cellulose and modified lignin (CLE) have been prepared to be used in advanced wound management.

Through ATR-FTIR spectroscopy, the achievement of the cross-linking reaction between the two natural polymers was confirmed, through the appearance of adsorption bands characteristic of the formation of new ether bonds. It was demonstrated by SEM that the LE contributes to the formation of a more heterogeneous porous architecture, with larger and more irregular pores, compared to the cellulose-based hydrogel (CLE 1). This morphological aspect contributes to the high swelling degree of CLE hydrogels, and also to their superior PrHy encapsulation capacity compared to CLE 1. It was observed that a 60% LE content (CLE 7, 5490%) leads to an increase in Q_{max} to almost four times higher than seen with the CLE 1 sample (1460%). The release kinetics of PrHy indicate for all

hydrogels a non-Fickian transport mechanism, where both the water diffusion rate and the relaxation rate of the polymer chains control the overall drug release process. The influence of the composition of CLE hydrogels can also be observed on the mechanical properties of the samples. The increase in the LE content in the structure of the hydrogels causes a decrease in the compression modulus, due to the fact that the presence of LE prevents the formation of cross-linking bridges between the cellulose chains, which results in the formation of softer and more porous hydrogels, suitable for being used in wound healing. Moreover, the values obtained for the mucoadhesion force of the CLE hydrogels show that the samples fall within the allowed range for the adhesion process of oral dressings, which recommends their use as oral wound dressings. Studies on the antimicrobial activity of CLE hydrogels against *Escherichia coli* and *Staphylococcus aureus* show that all the hydrogels are effective against these bacteria, starting from CLE 4, which demonstrates the real potential of these materials to be used as antibacterial dressings in medical treatments. An additional improvement in the antimicrobial properties of the CLE hydrogels was induced by the presence of PrHy in the P-CLE hydrogels. In vitro biocompatibility studies indicate that both CLE and P-CLE hydrogels have good viability and can be considered as non-cytotoxic materials. Furthermore, by adding LE into the composition of CLE hydrogels, an obvious improvement in cell viability is achieved.

The entire set of characterization techniques used in the study have revealed that these new CLE hydrogels are biocompatible, have high swelling capacity and antibacterial properties, can release drugs in a controlled manner, and present mucoadhesiveness. Overall, the findings of the study highlight the fact that the CLE hydrogels can be used as possible oral dressings in wound management.

Author Contributions: Conceptualization, D.E.C. and G.C.; methodology, D.E.C.; validation, D.E.C., R.N., D.M.S., D.R., R.N.D.-N., N.S. and F.C.; formal analysis, D.E.C., R.N., D.M.S., D.R., R.N.D.-N., N.S. and F.C.; investigation, D.E.C., R.N., D.M.S., D.R., R.N.D.-N., N.S. and F.C.; resources, D.E.C. and G.C.; data curation, D.E.C., R.N., D.M.S., D.R., R.N.D.-N., N.S. and F.C.; writing—original draft preparation, D.E.C., R.N., D.M.S., D.R., R.N.D.-N., N.S. and F.C; writing—review and editing, D.E.C. and F.C.; visualization, R.N., D.M.S., D.R., R.N.D.-N., N.S. and G.C.; supervision, D.E.C. and F.C. All authors have read and agreed to the published version of the manuscript.

Funding: This research received no external funding.

Institutional Review Board Statement: Not applicable.

Informed Consent Statement: Not applicable.

Data Availability Statement: Data are contained within the article.

Acknowledgments: We thank Gina-Mihaela Pricope from the Veterinary and Food Safety Laboratory, Food Safety Department, Iasi, Romania, for performing the antimicrobial tests.

Conflicts of Interest: The authors declare no conflict of interest.

References

1. Ghomi, E.R.; Khalili, S.; Khorasani, S.N.; Neisiany, R.E.; Ramakrishna, S. Wound dressings: Current advances and future directions. *J. Appl. Polym. Sci.* **2019**, *136*, 47738. [CrossRef]
2. Zhang, W.; Liu, W.; Long, L.; He, S.; Wang, Z.; Liu, Y.; Yang, L.; Chen, N.; Hu, C.; Wang, Y. Responsive multifunctional hydrogels emulating the chronic wounds healing cascade for skin repair. *J. Control. Release* **2023**, *354*, 821–834. [CrossRef]
3. Lei, J.; Sun, L.; Li, P.; Zhu, C.; Lin, Z.; Mackey, V.; Coy, D.H.; He, Q. The wound dressings and their applications in wound healing and management. *Health Sci. J.* **2019**, *13*, 662.
4. Gupta, A.; Kowalczuk, M.; Heaselgrave, W.; Britland, S.T.; Martin, C.; Radecka, I. The production and application of hydrogels for wound management: A review. *Eur. Polym. J.* **2019**, *111*, 134–151. [CrossRef]
5. Nguyen, H.M.; Le, T.T.N.; Nguyen, A.T.; Le, H.N.T.; Pham, T.T. Biomedical materials for wound dressing: Recent advances and applications. *RSC Adv.* **2023**, *13*, 5509–5528. [CrossRef] [PubMed]
6. Han, Z.; Deng, L.; Chen, S.; Wang, H.; Huang, Y. Zn^{2+}-Loaded adhesive bacterial cellulose hydrogel with angiogenic and antibacterial abilities for accelerating wound healing. *Burn. Trauma* **2023**, *11*, tkac048. [CrossRef]
7. Chen, A.; Deng, S.; Lai, J.; Li, J.; Chen, W.; Varma, S.N.; Zhang, J.; Lei, C.; Liu, C.; Huang, L. Hydrogels for oral tissue engineering: Challenges and opportunities. *Molecules* **2023**, *28*, 3946. [CrossRef]

8. Wang, L.; Zhou, M.; Xu, T.; Zhang, X. Multifunctional hydrogel as wound dressing for intelligent wound monitoring. *Chem. Eng. J.* **2022**, *433*, 134625. [CrossRef]
9. Kundu, R.; Mahada, P.; Chhirang, B.; Das, B. Cellulose hydrogels: Green and sustainable soft biomaterials. *Curr. Res. Green Sustain. Chem.* **2022**, *5*, 100252. [CrossRef]
10. Seddiqi, H.; Oliaei, E.; Honarkar, H.; Jin, J.F.; Geonzon, L.C.; Bacabac, R.G.; Klein-Nulend, J. Cellulose and its derivatives: Towards biomedical applications. *Cellulose* **2021**, *28*, 1893–1931. [CrossRef]
11. Deng, Y.; Chen, J.; Huang, J.; Yang, X.; Zhang, X.; Yuan, S.; Liao, W. Preparation and characterization of cellulose/flaxseed gum composite hydrogel and its hemostatic and wound healing functions evaluation. *Cellulose* **2020**, *18*, 1–8. [CrossRef]
12. Nicu, R.; Ciolacu, D.E.; Petrovici, A.-R.; Rusu, D.; Avadanei, M.; Mihaila, A.C.; Butoi, E.; Ciolacu, F. 3D Matrices for enhanced encapsulation and controlled release of anti-inflammatory bioactive compounds in wound healing. *Int. J. Mol. Sci.* **2023**, *24*, 4213. [CrossRef]
13. Meng, Y.; Lu, J.; Cheng, Y.; Li, Q.; Wang, H. Lignin-based hydrogels: A review of preparation, properties, and application. *Int. J. Biol. Macromol.* **2019**, *135*, 1006–1019. [CrossRef]
14. Nan, N.; Hu, W.; Wang, J. Lignin-based porous biomaterials for medical and pharmaceutical applications. *Biomedicines* **2022**, *10*, 747. [CrossRef] [PubMed]
15. Eivazzadeh-Keihan, R.; Aliabadi, H.A.M.; Radinekiyan, F.; Sobhani, M.; Khalili, F.; Maleki, A.; Madanchi, H.; Mahdavi, M.; Shalan, A.E. Investigation of the biological activity, mechanical properties and wound healing application of a novel scaffold based on lignin–agarose hydrogel and silk fibroin embedded zinc chromite nanoparticles. *RSC Adv.* **2021**, *11*, 17914–17923. [CrossRef] [PubMed]
16. Jaiswal, L.; Shankar, S.; Rhim, J.W.; Hahm, D.H. Lignin-mediated green synthesis of AgNPs in carrageenan matrix for wound dressing applications. *Int. J. Biol. Macromol.* **2020**, *159*, 859–869. [CrossRef]
17. Ciolacu, D.; Oprea, A.M.; Anghel, N.; Cazacu, G.; Cazacu, M. New cellulose–lignin hydrogels and their application in controlled release of polyphenols. *Mater. Sci. Eng. C* **2012**, *32*, 452–463. [CrossRef]
18. Zmejkoski, D.; Spasojević, D.; Orlovska, I.; Kozyrovska, N.; Soković, M.; Glamočlija, J.; Dmitrović, S.; Matović, B.; Tasić, N.; Maksimović, V.; et al. Bacterial cellulose-lignin composite hydrogel as a promising agent in chronic wound healing. *Int. J. Biol. Macromol.* **2018**, *118*, 494–503. [CrossRef]
19. *ISO 16649-2:2001*; Microbiology of Food and Animal Feeding Stuffs—Horizontal Method for the Enumeration of Beta-Glucuronidase-Positive *Escherichia coli*—Part 2: Colony-Count Technique at 44 °C Using 5-Bromo-4-chloro-3-indolyl beta-D-glucuronide. ISO: Geneva, Switzerland, 2001.
20. *ISO 6888-3:2003*; Microbiology of Food and Animal Feeding Stuffs—Horizontal Method for the Enumeration of Coagulase-Positive *Staphylococci* (*Staphylococcus aureus* and Other Species)—Part 3: Detection and MPN Technique for Low Numbers. ISO: Geneva, Switzerland, 2003.
21. *ISO 10993-5:2009*; Biological Evaluation of Medical Devices Part 5: Tests for In Vitro Cytotoxicity. ISO: Geneva, Switzerland, 2009.
22. Lu, X.; Gu, X. A review on lignin-based epoxy resins: Lignin effects on their synthesis and properties. *Int. J. Biol. Macromol.* **2023**, *229*, 778–790. [CrossRef] [PubMed]
23. Mota, L.O.; Gimenez, I.F. Cellulose-based materials crosslinked with epichlorohydrin: A mini review. *Rev. Virtual Quim.* **2023**, *15*, 159–170. [CrossRef]
24. Sezer, S.; Şahin, I.; Öztürk, K.; Şanko, V.; Koçer, Z.; Sezer, U.A. Cellulose-Based Hydrogels as Biomaterials. In *Cellulose-Based Superabsorbent Hydrogels, Polymers and Polymeric Composites: A Reference Series*; Mondal, M.I.H., Ed.; Springer: Cham, Germany, 2019; Chapter 39; pp. 1178–1203.
25. Sathawong, S.; Sridach, W.; Techato, K. Lignin: Isolation and preparing the lignin based hydrogel. *J. Environ. Chem. Eng.* **2018**, *6*, 5879–5888. [CrossRef]
26. Măluțan, T.; Nicu, R.; Popa, V.I. Lignin modification by epoxidation. *BioResources* **2008**, *3*, 1371–1376. [CrossRef]
27. Ciolacu, D.; Cazacu, G. New green hydrogels based on lignin. *J. Nanosci. Nanotechnol.* **2018**, *18*, 2811–2822. [CrossRef] [PubMed]
28. Muharam, S.; Fitri, A.; Yuningsih, L.M.; Putri, Y.M.T.A.; Rahmawati, I. Synthesis and characterization of controlled-release urea fertilizer from superabsorbent hydrogels. *Indones. J. Chem.* **2020**, *20*, 616–625. [CrossRef]
29. Oh, S.Y.; Yoo, D.I.; Shin, Y.; Seo, G. FTIR analysis of cellulose treated with sodium hydroxide and carbon dioxide. *Carbohydr. Res.* **2005**, *340*, 417–428. [CrossRef]
30. Salim, R.M.; Asik, J.; Sarjadi, M.S. Chemical functional groups of extractives, cellulose and lignin extracted from native Leucaena leucocephala bark. *Wood Sci. Technol.* **2021**, *55*, 295–313. [CrossRef]
31. Oh, S.Y.; Yoo, D.I.; Shin, Y.; Kim, H.C.; Kim, H.Y.; Chung, Y.S.; Park, W.H.; Youk, J.H. Crystalline structure analysis of cellulose treated with sodium hydroxide and carbon dioxide by means of X-ray diffraction and FTIR spectroscopy. *Carbohydr. Res.* **2005**, *340*, 2376–2391. [CrossRef] [PubMed]
32. Carrillo, F.; Colom, X.; Sunol, J.J.; Saurina, J. Structural FTIR analysis and thermal characterization of lyocell and viscose-type fibres. *Eur. Polym. J.* **2004**, *40*, 2229–2234. [CrossRef]
33. Auxenfans, T.; Crônier, D.; Chabbert, B.; Paës, G. Understanding the structural and chemical changes of plant biomass following steam explosion pretreatment. *Biotechnol. Biofuels* **2017**, *10*, 36. [CrossRef]
34. Nelson, M.L.; O'Connor, R.T. Relation of certain infrared bands to cellulose crystallinity and crystal lattice type. Part II. A new infrared ratio for estimation of crystallinity in celluloses I and II. *J. Appl. Polym. Sci.* **1964**, *8*, 1325–1341. [CrossRef]

35. Horikawa, Y.; Hirano, S.; Mihashi, A.; Kobayashi, Y.; Zhai, S.; Sugiyama, J. Prediction of lignin contents from infrared spectroscopy: Chemical digestion and lignin/biomass ratios of Cryptomeria japonica. *Appl. Biochem. Biotechnol.* **2019**, *188*, 1066–1076. [CrossRef]
36. Ciolacu, D.E.; Rusu, D.; Darie-Nita, R.N.; Tîmpu, D.; Ciolacu, F. Influence of gel stage from cellulose dissolution in NAOH-water system on the performances of cellulose allomorphs-based hydrogels. *Gels* **2022**, *8*, 410. [CrossRef]
37. Mezger, T. *The Rheology Handbook: For Users of Rotational and Oscillatory Rheometers*; European Coatings: Wilmington, NC, USA, 2020.
38. Haider, M.S.; Ahmad, T.; Yang, M.; Hu, C.; Hahn, L.; Stahlhut, P.; Groll, J.; Luxenhofer, R. Tuning the thermogelation and rheology of poly(2-oxazoline)/poly(2-oxazine)s based thermosensitive hydrogels for 3D bioprinting. *Gels* **2021**, *7*, 78. [CrossRef]
39. Balmforth, N.J.; Frigaard, I.A.; Ovarlez, G. Yielding to stress: Recent developments in viscoplastic fluid mechanics. *Annu. Rev. Fluid Mech.* **2014**, *46*, 121–146. [CrossRef]
40. Baron, R.I.; Duceac, I.A.; Morariu, S.; Bostanaru-Iliescu, A.C.; Coseri, S. Hemostatic cryogels based on oxidized pullulan/dopamine with potential use as wound dressings. *Gels* **2022**, *8*, 726. [CrossRef]
41. Zahouani, H.; Pailler-Mattei, C.; Sohm, B.; Vargiolu, R.; Cenizo, V.; Debret, R. Characterization of the mechanical properties of a dermal equivalent compared with human skin in vivo by indentation and static friction tests. *Skin Res. Technol.* **2009**, *15*, 68–76. [CrossRef]
42. Pailler-Mattei, C.; Bec, S.; Zahouani, H. In vivo measurements of the elastic mechanical properties of human skin by indentation tests. *Med. Eng. Phys.* **2008**, *30*, 599–606. [CrossRef] [PubMed]
43. Mura, P.; Cirri, M.; Mennini, N.; Casella, G.; Maestrelli, F. Polymeric mucoadhesive tablets for topical or systemic buccal delivery of clonazepam: Effect of cyclodextrin complexation. *Carbohydr. Polym.* **2016**, *152*, 755–763. [CrossRef] [PubMed]
44. Li, J.; Mooney, D.J. Designing hydrogels for controlled drug delivery. *Nat. Rev. Mater.* **2016**, *1*, 16071. [CrossRef] [PubMed]
45. Ciolacu, D.E.; Nicu, R.; Ciolacu, F. Cellulose-Based Hydrogels as Sustained Drug-Delivery Systems. *Materials* **2020**, *13*, 5270. [CrossRef]
46. Ganji, F.; Vasheghani-Farahani, S.; Vasheghani-Farahani, E. Theoretical description of hydrogel swelling: A Review. *Iran. Polym. J.* **2010**, *19*, 375–398.
47. Peppas, N.A.; Khare, A.R. Preparation, structure and diffusional behavior of hydrogels in controlled release. *Adv. Drug Deliv. Rev.* **1993**, *11*, 1–35. [CrossRef]
48. Wang, Q.Q.; Zhang, C.F.; Chu, C.H.; Zhu, X.F. Prevalence of Enterococcus faecalis in saliva and filled root canals of teeth associated with apical periodontitis. *Int. J. Oral Sci.* **2012**, *4*, 19–23. [CrossRef] [PubMed]
49. Prudêncio, C.V.; dos Santos, M.T.; Vanetti, M.C.D. Strategies for the use of bacteriocins in Gram-negative bacteria: Relevance in food microbiology. *J. Food Sci. Technol.* **2015**, *52*, 5408–5417. [CrossRef] [PubMed]
50. Alghamdi, S. Isolation and identification of the oral bacteria and their characterization for bacteriocin production in the oral cavity. *Saudi J. Biol. Sci.* **2022**, *29*, 318–323. [CrossRef] [PubMed]
51. El-Nemr, K.F.; Mohamed, H.R.; Ali, M.A.; Fathy, R.M.; Dhmees, A.S. Polyvinyl alcohol/gelatin irradiated blends filled by lignin as green filler for antimicrobial packaging materials. *Iran. Polym. J.* **2020**, *100*, 1578–1602. [CrossRef]
52. Kaur, R.; Uppal, S.K.; Poonam Sharma, P. Antioxidant and antibacterial activities of sugarcane bagasse lignin and chemically modified lignins. *Sugar Tech.* **2017**, *19*, 675–680. [CrossRef]
53. Medina, J.D.C.; Woiciechowski, A.L.; Filho, A.Z.; Bissoqui, L.; Noseda, M.D.; Vandenberghe, L.P.S.; Zawadzki, S.F.; Soccol, C.R. Biological activities and thermal behavior of lignin from oil palm empty fruit bunches as potential source of chemicals of added value. *Ind. Crop Prod.* **2016**, *94*, 630. [CrossRef]
54. Ahangar, P.; Mills, S.J.; Smith, L.E.; Gronthos, S.; Cowin, A.J. Human gingival fibroblast secretome accelerates wound healing through anti-inflammatory and pro-angiogenic mechanisms. *NPJ Regen Med.* **2020**, *5*, 24. [CrossRef] [PubMed]
55. Nakasone, K.; Kobayashi, T. Cytocompatible cellulose hydrogels containing trace lignin. *Mater. Sci. Eng. C* **2016**, *64*, 269–277. [CrossRef]

Table 2
X-ray diffraction parameters of untreated and CBD-treated cellulose allomorphs.

Samples	*D*, nm				*d*-Spacing, Å				*CrI*, %
	(101)	$(10\bar{1})$	(002)	(040)	(101)	$(10\bar{1})$	(002)	(040)	
BI	5.7	5.2	9.2	9.3	5.90	5.29	3.90	2.62	75.32
BI-CBD	6.0	5.1	8.1	10.6	5.93	5.18	3.77	2.60	70.40
BII	5.0	8.2	8.8	10.2	7.14	4.83	4.34	2.61	64.97
BII-CBD	5.5	7.8	7.0	16.3	7.32	4.65	4.03	2.59	61.41
BIII	4.8	8.5	8.5	11.6	7.47	4.38	4.38	2.66	57.42
BIII-CBD	4.2	7.2	7.2	14.3	7.26	3.98	3.98	2.57	52.50
Ba	–	–	–	–	–	–	–	–	20.21
Ba-CBD	–	–	–	–	–	–	–	–	14.63

and retaining a certain disorganized state at the level of a supramolecular structure. The X-ray diffraction of Ba clearly indicated an amorphous structure due to the absence or strong reduction of all the peaks characteristic to cellulose I.

The changes which took place during the CBD adsorption on the cellulose allomorphs, regarding the crystallite dimension (*D*), lattice spacing (*d*-spacings) and the crystallinity index (*CrI*), are presented in Table 2. The action of CBD on the cellulose allomorphs was reflected in a decrease in the crystallinity index, indicating a slight penetration of CBD between the chains which consequently led to a less dense and less ordered structure. Overall, the CBDs were responsible for the disruption of the intermolecular hydrogen bonds within the supramolecular structure of allomorphs and the smaller crystallites were released into a water-based medium (Ciolacu et al., 2010; Hall et al., 2011).

The CBD adsorption process was reflected in a decrease of the crystallite sizes in the (002) direction for all cellulose allomorphs. The preference of the CBD to the hydrophobic (002) crystal face of the cellulose has also been confirmed by other studies (Ciolacu et al., 2010; Liu, 2013; Mazeau, 2011; Široký et al., 2012). The suggested mechanism for the binding of CBD to cellulose proposed the attachment of this protein to the (002) plane probably exposed at the edges of the perfect cellulose microcrystals.

It has been established that at least three aromatic residues on a CBD surface are necessary for cellulose–CBD binding activity (Guo and Catchmark, 2013; Zhang et al., 2012). Another requirement is the position of the cellulose binding residues, which should be on a planar face without topographic obstacles that enable proximity between the aromatic residues of the CBD and the glucose rings of the cellulose (Yaniv et al., 2012). The presented results imply that the surface of the CBD interacted selectively with the (002) plane of the crystalline cellulose, thus establishing hydrogen bonds between the equatorial hydroxyls of the glucose rings and polar amino acid chains. The planar face formed by the proposed cellulose binding amino-acid residues is indicated.

The three-dimensional structure of the CBD of cellulase Cel9B from *P. barcinonensis* was determined using the online modeling software Swiss-Model (Expasy) based on sequence homology with available crystallized proteins. The CBD (residues 846-997 GenBank entry: CAB38941.1) belongs to the CBM3b family and shows 45.39% sequence identity with the CBM3b of ScaA from *Acetivibrio cellulolyticus* (PDB entry: 3zucA; Yaniv et al., 2012), the template sequence used by the program to generate the model. The amino acids involved in cellulose binding were deduced by sequence alignment with the CBM3b of *A. cellulolyticus* ScaA and CBM3b of ScaA from *Bacteroides cellulosolvens* (PDB entry: 2xbt; Yaniv et al., 2012). They are aspartate D903, tyrosine Y904, arginine R953 and tryptophan W959, in agreement with the 3D structure where they formed a planar face.

As is known, the crystallite sizes of the (101), $(10\bar{1})$ and (002) diffraction planes measure the crystallite width, while the reflection at (040) indicates the crystallite length. The (040) reflection was used to measure the lateral length of cellulosic samples because this occurs in a direction orthogonal to the longitudinal direction of the microfibril. In the present case it was recorded an increase of the crystallite size in this direction, probably because of the recrystallization of the disordered cellulose chains on the microfibril surface after the CBD action (Penttilä et al., 2013).

Taking into account the *d*-spacings for the cellulose allomorphs, cellulose I presented the smaller *d*-spacing if compared to cellulose II and III. Based on the literature, the smaller *d*-spacing in cellulose I indicate a stronger hydrophobic interaction (Wada et al., 2010). In addition, the allomorphs treated with CBD presented a decrease of lattice spacings in all independent reflections.

3.1.3. ATR-FTIR spectroscopy

ATR-FTIR is one of the best available techniques to obtain structural information about hydrogen bonding, cellulose crystallinity and even to investigate the structural changes during cotton cellulose formation (Liu, 2013). It requires minimal sample preparation, permits routine analysis, is easy to operate, and has been widely used in polymer characterization, providing information about chemical nature, conformational order, state of order, orientation and also a clear relationship between the interactions of hydroxyl groups and crystallinity in cellulose (Široký et al., 2010).

The ATR-FTIR analysis of the cellulose allomorphs treated with CBD was performed. Generally, there is a limited research in this area regarding the cellulose allomorphs, so this study could bring new insights to understand the changes in supramolecular structure when treated with CBD.

A strong and broad FTIR band is commonly observed within the range of 3700–3000 cm^{-1} in the spectra of cellulose allomorphs and CBD, corresponding to the absorption of hydroxyl groups (figure not shown). Following the chemical modifications from BI to BII and BIII and further to Ba, which is accompanied by a decrease in the crystallinity index, the absorbance of the OH stretching vibration in the overall range decreased considerably. At the same time, the band at 897 cm^{-1}, corresponding to the C–H bending mode, showed a remarkable increase in its intensity. The band from 2900 cm^{-1} is assigned to C–H stretching and appears in all spectra, with varied intensities and shapes.

The main differences in FTIR spectra between the cellulosic samples and the CBD are the presence of amide I (1700–1600 cm^{-1}) and amide II (1600–1500 cm^{-1}) bands, which are not in the spectra of allomorphic forms of cellulose or in amorphous cellulose. However, for the allomorphs of cellulose in the range of 1700–1500 cm^{-1} one peak at 1645 cm^{-1} appears which is assigned to the absorbed water (Široký et al., 2010).

In the structure of cellulose there are three hydroxyl groups which are involved in different inter- and intramolecular hydrogen bonds, forming a network with a significant role with respect to crystallinity and chain conformation. In cellulose I, the intramolecular hydrogen bonds are established between the hydroxyl groups on C(3) of the glucopyranose rings and the ring oxygens O(5′) of the neighboring glucose units and also between the hydroxyls

groups on C(2′) and C(6) of glucose units, in the same molecular chains. Regarding the intermolecular hydrogen bonding it is established between the hydroxyls on C(6) of one cellulose molecule and C(3′) of the adjacent molecular chains (Krässig, 1993). Cellulose II is more densely packed than cellulose I due to a much complex hydrogen bonding network.

It is known that for cellulose I, the FTIR assignments for the intramolecular hydrogen bonding of O(2′)H···O(6) and O(3)H···O(5′) are generally shown at 3410–3455 cm^{-1} and 3340–3375 cm^{-1}, respectively, while the intermolecular hydrogen bonding of O(6)H···O(3′) within the cellulose crystalline structure is shown at 3230–3310 cm^{-1} (Salmén et al., 2005). Besides, in amorphous cellulose the hydrogen bonds are assigned to a frequency of 3420 cm^{-1} corresponding to the O(2′)H···O(6) intramolecular hydrogen bonds (Široký et al., 2010).

Consistent adsorption bands around the 3336 and 3275 cm^{-1} were observed for all cellulose allomorphs which were assigned to the intramolecular hydrogen bonding of O(3)H···O(5′) and to the intermolecular hydrogen bonding of O(6)H···O(3), respectively. For the intramolecular hydrogen bonding of O(2)H···O(6), a small shoulder in FTIR spectra of cellulose allomorphs was observed. In order to improve the resolution of the spectra, the deconvolution of each spectrum, from a background scattering using a Gaussian function curve fitting analysis, was performed.

Taking into account the modifications of the hydrogen bonds which took place during the CBD adsorption process, a decrease was observed of OH stretching vibration within the range of 4000–2500 cm^{-1} for the CBD-treated cellulose allomorphs. These changes can be correlated with the disruption of intra- and intermolecular hydrogen bonds. Also, the maximum absorbance of hydrogen-bonded OH stretching was shifted to a lower wavenumber after the adsorption process (i.e., from 3337 cm^{-1} for BI to 3336 cm^{-1} for BI-CBD).

It is generally accepted that in the structure of native cellulose intramolecular hydrogen bonds of types O(3)H···O(5) and O(2)H···O(6) are present on both sides of the chain. The bond length of O(3)H···O(5) is reported to be 2.75 Å and the length of O(2)H···O(6) is reported to be 2.87 Å. The intermolecular hydrogen bond O(6)H···O(3) is estimated to have a length of 2.79 Å. It is known and accepted that these hydrogen bonds play an important role in determining the conformational and mechanical properties of cellulose materials (Ciolacu et al., 2010).

In Table 3 are collected the data regarding the length of intra- and intermolecular hydrogen bonds (R), the energy of hydrogen bonds (E_H) and the relative crystallinity index corresponding to the untreated and CBD-treated celluloses allomorphs and amorphous cellulose. It can be observed that the hydrogen bonds of CBD-treated cellulose become higher than the corresponding cellulose allomorphs, fact which evidences that the hard-segment domains are packed in a less ordered arrangement. It is known that shorter hydrogen bonds are generally stronger (Ciolacu et al., 2010). It has also been observed that the intermolecular bonds of O(6)H···O(3) have the highest E_H values. The decrease of E_H after the CBD binding process was recorded, indicating a decrease of the number of hydrogen bonds and consequently a decrease of the crystallinity degree of treated cellulose allomorphs. These data are in good agreement with those obtained from XRD measurements.

It is generally known that the amide I absorption band is located within the region between 1700 and 1600 cm^{-1}, which is the most sensitive spectral region for the identification of protein's secondary structural components, due to the C=O stretch vibrations of peptide linkages coupled with in-plane NH bending and CN stretching (Pelton and McLean, 2000). The amide II band is presented in the 1600–1500 cm^{-1} range, deriving mainly from in-plane NH bending and from the CN stretching vibration, and showing much less protein conformational sensitivity than amide I. The structural modifications which appear due to the adsorption process are evidenced by the presence of the peak at 1647 cm^{-1} for amide I and a peak at 1541 cm^{-1} for amide II. Moreover, the intensity of these increased progressively from Ba-CBD to BI-CBD.

Within the range of 1500–1250 cm^{-1}, the decrease of the intensity's band at 1430 cm^{-1} reflects a decrease of the crystallinity degree of the samples, fact which takes place after the treatment of cellulose allomorphs with CBD (spectra not shown). It is known that the absorption band from 1430 cm^{-1}, assigned to symmetric CH_2 bending is typical for crystalline regions from cellulose, while the absorption band at 898 cm^{-1} assigned to C–O–C stretching of β-(1,4)-glycosidic linkage, is typical of amorphous regions (Široký et al., 2010). The crystallinity ratios shown in Table 3 are in good correlation with the data of the crystallinity index obtained from XRD measurements. Generally, the index of asymmetry (a/b) provides information about the sample's uniformity and the decrease of the uniformity for all CBD-treated cellulose samples proves the conformational changes of the cellulose structure during random CBD absorption into fibers (Table 3).

3.2. CBD desorption from different cellulose allomorphs

The contact of the CBDs with the cellulose surface is usually dynamic, even if occasionally the interaction is irreversible. Generally, it is considered that the binding of CBD to cellulose can be classified as reversible for family I, or irreversible for families II and III (Levy and Shoseyov, 2002). Thus, it was shown that the CBD of bacterial cellulases from *Cellulomonas fimi* (family II) bind irreversibly to crystalline cellulose, while other researchers have reported completely reversible binding for the CBD of family I from *Trichoderma reesei* CBHI. Recent studies suggest that the binding of *Thermobifida fusca* cellulase (family III) onto bacterial cellulose was only partially reversible (Moran-Mirabal et al., 2011; Wang et al., 2012). Even the desorption process is still not entirely understood, it is known that it depends on the characteristics of the CBD-cellulose interactions and the properties of the cellulose itself.

In this study, the reversibility of the adsorption of CBD from *P. barcinonensis* was investigated as a function of different conditions

Table 3
The length of intra- and intermolecular hydrogen bonds and the relative crystallinity index of untreated and CBD-treated cellulose allomorphs and amorphous cellulose.

Sample	Inter-molecular hydrogen bonds of O(6)H···O(3)		Intra-molecular hydrogen bonds of O(3)H···O(5)		Intra-molecular hydrogen bonds of O(2)H···O(6)		$Cr.R._1$	$Cr.R._2$	a/b
	R, Å	E_H, kJ	R, Å	E_H, kJ	R, Å	E_H, kJ			
BI	2.766	5.67	2.710	4.76	2.814	2.75	1.624	1.076	1.1
BI-CBD	2.769	5.46	2.731	4.55	2.814	2.73	1.159	0.373	0.7
BII	2.767	5.62	2.714	4.72	2.814	2.71	0.600	0.929	0.9
BII-CBD	2.768	5.52	2.725	4.60	2.815	2.67	0.399	1.043	0.8
BIII	2.767	5.59	2.718	4.68	2.815	2.66	0.760	1.104	1.0
BIII-CBD	2.771	5.29	2.720	4.66	2.815	2.65	0.658	0.799	0.6
Ba	2.769	5.44	2.716	4.70	2.815	2.62	0.520	0.516	0.8
Ba-CBD	2.770	5.36	2.718	4.67	2.816	2.60	0.347	0.210	0.5

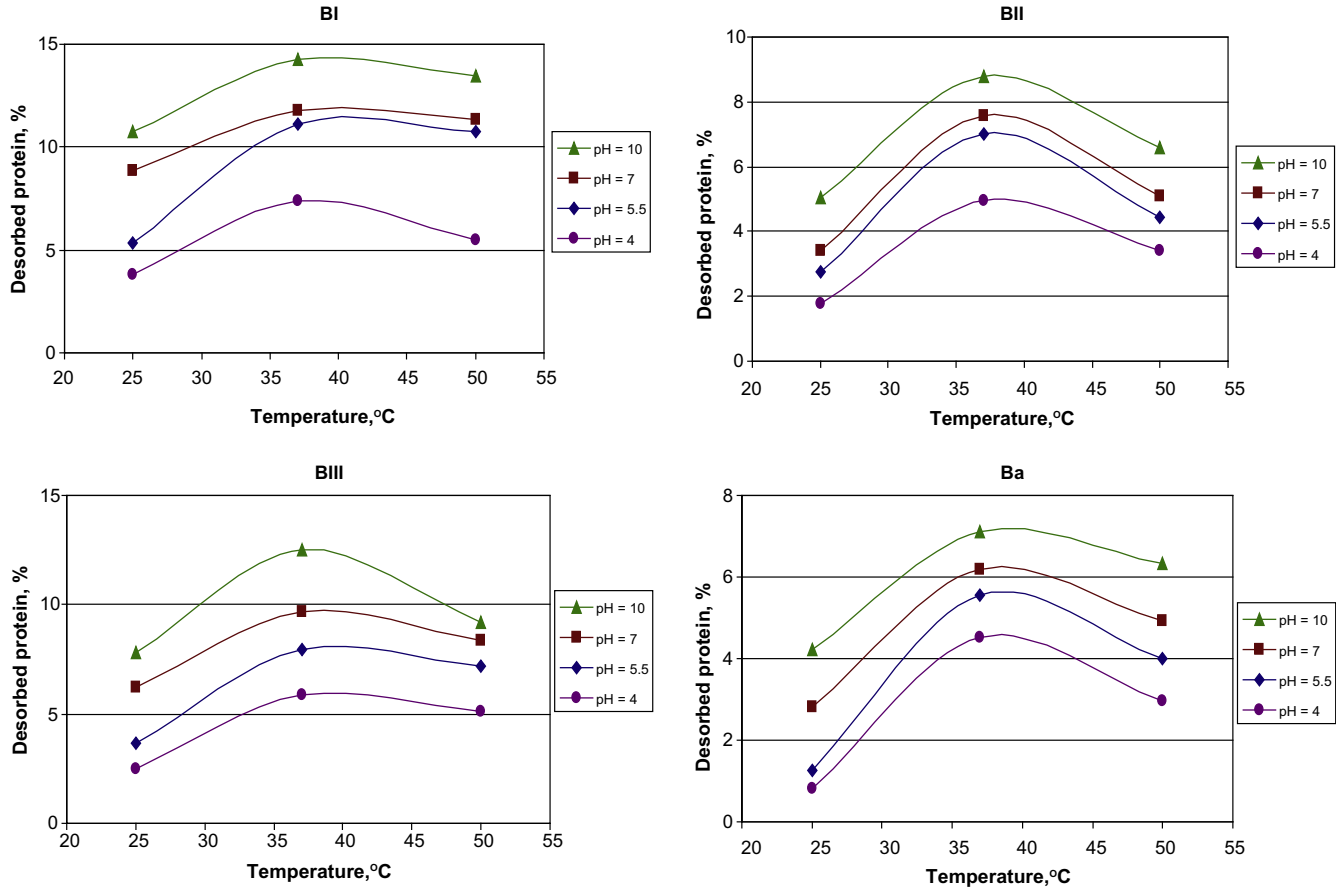

Fig. 2. Desorption process of CBD from cellulose allomorphs (BI, BII and BIII) and amorphous cellulose (Ba) at different temperatures (25, 37, and 50 °C) and within buffers solutions of different pHs (4, 5.5, 7 and 10).

of temperature (25, 37 and 50 °C) and pH (from acidic pHs 4 and 5.5 to a neutral pH 7, and alkaline pH 10), and was determined in percents from the initially adsorbed protein.

It can be observed from the results collected in Fig. 2 that the cellulose I substrate (BI-CBD) presented the highest desorption values, followed by cellulose III and II, respectively.

One consideration which could explain this behavior is the differences in the crystalline structure of the allomorphs. Thus, in cellulose I the chains are oriented in a parallel arrangement, while cellulose II has an antiparallel structure with a stronger hydrogen bonds network, which does not permit a higher binding of CBD or a significant desorption, in comparison with cellulose I. The values corresponding to the partial reversibility of CBD from cellulose III substrate are explained by the reversibility in the presence of the water-based medium of the allomorphic form of cellulose III to cellulose I, a fact also demonstrated by XRD.

The highest desorption values were recorded at a temperature of 37 °C and a pH 10, for all cellulose allomorphs (BI-CBD, 14.26%; BIII-CBD, 12.52%; BII-CBD, 8.8%), while for Ba-CBD was found to be 7.11%. At the same temperature but at a pH 4, the smallest values for the desorption process were obtained (BI-CBD, 7.37%; BIII-CBD, 5.86%; BII-CBD, 4.96%). The amount of desorbed protein was thus almost doubled when pH was increased from pH 4 to pH 10.

The lowest desorption was recorded at a temperature of 25 °C and a pH of 5.5, being 5.35% for BI-CBD, 3.69% for BIII-CBD, 2.75% for BII-CBD and 1.26% for Ba-CBD. Also, the increase in the temperature from 37 to 50 °C resulted in a decrease in the percent of desorbed protein, although smaller than at 25 °C. These data indicated that the alkaline conditions permitted the highest desorption (until 15%) and also underline the incomplete desorption of CBD from cellulosic substrate. Thus, over 86% of the bound protein remained bounded on fibers after the washing process, a fact which has also been confirmed by other researchers (Cavaco-Paulo et al., 1999; Ma et al., 2008).

It can be concluded that the reaction conditions, as temperature or pH, have an important influence on the desorption capacity, as a result of the nature of hydrophobic interactions formed between the CBD and the cellulose allomorphs.

This investigation opens up new directions for research into CBDs adsorption/desorption studies, which could help in the designing of more effective biotechnological processes and industrial applications.

4. Conclusions

The highest adsorption of CBD from *P. barcinonensis* was recorded for cellulose I and this process depending on the specific surface area, porosity and crystalline structure. XRD data emphasized the alteration of cellulose allomorphs structure and showed the CBD's preferential affinity to (002) plane. ATR-FTIR spectroscopy was used to emphasize the disruption of intra- and intermolecular hydrogen bonds within cellulose structure and the CBD binding by the presence of amide I and II absorption bands. The cellulose I substrate presented the highest desorption capacity at a temperature of 37 °C and a pH 10, followed by cellulose III and II.

Acknowledgement

This research was supported by the Marie Curie Transfer of Knowledge Fellowship of the EC FP6 under the contract no. MTKD-CT-2005-029540-POLYSURF.

Appendix A. Supplementary data

Supplementary data associated with this article can be found, in the online version, at http://dx.doi.org/10.1016/j.biortech.2014.01.027.

References

Abbott, D.W., Boraston, A.B., 2012. Quantitative approaches to the analysis of carbohydrate-binding module function. In: Gilbert, H.J. (Ed.), Cellulases, Methods in Enzymology, vol. 510. Elsevier Inc., New York, pp. 211–231 (Chapter 11).

Cavaco-Paulo, A., Morgado, J., Andreaus, J., Kilburn, D., 1999. Interactions of cotton with CBD peptides. Enzyme Microb. Technol. 25, 639–643.

Chiriac, A.I., Cadena, E.M., Vidal, T., Torres, A.L., Diaz, P., Pastor, F.I.J., 2010. Engineering a family 9 processive endoglucanase from *Paenibacillus barcinonensis* displaying a novel architecture. Appl. Microbiol. Biotechnol. 86, 1125–1134.

Ciolacu, D., Kovac, J., Kokol, V., 2010. The effect of the cellulose-binding domain from *Clostridium cellulovorans* on the supramolecular structure of cellulose fibers. Carbohyd. Res. 345, 621–630.

Ciolacu, D., Ciolacu, F., Popa, V.I., 2011. Amorphous cellulose – structure and characterization. Cell. Chem. Technol. 45 (1–2), 13–21.

Ford, E.N.J., Mendon, S.K., Thames, S.F., James, W., Rawlins, J.W., 2010. X-ray diffraction of cotton treated with neutralized vegetable oil-based macromolecular crosslinkers. J. Eng. Fiber Fabr. 5, 10–20.

Goldstein, M.A., Takagi, M., Hashida, S., Shoseyov, O., Doi, R.H., Segel, I.H., 1993. Characterization of the cellulose-binding domain of the *Clostridium cellulovorans* cellulose-binding protein A. J. Bacteriol. 175 (18), 5762–5768.

Guo, J., Catchmark, J.M., 2013. Binding Specificity and thermodynamics of cellulose-binding modules from *Trichoderma reesei* Cel7A and Cel6A. Biomacromolecules 14, 1268–1277.

Hall, M., Bansal, P., Lee, J.H., Realff, M.J., Bommarius, A.S., 2011. Biological pretreatment of cellulose: Enhancing enzymatic hydrolysis rate using cellulose-binding domains from cellulases. Bioresour. Technol. 102, 2910–2915.

Ioelovich, M., Leykin, A., 2011. Study of sorption properties of cellulose and its derivatives. BioResources 6 (1), 178–195.

Krässig, H.A., 1993. Cellulose: Structure Accessibility and Reactivity. In: Huglin, M.B. (Ed.). Gordon and Breach Science Publishers, Philadelphia (vol. 11).

Levy, I., Shoseyov, O., 2002. Cellulose-binding domains-biotechnological applications. Biotechnol. Adv. 20, 191–213.

Liu, Y., 2013. Recent progress in fourier transform infrared (FTIR) spectroscopy study of compositional, structural and physical attributes of developmental cotton fibers. Materials 6, 299–313.

Ma, A., Hu, Q., Qu, Y., Bai, Z., Liu, W., Zhuang, G., 2008. The enzymatic hydrolysis rate of cellulose decreases with tight adsorption of cellobiohydrolase. Enzyme Microb. Technol. 42, 543–547.

Mazeau, K., 2011. On the external morphology of native cellulose microfibrils. Carbohydr. Polym. 84, 524–532.

Moran-Mirabal, J.M., Bolewski, J.C., Walker, L.P., 2011. Reversibility and binding kinetics of *Thermobifida fusca* cellulases studied through fluorescence recovery after photobleaching microscopy. Biophys. Chem. 155 (1), 20–28.

Ogeda, T.L., Silva, I.B., Fidale, L.C., El Seoud, O.A., Petri, D.F.S., 2012. Effect of cellulose physical characteristics, especially the water sorption value, on the efficiency of its hydrolysis catalyzed by free or immobilized cellulose. J. Biotechnol. 157, 246–252.

Pareek, N., Gillgren, T., Jönsson, L.J., 2013. Adsorption of proteins involved in hydrolysis of lignocellulose on lignins and hemicelluloses. Bioresource Technol. 148, 70–77.

Pastor, F.I.J., Pujol, X., Blanco, A., Vidal, T., Torres, A.L., Diaz, P., 2001. Molecular cloning and characterization of a multidomain endoglucanase from *Paenibacillus* sp BP-23: evaluation of its performance in pulp refining. Appl. Microbiol. Biotechnol. 55, 61–68.

Pelton, J.T., McLean, L.R., 2000. Spectroscopic methods for analysis of protein secondary structure. Anal. Biochem. 277, 167–176.

Penttilä, P.A., Várnai, A., Pere, J., Tammelin, T., Salmén, L., Siika-aho, M., Viikari, L., Serimaa, R., 2013. Xylan as limiting factor in enzymatic hydrolysis of nanocellulose. Bioresource Technol. 129, 135–141.

Salmén, L., Åkertholm, M., Hinterstoisser, B., 2005. Two-dimensional fourier transform infrared spectroscopy applied to cellulose and paper. In: Dumitriu, S. (Ed.), Polyssaccharides: Structural Diversity and Functional Versatility, second ed. Marcel Dekker, New York, USA, pp. 159–189.

Sánchez, M.M., Irwin, D.C., Pastor, F.I.J., Wilson, D.B., Diaz, P., 2004. Synergistic activity of *Paenibacillus* sp. BP-23 cellobiohydrolase Cel48C in association with the contiguous endoglucanase Cel9B and with endo- or exo-acting glucanases from *Thermobifida fusca*. Biotechnol. Bioeng. 87, 161–169.

Sánchez, M.M., Fritze, D., Blanco, A., Spröer, C., Tindall, B.J., Schumann, P., Kroppenstedt, R.M., Diaz, P., Pastor, F.I.J., 2005. *Paenibacillus barcinonensis* sp. nov., a xylanase-producing bacterium isolated from a rice field in the Ebro River delta. Int. J. Syst. Evol. Microbiol. 55, 935–939.

Shoseyov, O., Warren, R.A.J., 1997. Cellulose binding domains – a novel fusion technology for efficient, low cost purification and immobilization of recombinant proteins. Innovations 7, 1–3.

Shoseyov, O., Shani, Z., Levy, I., 2006. Carbohydrate binding modules: biochemical properties and novel applications. Microbiol. Mol. Biol. R. 70 (2), 283–295.

Široký, J., Blackburn, R.S., Bechtold, T., Taylor, J., White, P., 2010. Attenuated total reflectance fourier-transform infrared spectroscopy analysis of crystallinity changes in lyocell following continuous treatment with sodium hydroxide. Cellulose 17, 103–115.

Široký, J., Benians, T.A.S., Russell, S.J., Bechtold, T., Knox, J.P., Blackburn, R.S., 2012. Analysis of crystallinity changes in cellulose II polymers using carbohydrate-binding modules. Carbohydr. Polym. 89, 213–221.

Wada, M., Ike, M., Tokuyasu, K., 2010. Enzymatic hydrolysis of cellulose I is greatly accelerated via its conversion to the cellulose II hydrate form. Polym. Degrad. Stab. 95, 543–548.

Wang, Q.Q., Zhu, J.Y., Hunt, C.G., Zhan, H.Y., 2012. Kinetics of adsorption, desorption, and re-adsorption of a commercial endoglucanase in lignocellulosic suspensions. Biotechnol. Bioeng. 109 (8), 1965–1975.

Yaniv, O., Halfon, Y., Shimon, L.J.W., Bayer, E.A., Lamed, R., Frolowa, F., 2012. Structure of CBM3b of the major cellulosomal scaffoldin subunit ScaA from *Acetivibrio cellulolyticus*. Acta Crystallogr. F F68, 8–13.

Zhang, M., Wu, S.C., Zhou, W., Xu, B., 2012. Imaging and measuring single-molecule interaction between a carbohydrate-binding module and natural plant cell wall cellulose. J. Phys. Chem. B. 116, 9949–9956.

Carbohydrate Polymers 151 (2016) 392–400

Contents lists available at ScienceDirect

Carbohydrate Polymers

journal homepage: www.elsevier.com/locate/carbpol

Physically and chemically cross-linked cellulose cryogels: Structure, properties and application for controlled release

Diana Ciolacu[a,*], Cyrielle Rudaz[b], Mihai Vasilescu[c], Tatiana Budtova[b,*]

[a] "Petru Poni" Institute of Macromolecular Chemistry, Department of Physical Chemistry of Polymers, 41A Grigore Ghica Voda Alley, 700487 Iasi, Romania
[b] MINES ParisTech, PSL Research University, CEMEF—Centre de Mise en Forme des Matériaux, CNRS UMR 7635, CS 10207 rue Claude Daunesse, 06904 Sophia Antipolis, France
[c] "Babes-Bolyai" University, Faculty of Physics, Mihail Kogalniceanu, 1, 3400 Cluj-Napoca, Romania

ARTICLE INFO

Article history:
Received 15 February 2016
Received in revised form 9 May 2016
Accepted 23 May 2016
Available online 24 May 2016

Keywords:
Cellulose
Cross-linking
Cryogel
Hydrogel
Swelling
Controlled release

ABSTRACT

Porous cellulose matrices were prepared via cellulose dissolution in 8 wt% NaOH-water, physical gelation and chemical cross-linking with epichlorohydrin (ECH), coagulation in water and lyophilisation. Cellulose and cross-linker concentration were varied. The behaviour of gels upon coagulation and the swelling of cryogels in water were analysed. An anomalous high swelling at cross-linker concentration around stoichiometric molar ratio with cellulose was observed. Cellulose cryogel morphology, crystallinity and density were studied. The influence of chemical cross-linking on cellulose swelling was explained by suggesting that ECH acts as a spacer preventing cellulose chains tight packing during coagulation. Cellulose was loaded with a model drug, procaine hydrochloride, and the kinetics of its release was investigated.

1. Introduction

Cellulose is a versatile polymer which exists in various forms, can be functionalized and is used to make different materials. For example, native cellulose reinforces plant cell walls, and natural fibres can be used to reinforce plastics; man-made cellulose materials are fibres, films, sponges and aerogels; cellulose esters can be thermoplastic and ethers can be water-soluble (Klemm, Heubletin, Fink, & Bohn, 2005; Ciolacu & Popa, 2010; Qiu & Hu, 2013). So-called cellulose hydrogels is a special class of cellulose wet materials which can be based either on cellulose I (case of bacterial or nano/microfibrillated cellulose) (Klemm et al., 2011; Saito, Uematsu, Kimura, Enomaea, & Isogai, 2011) or cellulose II (when prepared via cellulose dissolution followed by coagulation in water) (Sannino, Demitri, & Madaghiele, 2009; Chang & Zhang, 2011; Chang, Duan, Cai, & Zhang, 2010). Both types show high water retention, from several hundred to several thousand percent.

Hydrogels, by definition, are the networks that are swollen in aqueous media. They are widely applied in medicine and pharmacology, food, cosmetics, engineering and hygienic applications. The classical examples of synthetic polymers that are used for synthesizing hydrogels are poly(hydroxyethyl methacrylate), polyvinyl alcohol, polyacrylamides, polyacrylates, etc. Cellulose ethers carrying methyl-, carboxymethyl-, hydroxypropyl- or hydroxyethyl groups or their various combinations and which are water-soluble can also form hydrogels (Ahmed, 2015). The main principle is that aqueous medium is a solvent for the matter constituting the gel whatever is gelation mechanism and the nature of the bonds which "keep together" the macromolecules: physical (hydrogen, hydrophobic or van der Waals) or chemical (covalent or ionic). It should be noted that because water is cellulose anti-solvent, the term "hydrogel" is, strictly speaking, not applicable for cellulose I and II. However, we shall use it in the following for simplicity. Cellulose and cellulose derivatives' based hydrogels are very attractive materials for bio-medical applications (as matrices for drug delivery, for tissue engineering, scaffolds) due to their biocompatibility and biodegradability (Chang, Duan et al., 2010; Klemm et al., 2011; Peng, Dhar, Liu, & Tam, 2011; Bhattacharya et al., 2012; Qiu & Hu, 2013).

In this work we shall focus on cellulose II based hydrogels. They are obtained as an inevitable step during cellulose processing, i.e. cellulose coagulation into water from any solution. One of the oldest examples is cellulose hydrogels obtained during cellulose regeneration from viscose (Ando & Konishi, 2000; Saito, Sakurai, Sakakibara, & Saga, 2003). Cellulose II hydrogels can also

* Corresponding authors.
E-mail addresses: dciolacu@icmpp.ro (D. Ciolacu), Tatiana.Budtova@mines-paristech.fr (T. Budtova).

http://dx.doi.org/10.1016/j.carbpol.2016.05.084
0144-8617/

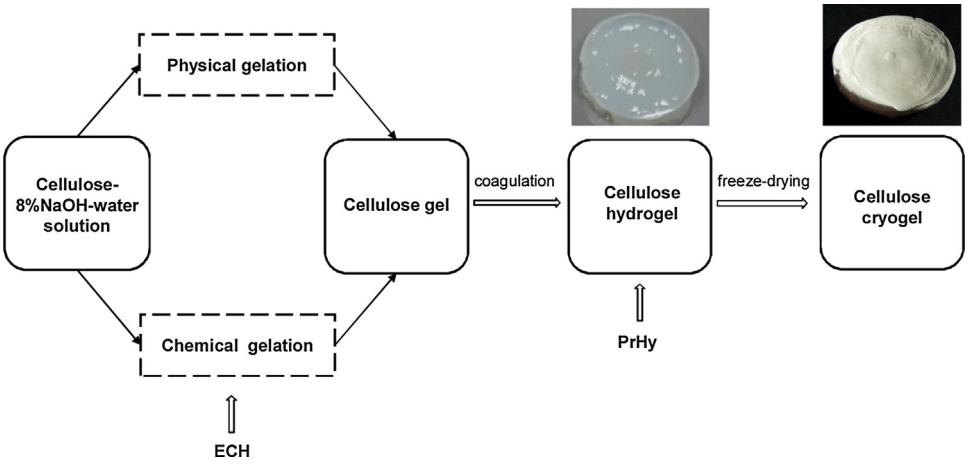

Fig. 1. Schematic presentation of physically and chemically cross-linked cellulose cryogels loaded with PrHy.

be obtained when coagulating cellulose from solution in direct solvents: NMMO monohydrate (Chang & Zhang, 2011), LiCl/DMAc (de Oliveira & Glasser, 1996; Xia, Patchan, Maranchi, & Trexler, 2015), ionic liquids (Turner, Spear, Holbrey, & Rogers, 2004; Sescousse, Gavillon, & Budtova, 2011a) and 6–10 wt% NaOH-water based solvent (Gavillon & Budtova, 2008; Sescousse, Gavillon, & Budtova, 2011b; Luo & Zhang, 2013). In the latter solvent, cellulose solutions are gelling forming a physical gel (Budtova & Navard, 2016). Using a cross-linker such as epichlorhydrin (ECH), it is also possible to obtain cellulose chemical gel (Zhou, Chang, Zhang, & Zhang, 2007; Chang, Zhang, Zhou, Zhang, & Kennedy, 2010; Ciolacu, Oprea, Anghel, Cazacu, & Cazacu, 2012; Qin, Lu, & Zhang, 2013).

Various properties of cellulose II hydrogels prepared from NaOH-based solvent had already been studied. It was shown that after being freeze-dried, cellulose is re-swelling in water at room temperature up to 3000–6000% (Zhou et al., 2007). The increase of cellulose and ECH concentration leads to the decrease of swelling (Qin et al., 2013): for example, for hydrogels prepared from 5 wt% cellulose solution, the degree of swelling decreased from 2300 to 1400% for ECH content from 5 to 15%. The compressive modulus of hydrogels increased with the increase of ECH concentration. Light transmittance of visible light can reach 90% for hydrogels prepared from 2 wt% cellulose solution (Chang, Zhang et al., 2010).

Cellulose and cellulose-lignin hydrogels, synthesized by dissolving cellulose in 8 wt% NaOH-water, followed by the chemical cross-linking with epichlorohydrin, were further used as a matrix for controlled release of polyphenols obtained by extraction from grapes seeds of *Chambourcin* type (Ciolacu et al., 2012). The swelling capacity of hydrogels increased from 1145 to 3061 wt% with the increase of lignin content.

The aim of this paper was to advance in the understanding of the physical properties of cellulose II based hydrogels prepared from cellulose-8% NaOH-water solutions and the influence of ECH concentration. The reason was our discovery of an anomalous swelling of cellulose hydrogels: we found an increase of hydrogel swelling degree with the increase of ECH concentration, with maximum swelling being at approximately cellulose:ECH stoichiometric ratio. In this work we focused on the differences induced by physical (without ECH) and chemical (ECH-induced) gelation on cellulose hydrogels' swelling in water after synthesis and after freeze drying (cryogels), and on cryogels' structure, morphology and density. Furthermore, the ability of freeze-dried cellulose hydrogels to function as drug delivery systems was studied. Cellulose hydrogels were loaded with procaine hydrochloride (PrHy) and the kinetics of its release in water was investigated.

2. Materials and methods

2.1. Materials

Microcrystalline cellulose Avicel PH-101 DP of 180 as given by the manufacturer was purchased from Sigma-Aldrich. Sodium hydroxide (NaOH) in pellets with a purity ≥97% was supplied by Merck. Epichlorohydrin (ECH), b.p. 115–117 °C and purity >98% (Fluka), was used without further purification. Procaine hydrochloride (PrHy) with m.p. 155–156 °C and purity ≥97% were supplied by Sigma-Aldrich.

2.2. Methods

2.2.1. Preparation of neat cellulose cryogels and their drug-loaded counterparts

Cellulose–8 wt% NaOH-water solutions were prepared according to a standard procedure (Egal, Budtova, & Navard, 2007; Gavillon & Budtova, 2008; Sescousse & Budtova, 2009). Briefly, cellulose was swollen in distilled water for 2 h at 5 °C, 18 wt% NaOH aqueous solution was added to reach 8 wt% solvent concentration and the whole was mixed at −6 °C with an overhead mixer at 800 rpm for 2 h. Two cellulose concentrations were prepared, 5 and 7 wt%.

Two types of samples were synthesized: physically and chemically cross-linked cellulose (Fig. 1). To prepare physically cross-linked samples, solutions were poured into moulds and kept at room temperature for 24 h. In these conditions cellulose-NaOH solutions undergo physical gelation (Roy, Budtova, & Navard, 2003). Cross-linked cellulose was synthesised by adding ECH dropwise into a fresh cellulose-8% NaOH solution, stirring vigorously for 15–20 min, rapidly pouring into moulds and keeping the system for 24 h at room temperature. Samples after physical or chemical gelation will be called "gels" (each time the gelation mode will be specified). Epichlorohydrin concentration was varied to reach different molar ratios of ECH (*n mol ECH*) to anhydroglucose units, AGU (*n mol AGU*):

$$R = nmolECH/nmolAGU \quad (1)$$

The gels were then immersed in a non-solvent bath (water) and washed many times to coagulate cellulose and remove NaOH, resulting in cellulose "hydrogels".

Loading of cellulose with procaine was performed as follows: hydrogels (cross-linked and not) were placed in 50 mL procaine hydrochloride (PrHy) solution of different concentrations (hydrogels from 5 wt% cellulose solution in 2, 4 and 8 g/L PrHy and from

7 wt% solution in 5.2 g/L PrHy) and left for 24 h at room temperature for PrHy to diffuse in cellulose samples.

To obtain dry samples that will be called "cellulose cryogels", hydrogels were first placed in liquid nitrogen for 3 min and then freeze-dried in Cryotec Cosmos 80 for 48 h.

The sample' notation is "X% RY-Z" with X cellulose concentration in wt% in solution (i.e. 5 or 7 wt%), RY the molar ratio of ECH to AGU (Y = 0.25, 0.5, 1, 2 and 4) and Z the concentration of PrHy solution. Samples "X% R0-Z" correspond to non-cross-linked cellulose (Y = 0) and samples "X% RY" correspond to drug-free cellulose cryogels that were used for structural characterisation.

2.2.2. Characterisation of neat cellulose cryogels

Solid state ^{13}C CP/MAS NMR (NMR) measurements were performed at Larmor frequency (150.92 MHz) by using a Bruker AVANCE-600 NMR spectrometer (14.1 T). Cellulose cryogels were packed in a ZrO rotor with an outer diameter of 3.2 mm. Standard CP/MAS experiments were performed at a spinning frequency of 8 kHz, using a ^{1}H 90° pulse length of 3 μs. The CP transfer was optimized for the first Hartmann—Hahn matching condition and a contact pulse of 1.5 ms. Chemical shift of the ^{13}C nuclei was estimated by using an external reference of TMS (tetramethilsilane, $\delta = 0$ ppm) and were expressed in parts per million (ppm). For the deconvolution of the spectra we have used the Dmfit program, which enables fitting solid state NMR spectra, including 1D and 2D datasets (Massiot et al., 2002). For the shape of the resonance lines we have used a combination of Gaussian/Lorentzian lines. The crystallinity index (CrI_{NMR}) was determined with the following equation (Zuckerstätter et al., 2009):

$$CrI_{NMR}(\%) = [A_O/(A_O + A_D)] \times 100 \quad (2)$$

where A_0 (ordered) and A_D (disordered) represent the signal areas obtained by integrating the signal from 87 to 93 ppm and 80–87 ppm, respectively.

X-ray diffraction analysis (XRD) was performed on a Bruker-AXS D8 ADVANCE apparatus, equipped with a transmission type goniometer using Ni-filtered, Cu-Kα radiation at 40 kV. The goniometer was scanned stepwise every 0.10 from 10 to 40 in the 2θ range. The resulting diffraction patterns exhibited peaks which were deconvoluted from a background scattering by using Lorenzian functions, while the diffraction pattern of an artificially made amorphous sample was approximated by a Gaussian function curve fitting analysis. Each individual crystalline peak were extracted by a curve-fitting process from the diffraction intensity profiles and all the iterations were repeated until a R2 value of 0.98–0.99 and a F-value > 8000 was obtained (Ciolacu, 2007; Ciolacu, Ciolacu, & Popa, 2008; Ciolacu, Gorgieva, Tampu, & Kokol, 2011). The structural parameters were calculated using TOPAS 4.2 (Bruker-AXS, Germany) and DIFFRAC.EVA V1.1 (Bruker-AXS, Germany) software. The deconvolution of the peaks was performed using PeakFit 4.11. The crystallinity index (CrI_{XRD}) of cellulose cryogels was calculated using the following approach:

$$CrI_{XRD}(\%) = [S_C/(S_C + S_A)] \times 100 \quad (3)$$

where S_C and S_A are the surfaces of the crystalline and amorphous areas, respectively

Differential scanning calorimetry (DSC) measurements were conducted on a DSC 200 F3 Maia (Netzsch, Germany). First, all samples were conditioned in a desiccator prior measurements at a constant relative humidity (RH) of 65% and a temperature of 25 °C, until constant weights was achieved. The samples were then heated from −50 to 170 °C under nitrogen atmosphere, at a heating rate of 10 °C/min. The cellulose cryogel crystallinity index (CrI_{DSC}), determined from DSC measurements, was calculated as the ratio between the dehydration heat of a preconditioned sample at constant relative humidity (ΔH_S, J/g) and the dehydration heat of the completely amorphous cellulose, preconditioned under the same conditions ($\Delta H_0 = 411.29$, J/g) (Chang, Lue, & Zhang, 2008; Ciolacu, Ciolacu, & Popa, 2011):

$$CrI_{DSC}(\%) = [(\Delta H_0 - \Delta H_S)/\Delta H_0] \times 100 \quad (4)$$

Dynamic water vapors sorption (DVS) capacity of the cellulose cryogel was measured by using a fully automated gravimetric analyzer IGAsorp (Hiden Analytical, Warrington, UK). The IGAsorp is a standard sorption equipment, with a sensitive microbalance (resolution 1 μg and capacity 200 mg), which records the evolution of sample weight at a given temperature and relative humidity (RH). Before sorption measurements, cellulose cryogel was dried at 25 °C and RH <1% under nitrogen flow until the constant weight which was considered as the dry mass. In order to measure the sorption curve, the vapour pressure was increased from 0 to 85% in 10% humidity steps (with an accuracy of ±1%), at each step sample was left to reach equilibrium for 20–25 min.

Bulk density (ρ_{bulk}) was measured by powder pycnometer Geopyc 1360 Envelope Density Analyzer, Micromeritics, with DryFlo powder.

Scanning Electron Microscopy (SEM) observations of the internal morphology of cellulose cryogels were performed by using a Quanta 200 type scanning electron microscope, operating at 30 kV with secondary electrons, in low vacuum mode.

The kinetics of cellulose cryogels swelling in water was studied during 24 h at 37 °C. The samples were periodically removed from water, gently wiped with a soft tissue to remove surface water and then quickly weighed.

2.2.3. Measurements of PrHy concentration: drug release study

UV-VIS spectrophotometer Jasco V-550 was used to measure the concentration of PrHy in water at 291 nm using 10 mm quartz cells. First, the absorption spectrum of PrHy was recorded and the maximum absorption was detected at 291 nm. The calibration curve was established using different solutions of known PrHy concentrations, in the range of 10^{-4} to 10^{-2} g/mL. The calibration curve dependence was $y = 62.832x + 0.0309$, where "y" is the absorbance and "x" is PrHy concentration, with a correlation coefficient of $R^2 = 0.998$.

Finally, the kinetics of in vitro PrHy release was studied using a standard dissolution set-up (Ciolacu et al., 2012): cellulose cryogel loaded with the drug was placed in water at 37 ± 0.5 °C, 1 mL aliquots of solution were withdrawn periodically, the absorbance measured and PrHy concentration calculated using the calibration. In order to maintain the solution concentration, the extracted solution was reintroduced in the system.

3. Results

3.1. Influence of cross-linking on cellulose structure and crystallinity studied by NMR, XRD and DSC

Three methods, NMR, XRD and DSC, were used to analyze the changes in cellulose structure and crystallinity upon cross-linking with ECH; samples without drug were studied.

The solid-state ^{13}C NMR spectra of cellulose cryogels prepared from 5% cellulose solutions via physical gelation (5% R0) and chemically cross-linked (5% R1 and 5% R2) are shown in Fig. S1 (Supplementary material). For the sample 5% R0, a narrow signal at 105.63 ppm is assigned to C_1 anomeric carbon, followed by the signal assigned to C_4 atoms at 87.95 ppm and a broad signal at 84.38 ppm corresponds to cellulose in disordered regions (Fig. S1, Supplementary material). The signals from C_2, C_3, and C_5 atoms give rise to a cluster of resonance lines observed in the region of 78–70 ppm, which form a triplet at 74.95, 76.81, and 73.11 ppm,

Table 1
Crystallinity indexes obtained with solid state ^{13}C NMR (CrI_{NMR}), XRD (CrI_{XRD}) and DSC (CrI_{DSC}) and dehydration heat (ΔH) for cellulose cryogels.

Sample	CrI_{NMR} (%)	CrI_{XRD} (%)	CrI_{DSC} (%)	ΔH (J/g)
5% R0	63	65	32	278
5% R1	40	59	30	289
5% R2	23	45	24	313
7% R0	64	68	42	237
7% R0.5	51	61	40	248
7% R1	44	55	27	300

respectively, and the signal at 62.38 is associated with C_6 of the primary group. (Kono, Numata, Erata, & Takai, 2004, Östlund, Idström, Olsson, Larsson, & Nordstierna, 2013).

Chemical cross-linking leads to spectra modifications compared to cellulose 5% R0 sample: with the increase of ECH concentration there is a loss in the resolution of C_4 and C_6 and the peak corresponding to $C_{2,3,5}$ is broadened. Similar trends were reported in literature (Zhou et al., 2007; Chang, Zhang et al., 2010) and interpreted as the lower mobility of carbons on AGU due to the cross-linking of cellulose with ECH.

The deconvolution of ^{13}C NMR spectra of cellulose cryogels and the quantification of each peak surface area have been performed. Each peak area was normalized with the area of C_1 signal, and the area under $C_{2,3,5}$ and C_6 signals was plotted as a function of ECH molar ratio R (Fig. S2, Supplementary material). The surface area under C_6 peak is independent on R, whereas the surface under $C_{2,3,5}$ increases with R; a similar result was obtained in (Rudaz, 2013). Considering this result together with the observations made by (Luby, Kuniak & Fanter, 1979) who reported that in the cross-linking reaction of cellulose with ECH the most reactive hydroxyl groups are C_2, followed by C_6 and C_3, we conclude that the cross-linking occurred via C_2 bonding, as shown in the inset of Fig. S1 (Supplementary material). In general, it is known that the relative reactivities of cellulose hydroxyls in NaOH-based medium increase in the order $C_3 < C_6 < C_2$ (Rowland, Roberts, & Wade, 1969; Klemm, Philipp, Heize, Heinze, & Wagwnknecht, 1998, chapter 2).

The crystallinity was calculated using Eq. (2) (Table 1). The signal assignment includes separate lines for crystalline cellulose II (86–92 ppm), a partially ordered signal (82–92 ppm), as well as resonances attributed to non-crystalline or disordered cellulose (78–88 ppm). After physical gelation (5% R0 and 7% R0 samples) the crystallinity index is 63–64%, while after a chemical cross-linking the crystallinity decreases with the increase of ECH concentration.

The evolution of cellulose structure upon chemical cross-linking analysed with XRD is shown in Fig. S3 (shown in Supplementary material) for cellulose cryogels prepared from 5 wt% solution; similar results were obtained for the samples from 7 wt% solutions. X-ray patterns from chemically cross-linked cellulose show that the location of the main peaks is the same as for physically gelled cellulose, but the scattering intensities are significantly decreased. Similar to the results obtained with NMR, the crystallinity index calculated with Eq. (3) decreases with the increase of ECH concentration (Table 1).

Finally, the effect of the cross-linking reaction on cellulose structure was investigated by using DSC method, which allows measuring the enthalpy of solvent evaporation, considered to be related to crystallinity index (Ciolacu, Ciolacu et al., 2011; Ciolacu et al., 2012). The enthalpy increases with the increase of ECH concentration for both initial cellulose concentrations (Table 1), indicating the increasing amount of adsorbed humidity, which is directly related to the amorphous fraction of cellulose (Ciolacu, Ciolacu et al., 2011). Moreover, the crystallinity index (CrI_{DSC}), determined by using Eq. (4), shows a decrease of the crystallinity with the increase of ECH concentration (Table 1).

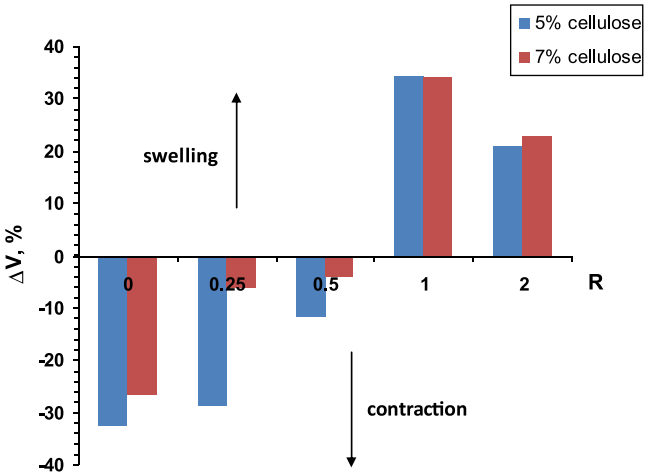

Fig. 2. Volume variation as a function of R, for samples prepared from 5 and 7 wt% cellulose solutions.

The absolute values of crystallinity determined with NMR, XRD and DSC depend on the type of method due to the differences in the measurement principle. The highest values are obtained by XRD (CrI_{XRD}), followed by ^{13}C NMR (CrI_{NMR}), and then by DSC (CrI_{DSC}). Generally, the NMR method gives lower crystallinities than the XRD due to the fact that the carbons in the amorphous region (including carbons on the crystallite surface) have a chemical shift distinct from carbons in the crystalline region, and XRD does not distinguish cellulose chains on the surface of cellulose crystallites, as NMR does (Park, Johnson, Ishizawa, Parilla, & Davis, 2009). Despite the differences in the absolute values, all three methods show that the crystallinity of chemically cross-linked cellulose is lower than that of physically cross-linked, with the crystallinity decreasing with the increase of ECH concentration within the studied range Chemical cross-linking seems to perturb "packing" of cellulose chains leading to lower crystallinity.

3.2. *Influence of cross-linking on swelling of gels and cryogels in water and humidity adsorption by cellulose cryogel*

It is known that cellulose gel obtained with physical gelation shrinks during cellulose coagulation by about 40 vol% (Sescousse & Budtova, 2009); similar result was reported for cellulose coagulated from NMMO monohydrate solutions (Innerlohinger, Weber, & Kraft, 2006). The reason is that a solvent is exchanged to non-solvent and thus polymer chains contract. The goal of this part was to investigate the influence of cross-linking on the degree of swelling of cellulose hydrogel and of cryogel placed in water. Two types of swelling experiments were thus performed: (i) gels just after synthesis were placed in water and their volume and weight at equilibrium, i.e. after cellulose complete coagulation, was measured and (ii) cellulose cryogels swelling in water was recorded.

Fig. 2 shows volume variation $\Delta V(\%)$ (Eq. (5)) between the gel V_{gel} (gelation after 24 h at room temperature) and hydrogel $V_{swolleninwater}$ (coagulated cellulose completely washed from NaOH):

$$\Delta V, \% = \frac{V_{swolleninwater} - V_{gel}}{V_{gel}} \times 100\% \quad (5)$$

A negative ΔV corresponds to shrinkage and positive to swelling of cellulose after coagulation. For both cellulose concentrations, gels with R < 0.5 shrink when placed in the coagulation bath. The shrinkage of chemically cross-linked cellulose is lower compared to physical cellulose gels. At R = 1–2 cellulose is swelling during coagulation: sample volume increases by 20–30% as compared with the

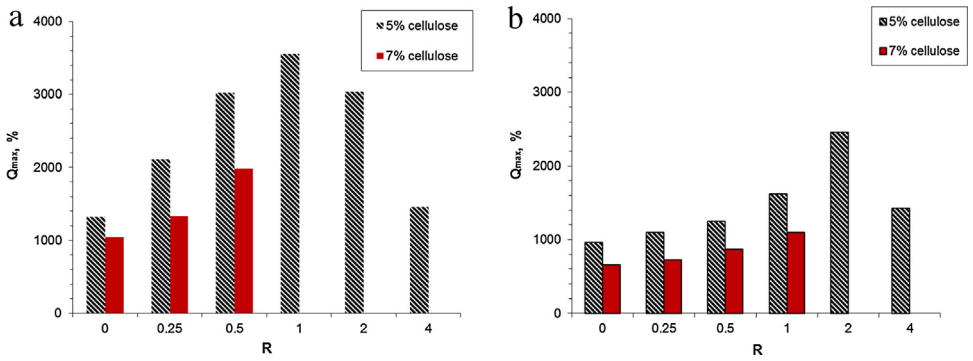

Fig. 3. Swelling degree of (a) cellulose hydrogels (never dried, at equilibrium) and (b) of cellulose cryogels in water at 37 °C, prepared from 5 and 7 wt% cellulose solutions, as a function of R.

gel after synthesis. This is a very interesting phenomenon that has never been reported before.

Usually, for hydrogels the relevant parameter is the degree of swelling Q_{max} *(%)* which is calculated towards the dry weight of the polymer as follows:

$$Q_{\max} = \frac{W_{sw} - W_{dry}}{W_{dry}} \times 100\,(\%) \qquad (6)$$

where W_{dry} and W_{sw} are the weight of dry and swollen network, respectively. Fig. 3a shows the influence of ECH concentration on cellulose hydrogels (never dried, at equilibrium) degree of swelling. The swelling ratio increases dramatically up to the maximal value of Q = 3500% for R = 1 and then decreases at higher R values, reaching Q ≈ 1500%. The increase in swelling with the increase of cross-linker concentration is "against" the trends known for classical polymer gels for which the increase in cross-linking leads to the decrease of swelling. Higher is cellulose concentration, lower is swelling, as expected (Fig. 3a). Another interesting point is that with the increase of ECH concentration samples become more and more transparent: for example, samples prepared with R = 0 or R = 0.25 are opaque whereas with R ≥ 2 they are completely transparent. The transition from opaque to transparent coagulated swollen cellulose stands between R = 1 and 2. It may be deduced that the increase of cross-linking thus leads to a more homogeneous structure of coagulated cellulose.

Similar to hydrogels, the degree of swelling of cryogels in water first increases and then decreases with the increase of ECH concentration, for both studied cellulose concentrations (Fig. 3b). However, the absolute values of cryogel swelling are lower: for example, for samples prepared from 5 wt% solution the minimal swelling of cryogel is around 900% and the maximal is around 2500% while for hydrogels it is 1300% and 3500%, respectively. Lower swelling of dried compared to never-dried cellulose is due to the well-known hornification phenomenon. What is important is that even freeze-dried samples show the "anomalous" swelling, i.e. increase in swelling degree with the increase of ECH concentration, up to a certain value.

Next we studied the adsorption of water vapours by cellulose cryogels using DVS method. Sorption/desorption isotherms (expressed as $\Delta M, \% = [(M_{RH} - M_{dry})/M_{dry}] \times 100$ where M_{dry} and M_{RH} is the weight of dry sample and at a given RH, respectively) are presented in Fig. S4 (Supplementary material). All curves show an important hysteresis due to the irreversible adsorption of water molecules on the surface of cryogel pores. Higher cellulose concentration induces lower adsorption, as observed for the swelling degree. Finally, higher the concentration of ECH, higher is humidity adsorption at any given cellulose concentration: (Fig. S4a, Supplementary material). Summarising, various independent methods confirm the increase in swelling and adsorption capacity of cellulose cryogel with the increase of cross-linker concentration in the region of low ECH concentrations.

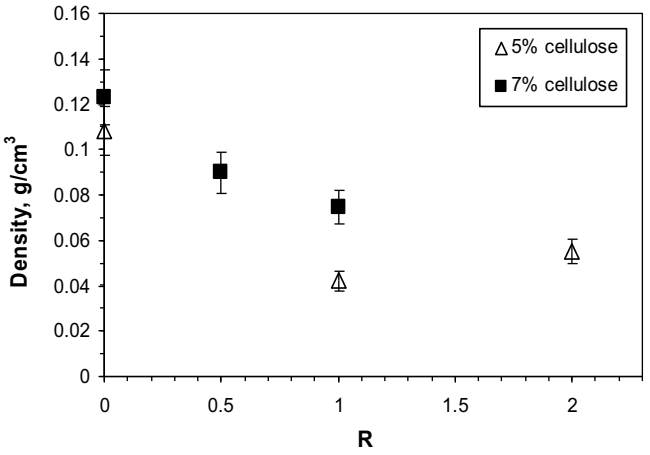

Fig. 4. Bulk density of cellulose cryogels synthesized from 5 and 7 wt% solutions, as a function of R.

3.3. Density and morphology of cellulose cryogel

The bulk density of cellulose cryogels is shown in Fig. 4. The density decreases with the increase of ECH concentration, as expected, because of gels swelling during coagulation at R > 1.

The influence of chemical cross-linking on cellulose cryogel morphology was investigated by SEM (Fig. 5). For physically cross-linked sample (5% R0, Fig. 5a) the morphology is very heterogeneous. The increase of ECH concentration (samples 5%R1 and 5%R2, Fig. 5b and c, respectively) leads to the increase of pore size and disappearance of denser regions, the morphology is foam-like. At high cross-linking (5% R4) the morphology again becomes extremely heterogeneous, with denser regions on one hand and some pores reaching 200 μm on the other hand (Fig. 5d).

3.4. Kinetics of cellulose cryogel swelling in water and PrHy release

In order to understand the release of a drug from a matrix, the kinetics of matrix evolution (if any) must be first studied in the same conditions. As mentioned above, cellulose cryogels are swelling when immersed in water, and the degree of swelling depends on cellulose and ECH concentration (Fig. 6). If the time scale of matrix swelling and of drug release is comparable, the latter will depend on matrix evolution in time.

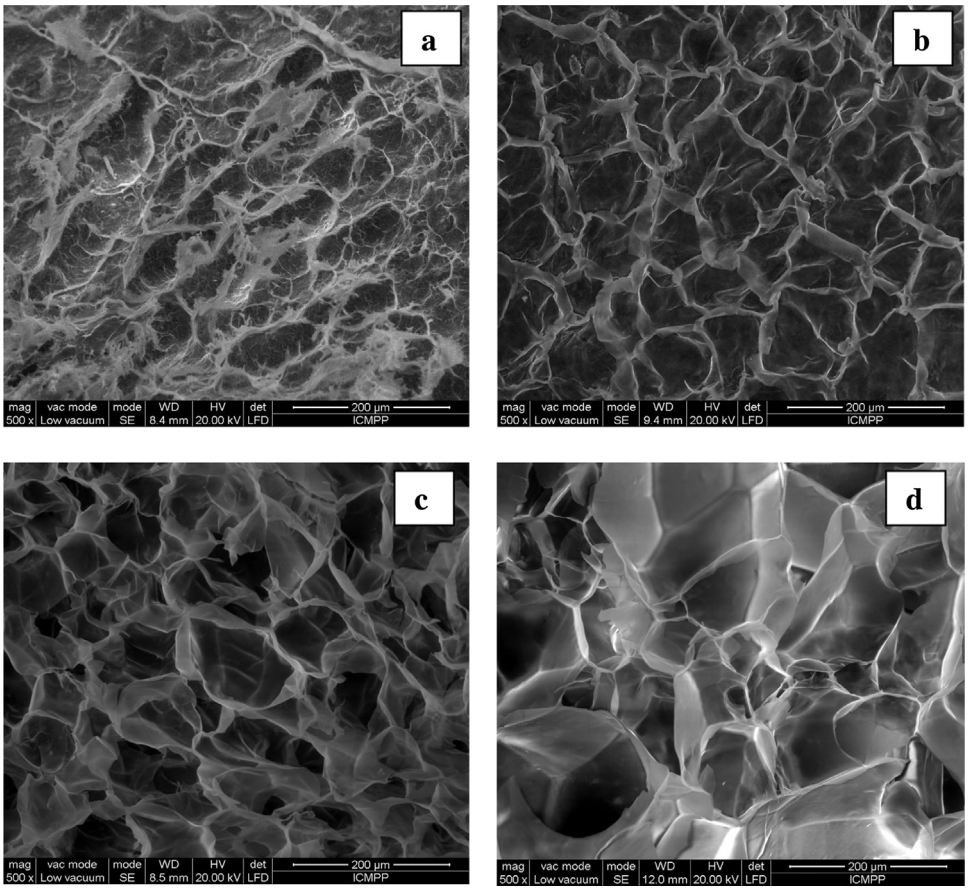

Fig. 5. SEM images of cellulose cryogels: (a) physically cross-linked, 5% R0 and chemically cross-linked (b) 5% R1, (c) 5% R2 and (d) 5% R4.

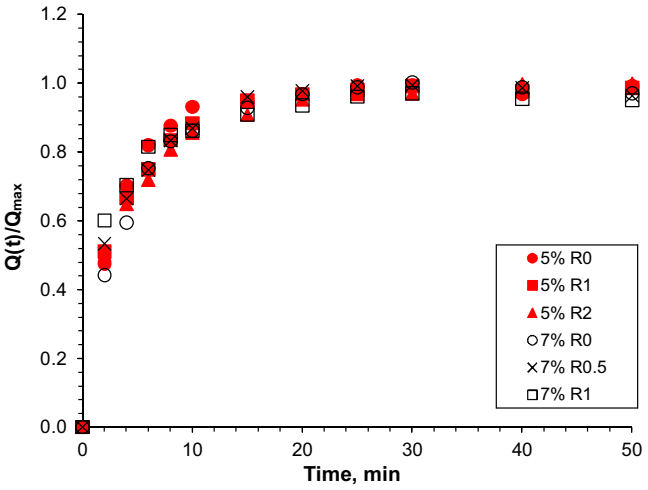

Fig. 6. Evolution of the reduced swelling degree as a function of time, at 37 °C, for cellulose cryogels from 5 wt% (filled points) and 7 wt% (open points) solutions with different ECH concentrations.

Fig. 6 shows that the equilibrium swelling is reached in about 20 min for all samples studied. The kinetics of swelling can be fitted, in a very general way, with the following equation:

$$Q(t)/Q_{max} = 1 - exp(-kt) \quad (7)$$

where t is time and k is a constant. Because all swelling data fall together (Fig. 6), k does not depend either on cellulose concentration or type of cross-linking and varies from 0.21 to 0.27 min^{-1}. The reason is that cellulose concentration in the cryogels is very low and pores are very large (Fig. 5); the diffusion of water is thus not sensitive to the variations in cellulose cryogels morphology.

Fig. 7a and b shows the examples of the release profiles of PrHy from cellulose cryogels made from physically gelled 5 wt% solutions, immersed in water at 37 °C and pH 6.5, for various loaded procaine concentrations. The release is completed in about 3 h, it is much slower than cryogel swelling in water. As expected, higher the initial drug concentration, higher amount of drug is released. Fig. 7b shows that higher swelling of cellulose leads to more uptake of drug during loading.

It is of interest to compare the results obtained with the kinetics of PrHy release from other cellulose matrices. For example, PrHy release was completed after 30 min from freeze-dried cellulose nanocrystals (CNC) modified with chitosan oligosaccharide at pH 8 (Akhlaghi, Berry, & Tam, 2013); similar, and even slightly quicker kinetics was reported for freeze-dried oxidated and not CNC (Akhlaghi, Tiong, Berry, & Tam, 2014). When cellulose nanofibers were grafted with polyethyleneimine and freeze-dried, the release of sodium salicylate at pH 7.4 and 2 was much slower (10–12 h) as compared to non-modified nanofibers in the same conditions (Zhao et al., 2015). One of the reasons of the burst release from nanocellulose-based matrices is lower cellulose concentration than in prepared here cryogels. Another reason can be different morphologies: cellulose II cryogels are foam-like, with continuous walls, while nanocellulose cryogels are built of a network of thin fibrils. Drug diffusion in cellulose II cryogels is thus much slower. Even slower kinetics (~10 h) was reported for the release of polyphenols from grape seeds of *Chambourcin* type in water:ethanol (19:1) solution at 37 °C from cellulose II-lignin hydrogels. It was shown that one of the factors which control the process was the lignin content within the matrices (Ciolacu et al., 2012).

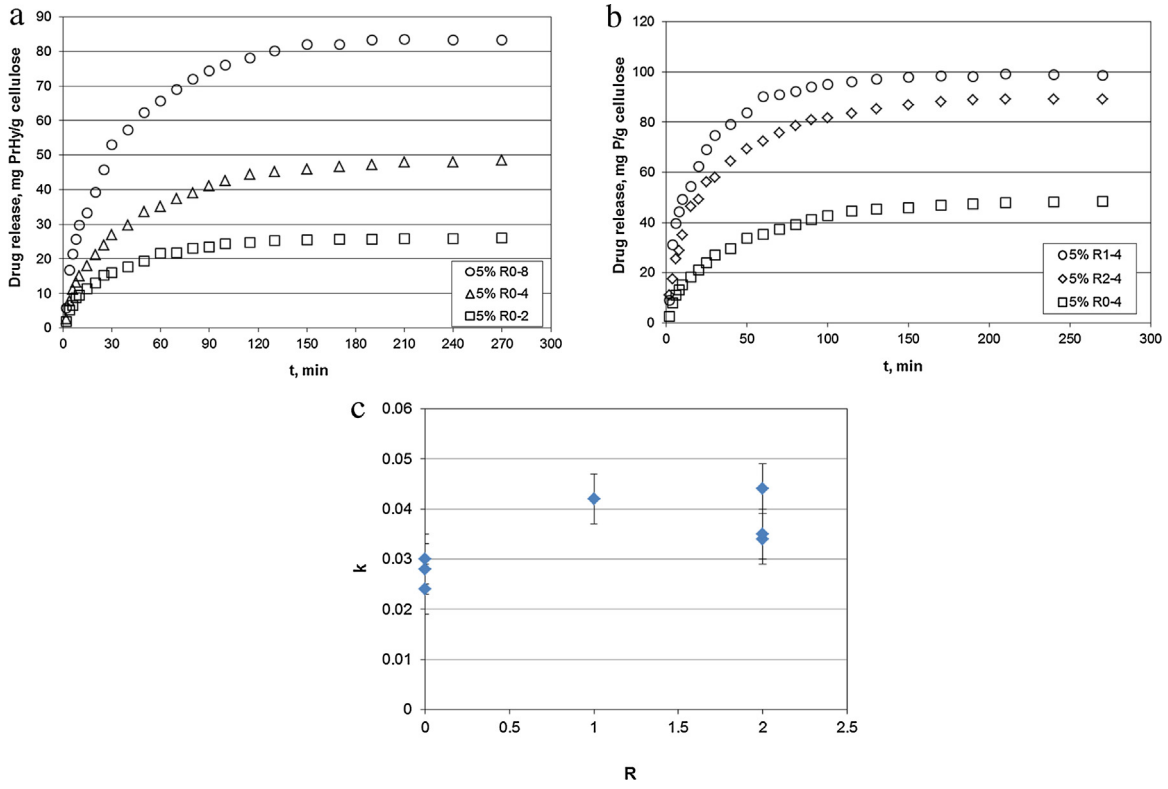

Fig. 7. Release profiles (a and b) and rate of release (c) of procaine in water at 37 °C from: (a) cellulose cryogels 5% R0 loaded with different amount of PrHy; (b) cellulose cryogels loaded with 4 g/L PrHy at different R and (c) cellulose cryogels prepared from 5 wt% solutions as a function of R.

To perform an adequate quantitative comparison of the kinetics of PrHy release from different cellulose cryogels is difficult because samples are swelling to various degrees and releasing the drug at the same time. In a very rough approximation, we used the same general approach as given in Eq. (7): $M(t)/M_{max} = 1-exp(-nt)$ where $M(t)$ and M_{max} are the mass of PrHy released in time and at equilibrium, respectively, and n is constant which characterizes the rate of release. The dependence of n for cellulose cryogels made from 5 wt% solutions is shown in Fig. 7c. Even with large cumulated experimental and approximation errors, the rate of release is higher for chemically cross-linked cellulose compared to their physically cross-linked counterparts. Lower cryogel density and larger pores are the reasons of the quicker release.

Procaine is an asymmetric molecule from amino-ester group; its molecular weight is 236 g/mol. Thus, as expected, the rate of PrHy release is one order of magnitude lower that the rate of cryogels swelling in water.

4. Discussion

Cellulose solutions undergo a physical gelation in 7–9 wt% NaOH-water solvent with the increase of time and temperature (Roy et al., 2003). Gelation occurs due to cellulose chains self-association because of the preferential cellulose–cellulose and not cellulose-solvent interactions; this physical gelation is accompanied by a micro-phase separation. By adding a cross-linker (ECH) in cellulose-NaOH-water solution, cellulose chains become chemically cross-linked. Two mechanisms are therefore present and can possibly compete: physical gelation due to chains self-association and chemical cross-linking (Fig. 8a).

Now we summarise the experimental results obtained on the structure and properties of physically and chemically gelled cellulose:

i) NMR, XRD and DSC show that in the presence of ECH cellulose crystallinity decreases compared to cellulose II obtained via physical gelation.
ii) The swelling of cellulose gel (never-dried, during coagulation) and of dry cellulose cryogels in water increases with the increase of ECH concentration, in the region of [ECH] <2.
iii) Humidity adsorption by cellulose cryogels increases in the presence of ECH.
iv) Density of chemically cross-linked cellulose cryogels is lower than that of their physically gelled counterparts.

Based on these results, we suggest that chemical bonds act as "spacers" preventing, at least partly, the self-association of cellulose chains, as shown on a sketch in Fig. 8a.

If accepting this hypothesis, it is then easy to interpret the experimental results obtained on the crystallinity and anomalous swelling of chemically cross-linked cellulose. A schematic presentation of the structure of physical and chemical cellulose gels is shown in Fig. 8b. Chemical gelation (i) perturbs cellulose chains self-association and packing which leads to the decrease of crystallinity; (ii) leads to a more homogeneous morphology which results in transparent swollen coagulated cellulose hydrogels; (iii) increases swelling in water and adsorption of water vapours due to a more porous structure.

As a consequence, the difference in the structure and swelling of physical *vs.* chemically cross-linked cellulose influences their release properties: in chemically cross-linked cellulose larger amount of drug can be loaded and the release kinetics is faster compared to physically cross-linked matrix. By varying cellulose concentration and the amount of cross-linker it is possible to prepare versatile cellulose hydrogels and dry porous networks with controlled morphology and porosity.

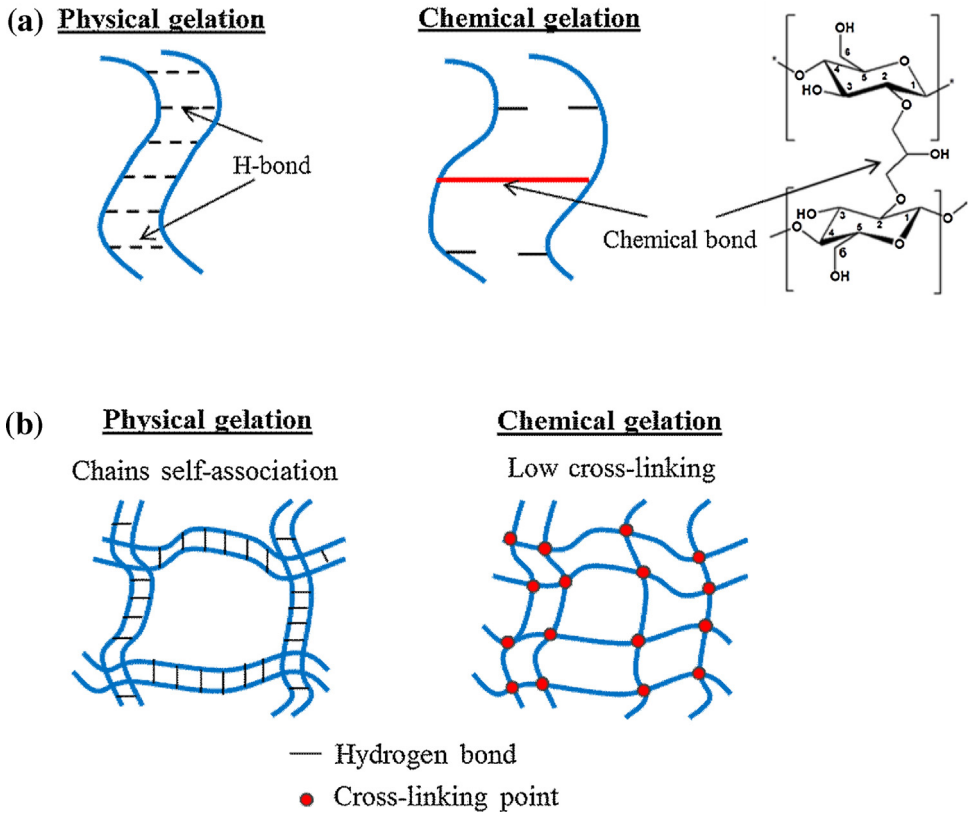

Fig. 8. (a) A sketch of network formation in cellulose solutions: physical gelation via self-association of chains and chemical cross-linking; (b) a schematic presentation of the structures of physical and chemical cellulose gels.

5. Conclusions

Cellulose cryogels were prepared from cellulose-8%NaOH-water solutions by gelation, coagulation in water followed by freeze-drying. Gelation was physical ("aging" of cellulose solutions) and chemical (cross-linking with different amounts of ECH).

NMR, XRD and DSC showed that the crystallinity of chemically cross-linked cellulose is lower than that of physically cross-linked counterparts, and it decreases with the increase of ECH concentration in solution. An anomalous swelling of chemically cross-linked cellulose gels was recorded: while physical gels contract during coagulation in water and become opaque, chemically cross-linked gels swell and become transparent. The degree of swelling of cellulose cryogels in water varies from 700 to 2500% depending on cellulose and ECH concentration in solution, and it increases with the increase of ECH concentration, confirming the results obtained on the never-dried cellulose hydrogels. The density of cellulose cryogels decreases with the increase of ECH concentration.

The results obtained allowed suggesting a hypothesis explaining the difference in structure formation during cellulose physical and chemical gelation: while during physical gelation chains are self-associating forming a heterogeneous network with "thick" walls and pores of various sizes, chemical bonds act as spacers between chains perturbing their self-association and preventing packing. This results in a more homogeneous chemical networks with higher swelling and transparency in the wet state, and lower density in the dry state.

The release of procaine was studied using UV–vis spectroscopy to test physically and chemically cross-linked cellulose as matrices for controlled release applications. It was shown that in order to interpret the release profiles, the swelling of cellulose cryogels must be taken into account. The kinetics and amount of drug released can be tuned by cellulose concentration, type of gelation and ECH concentration. It was also shown that in order to understand the kinetics of procaine release, the swelling of cellulose cryogel matrix in water must be taken into account as far as both processes, release and swelling, occur simultaneously.

Acknowledgments

This work was supported by a grant of the Romanian National Authority for Scientific Research and Innovation, CNCS—UEFISCDI, project number PN-II-RU-TE-2014-4-0558. A part of this work was also financial supported by French National Agency for Research (ANR), "Nanocel" project ANR-09-HABISOL-010.

Appendix A. Supplementary data

Supplementary data associated with this article can be found, in the online version, at http://dx.doi.org/10.1016/j.carbpol.2016.05.084.

References

Ahmed, E. M. (2015). Hydrogel: Preparation, characterization, and applications: a review. *Journal of Advanced Research*, *6*(2), 105–121.

Akhlaghi, S. P., Berry, R. C., & Tam, K. C. (2013). Surface modification of cellulose nanocrystal with chitosan oligosaccharide for drug delivery applications. *Cellulose*, *20*, 1747–1764.

Akhlaghi, S. P., Tiong, D., Berry, R. M., & Tam, K. C. (2014). Comparative release studies of two cationic model drugs from different cellulose nanocrystal derivatives. *European Journal of Pharmaceutics and Biopharmaceutics*, *88*, 207–215.

Ando, H., & Konishi, T. (2000). Structure analysis of regenerated cellulose hydrogels by small-angle and ultra-small-angle X-ray scattering. *Physical Review E: Statistical Physics, Plasmas, Fluids and Related Interdisciplinary Topics*, *62*(1), 727–733.

Bhattacharya, M., Malinen, M. M., Lauren, P., Lou, Y.-R., Kuisma, S. W., Kanninen, L., et al. (2012). Nanofibrillar cellulose hydrogel promotes three-dimensional liver cell culture. *Journal of Controlled Release*, *164*, 291–298.
Budtova, T., & Navard, P. (2016). Cellulose in NaOH–water based solvents: a review. *Cellulose*, *23*, 5–55.
Chang, C., & Zhang, L. (2011). Cellulose-based hydrogels: present status and application prospects. *Carbohydrate Polymers*, *84*, 40–53.
Chang, C., Lue, A., & Zhang, L. (2008). Effects of crosslinking methods on structure and properties of cellulose/PVA hydrogels. *Macromolecular Chemistry and Physics*, *209*, 1266–1273.
Chang, C., Duan, B., Cai, J., & Zhang, L. (2010). Superabsorbent hydrogels based on cellulose for smart swelling and controllable delivery. *European Polymer Journal*, *46*(1), 92–100.
Chang, C., Zhang, L., Zhou, J., Zhang, L., & Kennedy, J. F. (2010). Structure and properties of hydrogels prepared from cellulose in NaOH/urea aqueous solutions. *Carbohydrate Polymers*, *82*, 122–127.
Ciolacu, D., & Popa, V. I. (2010). *Cellulose allomorphs: structure, accessibility and reactivity. Series: polymer science and technology*. United States: Nova Science Publishers, Inc.
Ciolacu, D., Ciolacu, F., & Popa, V. I. (2008). Supramolecular structure—a key parameter for cellulose biodegradation. *Macromolecular Symposia*, *272*(1), 136–142.
Ciolacu, D., Oprea, A., Anghel, N., Cazacu, G., & Cazacu, M. (2012). New cellulose—lignin hydrogels and their application in controlled release of polyphenols. *Materials Science and Engineering: C*, *32*, 452–463.
Ciolacu, D. (2007). On the supramolecular structure of cellulose allomorphs after enzymatic degradation. *Journal of Optoelectronics and Advanced Materials*, *9*(4), 1033–1037.
Ciolacu, D., Ciolacu, F., & Popa, V. I. (2011). Amorphous cellulose—structure and characterization. *Cellulose Chemistry and Technology*, *45*(1–2), 13–21.
Ciolacu, D., Gorgieva, S., Tampu, D., & Kokol, V. (2011). Enzymatic hydrolysis of different allomorphic forms of microcrystalline cellulose. *Cellulose*, *18*, 1527–1541.
de Oliveira, W., & Glasser, W. G. (1996). Hydrogels from polysaccharides. 1. Cellulose beads for chromatographic support. *Journal of Applied Polymer Science*, *60*, 63–73.
Egal, M., Budtova, T., & Navard, P. (2007). Structure of aqueous solutions of microcrystalline cellulose/sodium hydroxide below 0 °C and the limit of cellulose dissolution. *Biomacromolecules*, *8*(7), 2282–2287.
Gavillon, R., & Budtova, T. (2008). Aerocellulose: new highly porous cellulose prepared from cellulose-NaOH aqueous solutions. *Biomacromolecules*, *9*(1), 269–277.
Innerlohinger, J., Weber, H. K., & Kraft, G. (2006). Aerocellulose: aerogels and aerogel-like materials: made from cellulose. *Macromolecular Symposia*, *244*, 126–135.
Klemm, D., Philipp, B., Heize, T., Heinze, U., & Wagwnknecht, W. (1998). *General considerations on structure and reactivity of cellulose*. pp. 9–167. *Comprehensive cellulose chemistry. Functionalization of cellulose* (Vol. 2) Weinheim: WILEY-VCH.
Klemm, D., Heubletin, B., Fink, H.-P., & Bohn, A. (2005). Cellulose: fascinating biopolymer and sustainable raw material. *Angewandte Chemie International Edition*, *44*, 3358–3393.
Klemm, D., Kramer, F., Moritz, S., Lindström, T., Ankerfors, M., Gray, D., et al. (2011). Nanocelluloses: a new family of nature-based materials. *Angewandte Chemie International Edition*, *50*, 5438–5466.
Kono, H., Numata, Y., Erata, T., & Takai, M. (2004). ^{13}C and ^{1}H resonance assignment of mercerized cellulose II by two-dimensional MAS NMR spectroscopies. *Macromolecules*, *37*, 5310–5316.
Luby, P., Kuniak, L., & Fanter, C. (1979). Cross-linking statistics, 3. Relation between relative reactivity and accessibility of cellulose hydroxyl groups. *Die Makromolekulare Chemie*, *180*, 2379–2386.
Luo, X., & Zhang, L. (2013). New solvents and functional materials prepared from cellulose solutions in alkali/urea aqueous system. *Food Research International*, *52*, 387–400.
Massiot, D., Fayon, F., Capron, M., King, I., Le Calvé, S., Alonso, B., et al. (2002). Modelling one-and two-dimensional solid-state NMR spectra. *Magnetic Resonance in Chemistry*, *40*, 70–76.
Östlund, Å., Idström, A., Olsson, C., Larsson, P. T., & Nordstierna, L. (2013). Modification of crystallinity and pore size distribution in coagulated cellulose films. *Cellulose*, *20*, 1657–1667.
Park, S., Johnson, D. K., Ishizawa, C. I., Parilla, P. A., & Davis, M. F. (2009). Measuring the crystallinity index of cellulose by solid state 13C nuclear magnetic resonance. *Cellulose*, *16*, 641–647.
Peng, B. L., Dhar, N., Liu, H. L., & Tam, K. C. (2011). Chemistry and applications of nanocrystalline cellulose and its derivatives: a nanotechnology perspective. *The Canadian Journal of Chemical Engineering*, *89*, 1191–1206.
Qin, X., Lu, A., & Zhang, L. (2013). Gelation behavior of cellulose in NaOH/urea aqueous system via cross-linking. *Cellulose*, *20*, 1669–1677.
Qiu, X., & Hu, S. (2013). Smart materials based on cellulose: a review of the preparations, properties and applications. *Materials*, *6*, 738–781.
Rowland, S. P., Roberts, E. J., & Wade, C. P. (1969). Selective accessibilities of hydroxyl groups in the microstructure of cotton cellulose. *Textile Research Journal*, *39*, 530–542.
Roy, C., Budtova, T., & Navard, P. (2003). Rheological properties and gelation of aqueous cellulose–NaOH solutions. *Biomacromolecules*, *4*, 259–264.
Rudaz, C. (2013). *Cellulose and pectin aerogels: towards their nano-structuration. PhD thesis*. Mines ParisTech.
Saito, H., Sakurai, A., Sakakibara, M., & Saga, H. (2003). Preparation and properties of transparent cellulose hydrogels. *Journal of Applied Polymer Science*, *90*, 3020–3025.
Saito, T., Uematsu, T., Kimura, S., Enomaea, T., & Isogai, A. (2011). Self-aligned integration of native cellulose nanofibrils towards producing diverse bulk materials. *Soft Matter*, *7*, 8804–8809.
Sannino, A., Demitri, C., & Madaghiele, M. (2009). Biodegradable cellulose-based hydrogels: design and applications. *Materials*, *2*, 353–373.
Sescousse, R., & Budtova, T. (2009). Influence of processing parameters on regeneration kinetics and morphology of porous cellulose from cellulose–NaOH–water solutions. *Cellulose*, *16*(3), 417–426.
Sescousse, R., Gavillon, R., & Budtova, T. (2011a). Aerocellulose from cellulose-ionic liquid solutions: preparation: properties and comparison with cellulose–NaOH and cellulose–NMMO routes. *Carbohydrate Polymers*, *83*, 1766–1774.
Sescousse, R., Gavillon, R., & Budtova, T. (2011b). Wet and dry highly porous cellulose beads from cellulose–NaOH–water solutions: influence of the preparation conditions on beads shape and encapsulation of inorganic particles. *Journal of Materials Science*, *46*, 759–765.
Turner, M. B., Spear, S. K., Holbrey, J. D., & Rogers, R. D. (2004). Production of bioactive cellulose films reconstituted from ionic liquids. *Biomacromolecules*, *5*, 1379–1384.
Xia, Z., Patchan, M., Maranchi, J., & Trexler, M. (2015). Structure and relaxation in cellulose hydrogels. *Journal of Applied Polymer Science*, *132*, 42071–42075.
Zhao, J., Lu, C., He, X., Zhang, X., Zhang, W., & Zhang, X. (2015). Polyethylenimine-grafted cellulose nanofibril aerogels as versatile vehicles for drug delivery. *ACS Applied Materials & Interfaces*, *7*, 2607–2615.
Zhou, J., Chang, C., Zhang, R., & Zhang, L. (2007). Hydrogels prepared from unsubstituted cellulose in NaOH/urea aqueous solution. *Macromolecular Bioscience*, *7*, 804–809.
Zuckerstätter, G., Schild, G., Wollboldt, P., Röder, T., Weber, H. K., & Sixta, H. (2009). The elucidation of cellulose supramolecular structure by 13C CP-MAS NMR. *Lenzinger Berichte*, *87*, 38–46.